Theory of Adaptive Fiber Composites

SOLID MECHANICS AND ITS APPLICATIONS
Volume 161

Series Editor: G.M.L. GLADWELL
Department of Civil Engineering
University of Waterloo
Waterloo, Ontario, Canada N2L 3GI

Aims and Scope of the Series

The fundamental questions arising in mechanics are: *Why?, How?,* and *How much?* The aim of this series is to provide lucid accounts written by authoritative researchers giving vision and insight in answering these questions on the subject of mechanics as it relates to solids.

The scope of the series covers the entire spectrum of solid mechanics. Thus it includes the foundation of mechanics; variational formulations; computational mechanics; statics, kinematics and dynamics of rigid and elastic bodies: vibrations of solids and structures; dynamical systems and chaos; the theories of elasticity, plasticity and viscoelasticity; composite materials; rods, beams, shells and membranes; structural control and stability; soils, rocks and geomechanics; fracture; tribology; experimental mechanics; biomechanics and machine design.

The median level of presentation is the first year graduate student. Some texts are monographs defining the current state of the field; others are accessible to final year undergraduates; but essentially the emphasis is on readability and clarity.

For other titles published in this series, go to
www.springer.com/series/6557

Tobias H. Brockmann

Theory of Adaptive Fiber Composites

From Piezoelectric Material Behavior to Dynamics of Rotating Structures

Springer

T.H. Brockmann
Donauwörth
Germany
tobias.brockmann@eurocopter.com

Approved Dissertation – Helmut-Schmidt-Universität, Hamburg, Germany

ISSN 0925-0042
ISBN 978-90-481-2434-3 e-ISBN 978-90-481-2435-0
DOI 10.1007/978-90-481-2435-0
Springer Dordrecht Heidelberg London New York

Library of Congress Control Number: 2009925999

Contents

List of Figures

List of Tables

List of Symbols

Indices

1, 2, 3	axial directions in the material coordinate system
s, n, x	axial directions in the shell coordinate system
x, y, z	axial directions in the beam coordinate system
i, f, m	association with inclusion respectively fiber phase or matrix phase
i, j, k	association with branches, junctions, and cells of a cross-section
†, ‡	association with unknown respectively prescribed degrees of freedom
EA, GL	association with Euler Almansi or Green Lagrange approach

Greek Symbols

α	rotation angle
$\boldsymbol{\alpha}$	vector of thermal strain coefficients
β, $\boldsymbol{\beta}$	rotation angle; column matrix of rotational parameters
$\mathbf{\beta}$	inverse dielectric permittivity matrix
γ	shear strain component
$\mathbf{\Gamma}$	constraint matrix
$\delta(\cdot)$	virtual quantity
ϵ, $\boldsymbol{\epsilon}$	dielectric permittivity, matrix
ε	normal strain component
$\boldsymbol{\varepsilon}$, $\boldsymbol{\varepsilon}$	strain tensor, column matrix
ζ	generating half angle
η	warping influence function
ϑ	shell middle surface rotation
θ	integrands of warping displacement
Θ	warping function
κ, $\boldsymbol{\kappa}$	shell bending curvature; shell curvature column matrix
λ	decay length parameter; eigenvalue
Λ, $\partial\Lambda$	spatial domain, surrounding boundary
$\boldsymbol{\mu}$	column matrix of remaining strain/electric field strength measures

ν	inclusion respectively fiber fraction
$\boldsymbol{\nu}$	column matrix of all degrees of freedom
ξ	normalized lengthwise coordinate
$\boldsymbol{\Xi}$	concentration matrix for strains and electric field strengths
ρ	mass density
ϱ	material, geometry, and load case constant
σ, $\boldsymbol{\sigma}$, $\boldsymbol{\upsigma}$	normal stress component, column matrix, tensor
$\boldsymbol{\varsigma}$	column matrix of integrands for side conditions of variational prob.
$\boldsymbol{\Sigma}$	concentration matrix for stresses and electric flux densities
τ	shear stress component
υ	unidirectional electrostatic field transition
$\boldsymbol{\Upsilon}$	equivalent inclusion constraint matrix
ϕ	beam twisting angle
Φ	warping influence abbreviation
φ	electric potential
$\boldsymbol{\varphi}$	column matrix of all electric degrees of freedom
$\boldsymbol{\chi}$	strain and electric field strength column matrix
$\hat{\boldsymbol{\chi}}$, $\check{\boldsymbol{\chi}}$	rearranged strain and electric field strength column submatrix
ψ	shell twisting curvature
ω	natural frequency
Ω	rotor angular velocity

Latin Symbols

a	cross-sectional dimension; height
$\mathtt{a}$	beam constitutive coefficient ratio
$\boldsymbol{a}$	acceleration vector
$\mathfrak{A}$	Lamé parameter
A, $\boldsymbol{A}$	area, normal vector
$\mathbf{A}$	matrix of interpolation functions
$\mathtt{A}$, $\mathbb{A}$	shell extensional coefficient, matrix
b	lengthwise dimension; width
$\mathbf{B}$	matrix of interpolation functions
$\mathtt{B}$, $\mathbb{B}$	shell coupling coefficient, matrix
c	geometry factor
$\mathbb{C}$, $\bar{\mathbb{C}}$	electromechanical property matrix, with modified signs
C, $\mathbf{C}$	mechanical stiffness coefficient, matrix
$\mathrm{d}\,(\cdot)$	differential quantity
d, $\mathbf{d}$	induced strain piezoelectric coupling coefficient, matrix
$\mathtt{D}$, $\mathbb{D}$	shell bending coefficient, matrix
D, $\boldsymbol{D}$	electric flux density component, vector
e, $\mathbf{e}$	induced stress piezoelectric coupling coefficient, matrix
$\boldsymbol{e}$	orthonormal base vector
E, $\bar{E}$	electric field strength component, with modified sign
$\boldsymbol{E}$, $\bar{\boldsymbol{E}}$	electric field strength vector, with modified sign

$\mathbb{E}$, $\bar{\mathbb{E}}$	normal mode electromechanical property matrix, with modified signs
$\mathbf{E}$	transformation matrix between Cartesian/curvilinear coordinates
f	Hermite polynomial; group association of electr. paralleled laminae
$\hat{\boldsymbol{f}}$, $\check{\boldsymbol{f}}$, $\boldsymbol{F}$	area, volume, general force vector
$\bar{\mathbb{F}}$	partially inverted normal mode electromechanical property matrix
g	Hermite polynomial
$\boldsymbol{g}$	column matrix of applied electric loads
G, g	electric loads—internal, applied per unit length
$\mathbb{G}$, $\bar{\mathbb{G}}$	shear mode electromechanical property matrix, with modified signs
$\mathbf{G}$, $\hat{\mathbf{G}}$, $\check{\mathbf{G}}$	geometric stiffness matrices of know initial internal loads
h	cubic Hermite polynomial
H, h	laminae thickness, ratio
$\boldsymbol{h}$	column matrix to match homogeneous solution to initial conditions
$\mathbf{H}$	modal matrix
$\mathbf{I}$	identity matrix
$\mathbf{J}$	matrix of strain relations between beam and wall
$\mathbb{J}$	matrix of strain/electric field strength relations between beam/wall
k, K	laminae counter, total laminae number
$\mathbf{K}$	matrix of cross-sectional properties
$\mathbb{K}$	laminate constitutive matrix
$\hat{\mathbb{K}}$, $\mathring{\mathbb{K}}$, $\check{\mathbb{K}}$	laminate constitutive submatrices with rearranged components
l	length
L, l	element node position, element length
$\boldsymbol{l}$	column matrix of all actual applied loads
$\boldsymbol{L}$, $\hat{\boldsymbol{L}}$, $\check{\boldsymbol{L}}$	internal load column matrix, rearranged column submatrices
m, $\mathtt{m}$	mass, per unit length
m, $\mathtt{m}$	applied moment per unit length—arbitrary, constant
M	internal moment
$\mathbf{M}$, $\boldsymbol{m}$	inertia property element or system matrix, column matrix
$\boldsymbol{M}$	column matrix of shell out-of-plane resultants
n	shell through thickness coordinate; angular frequency multipl. factor
$\mathtt{n}$	beam geometry ratio
n, $\mathtt{n}$	applied normal force per unit length—arbitrary, constant
$\boldsymbol{n}$	column matrix of applied mechanical loads
N	total laminate thickness; normal force
$\boldsymbol{N}$	column matrix of shell in-plane resultants
$\boldsymbol{p}$, $\boldsymbol{P}$	position vector in deformed state, undeformed state
p, $\boldsymbol{p}$	relative sign of electric field strength, vector
$\mathbf{P}$, $\boldsymbol{p}$	internal loads element or system matrix, column matrix
$\mathbf{p}$, $\boldsymbol{p}$	beam constitutive submatrix, column submatrix
$\mathtt{P}$, $\mathbb{P}$	beam constitutive coefficient, matrix
q	cross-sectional quadrant
q, $\mathtt{q}$	applied transv. force/bimoment per unit length—arbitrary, constant
$\hat{q}$, $\check{q}$, Q	area, volume, general electric charge
Q	internal transverse force respectively warping bimoment

$\tilde{\mathbb{Q}}$	planar electromechanical property matrix
$\mathbb{Q}$, $\bar{\mathbb{Q}}$	rotated planar electromech. property matrix, with modified signs
$\mathtt{Q}$, $\bar{\mathtt{Q}}$	rotated planar electromech. property coefficient, with modified signs
$\boldsymbol{r}$	position vector in moving reference frame
R	radius of shell curvature
$\mathbf{R}$	engineering strain correction matrix; rotational transform. matrix
s, S	curvilinear coordinate, total path length
$\boldsymbol{s}$	distance vector; position vector
$\mathbf{S}$	mechanical compliance matrix
t	time coordinate
T	temperature
$\mathbf{T}$	mechanical transformation matrix
$\mathbb{T}$, $\tilde{\mathbb{T}}$	spatial, planar electromechanical transformation matrix
u	displacement in axial direction of the beam
$\mathfrak{u}$	displacement tangential to shell middle surface
$\boldsymbol{u}$	displacement vector; column matrix of mechanical degrees of freedom
$\mathcal{U}$	internal work contributions
$\mathcal{U}_0$	electroelastic energy density
v	displacement in transverse direction of the beam
$\mathfrak{v}$	displacement tangential to shell middle surface
V	volume
$\mathcal{V}$	external work contributions
w	displacement in transverse direction of the beam
$\mathfrak{w}$	displacement normal to shell middle surface
W	warping resultant
$\mathcal{W}$	work
x	lengthwise coordinate
$\boldsymbol{x}$, $\boldsymbol{X}$	momentary and reference particle position vector
X, $\bar{X}$	blade length from bolt to tip, radius of blade bolt position
y	transverse coordinate
$\boldsymbol{Y}$	column matrix of stresses and electric flux densities
z	transverse coordinate
$\boldsymbol{Z}$, $\bar{\boldsymbol{Z}}$	column matrix of strains and electric field strengths

1

Introduction

In this first chapter, we discuss the definition of adaptive structural systems as well as their associated constituents and relevant applications. On this basis, the targets of the work at hand are set and the necessary steps are illustrated.

1.1 Adaptive Structural Systems

According to *Beitz and Küttner* [11], a system is characterized by the delimitation from its environment. Consequently, the links to the environment, represented by input and output values, pass through the system's boundaries. A system may be divided into subsystems. For a structural system, the input and output values are mechanical loads or displacements. An adaptive system, sometimes also called smart or intelligent, is able to respond to changing environmental conditions. To realize an adaptive structural system, the structural properties need to be complemented by sensory capabilities, control resources, and actuation authority. This multiplicity of functions may be implemented by means of discrete subsystems, for example a host structure, load cells, control unit, and hydraulic actuators. A higher degree of integration can be achieved by making use of multifunctional materials which, in addition to their structural properties, are able to provide actuation authority and might even have sensory capabilities. Since such materials themselves do not have any kind of control resources, the term smart or intelligent appears to be an overstatement.

Due to the reversibility of the piezoelectric effect, materials exhibiting such an electromechanical coupling may be used to handle actuation as well as sensing tasks. The different piezoelectric materials are able to provide these properties in a frequency spectrum ranging beyond the level of acoustics. On the one hand, there are several monocrystals and polycrystalline ceramics, which are hard and brittle and therefore are suitable only for relatively small strains. On the other hand, there are semicrystalline polymers, which are soft and elastic but show less pronounced coupling properties. Another kind of

T.H. Brockmann, *Theory of Adaptive Fiber Composites*,
Solid Mechanics and Its Applications 161,

electromechanical coupling occurs in electrostrictive materials. This non-linear behavior is limited to actuation and typically applies also to some polycrystalline ceramics with similar consequences. Magnetostrictive materials may be used for actuation and sensing by virtue of non-linear magnetomechanical coupling. Thus, alloys of iron and rare earth elements are able to handle slightly higher strains than those that occur in electromechanical coupling examples in a frequency range up to the level of acoustics. To establish or detect the associated magnetic fields, comparatively massive devices need to be employed. Actuation with large strains may be realized by using phase changes of shape memory alloys. This highly non-linear thermomechanical coupling, however, is confined to very low frequencies. Carbon nanotubes possess excellent mechanical properties and their use for actuation as well as sensing is a promising subject of intense research activity in the field of material science.

The perfect multifunctional material is not yet available. However, many adaptive structural systems based on the above or alternative materials have been investigated and several have found their way into service. Typical application areas are the modification of shape or stiffness and especially the reduction of noise and vibration. When a structure is able to adapt to various operating conditions, design and dimensioning may differ substantially from that for conventional structures in so far as these are able to fulfill the mission at all. Therefore, possible implications of employing such adaptive structural systems are the extension of the operational range and a reduction in weight. Both criteria are of particular interest for spacecraft and aircraft applications where extreme environmental conditions need to be handled and a high degree of integration is entailed by high costs of space and weight. With the maturing of appropriate technologies, other application emerge: automobiles, gas turbines, machine tools, measurement machines, and sports equipment.

1.2 Objective and Scope

Piezoelectric ceramics have been found to be the most useful material class for integrating actuation and sensing functions into structures. To alleviate the mechanical shortcomings of these multifunctional materials, they may be embedded in the shape of fibers into a conventional material matrix. Consequently, the anisotropic constitutive properties can be tailored according to requirements and the failure behavior improves. With their inherited fast response in actuation as well as sensing, such adaptive fiber composites are well-suited to noise and vibration reduction. Helicopter rotor systems provide an interesting and widely perceptible field of application. Their oscillations can be reduced with the aid of aerodynamic coupling and fast manipulation of the angle of attack, induced by twist actuation of the rotor blade. On the one hand, the sensing properties may be used to determine the current state of deformation, while on the other hand, the actuation properties may be used to attain the required state of deformation. The implementation of such con-

cepts requires a comprehensive knowledge of the theoretical context from the examination of the material behavior to the simulation of the rotating structure. Control resources are also part of adaptive structural systems, but the associated means and algorithms represent a relatively self-contained topic, on which we will not focus in particular.

1.3 Outline and Overview

Chapter 2 describes the problem areas and solution approaches in helicopter rotor systems to exemplify the application of adaptive structural systems. Chapter 3 gives the necessary mathematical and physical fundamentals and completes these with a systematic approach to variational principles. Chapter 4 examines the constitutive properties of piezoelectric materials and deduces simplifying assumptions. Chapter 5 describes an enhanced method for determining constitutive properties of piezoelectric composites, compares it with alternative approaches, and validates it by using experimental results and finite element modeling. Chapter 6 derives a comprehensive description of composite shells containing piezoelectric layers. Chapter 7 develops a novel beam theory accounting for more than membrane-only wall properties of arbitrary cross-sections without additional degrees of freedom, as well as for shear flexibility and torsional warping effects. Chapter 8 shows how the principle of virtual work is able to obtain constitutive coefficients, equilibrium and boundary conditions, and rotation-induced prestress effects. Chapter 9 obtains the solutions to the static problem of the non-rotating structure in analytic fashion and to the dynamic problem of the rotating structure with the aid of finite element discretization. Chapter 10 uses the analytic solution for design optimization and checks the developed beam finite elements against an independent approach with commercial shell finite elements. Chapter 11 reviews the achievements concerning theory development and validation results and provides an outlook to possible extensions, implementations, and applications.

2

Helicopter Applications

"The air was drowsy with the murmur of bees and helicopters."

In *The Brave New World* of *Huxley* [102], the helicopter represents the dominant means of personal transportation. Huxley's shining but essentially dark vision of the future is still in the future for the most part. No one today would seriously dare to compare the noise of helicopters with the buzzing of bees. Noise and vibrations limit the use of helicopters: they are too noisy in towns, too easily detected in warfare. Cabin noise stresses both pilots and passengers. Vibrations can fatigue components and imply frequent and expensive inspections. Adaptive structural systems can mitigate these effects and improve flight performance. Vibration induced problems had to be addressed since the early days of rotorcraft development; noise related problems become more and more critical with today's versatile deployment. Figure 2.1 shows how these problems are interrelated and points at their economic impact.

2.1 Noise and Vibration

This section gives an overview of the causes of helicopter noise and vibration, as well as of their effects on the aircraft and its environment.

2.1.1 Generation

Structural vibration and the emitted noise of a rotorcraft are closely related. This concerns especially those parts with aeroelastic interaction where aerodynamic loads and mechanical reactions excite the structure on the one hand and cause acoustic effects in the circumfluent air on the other hand. The induced vibrations tend to spread over the entire system and might initiate noise emission or other problems at different locations.

T.H. Brockmann, *Theory of Adaptive Fiber Composites*,
Solid Mechanics and Its Applications 161,

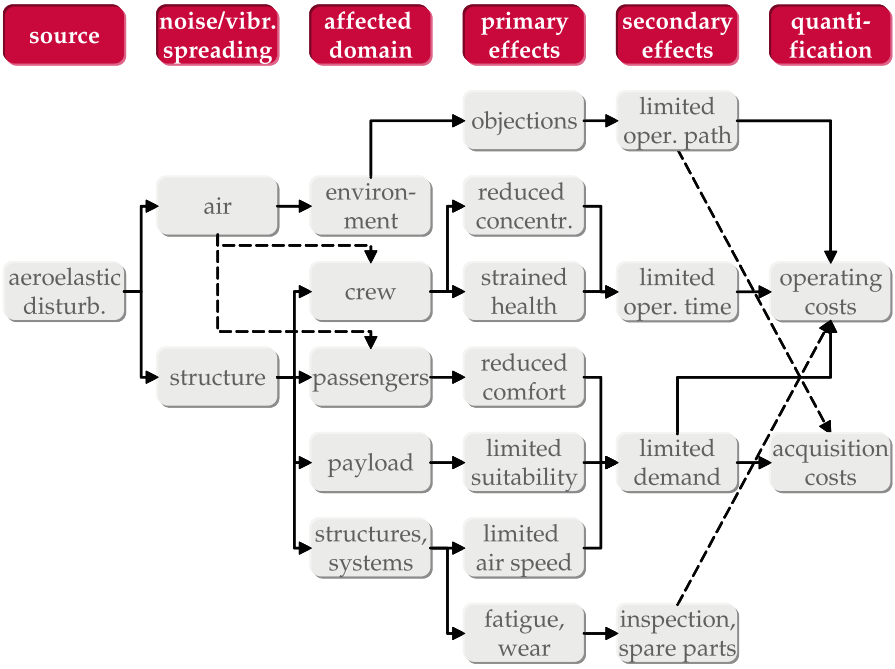

Fig. 2.1. Complexity of noise- and vibration-related problems of the helicopter.

Main Rotor

The main rotor of a helicopter is very susceptible to oscillations. The slender blades have considerable aerodynamic damping only in the flapwise direction. To attain balanced a lift on advancing and retreating blades in non-hover flight, the swash plate mechanism of the rotor hub varies the angle of attack. The resulting aerodynamic flow is complicated, leading to undesirable structural and acoustic effects. The subsequent Section 2.2 gives a detailed description of the rotor-related processes.

Tail Rotor

The lateral thrust of the tail rotor of a helicopter has to compensate for the main rotor torque. For maximum effectiveness, it is operated with a rotational speed as high as permitted by the blade tip velocity, but well below the speed of sound. In general, the noise- and vibration-generating mechanisms are similar to those of the main rotor. While there is no cyclic blade pitch, the interaction with the main rotor outflow has to be taken into account. Due to the comparatively small diameter of the tail rotor, its rotational speed is significantly higher than that of the main rotor and thus the emitted noise and vibrations have higher frequencies, see *Staufenbiel et al.* [168].

Engine and Drivetrain

In the early days of helicopter development, the engine was a major source of noise and vibration. Contemporary turboshaft engines with optimized compressors produce excitations at higher frequencies with lower intensities, becoming significant only in certain flight situations, see *Allongue et al.* [5]. Another subordinate source of oscillations is the tooth engagement in the gearbox, as reported by *Gembler* [79].

2.1.2 Areas of Relevance

The noise and vibration sources discussed above have very different characteristics. Consequently, the various implications and their respective perception depend strongly on the location of the observer. The situation will be discussed briefly in the following from the three basic points of view.

Noise in the Distance

The sound radiated by the rotorcraft into its environment is what the critical observer perceives as noise pollution and what delivers a characteristic acoustic signature for aircraft detection and classification. The typical rotorcraft sound is composed of several components with destinctive directivity and intensity, depending on the flight conditions. In general, at a distance, the main rotor noise is dominant, the high frequency emissions of the tail rotor have some relevance, and the engine noise is secondary.

Vibrations of the Structure

The vibrations generated by the different sources all over the rotorcraft are transmitted throughout the entire structure. For example, the loads, due to the various processes occurring at the main rotor blades, are transmitted via the rotor hub to the main drive shaft and then via the bearings, casing, and mounting of the gearbox to the fuselage. Thus, the effects of the spreading oscillations can be reduced by improvements at their point of origin or by decoupling somewhere on the path of propagation. Vibration fosters wear and fatigue. This entails intensive maintenance with regular exchange of critical parts.

Noise and Vibrations Inside the Cabin

Oscillations travel through the structure to the cabin and reach pilots and passengers, as well as vibration sensitive navigation equipment; some of this energy is radiated to the air inside the cabin. In addition to this structural sound path, there is the direct air sound path, see *Gembler* [79]; for example

the noise emitted by the gearbox casing is transferred through the air volumes in between. There is also an aerodynamic interaction between the fuselage and the passing blades of the main rotor, which especially hits the window and panel areas close to the pilots. Seats with vibration isolation and active head sets can partially decouple the human body from the structure and surrounding air respectively, to retain the health and concentrativeness of crew and passengers.

2.2 Main Rotor

As has been shown in the previous section, the main rotor plays the decisive role for many noise and vibration problems. It is best to tackle such a problem at the source before diffusion and diversification. Figure 2.2 shows the excitation mechanisms at the main rotor. Their characteristics are discussed in detail based on the investigations of *Brentner and Farassat* [25], *Schmitz and Yu* [161], *Edwards and Cox* [71].

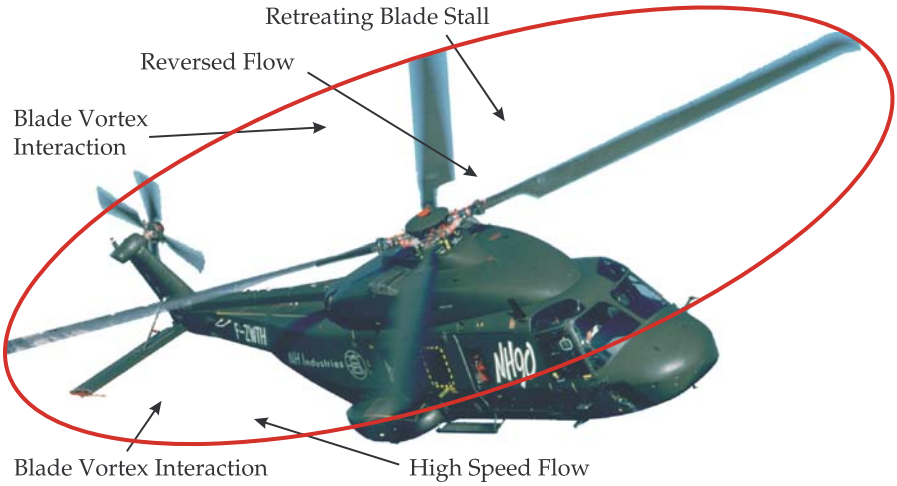

Fig. 2.2. Aerodynamic sources of noise and vibration at the helicopter main rotor; original photograph by *Eurocopter*.

2.2.1 Rotational Sources

Rotational noise comprises two mechanisms related to linear aerodynamic theory: thickness noise caused by the displacement and reconnection of the air by the rotor blades; loading noise due to the forces that the rotor blades exert on the air. For a fixed location of the rotor plane, these processes occur

periodically with the blade passage frequency, delivering a discrete spectrum with corresponding higher harmonic frequencies. As both effects depend on the relative velocity of the blade against the surrounding medium, the sound waves originate in the forward flight situation from the advancing side of the rotor plane and propagate ahead of the blade in the flight direction. While the thickness noise radiates mainly in the rotor plane, the emission of loading noise tends slightly downwards.

2.2.2 Impulsive Sources

The impulsive noise of a helicopter leads to several effects with pulsing characteristic and high amplitudes at discrete frequencies. Again, we are concerned with the higher harmonics of the blade passage frequency. These types of noise occur in different flight situations and are recognized by the human ear as extremely annoying.

Blade Vortex Interaction

As for any airfoil, a vortex wake is shed at the tip of a rotor blade. In forward flight, the rotor plane is tilted slightly forward, so these tip vortices do not come into direct contact with the rotor again. In steady descending flight however, the blades pass through the tip vortices of their predecessors. This means that the strength and size of the vortex, as well as interaction angle and vertical separation of blade and vortex line are important. Especially when they are almost in parallel, the interaction is comparable to a rapid change in the angle of attack with the respective consequences. The effect is aerodynamically similar to ordinary loading noise, but with an impulsive character. Most relevant are the outer blade regions on the advancing side, while blade vortex interaction (BVI) noise is recognizable also on the retreating side. The radiation takes place below and ahead of the blade.

High Speed Flow Conditions

In forward flight, the blade rotational speed and the flight speed are superimposed; these components add up on the advancing side of the rotor plane. When this leads to blade tip velocities close to sonic speed, the maximum cruising velocity is reached. In such a critical flow condition, the transonic flow region mainly on the upper side of the airfoil expands with a shock at its end due to compressibility effects. This increases noise radiation and profile drag, which is accountable for the induction of vibrations. Just like the thickness noise, the high-speed impulsive (HSI) noise propagates ahead of the blade in the rotor plane.

Retreating Blade Stall

On the retreating side of the rotor plane, the flight velocity is subtracted from the blade rotational speed. This leads, especially at the inner region of the rotor blades, to very low flow rates at high angles of attack resulting in stall. Close to the center, the flow is approaching from the backside of the profile. Due to the relatively low velocities, the energy radiated as noise is smaller than in other impulsive cases. However, the vibrations excited by the periodic and local loss of lift are more noticeable.

2.2.3 Broadband Sources

Broadband noise is essentially generated by random pressure fluctuations on the blade surface; it can be classified as non-deterministic loading noise. A reason for such random pressure fluctuations can be turbulence, existing in the surrounding atmosphere, caused by the interactions of the preceding blades, or generated on the blade itself. Mechanisms for the latter case are the separation and reattachment of boundary layers, the tip vortex formation, laminar vortex shedding, and trailing edge noise. The directivity of the broadband noise is mostly out of the rotor plane.

2.3 Passive Concepts

The examination of the helicopter main rotor has yielded a multitude of excitation mechanisms for noise and vibration. Dealing with such a complicated system, it is unlikely that a single solution exists to produce relief in all aspects. Thus, a variety of partially very different approaches has been discussed and developed. In this section, the major ideas involving non-active elements will be presented for the classical helicopter configuration. Details on these elements are given by *Bielawa* [21], *Bramwell et al.* [23].

2.3.1 External Devices

As vibrations have historically been the dominant problem and are easier to solve without a detailed understanding of their generation processes, a number of devices to improve the situation locally at specific mount points have been developed.

Absorbers

The usual absorber devices consist of mass elements connected by springs or elastic mountings. Often the spring stiffness is provided by the centrifugal force field, for example in blade-appended pendulum absorbers, shown in Figure 2.3, to compensate out-of-plane loads, or hub attached bifilar absorbers,

exemplified in Figure 2.4, for in-plane loads. As an explicit limitation, such devices are adjusted to a specific frequency proportional to the rotor speed and thus exhibit only a certain degree of self-tuning. In general, they are relatively simple in design and application but introduce additional weight, drag, and maintenance effort for moving parts.

Fig. 2.3. Blade-mounted pendulum absorber; original photograph by *Domke* [63].

Fig. 2.4. Hub-mounted bifilar absorber; original photograph by *Domke* [63].

Dampers

The task of damper elements is to reduce the amplitudes of an oscillation below a critical margin. Most often they are applied at the blade root in the lead lag direction, as the oscillations in the rotor plane are only slightly damped by the aerodynamic forces. Different variants are given in Figures 2.5 and 2.6.

Fig. 2.5. Lead lag damper between blade attachments; original photograph by *Domke* [63].

Fig. 2.6. Lead lag damper at blade attachment; original photograph by *Domke* [63].

2.3.2 Aeroelastic Conformability

When attempting to alter the elastomechanic and aerodynamic behavior of the rotor blade with its diverse couplings, and thus the susceptibility to vi-

bration and noise, complicated interrelations have to be kept in mind. As the blade responds to a composition of several excitation loads, these interrelations might lead to a significant reduction or cancellation of vibrations, in principle just like an absorber. Regrettably, this composition depends on the flight situation and therefore a beneficial coupling effect for a specific case might lead to adverse effects in other situations.

Elastomechanic Modifications

There are many parameters that can be adjusted to achieve desired features. A number of tuning/coupling effects can be achieved by the arrangement of the neutral axis, principal axes of inertia, or shear center relative to the position and direction of the loads. Moreover, the exploitation of the anisotropic properties of fibrous composites allows for additional tailorable couplings. Unlike the traditional rotor blade with almost constant structural properties over the blade length, future blades may be developed with the aid of advanced computational methods to evaluate arbitrary designs.

Aerodynamic Modifications

Similar progress has taken place in the sector of aerodynamics and with increasing insight especially into the phenomena of noise generation, more efficient blade designs have emerged. As many problems are closely related to the outer blade regions, the blade tip has been object of intense studies. Different variants of blade tip shapes are shown in Figure 2.7. Benefits are attained for the BVI noise by diffusing the tip vortex, as well as for the HSI noise by reducing the intensity of the transonic flow. For the latter case, a reduction of the blade tip speed can be considered at the expense of performance, which

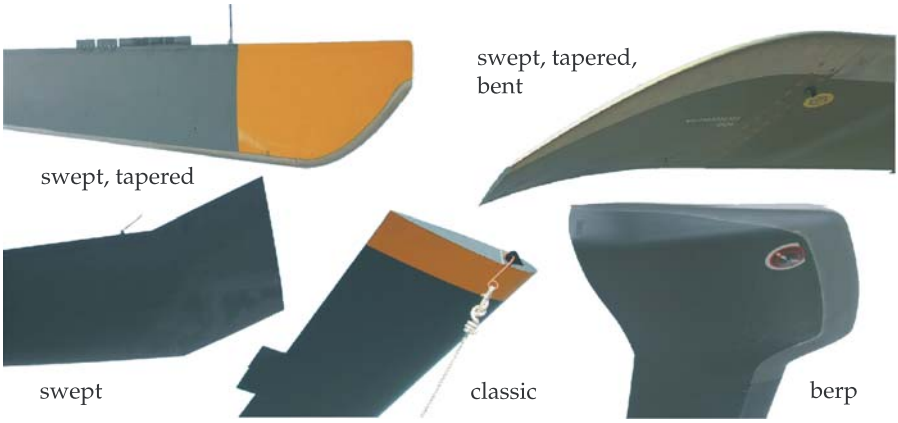

Fig. 2.7. Main rotor blade tip shapes; original photographs by *Domke* [63].

then has to be gained by further costly sanctions. Modulated blade spacing is conceptually quite different, see *Edwards and Cox* [71]. In contrast to the traditional evenly spaced rotor, several blade passage frequencies with individual sets of harmonics are generated, and thus the energy is distributed. Practically, this means, for example, that the vortex wakes of the preceding blades are hit with different delays and at different positions.

2.4 Active and Adaptive Concepts

The passive methods available for the reduction of noise and vibration are not able to achieve completely satisfying results. The most serious drawback is that they are usually optimal only to a specific situation and are not able to extend their usefulness in a more general way. This is especially critical in maneuver flight with rapidly changing conditions which are very difficult to predict. Different concepts involving control systems have been developed for active intervention, ranging with an increasing degree of structural integration from active, covered by *Bielawa* [21] and *Bramwell et al.* [23], to adaptive, discussed for example by *Büter* [40].

2.4.1 Pitch Control at the Blade Root

In order to achieve equal lift on the advancing and retreating side of the rotor in spite of the unsymmetric flow velocity distribution, the common helicopter concept makes use of a varying angle of attack. This is introduced with the necessary cycle duration of one revolution by the swash plate mechanism. The idea is to actively control the blade pitch, and cancel or reduce the appearing vibrations by superposition of an adequate signal.

Higher Harmonic Control

As most of the characteristic perturbations occur with the blade passage frequency and its higher harmonics, the simplest approach is to employ such signals to achieve cancellation. With sensors at relevant points of the airframe, the vibratory load factors are measured and then processed by a control system. The necessary motion is produced by stationary hydraulic actuators, inducing a vertical displacement of the swash plate and thus a collective actuation of the blades. Such an actuation mechanism may also modify the inclination of the swash plate, but it still is not possible to respond to events at an individual blade.

Individual Blade Control

To improve this situation, the blade root actuation mechanism was advanced by inserting hydraulic actuators between the swash plate and blade roots in

the control rods. With an adequate control algorithm, it would be possible to implement a very flexible and powerful noise and vibration suppression system. For example, the blade vortex interaction might be alleviated significantly by steering the blade in the ideal case around the approaching vortex. Admittedly, the expenditure for such a hydraulic system in the rotating part of the rotor hub is very high and therefore has been implemented only in prototype aircraft.

2.4.2 Discrete Flap Actuation

Apart from further development of control algorithms, there is a need for efficient actuation mechanisms. The integration of flaps into rotor blades presents some challenges. In order to be aerodynamically effective, the intervention needs to be located in the outer blade region, where extreme centrifugal loads are present. Moreover, spatial restrictions apply there, and the mass distribution preferably should not be altered. Under these conditions, the application of hydraulic systems is hardly conceivable, and multifunctional materials come into operation. Piezoelectric ceramics with their dynamic capabilities over a broad frequency range are used for such actuators. Different configurations have been in discussion or realized, like leading or trailing edge flaps, as shown in Figure 2.8, and the related active blade tips. Still, a discrete flap always disturbs the air flow and consequently reduces the aerodynamic performance, particularly in the extreme flow conditions exhibited by a helicopter rotor. Although the actuators themselves are designed to operate without too many moving parts, quite a few hinges and connections are necessary and these increase complexity and maintenance effort.

Fig. 2.8. Experimental rotor blade with trailing edge flaps; from *Klöppel et al.* [112].

2.4.3 Integral Blade Actuation

Multifunctional materials are currently not able to provide the performance needed for blade-root actuation. In order to influence the aerodynamically

interesting outer region of the blades, they can be applied to induce twist or manipulate the blade shape in other ways. A number of schemes to twist the blades have been developed involving directionally attached monolithic piezoelectric ceramics or passive couplings of the anisotropic blade skin to convert the excitation of an actuator. The highest degree of integration is reached with the distributed application of piezoelectric fiber composites, see Figure 2.9, with tailorable active, sensoric, and passive properties. In such a configuration, adaptive layers are used as, or merged into, the blade skin and therefore provide actuation authority without moving parts or flow disturbance, and with only a minor weight penalty as they contribute to the passive structural behavior. Certain limitations in the material properties have to be considered for piezoelectric fibers. Due to their ceramic nature, they are relatively brittle and should carry loads in compression rather than in tension.

Fig. 2.9. Scaled active twist rotor blade with piezoelectric fiber composite patches attached to the spar; from *Cesnik* [44].

2.5 Adaptive Beam Aspects

In this discussion, the integral blade actuation has been identified to be a promising development direction to alleviate noise and vibration problems of rotorcraft in the long term. While other technologies based on conventional materials or designs are closer to the market introduction, fundamental questions need to be answered with regard to material science and structural mechanics for the integral blade actuation. Thus, the focus of research is placed upon the application of adaptive fiber composites because of their versatile adjustable capabilities. With these it is possible to induce displacements or rotations with respect to the blade axis as well as deformations in the cross-sectional plane. The latter, also known as chamber variation, might be of interest for fixed-wing aircraft but is improbable for implementation on rotating-wing aircraft due to the complex load and excitation situation of the blade structure. Such a slender structure can be efficiently idealized as a beam. Further on, the set-up of a rotor blade with foam-filled chambers will require modeling by means of a thin-walled beam. Thus, an adequate and comprehensive theoretical framework for adaptive thin-walled beams will be developed here.

2.5.1 Beam Actuation Concepts

In Section 2.2, the essential noise and vibration phenomena occurring at the helicopter main rotor have been analyzed. They lead to bending oscillations of the blades, which may be modeled by thin-walled beams. Equipping such a structure with adaptive fiber composites permits different actuation schemes to compensate for bending-related displacements, see Figure 2.10. It is possible to accomplish this for static operation by inducing opposing displacements. Such bending actuation may be realized directly through expansion and contraction of opposing wall sectors and through shear deformation of transversely oriented wall sectors. Alternatively, coupling effects due to constitutive anisotropy of the walls may be exploited, for example transforming a lengthwise expansion of piezoelectric layers, which is applied consistently throughout the cross-section, into the desired beam bending. In a rotating environment, it is possible to amplify the rather small attainable displacements with the aid of aerodynamic forces. Since a small change in the angle of attack may lead to a significant change in lift and drag with the associated blade displacements, twist actuation becomes important. It can be achieved again either directly through the consistent induction of shear in the walls or via structural couplings related to the constitutive anisotropy of the walls as well as to the warping of the cross-section. The prior couples, for example, extension with torsion and the latter warping with torsion. Naturally, not all of the various actuation schemes are equally suitable for reducing the helicopter rotor problems. The research reported in the literature is clearly focused upon the direct torsion, see Section 2.5.3. Here a general approach

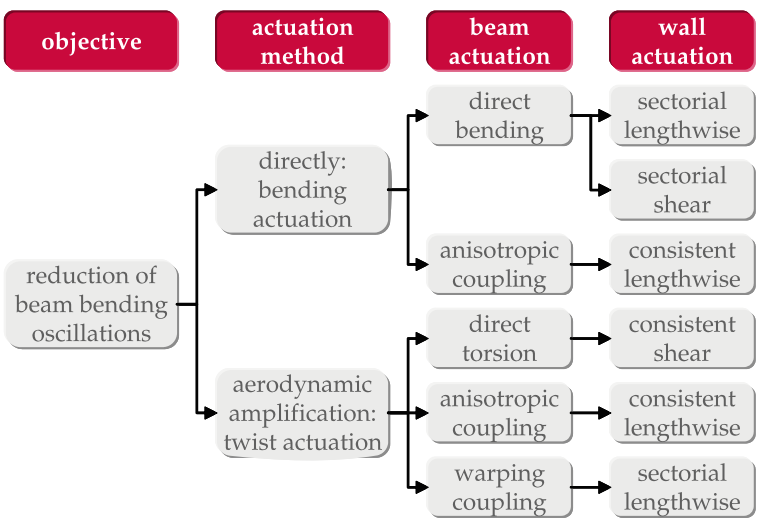

Fig. 2.10. Actuation schemes for the reduction of beam-bending oscillations in consideration of aerodynamic forces in a rotating environment.

will be developed, capable of describing all potential actuation schemes by means of a single theory of thin-walled beams incorporating adaptive fiber composites.

2.5.2 Adaptive System Concepts

Since the piezoelectric effect comprises two aspects, direct and converse, composites with such properties may be used for both sensing and actuation. Combining these two with a control unit makes an adaptive system. Both actuators and sensors may be either discrete, at a specific location, or integral, spatially distributed. The latter case typically can be accomplished with piezoelectric fiber composites. Figure 2.11 illustrates the possible combinations with elementary control schemes. Using open-loop control, a signal for the actuator is prescribed based on knowledge about the system. For a helicopter rotor, this usually involves higher harmonic frequencies, sufficiently covering a constant flight condition. For more versatile tasks, corresponding to changing flight conditions, closed-loop control provides actuator signals in response to sensor signals. Such control concepts for helicopter rotor blades have mainly been developed for pitch actuation at the blade root or the trailing edge flap, see for example *Konstanzer* [115]. Further on in Figure 2.11, passive control stands for the use of piezoelectric material with inductive resonant, resistive, capacitive, and switched shunt circuits, see *Lesieutre* [122]. A shunt circuit with a combination of resistance and inductance allows us to induce tunable damping and absorption of vibrations. The suitability of piezoelectric fiber composites for such an application has been demonstrated by *Adachi et al.* [3]. A single element acts in turn as actuator and sensor. For better efficiency, it should be of integral type, since neither electric nor aeroelastic amplification can be utilized.

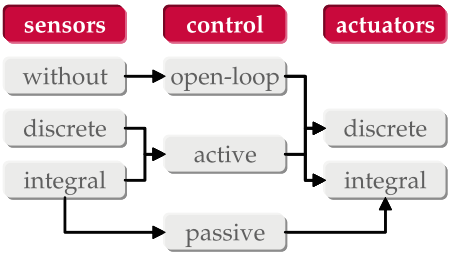

Fig. 2.11. Control of beam oscillations.

2.5.3 Development Status

The initial examinations of directly induced torsion were conducted for monolithic piezoelectric ceramics being attached in a $\pm 45°$ direction to the upper

and lower side of the blade. Modeling aspects are reported by *Chen and Chopra* [51,52], while experiments including hover testing of a scaled rotor are covered by *Park et al.* [138] and *Park and Chopra* [137]. The application of piezoelectric fiber composites has been carried out by *Du Plessis and Hagood* [65] in theory and experiment by means of a scaled rotor blade of a Boeing-Vertol CH-47D helicopter. Predictions of the static twist performance of a box beam were gained with the aid of a finite beam element model. Test results of this blade in the rotating environment are reported by *Rodgers and Hagood* [155]. Further development and testing of an active twist rotor with actuator patches of piezoelectric fiber composites attached to the spar, Figure 2.9, has been conducted according to *Cesnik et al.* [47]. In a series of wind tunnel experiments with open-loop control, it has been shown that the vibratory loads at the rotor hub can be reduced significantly, *Wilbur et al.* [180], and that there also is a potential for noise reduction, *Booth and Wilbur* [22]. The blades have been modeled with two cells and thin walls, determining the cross-sectional properties in a linear analysis and the global dynamic behavior in a non-linear analysis for small strains and finite rotations with beam finite elements, *Cesnik and Shin* [46], and with additional consideration of the aerodynamics, *Cesnik et al.* [48]. An asymptotic analysis approach led them to a beam description without explicit degrees of freedom for transverse shear and out-of-plane warping. A subsequent adjustment to a Timoshenko-like beam was described by *Cesnik and Palacios* [45]. Further modeling approaches are reported in the context of an aeroelastic analysis by *Wilkie and Park* [181] and of a multi-body simulation by *Ghiringhelli et al.* [82]. The former is restricted to extension, torsion, and structurally uncoupled uniaxial bending, while the latter use a finite element discretization of the cross-section to determine the beam stiffness and actuation properties. A review of previous work is presented in the references [26–37].

3

Fundamental Considerations

This chapter describes the fundamental theories for investigating physical systems with regard to deformable structures and dielectric domains as examined by mechanics and electrodynamics, respectively, within the field of theoretical physics, see for example *Schaefer and Päsler* [160]. It clarifies the essential interrelations and provides a consistent basis to serve as a reference for the subsequent chapters, where more detailed and specific models will be developed.

3.1 Mathematical Preliminaries

For the required representation of the laws of physics independent of a special coordinate system, tensor calculus is invaluable. As matrix calculus is quite convenient with regard to component representation and implementation, it shall be employed when applicable. The tensor- and the matrix-based observation concept include or depict vector algebra. We assume that the mathematical fundamentals are known and therefore give only a fragmentary overview to clarify notation and to introduce utilized rules and conventions. A useful and comprehensive collection of formulas is given by *Råde and Westgren* [147], while the tensors are the subject of *Sokolnikoff* [167], *Prager* [144], *Itskov* [105], *Brunk and Kraska* [38] as well as the matrices of *Lax* [119], *Zurmühl and Falk* [188].

3.1.1 Euclidean Vectors

The examinations will be accomplished in the three-dimensional Euclidean vector space, where the scalar product of vectors is defined beyond the properties of the affine space. Cartesian coordinates with their orthogonal, straight, and normalized base are sufficient for the problems at hand and therefore will be used.

T.H. Brockmann, *Theory of Adaptive Fiber Composites*,
Solid Mechanics and Its Applications 161,

Vectorial Products

The scalar or dot product processes two vectors, for example $\boldsymbol{v}$ and $\boldsymbol{w}$, of arbitrary dimension into a scalar. The scalar product is commutative:

$$\boldsymbol{v} \cdot \boldsymbol{w} = \begin{Bmatrix} v_1 \\ v_2 \\ \dots \end{Bmatrix} \cdot \begin{Bmatrix} w_1 \\ w_2 \\ \dots \end{Bmatrix} = v_1 w_1 + v_2 w_2 + \cdots , \qquad \boldsymbol{v} \cdot \boldsymbol{w} = \boldsymbol{w} \cdot \boldsymbol{v}. \tag{3.1}$$

The vector or cross product determines a so-called axial vector with orthogonal orientation from two spatial vectors. The vector product is anti-commutative:

$$\boldsymbol{v} \times \boldsymbol{w} = \begin{Bmatrix} v_1 \\ v_2 \\ v_3 \end{Bmatrix} \times \begin{Bmatrix} w_1 \\ w_2 \\ w_3 \end{Bmatrix} = \begin{Bmatrix} v_2 w_3 - v_3 w_2 \\ v_3 w_1 - v_1 w_3 \\ v_1 w_2 - v_2 w_3 \end{Bmatrix}, \qquad \boldsymbol{v} \times \boldsymbol{w} = -\boldsymbol{w} \times \boldsymbol{v}. \tag{3.2}$$

3.1.2 Tensor Representation

With the chosen type of coordinates and for the sake of simplicity, it can be abstained from the index notation. The classification of tensors with the applied typesetting conventions is given in Table 3.1.

Table 3.1. Tensors of different order.

Order	Denotation	Example
0^{th}	scalar	s
1^{st}	vector	$\boldsymbol{v}, \boldsymbol{w}$
2^{nd}	dyad	$\mathbf{c}, \mathbf{d}$
n^{th}	general tensor	

Tensorial Products

The double contracting or double inner product of general tensors results in a tensor with the added order of the multiplied tensors lowered by four. The employed symbol of two dots alludes to the two scalar products of the particular base vectors. In the case of two tensors of second order, the outcome is of zeroth order, leading to the denomination as a scalar product of dyads. The double contracting product is commutative, given here for the case of dyads:

$$\mathbf{c} \cdot\cdot \mathbf{d} = \mathbf{d} \cdot\cdot \mathbf{c}. \tag{3.3}$$

When only a single scalar product of base vectors is involved, the result of such a product has the added order of the multiplied tensors lowered by two. This contracting or inner product of general tensors thus comprises the scalar product of vectors as a special case. Further on, the tensorial or outer product

of general tensors leads to a result with a summed order of the multiplied tensors. Therefore, its application to vectors results in a dyad, giving reason to the denomination as the dyadic product of vectors often indicated by the symbol $\otimes$. The contracting product, Eq. (3.4a), and the tensorial product, Eq. (3.4b), of general tensors are non-commutative:

$$\boldsymbol{v} \cdot \mathbf{d} \neq \mathbf{d} \cdot \boldsymbol{v}, \tag{3.4a}$$

$$\boldsymbol{v}\mathbf{d} \neq \mathbf{d}\boldsymbol{v}. \tag{3.4b}$$

For the occurrence of a transposed dyad within consecutive contracting products, the following rearrangement is permissible:

$$\left(\mathbf{d}^T \cdot \boldsymbol{v}\right) \cdot \boldsymbol{w} = \boldsymbol{v} \cdot (\mathbf{d} \cdot \boldsymbol{w}) \,. \tag{3.5}$$

Theorems

Concerning the partial differentiation of tensors, the following abbreviations for gradient and divergence are introduced:

$$\begin{aligned} \operatorname{grad}(\cdot) &= \nabla(\cdot), \\ \operatorname{div}(\cdot) &= \blacktriangledown(\cdot). \end{aligned}$$

For the manipulation of equations with products containing these operators, Gauss's divergence theorem will be needed. It is given for the usual case with the product of a scalar and a vector in Eq. (3.6a) and for the contracting product of a transposed dyad and a vector in Eq. (3.6b):

$$\blacktriangledown (s\boldsymbol{v}) = s\blacktriangledown\boldsymbol{v} + \boldsymbol{v} \cdot \nabla s, \tag{3.6a}$$

$$\blacktriangledown \left(\mathbf{d}^T \cdot \boldsymbol{v}\right) = \boldsymbol{v} \cdot \blacktriangledown\mathbf{d} + \mathbf{d} \cdot\cdot \nabla\boldsymbol{v}. \tag{3.6b}$$

When Λ is a spatial domain with the closed boundary $\partial\Lambda$ and the respective unit vector field of the surface normals $\boldsymbol{e}_n$ is directed outwards, then Gauss's integral theorem states

$$\int_{\Lambda} \blacktriangledown\boldsymbol{v} \,\mathrm{d}V = \int_{\partial\Lambda} \boldsymbol{v} \cdot \mathrm{d}\boldsymbol{A} = \int_{\partial\Lambda} \boldsymbol{v} \cdot \boldsymbol{e}_n \,\mathrm{d}A. \tag{3.7}$$

3.1.3 Matrix Representation

Depending on the circumstances, it makes sense to apply either tensor or matrix calculus. Occasionally it may be useful to switch the representation. Typically, the results of a derivation requiring tensors are written in the more accessible matrix form. While operations involving scalars and vectors are applicable for both, the more general case is subjected to restrictions:

- A tensor of second order may be represented by a square matrix, but a general non-square matrix cannot be represented by a tensor.

- A tensor of more than second order cannot be represented by a single matrix without rearrangement of components.

However, the latter statement implies that tensors can be converted to matrices involving the rearrangement of components. Therewith tensors of second order may be expressed by column matrices, also referred to as vectors. This will be implemented in the following section for stresses and strains. The classification of matrices with the applied typesetting conventions is given in Table 3.2.

Table 3.2. Matrices of different dimensions.

Dimension	Denotation	Example
column	vector	$\boldsymbol{v}, \boldsymbol{w}$
row	transposed vector	$\boldsymbol{v}^T, \boldsymbol{w}^T$
general	matrix	$\mathbf{m}$

Substitution of Vectorial Products

Usually within the framework of matrix calculus, the vector operations are retained or may be replaced with pure matrix algebra. In matrix notation, the scalar product of two vectors may be represented by the matrix product of a row and a column matrix:

$$\boldsymbol{v} \cdot \boldsymbol{w} = \boldsymbol{w} \cdot \boldsymbol{v} \quad \leftrightarrow \quad \boldsymbol{v}^T \boldsymbol{w} = \boldsymbol{w}^T \boldsymbol{v}. \tag{3.8}$$

For the vector product, the components of one of the vectors need to be rearranged into a skew-symmetric matrix and then multiplied with the column matrix of the other:

$$\begin{aligned} &\boldsymbol{v} \times \boldsymbol{w} \quad \leftrightarrow \quad \langle \boldsymbol{v} \rangle \, \boldsymbol{w} = \langle \boldsymbol{w} \rangle^T \boldsymbol{v} \\ &\text{with } \boldsymbol{v} = \begin{Bmatrix} v_1 \\ v_2 \\ v_3 \end{Bmatrix} \quad \leftrightarrow \quad \langle \boldsymbol{v} \rangle = - \langle \boldsymbol{v} \rangle^T = \begin{bmatrix} 0 & -v_3 & v_2 \\ v_3 & 0 & -v_1 \\ -v_2 & v_1 & 0 \end{bmatrix}. \end{aligned} \tag{3.9}$$

3.2 Deformable Structures–Mechanical Fields

A mechanical system may consist of several different parts. When such a part is able to undergo deformations, it will be regarded as a deformable structure. It may be modeled with a certain complexity, for example with the aid of shell or beam theory, but can be traced back to the basic configuration of the continuum, which is the subject of investigation within the homonymous branch of mechanics. Such a continuum is a continuous domain of spatial,

planar, or linear extent filled with matter. It consists of elements denominated as particles, which are small in the macroscopic view and thus mathematically point-shaped but ample in the microscopic view compared with the materials texture. Introductory literature for this topic is given, for example, by *Becker and Gross* [9] as well as beyond by *Wempner* [177], *Green and Zerna* [88], *Sokolnikoff* [166].

3.2.1 Loads

Loads may be distinguished with respect to the location of their origin and nature of their action. External loads act from the outside of the mechanical system, while the internal loads appear within, and become visible when the system is cut. Applied or physical loads are regarded as given, whereas reactive or geometric loads are initially unknown, and result from restrictions on the motion and deformation. Loads may act upon a volume, a surface, or in ideal limit cases as line or point loads. They are representable by tensors of first order, thus taking the form of vectors. For a force $\boldsymbol{F}$ affecting a volume or an area, the vector fields of force density with a volume force $\check{\boldsymbol{f}}$ or an area force $\hat{\boldsymbol{f}}$ describe the three- or two-dimensional distribution respectively:

$$\check{\boldsymbol{f}} = \frac{\mathrm{d}\boldsymbol{F}}{\mathrm{d}V}, \tag{3.10a}$$

$$\hat{\boldsymbol{f}} = \frac{\mathrm{d}\boldsymbol{F}}{\mathrm{d}A}. \tag{3.10b}$$

While forces and moments are considered for the general mechanical system, the continuum usually is limited to the introduction of the concept of forces. From this point of view, the Cosserat theory is mentioned here as an exception, see *Rubin* [157] for details.

3.2.2 Stresses

The loading of a continuum due to external forces is characterized by the stresses observed at the individual particles. When the continuum is cut, the internal force $\mathrm{d}\boldsymbol{F}$ at a particle is found to be acting upon the associated surface element $\mathrm{d}A$ in the section plane. The stress vector $\hat{\boldsymbol{f}}$ can then be defined in accordance with Eq. (3.10b). The stress tensor $\boldsymbol{\sigma}$ again results from the stress vectors of three orthogonal section planes unfolding between the unit vectors $\boldsymbol{e}_1$, $\boldsymbol{e}_2$, $\boldsymbol{e}_3$ of the Cartesian coordinate system. Given by Eq. (3.11), it is commonly denominated as the Cauchy stress tensor and is of second order. Demanding the local balance of moments, its symmetry can be shown as elucidated by Figure 3.1. An alternative representation may be gained by resorting the six remaining independent components into a vector as of the right-hand side of Eqs. (3.12).

$$\boldsymbol{\sigma} = \left[\hat{\boldsymbol{f}}_1 \quad \hat{\boldsymbol{f}}_2 \quad \hat{\boldsymbol{f}}_3\right]^T, \tag{3.11}$$

$$\boldsymbol{\sigma} = \boldsymbol{\sigma}^T = \begin{bmatrix} \sigma_1 & \tau_{12} & \tau_{31} \\ \tau_{12} & \sigma_2 & \tau_{23} \\ \tau_{31} & \tau_{23} & \sigma_3 \end{bmatrix} \quad \leftrightarrow \quad \boldsymbol{\sigma} = \begin{Bmatrix} \sigma_1 \\ \sigma_2 \\ \sigma_3 \\ \tau_{23} \\ \tau_{31} \\ \tau_{12} \end{Bmatrix}. \tag{3.12}$$

In turn it is possible to deduce the stress vector $\hat{\boldsymbol{f}}_n$ acting upon a surface with the unit normal vector $\boldsymbol{e}_n$ from the stress tensor. Such an equilibrium relation is especially useful when it comes to the description of boundary conditions. This is the Cauchy theorem:

$$\hat{\boldsymbol{f}}_n = \boldsymbol{\sigma} \cdot \boldsymbol{e}_n \quad \leftrightarrow \quad \hat{\boldsymbol{f}}_n = \boldsymbol{\sigma}^T \boldsymbol{e}_n. \tag{3.13}$$

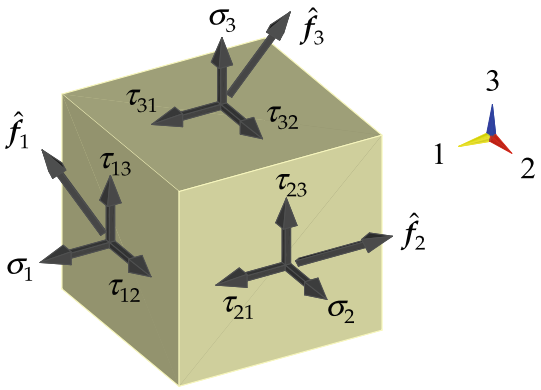

Fig. 3.1. Stress vectors with associated components by means of an infinitesimal volume element.

3.2.3 Mechanical Equilibrium

Transitioning from the stress state of a particle to the stress field of the continuum, the interaction of the Cauchy stress tensor components of neighboring points needs to be investigated. They have to satisfy the conditions of local equilibrium to be established with the aid of an arbitrary infinitesimal volume element. Such an element with faces in parallel to the planes of the Cartesian coordinate system is subjected to the volume force $\hat{\boldsymbol{f}}_\Lambda$ and on the faces to the components of the Cauchy stress tensor with additional increments in the form of the first element of Taylor expansions on one of the respective opposing faces. The balance of moments proves the symmetry of the stress tensor,

whereas the balance of forces leads to the equation of internal mechanical equilibrium

$$\blacktriangledown\boldsymbol{\sigma} + \check{\boldsymbol{f}}_{\Lambda} = 0 \quad \text{in } \Lambda. \tag{3.14}$$

Here the continuum is denoted by the domain Λ and the respective boundary $\partial\Lambda$ is subdivided to consider two types of boundary conditions. The area $\partial\Lambda_\sigma$ is subjected to the prescribed loads $\hat{\boldsymbol{f}}_{\partial\Lambda}$ of the physical boundary conditions in equilibrium with the boundary stresses expressed by application of the Cauchy theorem of Eq. (3.13) (Neumann boundary conditions):

$$\hat{\boldsymbol{f}}_{\partial\Lambda} = \boldsymbol{\sigma} \cdot \boldsymbol{e}_n \quad \text{on } \partial\Lambda_\sigma. \tag{3.15}$$

The prescribed displacements $\boldsymbol{u}_{\partial\Lambda}$ of the geometric boundary conditions are imposed on the area $\partial\Lambda_u$ (Dirichlet boundary conditions):

$$\boldsymbol{u}_{\partial\Lambda} = \boldsymbol{u} \quad \text{on } \partial\Lambda_u. \tag{3.16}$$

3.2.4 Strains

The deformation of a continuum may be described by the displacement $\boldsymbol{u}$ of its particles and their strain state. For that purpose, it is convenient to distinguish between the initial configuration of the undeformed and the current configuration of the deformed body. A particle can be identified either by its original position $\boldsymbol{X}$ in the initial configuration, Figure 3.2(a), thus tracking the particle's individual state at subsequent positions, or by its momentary position $\boldsymbol{x}$ in the current configuration, Figure 3.2(b), thus tracking the state of subsequent particles at this fixed position. The former is the Lagrangian approach, the latter case is called the Eulerian approach. The strain field of the continuum may be expressed by the difference of the squared lengths of a

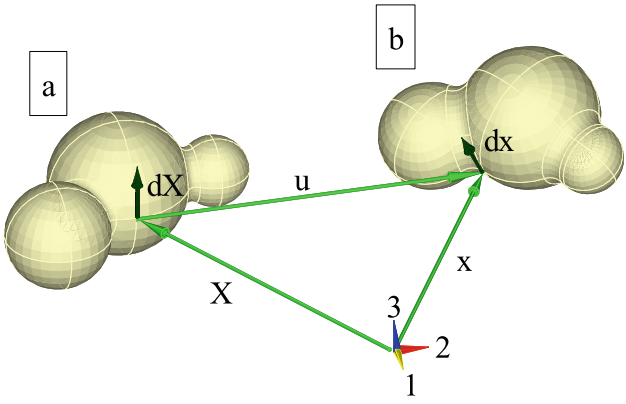

Fig. 3.2. Deformation of a continuum—(a) reference configuration with particle position $\boldsymbol{X}$ and (b) momentary configuration with particle position $\boldsymbol{x}$ in the inertial frame of reference.

line element in the deformed and undeformed state as $\mathrm{d}\boldsymbol{x}^T\,\mathrm{d}\boldsymbol{x} - \mathrm{d}\boldsymbol{X}^T\,\mathrm{d}\boldsymbol{X}$ with $\mathrm{d}\boldsymbol{x} = \mathrm{d}\boldsymbol{X} + \mathrm{d}\boldsymbol{u}$. Contingent upon the elimination either of $\mathrm{d}\boldsymbol{x}$ following the Lagrangian approach or of $\mathrm{d}\boldsymbol{X}$ for the Eulerian approach, the Green Lagrange $\boldsymbol{\varepsilon}_{\mathrm{GL}}$ and the Euler Almansi $\boldsymbol{\varepsilon}_{\mathrm{EA}}$ strain tensor may be derived. The former is expressible in terms of the displacement gradient:

$$\boldsymbol{\varepsilon}_{\mathrm{GL}} = \frac{1}{2}\left(\nabla\boldsymbol{u} + \nabla^T\boldsymbol{u} + \nabla^T\boldsymbol{u}\cdot\nabla\boldsymbol{u}\right). \tag{3.17}$$

The non-linear term is symmetric, as it is represented by a contracting product involving a dyad and its transpose. We will later demonstrate the evident symmetry of the linear terms. The general Green Lagrange strain tensor $\boldsymbol{\varepsilon}_{\mathrm{GL}}$ can represent finite deformations, but for many applications the displacement gradient remains small and so the non-linear term can be neglected. With this assumption, the difference in the gradients regarding the deformed and undeformed line element vanishes and both the Green Lagrange and Euler Almansi strain tensors become identical:

$$\boldsymbol{\varepsilon} = \frac{1}{2}\left(\nabla\boldsymbol{u} + \nabla^T\boldsymbol{u}\right) = \boldsymbol{\varepsilon}_{\mathrm{GL,lin}} = \boldsymbol{\varepsilon}_{\mathrm{EA,lin}}. \tag{3.18}$$

When the displacement gradient is split into its symmetric and skew symmetric portions, the infinitesimal strain tensor of Eq. (3.18) is identified to be the former, while the latter represents infinitesimal rotations that do not contribute to the strain field:

$$\nabla\boldsymbol{u} = \underbrace{\frac{1}{2}\left(\nabla\boldsymbol{u} + \nabla^T\boldsymbol{u}\right)}_{\boldsymbol{\varepsilon}=\nabla\boldsymbol{u}_{\mathrm{sym}}} + \underbrace{\frac{1}{2}\left(\nabla\boldsymbol{u} - \nabla^T\boldsymbol{u}\right)}_{\nabla\boldsymbol{u}_{\mathrm{skew}}}. \tag{3.19}$$

So the infinitesimal strain tensor is established as a symmetric tensor of second order. With provision for the engineering shear-strain measures aside the diagonal, the components can be assigned as given by the left-hand side of Eqs. (3.20). An alternative representation may be gained by resorting the six independent components into a vector as shown on the right-hand side of Eqs. (3.20):

$$\boldsymbol{\varepsilon} = \boldsymbol{\varepsilon}^T = \begin{bmatrix} \varepsilon_1 & \frac{1}{2}\gamma_{12} & \frac{1}{2}\gamma_{31} \\ \frac{1}{2}\gamma_{12} & \varepsilon_2 & \frac{1}{2}\gamma_{23} \\ \frac{1}{2}\gamma_{31} & \frac{1}{2}\gamma_{23} & \varepsilon_3 \end{bmatrix} \quad \leftrightarrow \quad \boldsymbol{\varepsilon} = \begin{Bmatrix} \varepsilon_1 \\ \varepsilon_2 \\ \varepsilon_3 \\ \gamma_{23} \\ \gamma_{31} \\ \gamma_{12} \end{Bmatrix}. \tag{3.20}$$

3.2.5 Transformations

The transformation of a tensor is accomplished by changing its base vector system. Such a change from the orthonormal base vectors $\boldsymbol{e}_1, \boldsymbol{e}_2, \boldsymbol{e}_3$ to the

arbitrarily rotated orthonormal base vectors $\boldsymbol{e}_s, \boldsymbol{e}_n, \boldsymbol{e}_x$ may be expressed with the aid of transformation coefficients in the form of directional cosines between these vectors, Eq. (3.21a), respectively, their scalar products, Eq. (3.21b):

$$c_{ai} = \cos\left(\boldsymbol{e}_a, \boldsymbol{e}_i\right) \quad \text{with } a \in [s, n, x] \text{ and } i \in [1, 2, 3]\,, \tag{3.21a}$$

$$c_{ai} = \boldsymbol{e}_a \cdot \boldsymbol{e}_i \quad \leftrightarrow \quad c_{ai} = \boldsymbol{e}_a^T \boldsymbol{e}_i. \tag{3.21b}$$

These transformation coefficients may be summarized in the transformation matrix $\mathbf{T}$ for the subsequent transformation of stresses, respectively strains, in matrix representation:

$$\underbrace{\begin{Bmatrix} \sigma_s \\ \sigma_n \\ \sigma_x \\ \tau_{nx} \\ \tau_{xs} \\ \tau_{sn} \end{Bmatrix}}_{\boldsymbol{\sigma}(s,n,x)} = \mathbf{T} \underbrace{\begin{Bmatrix} \sigma_1 \\ \sigma_2 \\ \sigma_3 \\ \tau_{23} \\ \tau_{31} \\ \tau_{12} \end{Bmatrix}}_{\boldsymbol{\sigma}(1,2,3)}, \qquad \begin{Bmatrix} \varepsilon_s \\ \varepsilon_n \\ \varepsilon_x \\ \frac{1}{2}\gamma_{nx} \\ \frac{1}{2}\gamma_{xs} \\ \frac{1}{2}\gamma_{sn} \end{Bmatrix} = \mathbf{T} \begin{Bmatrix} \varepsilon_1 \\ \varepsilon_2 \\ \varepsilon_3 \\ \frac{1}{2}\gamma_{23} \\ \frac{1}{2}\gamma_{31} \\ \frac{1}{2}\gamma_{12} \end{Bmatrix}. \tag{3.22}$$

As it is dealt with second-order tensors, the associated base vector pairs need to be considered, and thus products of the transformation coefficients appear in the transformation matrix:

$$\mathbf{T} = \begin{bmatrix} c_{s1}^2 & c_{s2}^2 & c_{s3}^2 & 2c_{s2}c_{s3} & 2c_{s3}c_{s1} & 2c_{s1}c_{s2} \\ c_{n1}^2 & c_{n2}^2 & c_{n3}^2 & 2c_{n2}c_{n3} & 2c_{n3}c_{n1} & 2c_{n1}c_{n2} \\ c_{x1}^2 & c_{x2}^2 & c_{x3}^2 & 2c_{x2}c_{x3} & 2c_{x3}c_{x1} & 2c_{x1}c_{x2} \\ c_{s1}c_{n1} & c_{s2}c_{n2} & c_{s3}c_{n3} & c_{s2}c_{n3} + c_{n2}c_{s3} & c_{s1}c_{n3} + c_{n1}c_{s3} & c_{s1}c_{n2} + c_{n1}c_{s2} \\ c_{s1}c_{x1} & c_{s2}c_{x2} & c_{s3}c_{x3} & c_{s2}c_{x3} + c_{x2}c_{s3} & c_{s1}c_{x3} + c_{x1}c_{s3} & c_{s1}c_{x2} + c_{x1}c_{s2} \\ c_{n1}c_{x1} & c_{n2}c_{x2} & c_{n3}c_{x3} & c_{n2}c_{x3} + c_{x2}c_{n3} & c_{n1}c_{x3} + c_{x1}c_{n3} & c_{n1}c_{x2} + c_{x1}c_{n2} \end{bmatrix}. \tag{3.23}$$

A significant simplification is to be noted when the rotation is performed around a common base vector. Thus, for example, for a rotation α around the coincident vectors $\boldsymbol{e}_2$ and $\boldsymbol{e}_n$, the transformation coefficients take the following form:

$$c_{s1}, c_{x3} = \cos\alpha, \qquad c_{x1} = \cos\left(\frac{\pi}{2} + \alpha\right), \qquad c_{s3} = \cos\left(\frac{\pi}{2} - \alpha\right), \tag{3.24a}$$

$$c_{n2} = \cos 0, \qquad c_{n1}, c_{s2}, c_{x2}, c_{n3} = \cos\frac{\pi}{2}. \tag{3.24b}$$

Therewith the transformation matrix reduces to

$$\mathbf{T} = \begin{bmatrix} \cos^2\alpha & 0 & \sin^2\alpha & 0 & -2\sin\alpha\cos\alpha & 0 \\ 0 & 1 & 0 & 0 & 0 & 0 \\ \sin^2\alpha & 0 & \cos^2\alpha & 0 & 2\cos\alpha\sin\alpha & 0 \\ 0 & 0 & 0 & -\sin\alpha & 0 & \cos\alpha \\ \cos\alpha\sin\alpha & 0 & -\sin\alpha\cos\alpha & 0 & \cos^2\alpha - \sin^2\alpha & 0 \\ 0 & 0 & 0 & \cos\alpha & 0 & \sin\alpha \end{bmatrix}. \tag{3.25}$$

As visible on the right-hand side of Eqs. (3.22), the transformation of strains does not yet cope with the engineering shear-strain measures introduced in the previous subsection. This can be accomplished, as shown for the planar case by *Jones* [107], by multiplication with the correction matrix $\mathbf{R}$:

$$\underbrace{\begin{Bmatrix} \varepsilon_s \\ \varepsilon_n \\ \varepsilon_x \\ \gamma_{nx} \\ \gamma_{xs} \\ \gamma_{sn} \end{Bmatrix}}_{\boldsymbol{\varepsilon}(s,x,n)} = \mathbf{R} \begin{Bmatrix} \varepsilon_s \\ \varepsilon_n \\ \varepsilon_x \\ \frac{1}{2}\gamma_{nx} \\ \frac{1}{2}\gamma_{xs} \\ \frac{1}{2}\gamma_{sn} \end{Bmatrix}, \quad \underbrace{\begin{Bmatrix} \varepsilon_1 \\ \varepsilon_2 \\ \varepsilon_3 \\ \gamma_{23} \\ \gamma_{31} \\ \gamma_{12} \end{Bmatrix}}_{\boldsymbol{\varepsilon}(1,2,3)} = \mathbf{R} \begin{Bmatrix} \varepsilon_1 \\ \varepsilon_2 \\ \varepsilon_3 \\ \frac{1}{2}\gamma_{23} \\ \frac{1}{2}\gamma_{31} \\ \frac{1}{2}\gamma_{12} \end{Bmatrix},$$

$$\text{with } \mathbf{R} = \begin{bmatrix} 1 & 0 & 0 & 0 & 0 & 0 \\ 0 & 1 & 0 & 0 & 0 & 0 \\ 0 & 0 & 1 & 0 & 0 & 0 \\ 0 & 0 & 0 & 2 & 0 & 0 \\ 0 & 0 & 0 & 0 & 2 & 0 \\ 0 & 0 & 0 & 0 & 0 & 2 \end{bmatrix}. \tag{3.26}$$

When these equations are utilized for the strain transformation relation on the right-hand side of Eqs. (3.22), the transformation matrix is multiplied from the left by the correction matrix and from the right by its inverse. For the rotation around a common base vector, it is straightforward to show that this results in a transposed and inverted transformation matrix:

$$\boldsymbol{\varepsilon}(s,x,n) = \mathbf{R}\mathbf{T}\mathbf{R}^{-1}\boldsymbol{\varepsilon}(1,2,3) = \left(\mathbf{T}^T\right)^{-1}\boldsymbol{\varepsilon}(1,2,3). \tag{3.27}$$

Complementarily, the stress transformation relation of the left-hand side of Eqs. (3.22) will be given in the corresponding form:

$$\boldsymbol{\sigma}(s,n,x) = \mathbf{T}\boldsymbol{\sigma}(1,2,3). \tag{3.28}$$

3.3 Dielectric Domains–Electrostatic Fields

In contrast to conductive material with the ability to accommodate electric flow fields, dielectric matter, as well as vacuum, may exhibit electrostatic fields. Although the physical condition of the examined dielectric domain is not limited to solid state, it may be described in analogy with deformable structures as a continuum. In comparison to the mechanical fields, the tensors characterizing the electrostatic fields will be one order lower. A comprehensive description of electrical engineering is given by *Paul* [140], while electromagnetic fields are detailed by *Fischer* [74], *Lehner* [120], and *Reitz et al.* [153].

3.3.1 Electric Charge

Length, mass, and time are the elementary quantities of mechanics. For electric phenomena, they have to be complemented with the electric charge Q. The charge of particles, usually denominated as charge carriers, implicates a repulsive or attractive force between them for charges of identical or opposite sign, respectively. When charge is distributed over a volume or an area, the scalar fields of the electric charge density with volume charge $\check{q}$ or area charge $\hat{q}$ describe the three- or two-dimensional distribution, respectively:

$$\check{q} = \frac{\mathrm{d}Q}{\mathrm{d}V}, \tag{3.29a}$$

$$\hat{q} = \frac{\mathrm{d}Q}{\mathrm{d}A}. \tag{3.29b}$$

With the exception of the limit case of vacuum, a dielectric holds charge carriers just like a conductor. The substantial difference and reason for the distinct types of electric fields is that in the dielectric the charge carriers are not able to move. Thus, the induced electric field is static, although magnitude and direction may change due to variable charges.

3.3.2 Electric Flux Density

The electrostatic field expands between charges separated by a dielectric and may be illustrated by the lines of electric flux connecting them. Positive and negative charges are sources and drains of the electric flux. So the electric flux only depends on the charges but not on the dielectric. The contribution of a charge Q can be expressed by the integral of the electric flux density $\boldsymbol{D}$, occasionally also denoted electric displacement, over an arbitrary enclosing envelope with the surface normal $\bar{\boldsymbol{e}}_n$ in an outward direction:

$$Q = \oint \boldsymbol{D} \cdot \mathrm{d}\boldsymbol{A} \quad \rightarrow \quad \mathrm{d}Q = \boldsymbol{D} \cdot \mathrm{d}\boldsymbol{A} = \boldsymbol{D} \cdot \bar{\boldsymbol{e}}_n \, \mathrm{d}A. \tag{3.30}$$

This is the Gaussian law of electrostatics in integral and differential form. The latter may be reorganized to express the electric flux density with the aid of the charge density of the dedicated area, as given by Eq. (3.29b), leading to the equivalent of the Cauchy theorem of mechanics from Eq. (3.13):

$$\frac{\mathrm{d}Q}{\mathrm{d}A} = \hat{q} = \boldsymbol{D} \cdot \bar{\boldsymbol{e}}_n = \boldsymbol{D}^T \bar{\boldsymbol{e}}_n. \tag{3.31}$$

3.3.3 Electrostatic Equilibrium

The charge affecting the surrounding domain Λ may be expressed in terms of the spatial charge density through integration of Eq. (3.29a) as well as in

terms of the electric flux density on its boundary $\partial\Lambda$ given by the Gaussian law in Eq. (3.30):

$$Q = \int_{\Lambda} \check{q}_{\Lambda} \, \mathrm{d}V, \tag{3.32a}$$

$$Q = \int_{\partial\Lambda} \boldsymbol{D} \cdot \mathrm{d}\boldsymbol{A}. \tag{3.32b}$$

The surface integral in Eq. (3.32b) can be transformed into a volume integral over the enclosed domain by using Gauss's integral theorem, Eq. (3.7). Equating with Eq. (3.32a) leads to the electrostatic equilibrium condition, which is known as one of Maxwell's equations in integral form:

$$\int_{\Lambda} \check{q}_{\Lambda} \, \mathrm{d}V = \int_{\Lambda} \blacktriangledown \boldsymbol{D} \, \mathrm{d}\boldsymbol{V}. \tag{3.33}$$

As the considered domain may be arbitrarily chosen, this relationship between spatial charge density and divergence of flux density needs to be satisfied at every point. Thus, the differential form of Maxwell's equation can be obtained:

$$\blacktriangledown \boldsymbol{D} - \check{q}_{\Lambda} = 0 \quad \text{in } \Lambda. \tag{3.34}$$

Just as in the mechanical case, the boundary $\partial\Lambda$ of the dielectric domain Λ is subdivided to consider two types of boundary conditions. The equilibrium between prescribed charges $\hat{q}_{\partial\Lambda}$ on the area $\partial\Lambda_D$ and the electric flux density can be established with Eq. (3.31). Since these charges are located on the outside, the appearing normal vector $\bar{\boldsymbol{e}}_n$ is pointing inward. Thus, for an outward oriented surface normal $\boldsymbol{e}_n = -\bar{\boldsymbol{e}}_n$ on the boundary of the dielectric domain, it may be written as

$$-\hat{q}_{\partial\Lambda} = \boldsymbol{D} \cdot \boldsymbol{e}_n \quad \text{on } \partial\Lambda_D. \tag{3.35}$$

For the area $\partial\Lambda_{\varphi}$, the electric potential $\varphi_{\partial\Lambda}$ is prescribed as

$$\varphi_{\partial\Lambda} = \varphi \quad \text{on } \partial\Lambda_{\varphi}. \tag{3.36}$$

3.3.4 Electric Field Strengths

The vector field of electric field strength $\boldsymbol{E}$ represents the force action of the charges already mentioned in Section 3.3.1. It is defined as the ratio of the vector of exerted force $\boldsymbol{F}$ and scalar of causative charge Q at every point within the field

$$\boldsymbol{E} = \frac{\boldsymbol{F}}{Q}. \tag{3.37}$$

The work $\mathrm{d}\mathcal{W}$ performed by a force along the differential distance vector $\mathrm{d}\boldsymbol{s}$ is formulated in Eq. (3.38a). Assuming that the considered field is a potential function field and thus irrotational, the work done by a charge may be

expressed as of Eq. (3.38b):

$$\mathrm{d}\mathcal{W} = \boldsymbol{F} \cdot \mathrm{d}\boldsymbol{s}, \tag{3.38a}$$

$$\mathrm{d}\mathcal{W} = -Q\,\mathrm{d}\varphi. \tag{3.38b}$$

Equating Eqs. (3.38a) and (3.38b) and couching the relation of force and charge as of Eq. (3.37), the electric field strength $\boldsymbol{E}$ may be determined as a function of the electric potential φ after auxiliary expansion with the unit vector $\boldsymbol{e}_s$ of the above-mentioned differential distance vector $\mathrm{d}\boldsymbol{s}$:

$$\begin{aligned} \boldsymbol{E} \cdot \mathrm{d}\boldsymbol{s} &= -\mathrm{d}\varphi, \\ \boldsymbol{E}\,\mathrm{d}s\boldsymbol{e}_s \cdot \boldsymbol{e}_s &= -\mathrm{d}\varphi\boldsymbol{e}_s, \\ \boldsymbol{E} &= -\frac{\mathrm{d}\varphi}{\mathrm{d}s}\boldsymbol{e}_s = -\nabla\varphi. \end{aligned} \tag{3.39}$$

Examining a single component E_i of the electric field strength vector $\boldsymbol{E}$, it may be described for a linear electric potential distribution between two points with the potentials φ_a and φ_b and the distance vector component s_i in the regarded direction by

$$E_i = -\frac{\varphi_b - \varphi_a}{s_i}. \tag{3.40}$$

3.4 Principle of Virtual Work

The field of analytical mechanics is characterized by variational principles postulated as axioms and dealing with scalar quantities like work or energy. In addition to the actual states of the mechanical system, there are virtual states, which in general are supposed to be independent of time, small, and admissible, but notional: they do not necessarily have to occur. From the mathematical point of view, these virtual states represent test functions. While for the case of actual quantities, the letter "d" is usually used to indicate differentially small values, such virtual values are denoted with the symbol "δ" following the notation in the calculus of variations. This approach can be applied to the electric properties of a system, too. The principles of mechanics may be found in *Päsler* [139], *Budó* [39], *Lanczos* [118], *Szabó* [172], or *Dym and Shames* [70], while the extension to coupled electrostatic fields is accredited to *Holland and EerNisse* [100] and given, for example, by *Ghandi and Hagood* [81].

3.4.1 General Principle of Virtual Work

This fundamental principle of physics is given by the axiom of Remark 3.1 in its most general formulation, where $\delta\mathcal{W}$ is the total virtual work of the system. For mechanical fields in deformable structures as well as for electrostatic fields in dielectric domains, it can be restated by the equality of internal $\delta\mathcal{U}$ and external $\delta\mathcal{V}$ contributions.

Remark 3.1. A physical system will be in equilibrium only if the total virtual work in accordance with the admissibility criteria vanishes.

$$\delta\mathcal{W} = \delta\mathcal{U} - \delta\mathcal{V} = 0. \tag{3.41}$$

Mechanical work at every particle of a continuum results from acting force and respective displacement or local stress and strain. correspondingly. So the above axiom of Remark 3.1 actually comprises two principles involving either virtual loads or virtual displacements. A brief derivation of both will be given in the following subsections. Similarly, the electric work can be treated, but we will present only one of the variants. The different formulations of the principle of virtual work are independent of a constitutive law and may be denoted as the weak forms of equilibrium, as only the equilibrium conditions have to be fulfilled in the integral mean. Weaker requirements with regard to differentiability of the involved functions have to be fulfilled, since the order of derivatives is reduced in comparison to the equilibrium formulation of Eqs. (3.14) and (3.34).

3.4.2 Principle of Virtual Displacements

The mechanical equilibrium of an infinitesimal volume element of a deformable structure, given by Eq. (3.14), may be multiplied with the vector field of virtual displacements $\delta\boldsymbol{u}$ and integrated over the domain Λ yielding

$$\int_{\Lambda} \delta\boldsymbol{u} \cdot (\blacktriangledown\boldsymbol{\sigma} + \check{\boldsymbol{f}}_{\Lambda})\,\mathrm{d}V = 0. \tag{3.42}$$

Separation of the terms leads to Eq. (3.43a), where the first term can be split into two parts with the aid of the divergence product rule of Eq. (3.6b), as shown in Eq. (3.43b). With the commutativity of the terms in the first integrand according to Eq. (3.3) and application of Gauss's integral theorem of Eq. (3.7) to the second integrand, while interchanging the multipliers according to Eq. (3.5), the formulation of Eq. (3.43c) is reached:

$$\int_{\Lambda} \delta\boldsymbol{u} \cdot \blacktriangledown\boldsymbol{\sigma}\,\mathrm{d}V + \int_{\Lambda} \delta\boldsymbol{u} \cdot \check{\boldsymbol{f}}_{\Lambda}\,\mathrm{d}V = 0, \tag{3.43a}$$

$$-\int_{\Lambda} \boldsymbol{\sigma} \cdot\cdot \nabla\delta\boldsymbol{u}\,\mathrm{d}V + \int_{\Lambda} \blacktriangledown\left(\boldsymbol{\sigma}^{T} \cdot \delta\boldsymbol{u}\right)\,\mathrm{d}V + \int_{\Lambda} \delta\boldsymbol{u} \cdot \check{\boldsymbol{f}}_{\Lambda}\,\mathrm{d}V = 0, \tag{3.43b}$$

$$-\int_{\Lambda} \nabla\delta\boldsymbol{u} \cdot\cdot \boldsymbol{\sigma}\,\mathrm{d}V + \int_{\partial\Lambda} \delta\boldsymbol{u} \cdot \boldsymbol{\sigma} \cdot \boldsymbol{e}_n\,\mathrm{d}A + \int_{\Lambda} \delta\boldsymbol{u} \cdot \check{\boldsymbol{f}}_{\Lambda}\,\mathrm{d}V = 0. \tag{3.43c}$$

The transformation of the volume integral over Λ into a surface integral over the volumes closed surface $\partial\Lambda$ allows for the application of the physical boundary conditions of Eq. (3.15). The virtual displacement gradient $\nabla\delta\boldsymbol{u}$ may be split into its symmetric and skew symmetric portions, as has been shown for the actual case in Eq. (3.19). The influence of the skew-symmetric portion in

the contracting product with the stress tensor $\boldsymbol{\sigma}$ disappears due to the symmetry of the latter. As the remaining part represents a virtual variant $\delta\boldsymbol{\varepsilon}$ of the linear Green strain tensor of Eq. (3.18), one obtains:

$$-\int_{\Lambda} \delta\boldsymbol{\varepsilon} \cdot\cdot\, \boldsymbol{\sigma}\, \mathrm{d}V + \int_{\partial\Lambda_\sigma} \delta\boldsymbol{u} \cdot \hat{\boldsymbol{f}}_{\partial\Lambda}\, \mathrm{d}A + \int_{\Lambda} \delta\boldsymbol{u} \cdot \check{\boldsymbol{f}}_{\Lambda}\, \mathrm{d}V = 0. \tag{3.44}$$

Consequently, with transition to the alternative vectorial arrangement of the stress and strain components as given on the right-hand sides of Eqs. (3.12) and (3.20), the final form in matrix representation is

$$\underbrace{\int_{\partial\Lambda_\sigma} \delta\boldsymbol{u}^T \hat{\boldsymbol{f}}_{\boldsymbol{\partial\Lambda}}\, \mathrm{d}A + \int_{\Lambda} \delta\boldsymbol{u}^T \check{\boldsymbol{f}}_{\boldsymbol{\Lambda}}\, \mathrm{d}V}_{\delta\mathcal{V}^{md}} = \underbrace{\int_{\Lambda} \delta\boldsymbol{\varepsilon}^T \boldsymbol{\sigma}\, \mathrm{d}V}_{\delta\mathcal{U}^{md}}. \tag{3.45}$$

This formulation of the principle of virtual work is the principle of virtual displacements, which appears in the literature sometimes under the name of the preceding. Naturally, the virtual strain energy $\delta\mathcal{U}^{md}$ exists only for mechanical systems with deformable parts. As the contained virtual strain tensor is assembled from derivatives of the virtual displacements, these have to be continuously differentiable. The virtual work of external impressed loads $\delta\mathcal{V}^{md}$ also includes the limiting cases of line or point loads. External reactive loads do not contribute when the virtual displacements are required to vanish at the points of action of these loads, and thus the virtual displacements have to comply with the actual geometric or displacement boundary conditions of Eq. (3.16). With these presumptions, the initial axiom of Remark 3.1 may now be reformulated for the virtual displacements.

Remark 3.2. A uniform mechanical system will be in equilibrium if the virtual work of the actual external and internal loads for arbitrary admissible virtual displacements vanishes.

3.4.3 Principle of Virtual Loads

The other formulation of the principle of virtual work for mechanical systems requires the introduction of virtual loads instead of virtual displacements. Therefore, only those variations of external loads and stress tensor are considered admissible that are compatible with the equations of equilibrium inside the mechanical system and on the boundary. The interior equilibrium of Eq. (3.14) for the virtual loading leads to the following form:

$$\blacktriangledown\delta\boldsymbol{\sigma} + \delta\check{\boldsymbol{f}}_{\Lambda} = 0 \quad \text{in } \Lambda. \tag{3.46}$$

As the actual external loads of the physical boundary conditions, given by Eq. (3.15), completely satisfy the equilibrium on the boundary $\partial\Lambda_\sigma$, the superimposed virtual external loads have to vanish there. On the boundary $\partial\Lambda_u$,

they indeed have to be in equilibrium with the virtual boundary stresses in accordance with the Cauchy theorem of Eq. (3.13):

$$\delta \boldsymbol{f}_{\partial \Lambda} = \delta \boldsymbol{\sigma} \cdot \boldsymbol{e}_n \quad \text{on } \partial \Lambda_u. \tag{3.47}$$

Now the virtual equilibrium of Eq. (3.46) may be multiplied by the vector field of actual displacements $\boldsymbol{u}$ and integrated over the Volume Λ yielding

$$\int_{\Lambda} \boldsymbol{u} \cdot (\blacktriangledown \delta \boldsymbol{\sigma} + \delta \check{\boldsymbol{f}}_{\Lambda}) \, \mathrm{d}V = 0. \tag{3.48}$$

When Eq. (3.48) is manipulated as before, considering the actual and virtual boundary conditions on $\partial \Lambda_u$ given by Eqs. (3.16) and (3.47), the principle of virtual loads, also known as the principle of complementary virtual work, may be formulated as

$$\underbrace{\int_{\partial \Lambda_u} \boldsymbol{u}_{\partial \Lambda}^T \delta \hat{\boldsymbol{f}}_{\partial \Lambda} \, \mathrm{d}A + \int_{\Lambda} \boldsymbol{u}^T \delta \check{\boldsymbol{f}}_{\Lambda} \, \mathrm{d}V}_{\delta \mathcal{V}^{ml}} = \underbrace{\int_{\Lambda} \boldsymbol{\varepsilon}^T \delta \boldsymbol{\sigma} \, \mathrm{d}V}_{\delta \mathcal{U}^{ml}}. \tag{3.49}$$

Here $\delta \mathcal{V}^{ml}$ is the complementary virtual work of external loads, and $\delta \mathcal{U}^{ml}$ the complementary virtual strain energy. The initial axiom of Remark 3.1 may now be reformulated for the virtual loads.

Remark 3.3. A uniform mechanical system will be in equilibrium if the virtual work of arbitrary compatible virtual external and internal loads for actual displacements vanishes.

3.4.4 Principle of Virtual Electric Potential

Electric systems may be treated like mechanical ones; the quantities appearing in electricity have a lower tensorial order: the mechanical displacement is a vector field, the electric potential is a scalar field. The electrostatic equilibrium of an infinitesimal volume element of a dielectric domain, given by Eq. (3.34), may be multiplied by the scalar field of a virtual electric potential $\delta \varphi$ and integrated over the Volume Λ, yielding

$$\int_{\Lambda} \delta \varphi (\blacktriangledown \boldsymbol{D} - \check{q}_{\Lambda}) \, \mathrm{d}V = 0. \tag{3.50}$$

Separation of the terms leads to Eq. (3.51a), where the first term can be split into two parts with the aid of the divergence product rule of Eq. (3.6a), as shown in Eq. (3.51b). With the commutativity of the terms in the first integrand according to Eq. (3.1) and application of Gauss's integral theorem of Eq. (3.7) to the second integrand, the formulation of Eq. (3.51c) is reached:

$$\int_{\Lambda} \delta\varphi \blacktriangledown \boldsymbol{D}\,\mathrm{d}V - \int_{\Lambda} \delta\varphi \check{q}_{\Lambda}\,\mathrm{d}V = 0, \tag{3.51a}$$

$$-\int_{\Lambda} \boldsymbol{D}\cdot\triangledown\delta\varphi\,\mathrm{d}V + \int_{\Lambda} \blacktriangledown(\delta\varphi\boldsymbol{D})\,\mathrm{d}V - \int_{\Lambda} \delta\varphi \check{q}_{\Lambda}\,\mathrm{d}V = 0, \tag{3.51b}$$

$$-\int_{\Lambda} \triangledown\delta\varphi\cdot\boldsymbol{D}\,\mathrm{d}V + \int_{\partial\Lambda} \delta\varphi\boldsymbol{D}\cdot\boldsymbol{e}_n\,\mathrm{d}A - \int_{\Lambda} \delta\varphi \check{q}_{\Lambda}\,\mathrm{d}V = 0. \tag{3.51c}$$

The transformation of the volume integral over Λ into a surface integral over the volume's closed surface $\partial\Lambda$ allows for the application of the surface flux boundary conditions of Eq. (3.35). The virtual electric potential gradient $\triangledown\delta\varphi$ may be represented by the virtual variant $\delta\boldsymbol{E}$ of the electric field strength vector of Eq. (3.39):

$$\int_{\Lambda} \delta\boldsymbol{E}\cdot\boldsymbol{D}\,\mathrm{d}V - \int_{\partial\Lambda_D} \delta\varphi\hat{q}_{\partial\Lambda}\,\mathrm{d}A - \int_{\Lambda} \delta\varphi\check{q}_{\Lambda}\,\mathrm{d}V = 0. \tag{3.52}$$

With rearrangement of terms and conversion to matrix representation, the principle of virtual electric potential takes its final form as

$$\underbrace{\int_{\partial\Lambda_D} \delta\varphi\hat{q}_{\partial\Lambda}\,\mathrm{d}A + \int_{\Lambda} \delta\varphi\check{q}_{\Lambda}\,\mathrm{d}V}_{\delta\mathcal{V}^{ep}} = \underbrace{\int_{\Lambda} \delta\boldsymbol{E}^T\boldsymbol{D}\,\mathrm{d}V}_{\delta\mathcal{U}^{ep}}. \tag{3.53}$$

Here $\delta\mathcal{V}^{ep}$ is the virtual work of external charges, and $\delta\mathcal{U}^{ep}$ the virtual work of internal charges. As the contained virtual electric field strength vector $\delta\boldsymbol{E}$ is assembled from derivatives of the virtual electric potential $\delta\varphi$, the latter has to be continuously differentiable. Further on, the virtual electric potential has to comply with the actual conductive boundary conditions of Eq. (3.36). The initial axiom of Remark 3.1 may now be reformulated for the virtual electric potential.

Remark 3.4. An electrostatic system will be in equilibrium if the virtual work of the actual external and internal charges for an arbitrary admissible virtual electric potential vanishes.

3.4.5 D'Alembert's Principle in the Lagrangian Version

The previous examinations of mechanical systems can be extended to accelerated motions by means of a rigid particle with the mass $\mathrm{d}m$ and volume $\mathrm{d}V$, which are proportional via the density ρ:

$$\mathrm{d}m = \rho\,\mathrm{d}V. \tag{3.54}$$

Following *Szabó* [172], the resultant $\mathrm{d}\boldsymbol{F}$ of impressed forces acting upon the particle may be split vectorially as follows:

$$\mathrm{d}\boldsymbol{F} = \mathrm{d}\boldsymbol{F}^{*} + \mathrm{d}\bar{\boldsymbol{F}}. \tag{3.55}$$

When $\mathrm{d}\boldsymbol{F}^*$ is equivalent to the inertia contributions for an acceleration $\boldsymbol{a}$ in accordance with the fundamental Newtonian law of motion, as given by Eq. (3.56a), then the remainder $\mathrm{d}\bar{\boldsymbol{F}}$ needs to take the form of Eq. (3.56b):

$$\mathrm{d}\boldsymbol{F}^* = \boldsymbol{a}\,\mathrm{d}m, \tag{3.56a}$$

$$\mathrm{d}\bar{\boldsymbol{F}} = \mathrm{d}\boldsymbol{F} - \boldsymbol{a}\,\mathrm{d}m. \tag{3.56b}$$

In compliance with *Lanczos* [118], $\mathrm{d}\bar{\boldsymbol{F}}$ may be called the effective force. As stated by Eq. (3.56b), it reflects the extension of the impressed force resultant $\mathrm{d}\boldsymbol{F}$ by the inertia term $-\boldsymbol{a}\,\mathrm{d}m$. In this way it is possible to reduce a problem of dynamics formally to one of statics and, thus, to deduce the differential equations describing the effects of accelerated motion. This is known as d'Alembert's principle. Because of its reactive character, as mentioned by *Budó* [39] and discussed in Section 3.4.2, the effective force $\mathrm{d}\bar{\boldsymbol{F}}$ does not perform virtual work. With the virtual displacements $\delta\boldsymbol{u}$, it may be written for the particle with the aid of Eq. (3.56b):

$$\delta\boldsymbol{u}^T\,\mathrm{d}\bar{\boldsymbol{F}} = \delta\boldsymbol{u}^T\,(\mathrm{d}\boldsymbol{F} - \boldsymbol{a}\,\mathrm{d}m) = 0. \tag{3.57}$$

For the rigid continuum of volume Λ consisting of such particles in accelerated motion, the virtual work may be formulated as given by Eq. (3.58). This extension of the principle of virtual displacements is referred to as d'Alembert's principle in the Lagrangian version:

$$\int_{\Lambda} \delta\boldsymbol{u}^T\,\mathrm{d}\bar{\boldsymbol{F}} = \int_{\Lambda} \delta\boldsymbol{u}^T\,(\mathrm{d}\boldsymbol{F} - \boldsymbol{a}\,\mathrm{d}m) = 0. \tag{3.58}$$

The result of impressed forces $\mathrm{d}\boldsymbol{F} = \mathrm{d}\boldsymbol{F}_{\Lambda} + \mathrm{d}\boldsymbol{F}_{\partial\Lambda}$ consists of contributions from volume $\check{\boldsymbol{f}}_{\Lambda}$ and area $\hat{\boldsymbol{f}}_{\partial\Lambda}$ loads and therefore may be replaced by means of Eqs. (3.10a) and (3.10b). Further on, the density ρ as given by Eq. (3.54) is introduced. Therewith the final representation of d'Alembert's principle in the Lagrangian version is obtained:

$$\underbrace{\int_{\partial\Lambda_\sigma} \delta\boldsymbol{u}^T\hat{\boldsymbol{f}}_{\partial\Lambda}\,\mathrm{d}A + \int_{\Lambda} \delta\boldsymbol{u}^T\check{\boldsymbol{f}}_{\Lambda}\,\mathrm{d}V}_{\delta\mathcal{V}^{md}} \underbrace{- \int_{\Lambda} \delta\boldsymbol{u}^T\boldsymbol{a}\rho\,\mathrm{d}V}_{\delta\mathcal{V}^{dl}} = 0. \tag{3.59}$$

The criteria of admissibility for the virtual displacements have been discussed in Section 3.4.2. As rigidity has been assumed in the case at hand, the occurring displacements do not cause strains. Therefore, virtual strains do not exist and, consequently, there are no contributions of internal loads to the virtual work. As expected, the virtual work of external impressed loads $\delta\mathcal{V}^{md}$ is identical to the term in the static principle of virtual displacements. The accelerated motion results in the additional term $\delta\mathcal{V}^{dl}$ representing the virtual work of the loads of inertia. In general, the principle may be formulated as follows:

Remark 3.5. A mechanical system of rigid parts in accelerated motion will be in equilibrium if the virtual work of the actual impressed and inertia loads for arbitrary admissible virtual displacements vanishes.

3.4.6 Summation of Virtual Work Contributions

In Sections 3.4.2 and 3.4.5, the virtual work contributions of a mechanical system being either static and deformable or dynamic and rigid were derived. They can be combined to picture a deformable dynamic system with the terms of Eqs. (3.45) and (3.59) as follows:

$$\delta\mathcal{V}^{md} + \delta\mathcal{V}^{dl} = \delta\mathcal{U}^{md}, \tag{3.60a}$$

$$\int_{\partial\Lambda_\sigma} \delta\boldsymbol{u}^T \hat{\boldsymbol{f}}_{\partial\Lambda}\,\mathrm{d}A + \int_{\Lambda} \delta\boldsymbol{u}^T(\check{\boldsymbol{f}}_{\Lambda} - \boldsymbol{a}\rho)\,\mathrm{d}V = \int_{\Lambda} \delta\boldsymbol{\varepsilon}^T\boldsymbol{\sigma}\,\mathrm{d}V. \tag{3.60b}$$

Alternatively, this formulation may be deduced starting from the interior conservation of momentum, Eq. (3.61), which upgrades the interior mechanical equilibrium, Eq. (3.14), with the inertia contributions of d'Alembert's principle, Eq. (3.56b). Thereby the derivation steps can be transferred from Section 3.4.2.

$$\blacktriangledown\boldsymbol{\sigma} + \check{\boldsymbol{f}}_{\Lambda} - \boldsymbol{a}\rho = 0 \quad \text{in } \Lambda. \tag{3.61}$$

The electric contributions from the principle of virtual potential, as derived in Section 3.4.4 and given by Eq. (3.53), still have to be incorporated. This can be achieved equivalently by the addition or subtraction of Eqs. (3.60b) and (3.53). In conformance with *Allik and Hughes* [4] and in view of the symmetry properties of the not yet introduced constitutive relation, the electrostatic expressions will be subtracted from the mechanical ones. The virtual work of external contributions takes the following form:

$$\begin{aligned}
\delta\mathcal{V} &= \delta\mathcal{V}^{md} + \delta\mathcal{V}^{dl} - \delta\mathcal{V}^{ep} \\
&= \int_{\partial\Lambda_\sigma} \delta\boldsymbol{u}^T \hat{\boldsymbol{f}}_{\partial\Lambda}\,\mathrm{d}A + \int_{\Lambda} \left(\delta\boldsymbol{u}^T\left(\check{\boldsymbol{f}}_{\Lambda} - \boldsymbol{a}\rho\right) - \delta\varphi\check{q}_{\Lambda}\right)\mathrm{d}V - \int_{\partial\Lambda_D} \delta\varphi\hat{q}_{\partial\Lambda}\,\mathrm{d}A \\
&= \int_{\partial\Lambda} \left\{\delta\boldsymbol{u}^T \quad -\delta\varphi\right\} \begin{Bmatrix} \hat{\boldsymbol{f}}_{\partial\Lambda} \\ \hat{q}_{\partial\Lambda} \end{Bmatrix} \mathrm{d}A + \int_{\Lambda} \left\{\delta\boldsymbol{u}^T \quad -\delta\varphi\right\} \begin{Bmatrix} \check{\boldsymbol{f}}_{\Lambda} - \boldsymbol{a}\rho \\ \check{q}_{\Lambda} \end{Bmatrix} \mathrm{d}V.
\end{aligned} \tag{3.62}$$

Since the forces $\hat{\boldsymbol{f}}_{\partial\Lambda}$ and charges $\hat{q}_{\partial\Lambda}$ on the boundary are zero apart from their respective working surface, the surface integrals may be summarized. Then the integrands can be collated in vector form, as shown in the last line. Similarly, the virtual work of internal contributions can be formulated, where the vectors of virtual strains $\delta\boldsymbol{\varepsilon}^T$ and virtual electric field strength $\delta\boldsymbol{E}^T$, as well as the vectors of actual stresses $\boldsymbol{\sigma}$ and actual electric flux density $\boldsymbol{D}$, can be merged:

$$\begin{aligned}
\delta\mathcal{U} &= \delta\mathcal{U}^{md} - \delta\mathcal{U}^{ep} \\
&= \int_{\Lambda} \delta\boldsymbol{\varepsilon}^T\boldsymbol{\sigma}\,\mathrm{d}V - \int_{\Lambda} \delta\boldsymbol{E}^T\boldsymbol{D}\,\mathrm{d}V \\
&= \int_{\Lambda} \left\{\delta\boldsymbol{\varepsilon}^T \quad \delta\bar{\boldsymbol{E}}^T\right\} \begin{Bmatrix} \boldsymbol{\sigma} \\ \boldsymbol{D} \end{Bmatrix} \mathrm{d}V.
\end{aligned} \tag{3.63}$$

Here the negative sign has been incorporated into the representation of the electric field strength by setting $\bar{\boldsymbol{E}} = -\boldsymbol{E}$.

3.5 Other Variational Principles

The principle of virtual work is suitable for solving a wide range of problems. There are tasks however where different but related formulations might be more useful. Thus, two prominent variational principles will be extended here to take into account materials with electromechanical couplings. This novel approach to Dirichlet's principle of minimum potential energy will be employed later in Section 6.3.2. In comparison to the principle of virtual work, the extended general Hamilton's principle is considered to be equivalent and even more versatile, but only its derivation will be demonstrated here.

3.5.1 Extended Dirichlet's Principle of Minimum Potential Energy

Another important principle of mechanics, see *Dym and Shames* [70] or *Sokolnikoff* [166] for details, will be extended here to electromechanically coupled problems. Let there be a function $\mathcal{U}_0$ to establish the following relation between the fields of mechanical stress $\boldsymbol{\sigma}$ and electric flux density $\boldsymbol{D}$ on the one hand, and the fields of mechanical strain $\boldsymbol{\varepsilon}$ and, for reasons to be clarified in Section 4.4.4, negative electric field strength $\bar{\boldsymbol{E}}$ on the other:

$$\begin{Bmatrix} \boldsymbol{\sigma} \\ \boldsymbol{D} \end{Bmatrix} = \frac{\partial \mathcal{U}_0}{\partial \begin{Bmatrix} \boldsymbol{\varepsilon} \\ \bar{\boldsymbol{E}} \end{Bmatrix}} = \begin{Bmatrix} \frac{\partial \mathcal{U}_0}{\partial \boldsymbol{\varepsilon}} \\ \frac{\partial \mathcal{U}_0}{\partial \bar{\boldsymbol{E}}} \end{Bmatrix}. \tag{3.64}$$

Such a function $\mathcal{U}_0$ can be shown to exist for conservative systems with their reversible processes, see *Dym and Shames* [70]. Thus, unlike the principle of virtual work derived above, the subsequent examination is limited to certain material properties. For mechanical fields, the demand for reversibility implies elastic material behavior, linear as well as non-linear. Hence, in the accustomed representations restricted to mechanical fields, the function $\mathcal{U}_0$ is called the elastic potential or strain energy density. In anticipation of subsequent chapters, it needs to be stated here that mechanical behavior as well as electromechanical coupling and electrostatic behavior of the considered piezoelectric materials is conservative as long as repolarization is avoided, see Figure 4.1. The function $\mathcal{U}_0$ will be determined and analyzed in Section 4.4.4 using the then available constitutive relation. For the extended examination at hand, the function $\mathcal{U}_0$ may be described as electroelastic energy density; sometimes it is termed electric enthalpy density, see *Tichý and Gautschi* [174]. Consequently, integration over the entire structure results in the electroelastic energy

$$\mathcal{U} = \int_{\Lambda} \mathcal{U}_0 \, \mathrm{d}V. \tag{3.65}$$

In the virtual work of internal contributions given by Eq. (3.63), the field quantities appearing in virtual and actual form are in no way connected. With the substitution of Eq. (3.64) into Eq. (3.63), this independence from

the material behavior is abolished:

$$\delta\mathcal{U} = \int_{\Lambda} \left\{ \delta\boldsymbol{\varepsilon}^T \quad \delta\bar{\boldsymbol{E}}^T \right\} \frac{\partial \mathcal{U}_0}{\partial \left\{ \begin{smallmatrix} \boldsymbol{\varepsilon} \\ \bar{\boldsymbol{E}} \end{smallmatrix} \right\}} \, \mathrm{d}V = \delta \int_{\Lambda} \mathcal{U}_0 \, \mathrm{d}V. \tag{3.66}$$

In the static portions of the virtual work of external contributions, the forces and charges acting on the constant volume and surface of the structure are not altered by the arbitrary variations $\delta\boldsymbol{u}$ of displacements and $\delta\varphi$ of electric potential respectively. Thus, the left-hand sides of Eqs. (3.45) and (3.53) may be written in the following form:

$$\delta\mathcal{V}^{md} = \delta \left(\int_{\partial\Lambda_\sigma} \boldsymbol{u}^T \hat{\boldsymbol{f}}_{\boldsymbol{\partial\Lambda}} \, \mathrm{d}A + \int_{\Lambda} \boldsymbol{u}^T \check{\boldsymbol{f}}_{\boldsymbol{\Lambda}} \, \mathrm{d}V \right), \tag{3.67a}$$

$$\delta\mathcal{V}^{ep} = \delta \left(\int_{\partial\Lambda_D} \varphi \hat{q}_{\partial\Lambda} \, \mathrm{d}A + \int_{\Lambda} \varphi \check{q}_{\Lambda} \, \mathrm{d}V \right). \tag{3.67b}$$

Equations (3.66) and (3.67) change the principle of virtual work of Eq. (3.41) to the following representation:

$$\delta \left(\mathcal{U} - \mathcal{V}^{md} + \mathcal{V}^{ep} \right) = 0. \tag{3.68}$$

To satisfy this statement, the expression in parentheses describing the potential energy is required to assume a stationary value. Furthermore, it can be shown that this extremum has to be the minimum of the potential energy, see *Sokolnikoff* [167] or *Knothe and Wessels* [113]. Thus, Dirichlet's principle of minimum potential energy can be extended to electromechanically coupled materials:

Remark 3.6. A uniform electromechanically coupled system will be in equilibrium for the set of displacements and electric potential satisfying the boundary conditions that produces the absolute minimum of potential energy.

$$\mathcal{U} - \mathcal{V}^{md} + \mathcal{V}^{ep} \;\Rightarrow\; \min. \tag{3.69}$$

3.5.2 Extended General Hamilton's Principle

D'Alembert's principle in the Lagrangian version, as derived in Section 3.4.5, uses infinitesimal virtual displacements about the instantaneous system state. For this reason, it is referred to as a differential principle. When infinitesimal virtual deviations from the entire motion of a system between two instants in time are examined, then it is an integral principle like Hamilton's principle, see *Goldstein* [86], *Sokolnikoff* [167], *Szabó* [172] or *Morgenstern and Szabó* [126]. Here the derivation from the prior to the latter principle will be demonstrated, starting with conversion of the virtual work of the inertia loads $\delta\mathcal{V}^{dl}$, included in Eq. (3.59). With Eq. (3.54) and acceleration as derivative of velocity, it

may be split as follows:

$$\begin{aligned}\delta\mathcal{V}^{dl} &= -\int_{\Lambda} \delta\boldsymbol{u}^T \boldsymbol{a}\,\mathrm{d}m \quad \text{with } \boldsymbol{a} = \frac{\mathrm{d}\boldsymbol{v}}{\mathrm{d}t} \\ &= -\int_{\Lambda} \delta\boldsymbol{u}^T \frac{\mathrm{d}\boldsymbol{v}}{\mathrm{d}t}\,\mathrm{d}m = -\frac{\mathrm{d}}{\mathrm{d}t}\int_{\Lambda} \delta\boldsymbol{u}^T \boldsymbol{v}\,\mathrm{d}m + \int_{\Lambda} \frac{\mathrm{d}}{\mathrm{d}t}\delta\boldsymbol{u}^T \boldsymbol{v}\,\mathrm{d}m. \end{aligned} \tag{3.70}$$

The last term, with the aid of Schwarz's theorem stating the possibility to interchange the order of taking partial derivatives and velocity as derivative of displacement, can be shown to represent the virtual change of kinetic energy $\mathcal{V}^{ke}$:

$$\begin{aligned}\delta\mathcal{V}^{ke} &= \int_{\Lambda} \frac{\mathrm{d}}{\mathrm{d}t}\delta\boldsymbol{u}^T \boldsymbol{v}\,\mathrm{d}m \quad \text{with } \frac{\mathrm{d}}{\mathrm{d}t}\delta\boldsymbol{u}^T = \delta\frac{\mathrm{d}\boldsymbol{u}^T}{\mathrm{d}t} = \delta\boldsymbol{v}^T \\ &= \int_{\Lambda} \delta\boldsymbol{v}^T \boldsymbol{v}\,\mathrm{d}m = \delta\frac{1}{2}\int_{\Lambda} |\boldsymbol{v}|^2\,\mathrm{d}m. \end{aligned} \tag{3.71}$$

Application of Eq. (3.71) to (3.70) leads to Lagrange's central equation:

$$\delta\mathcal{V}^{dl} = -\frac{\mathrm{d}}{\mathrm{d}t}\int_{\Lambda} \delta\boldsymbol{u}^T \boldsymbol{v}\,\mathrm{d}m + \delta\mathcal{V}^{ke}. \tag{3.72}$$

With its substitution into d'Alembert's principle in the Lagrangian version of Eq. (3.59), one obtains Eq. (3.73). Integration over the period of time from t_0 to t_1, where the virtual displacements are zero by definition at these end points such that $\delta\boldsymbol{u}(t_0) = \delta\boldsymbol{u}(t_1) = 0$, leads to the general Hamilton's principle of Eq. (3.74):

$$\delta\mathcal{V}^{md} + \delta\mathcal{V}^{ke} = \frac{\mathrm{d}}{\mathrm{d}t}\int_{\Lambda} \delta\boldsymbol{u}^T \boldsymbol{v}\,\mathrm{d}m, \tag{3.73}$$

$$\int_{t_0}^{t_1} \left(\delta\mathcal{V}^{md} + \delta\mathcal{V}^{ke}\right)\,\mathrm{d}t = 0. \tag{3.74}$$

Instead of using d'Alembert's principle in the Lagrangian version, Lagrange's central equation, Eq. (3.72), may be substituted into the complete principle of virtual work, Eq. (3.41) with (3.62) and (3.63). After the intermediate step of Eq. (3.75), this finally leads to the general Hamilton's principle with an extension to deformable piezoelectric bodies of Eq. (3.76):

$$\delta\mathcal{V}^{md} - \delta\mathcal{V}^{ep} + \delta\mathcal{V}^{ke} - \delta\mathcal{U}^{md} + \delta\mathcal{U}^{ep} = \frac{\mathrm{d}}{\mathrm{d}t}\int_{\Lambda} \delta\boldsymbol{u}^T \boldsymbol{v}\,\mathrm{d}m, \tag{3.75}$$

$$\int_{t_0}^{t_1} (\delta\mathcal{V}^{md} - \delta\mathcal{V}^{ep} + \delta\mathcal{V}^{ke} - \delta\mathcal{U}^{md} + \delta\mathcal{U}^{ep})\,\mathrm{d}t = 0. \tag{3.76}$$

4

Piezoelectric Materials

As pointed out in the introductory chapter, there are many multifunctional materials that can be applied to realize adaptive structural systems. They are distinguished by means of excitation mechanism, application range, and maturity of development. While research in material science will widen the choice in the future, currently only piezoelectric materials are suitable for the intended purpose. Therefore, the piezoelectric effect and its constitutive description is examined in detail in this chapter.

4.1 Piezoelectric Effect

Piezoelectricity represents the interdependence between mechanical and electrostatic fields, which is approximately proportional for the majority of applications. The direct piezoelectric effect describes the electrostatic reaction to a mechanical load, while the converse piezoelectric effect describes the mechanical reaction to an electrostatic load. Thorough portrayals of the physical background are given by *Cady* [41], *Ikeda* [103], *Tichý and Gautschi* [174] as well as application oriented presentations by *Chopra* [53], *Janocha* [106], *Elspass and Flemming* [72].

4.1.1 Historical Development

According to *Cady* [41], tourmaline crystals came from Ceylon to Europe in the early 18^{th} century and were found to possess a number of remarkable characteristics. Although a relationship between mechanical and electrical behavior had been expected by the scientific community, it could not be demonstrated experimentally for many years. Finally in 1880, the brothers Pierre and Jacques *Curie* [59,60] discovered the proportionality of pressure applied in specific directions and electric charges appearing with opposed signs on opposed surfaces. The following year, the term piezoelectric effect has been proposed for the observed behavior by *Hankel* [91]. The prefix

T.H. Brockmann, *Theory of Adaptive Fiber Composites*,
Solid Mechanics and Its Applications 161,

"piezo" is derived from the Greek verb "$\pi\iota\acute{\epsilon}\zeta\omega$" meaning to press or squeeze. The Curie brother also experimentally demonstrated the existence of the converse piezoelectric effect. Since then, other naturally occurring monocrystalline piezoelectric materials have been examined, the most important being quartz. Significant impetus has been generated by the discovery of piezoelectricity in polycrystalline ceramic materials like barium-titanate (BT) in the 1940's and lead-zirconate-titanate (PZT) in the 1950's; the latter still dominates transducer applications. Semicrystalline piezoelectric polymers on the basis of polyvinylidenefluoride (PVDF) usually in the form of thin films have been available since the late 1960's. Newer development tendencies are directed towards the improvement of PZT ceramics by doping them with additional components or producing artificial piezoelectric monocrystals, see *Nelson et al.* [131].

4.1.2 Crystal Structures

The piezoelectric effect is associated with the existence of an electric dipole in the elementary cell of the crystal structure. Such an electric dipole represents positive and negative charges with non-coinciding centers of concentration. The polar axis describes the dipole orientation with the polar direction from the negative to the positive center. Charge quantity and center-to-center spacing define the dipole moment. Relating the latter to the associated volume characterizes the polarization. An electric dipole and thus polarization can exist only when the elementary cell is not symmetric with respect to a point referred to as the inversion center, see *Giacovazzo* [83]. So the piezoelectric effect occurs only in such non-centrosymmetric crystals.

Polar Crystals and Polar-Neutral Crystals

The non-centrosymmetric crystals may be divided into two groups with respect to the occurrence of polar directions, see *Tichý and Gautschi* [174] or *Moulson and Herbert* [128]. When all dipoles are aligned with a unique polar direction, the crystals possess a spontaneous polarization and are denominated as polar crystals. The change of this existing polarization due to mechanical implications leads to the piezoelectric effect. Thermal influences may also change the spontaneous polarization of polar crystals; the resulting behavior is called the pyroelectric effect. In the case of non-unique polar directions, a neutralization occurs and prevents a spontaneous polarization. Therefore, such crystals are called polar-neutral crystals. Here the deformation causes a modification of the crystal symmetry, such that a unique polar direction emerges and the crystal becomes polarized along this direction. Thus, the polar-neutral crystals exhibit the piezoelectric effect but not the pyroelectric effect.

Ferroelectric Polar Crystals

There is an important subgroup of the polar crystals which possesses the ability to change the spontaneous polarization in reaction to electrostatic fields to another stable orientation, respectively, to a reverse configuration. Due to the analogy to ferromagnetic behavior, the name ferroelectricity has been introduced. Corresponding to the magnetic domains associated with the name of Pierre-Ernest Weiss, domains of largely uniform dipole orientations develop in the process of minimization of the free energy. These domains cause the non-linear properties of ferroelectric materials, especially with respect to the electrostatic polarization resulting in a hysteresis curve in alternating fields, Figure 4.1(a). In general, the polarization is also associated with a change in material properties and shape due to the implied modifications of the crystal structure. Therefore, the existence of a residual polarization in ferroelectric materials consequently leads to a lasting deformation, Figure 4.1(b). As repo-

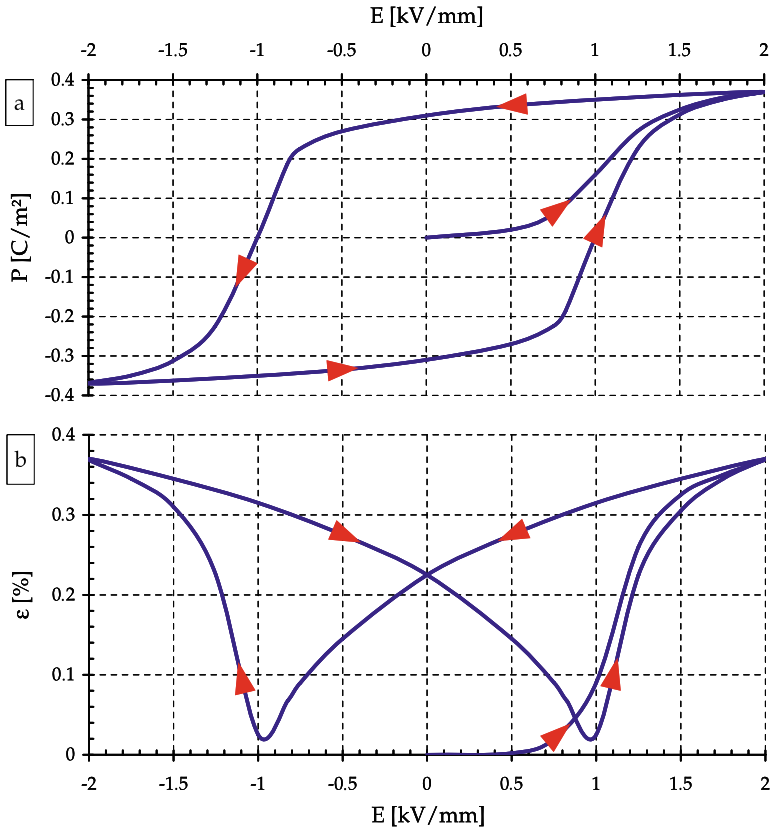

Fig. 4.1. Qualitative representation of hysteresis loops of PZT material; (a) polarization P and (b) strain ε as functions of the applied electric field strength E.

larization reduces the life span of ferroelectric material, it is usually polarized once and then operated within subcritical field levels. For PZT materials, this often is an electric field strength in the range between -0.5 and $1.5\ \mathrm{kV{\cdot}mm^{-1}}$. As shown in Figure 4.1(b), the electromechanical coupling is still not fully linear within this range. Details on the matters of hysteretic behavior and nonlinear coupling are provided, for example, by *Kamlah* [109] and *Zhou* [187]. Another ferroelectric characteristic is the limitation of the spontaneous polarization state to a certain temperature range. Above a critical temperature, called the Curie temperature, there is a phase change to a centrosymmetric crystal class, and the piezoelectric effect vanishes.

Monocrystalline Examples

The monocrystalline seignette salt $NaKC_4H_4O_6{\cdot}H_2O$ was the first found to belong to the group of ferroelectric polar crystals, while aluminum-boron-silicate $(Na, Ca)(Mg, Fe)_3B_3Al_6Si_6(O, OH, F)_{31}$, known as tourmaline, is an example of a non-ferroelectric polar crystal. Siliciumdioxide or quartz SiO_2 below a temperature of 573°C is a typical representative of a polar-neutral crystal. Recent developments in material science are concerned with ferroelectric single crystal systems like $(1-x)Pb(Mg_{1/3}Nb_{2/3})O_3{-}x\ PbTiO_3$ or $(1-x)Pb(Zn_{1/3}Nb_{2/3})O_3{-}x\ PbTiO_3$, where x indicates the share of lead-titanate. These materials with the abbreviations PMN-PT and PZN-PT have very competitive electromechanical properties.

Polycrystalline Characteristics

While monocrystals are characterized by a continuous spatial arrangement of elementary cells, polycrystals consist of a multitude of crystalline grains, so-called crystallites, with alike properties inside their boundaries but changing orientations across the boundaries. A regular spatial pattern of oriented crystallites is called texture. In order to exhibit the piezoelectric effect, such textures also must not possess an inversion center, otherwise, even when the crystallites are piezoelectric, the effect would be neutralized. Piezoelectric ceramics are a typical example of polycrystalline materials. Most prominent with respect to a broad application are barium-titanate $BaTiO_3$ and particularly lead-zirconate-titanate $Pb(Zr, Ti)O_3$. The structure of both materials may be summarized by the general formula $A^{2+}B^{4+}O_3^{2-}$. With respect to their ferroelectric nature, they switch from the non-centrosymmetric tetragonal crystal class to the centrosymmetric cubic crystal class when their respective Curie temperature is exceeded and thus loose their piezoelectric properties. Both configurations are shown in Figure 4.2 with the decisive asymmetric dislocation of the B^{4+} component.

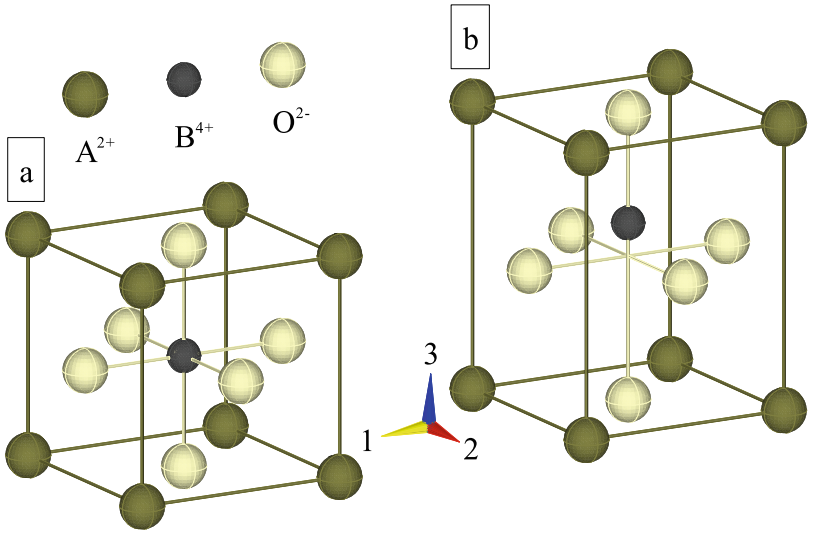

Fig. 4.2. Elementary crystal cell; (a) cubic configuration and (b) tetragonal configuration due to polarization along the e_3-direction.

Semicrystalline Characteristics

Semicrystalline polymers are thermoplastics and consist of crystallites surrounded by a transitional phase which again is embedded into an amorphous phase. Polyvinylidenefluoride is such a material with piezoelectric properties. Its long molecular chains, typical for a polymer, may be found in different configurations of spatial arrangement with a polar and a polar-neutral crystal structure for each of these configurations. Subjected to thermal, mechanical, and electrostatic influences, the properties may be altered significantly. The reaction on electrostatic influences points to the ferroelectric nature of semicrystalline polymers. Details are given, for example, by *Elspass and Flemming* [72].

4.2 Constitutive Formulation

The fundamental considerations of Chapter 3 are independent of the properties of the materials and therefore are not sufficient to describe the behavior of the mechanical or electrostatic system. The missing links are the constitutive relations between stresses and strains on the mechanical side, between flux density and field strength on the electrostatic side, and the connection between the mechanical and electrostatic side. Effects like piezoelectricity couple the mechanical and electrostatic fields. For the subsequent considerations identical material properties at every location of the continuum can be presumed due to its macroscopic homogeneity.

4.2.1 Mechanical Fields

We limit our examination to materials with a unique coherence between the present local stress and strain states, where deformation history or time-dependent processes do not matter. Under these conditions, the removal of loads leads to a complete reversal of deformations. In addition, we demand independence from mechanical field intensities within the intensity levels of interest:

Remark 4.1. The mechanical behavior of the materials will be assumed to be elastic and linear.

The Cauchy stress tensor $\boldsymbol{\sigma}$ and Green Lagrange strain tensor $\boldsymbol{\varepsilon}_{\mathrm{GL}}$ are of second order and may be connected for a general anisotropic linear elastic material via a fourth-order tensor. The originally 81 constants of such an elasticity tensor reduce to 36 due to the symmetry of the stress and strain tensor, and may be represented by a square matrix of dimension six. Because of the potential property of elastic materials, such a matrix is symmetric and thus the number of independent components is further reduced to 21. For small displacements, the mechanical constitutive relation with the stiffness matrix $\mathbf{C}$ or with the compliance matrix $\mathbf{S}$ reads

$$\boldsymbol{\sigma} = \mathbf{C}\boldsymbol{\varepsilon} \quad \text{or} \quad \boldsymbol{\varepsilon} = \mathbf{S}\boldsymbol{\sigma} \quad \text{with } \mathbf{S} = \mathbf{C}^{-1}. \tag{4.1}$$

Technically relevant applications are hardly concerned with complete anisotropy. Composites with a regular distribution of constituents along the principal axes are an example of a material with three orthogonal planes of symmetry. The description of such orthotropic properties requires nine independent matrix entries:

$$\begin{Bmatrix} \sigma_1 \\ \sigma_2 \\ \sigma_3 \\ \tau_{23} \\ \tau_{31} \\ \tau_{12} \end{Bmatrix} = \begin{bmatrix} C_{11} & C_{12} & C_{13} & 0 & 0 & 0 \\ C_{12} & C_{22} & C_{23} & 0 & 0 & 0 \\ C_{13} & C_{23} & C_{33} & 0 & 0 & 0 \\ 0 & 0 & 0 & C_{44} & 0 & 0 \\ 0 & 0 & 0 & 0 & C_{55} & 0 \\ 0 & 0 & 0 & 0 & 0 & C_{66} \end{bmatrix} \begin{Bmatrix} \varepsilon_1 \\ \varepsilon_2 \\ \varepsilon_3 \\ \gamma_{23} \\ \gamma_{31} \\ \gamma_{12} \end{Bmatrix}. \tag{4.2}$$

Composites with uniformly distributed unidirectional fibers aligned with a principal axis additionally possess a plane of isotropy in the transverse direction, where the material behavior is invariant to rotations. For such transversely isotropic properties, the number of constants is reduced to five. When the concerned axis of rotation is oriented in the $\boldsymbol{e}_3$-direction,

$$C_{22} = C_{11}, \qquad C_{23} = C_{13}, \qquad C_{55} = C_{44}, \qquad C_{66} = \frac{1}{2}\left(C_{11} - C_{12}\right). \tag{4.3}$$

If every arbitrary section plane is a plane of isotropy, the material is isotropic; there only two independent constants remain:

$$\begin{aligned} C_{33} &= C_{22} = C_{11}, \qquad C_{23} = C_{13} = C_{12}, \\ C_{44} &= C_{55} = C_{66} = \frac{1}{2}(C_{11} - C_{12}). \end{aligned} \tag{4.4}$$

4.2.2 Electrostatic Fields

Presuming that there is no electrostatic equivalent to mechanical inelasticity, compare with Remark 4.1, the essential demand concerning the properties of dielectric materials is independence of the electrostatic field intensities within the intensity levels of interest:

Remark 4.2. The electrostatic behavior of the materials will be assumed to be linear.

The electric flux density $\boldsymbol{D}$ and electric field strength $\boldsymbol{E}$ are vectors, i.e. tensors of first order and therefore may be related via a tensor of second order with nine constants for the three dimensions. Due to the potential property also observed for electrostatic fields, the tensor is symmetric and thus contains six independent entries. The electrostatic constitutive relation can be expressed with the aid of the dielectric permittivity matrix $\boldsymbol{\epsilon}$ (to be distinguished from the strains ε) or its inverse $\boldsymbol{\beta}$:

$$\boldsymbol{D} = \boldsymbol{\epsilon}\boldsymbol{E} \quad \text{or} \quad \boldsymbol{E} = \boldsymbol{\beta}\boldsymbol{D} \quad \text{with } \boldsymbol{\beta} = \boldsymbol{\epsilon}^{-1}. \tag{4.5}$$

Thereby these specifications occasionally are given relative to the dielectric permittivity of vacuum ϵ_0:

$$\boldsymbol{\epsilon} = \bar{\boldsymbol{\epsilon}}\epsilon_0 \quad \text{with } \epsilon_0 = 8.855 \times 10^{-12}\ \frac{\text{As}}{\text{Vm}}. \tag{4.6}$$

The rhombic crystal class as well as composites with adequate constituents and layout, for instance, possess orthotropic properties in analogy to the mechanical material properties. Therefore, only the three entries on the diagonal of the constitutive matrix are retained:

$$\begin{Bmatrix} D_1 \\ D_2 \\ D_3 \end{Bmatrix} = \begin{bmatrix} \epsilon_{11} & 0 & 0 \\ 0 & \epsilon_{22} & 0 \\ 0 & 0 & \epsilon_{33} \end{bmatrix} \begin{Bmatrix} E_1 \\ E_2 \\ E_3 \end{Bmatrix}. \tag{4.7}$$

Transversely isotropic properties, as exhibited, for example, by the tetragonal crystal class, require two dielectric constants and thus using the distinct axis again in the $\boldsymbol{e}_3$-direction this implies

$$\epsilon_{22} = \epsilon_{11}. \tag{4.8}$$

For isotropic properties, as exhibited for example by the cubic crystal class, there is only one dielectric constant:

$$\epsilon_{33} = \epsilon_{22} = \epsilon_{11}. \tag{4.9}$$

4.2.3 Electromechanical Coupling

In continuation of the presumptions formulated in Remarks 4.1 and 4.2, also the coupling between mechanical and electrostatic fields will be limited to the linear case, considering piezoelectricity but disregarding electrostriction and other highly non-linear effects.

Remark 4.3. The electromechanical coupling in the materials will be assumed to be linear.

The subsequent characterization of electromechanical coupling covers the various classes of piezoelectric materials. Details with respect to definition and determination of the constants describing these materials have been standardized by the *Institute of Electrical and Electronics Engineers* [104]. Stresses $\boldsymbol{\sigma}$ and strains $\boldsymbol{\varepsilon}$ on the mechanical side, as well as flux density $\boldsymbol{D}$ and field strength $\boldsymbol{E}$ on the electrostatic side, may be arbitrarily combined into four forms of coupled constitutive equations:

$$\begin{Bmatrix} \boldsymbol{\sigma} \\ \boldsymbol{D} \end{Bmatrix} = \overbrace{\begin{bmatrix} \mathbf{C}^{\boldsymbol{E}} & -\mathbf{e} \\ \mathbf{e}^T & \boldsymbol{\epsilon}^{\boldsymbol{\varepsilon}} \end{bmatrix}}^{\mathbb{C}} \begin{Bmatrix} \boldsymbol{\varepsilon} \\ \boldsymbol{E} \end{Bmatrix}, \qquad \begin{Bmatrix} \boldsymbol{\varepsilon} \\ \boldsymbol{D} \end{Bmatrix} = \overbrace{\begin{bmatrix} \mathbf{S}^{\boldsymbol{E}} & \mathbf{d} \\ \mathbf{d}^T & \boldsymbol{\epsilon}^{\boldsymbol{\sigma}} \end{bmatrix}}^{\mathbb{S}} \begin{Bmatrix} \boldsymbol{\sigma} \\ \boldsymbol{E} \end{Bmatrix}, \tag{4.10a}$$

$$\begin{Bmatrix} \boldsymbol{\sigma} \\ \boldsymbol{E} \end{Bmatrix} = \underbrace{\begin{bmatrix} \mathbf{C}^{\boldsymbol{D}} & -\mathbf{h} \\ -\mathbf{h}^T & \boldsymbol{\beta}^{\boldsymbol{\varepsilon}} \end{bmatrix}}_{\mathbb{S}^{-1}} \begin{Bmatrix} \boldsymbol{\varepsilon} \\ \boldsymbol{D} \end{Bmatrix}, \qquad \begin{Bmatrix} \boldsymbol{\varepsilon} \\ \boldsymbol{E} \end{Bmatrix} = \underbrace{\begin{bmatrix} \mathbf{S}^{\boldsymbol{D}} & \mathbf{g} \\ -\mathbf{g}^T & \boldsymbol{\beta}^{\boldsymbol{\sigma}} \end{bmatrix}}_{\mathbb{C}^{-1}} \begin{Bmatrix} \boldsymbol{\sigma} \\ \boldsymbol{D} \end{Bmatrix}. \tag{4.10b}$$

For the subsequent classification of the appearing constants, their determination by means of a test specimen should be kept in mind. The mechanical conditions of constant strain, satisfied by clamped configurations, are designated by $(\cdot)^{\boldsymbol{\varepsilon}}$ and those of constant stress, satisfied by free boundaries, by $(\cdot)^{\boldsymbol{\sigma}}$. The electrostatic conditions of constant field strength, satisfied with short circuited electrodes, are designated by $(\cdot)^{\boldsymbol{E}}$ and those of constant flux density, satisfied with open circuited electrodes, by $(\cdot)^{\boldsymbol{D}}$. The constants of the matrices $\mathbf{e}$ and $\mathbf{d}$ thus stand, respectively, for induced stress and strain, whereas the constants of the matrices $\mathbf{h}$ and $\mathbf{g}$ represent, respectively, sensed stress and strain. While the constitutive matrices of Eqs. (4.10a) and (4.10b) may be converted into one another by complete inversion, the sub-matrices within each line can be transformed as given below:

$$\mathbf{C}^{\boldsymbol{E}} = \left(\mathbf{S}^{\boldsymbol{E}}\right)^{-1}, \qquad \mathbf{e} = \mathbf{C}^{\boldsymbol{E}}\mathbf{d}, \qquad \boldsymbol{\epsilon}^{\boldsymbol{\varepsilon}} = \boldsymbol{\epsilon}^{\boldsymbol{\sigma}} - \mathbf{d}^T\mathbf{C}^{\boldsymbol{E}}\mathbf{d}; \tag{4.11a}$$

$$\mathbf{C}^{\boldsymbol{D}} = \left(\mathbf{S}^{\boldsymbol{D}}\right)^{-1}, \qquad \mathbf{h} = \mathbf{C}^{\boldsymbol{D}}\mathbf{g}, \qquad \boldsymbol{\beta}^{\boldsymbol{\varepsilon}} = \boldsymbol{\beta}^{\boldsymbol{\sigma}} + \mathbf{g}^T\mathbf{C}^{\boldsymbol{D}}\mathbf{g}. \tag{4.11b}$$

It is the forms of constitutive equations given by Eqs. (4.10a) that are used most often.The one on the left-hand side is suggested by the formulation of the virtual work of internal contributions in Eq. (3.63).

4.2.4 Spatial Rotation

The mechanical constitutive relations of Eqs. (4.1) are set up with respect to the orthonormal base vectors $\boldsymbol{e}_1, \boldsymbol{e}_2, \boldsymbol{e}_3$, which usually represent the principal axes of the material. When a material description in rotated coordinates with the orthonormal base vectors $\boldsymbol{e}_s, \boldsymbol{e}_n, \boldsymbol{e}_x$ is necessary, this can be achieved with the aid of the transformation relations of Eqs. (3.27) and (3.28) as follows:

$$\boldsymbol{\sigma}(s,n,x) = \mathbf{T}\mathbf{C}\mathbf{T}^T \boldsymbol{\varepsilon}(s,n,x)\,, \tag{4.12}$$

$$\boldsymbol{\varepsilon}(s,n,x) = \left(\mathbf{T}^{-1}\right)^T \mathbf{S}\mathbf{T}^{-1} \boldsymbol{\sigma}(s,n,x)\,. \tag{4.13}$$

As the electrodes necessary to capture the electrostatic fields are generally attached with respect to the associated principal axes, they follow the rotation and thus the electrostatic fields do not undergo the transformation. Nevertheless, their interaction with the mechanical fields via the electromechanical coupling coefficients needs to be taken into account. This is accomplished by extending the mechanical transformation matrix $\mathbf{T}$ with the identity matrix $\mathbf{I}$ for the transformation of the electromechanical constitutive relation of Eqs. (4.10). For the variant on the left-hand side of Eq. (4.10a), this means

$$\begin{Bmatrix} \boldsymbol{\sigma}(s,n,x) \\ \boldsymbol{D}(1,2,3) \end{Bmatrix} = \underbrace{\begin{bmatrix} \mathbf{T} & \\ & \mathbf{I} \end{bmatrix}}_{\mathbb{T}} \underbrace{\begin{bmatrix} \mathbf{C}^{\boldsymbol{E}} & -\mathbf{e} \\ \mathbf{e}^T & \boldsymbol{\epsilon}^{\boldsymbol{\varepsilon}} \end{bmatrix}}_{\mathbb{C}} \underbrace{\begin{bmatrix} \mathbf{T} & \\ & \mathbf{I} \end{bmatrix}^T}_{\mathbb{T}^T} \begin{Bmatrix} \boldsymbol{\varepsilon}(s,n,x) \\ \boldsymbol{E}(1,2,3) \end{Bmatrix}. \tag{4.14}$$

When the multiplication is executed for the sub-matrices, it can be recognized that the transformation behavior of the mechanical stiffness coefficients given by Eq. (4.12) is reproduced in the upper left part, and the unchanged dielectric permittivity coefficients remain in the lower right part of the resulting matrix. As expected, the electromechanical coupling coefficients to be found off the diagonal are transformed, preserving their properties of being transposed and negated to each other:

$$\mathbb{T}\mathbb{C}\mathbb{T}^T = \begin{bmatrix} \mathbf{T}\mathbf{C}^{\boldsymbol{E}}\mathbf{T}^T & -\mathbf{T}\mathbf{e} \\ \mathbf{e}^T\mathbf{T}^T & \boldsymbol{\epsilon}^{\boldsymbol{\varepsilon}} \end{bmatrix}. \tag{4.15}$$

4.2.5 Analogy of Electrically and Thermally Induced Deformations

The simulation of component parts exhibiting electromechanical coupling with the aid of commercial finite element packages is subject to some restrictions. Usually the piezoelectric effect is considered only in connection with volume elements, see *Freed and Babuska* [76]. For complex structures, the modeling with volume elements often does not represent a viable procedure with respect to implementation and calculation expenditure. A prominent example for this are structures with thin walls made of multiple layers. Their mechanical behavior may be simulated efficiently with layered structural shell elements,

which are in addition able to capture thermal effects. In the absence of further couplings, the temperature and its mechanical implications in general may be utilized to depict the electromechanical coupling. But a number of essential differences has to be considered:

- While the coupling of mechanical and electrostatic fields is mutual, the temperature has mechanical implications without a noticeable converse.
- While electrostatic fields may change almost instantaneously, the temperature is subject of a comparatively slow heat transfer problem.
- While electrostatic fields are vector fields, the temperature is a scalar field.

The first item restricts the exploitation of the analogy to the case of actuator applications and thus excludes sensor applications. Although the second item is not reflected in the constitutive relation, the usual treatment of the temperature in finite element codes confines such a simulation of electromechanical couplings to the static case. By virtue of the third item, it is dealt with a different number and arrangement of constitutive coefficients, but this fact does not cause any restrictions and can be handled by the subsequently described substitution. The mechanical constitutive relation of the general anisotropic case, given by Eq. (4.1), can be extended to thermal influences with the aid of the vector of thermal expansion and shear coefficients $\tilde{\boldsymbol{\alpha}}$ and the thermal gradient ΔT:

$$\varepsilon = \mathbf{S}\boldsymbol{\sigma} + \tilde{\boldsymbol{\alpha}}\Delta T \quad \text{with } \tilde{\boldsymbol{\alpha}} = \mathbf{d}\frac{\mathbf{E}}{\Delta T} + \boldsymbol{\alpha},\ \mathbf{S} = \mathbf{S}^{\boldsymbol{E}}. \tag{4.16}$$

When $\tilde{\boldsymbol{\alpha}}$ is substituted as outlined above and the compliance coefficients $\mathbf{S}^{\boldsymbol{E}}$ associated with the induced strain coefficients $\mathbf{d}$ are used, then the formulation turns into the upper part of the constitutive equations given on the right-hand side of Eqs. (4.10a). In addition, the actual thermal coefficients may be taken into consideration by the vector $\boldsymbol{\alpha}$. Thus, supplying specialized finite elements also capable of capturing anisotropic thermal effects with the constitutive coefficients and electric field strength of the electromechanically coupled problem, as given by Eq. (4.16), is a convenient procedure for the case of static actuation.

4.3 Constitutive Examination

Although examples of constitutive matrices have been shown, the material properties have not yet been specified and analyzed. These characteristics will be discussed in this section by means of piezoelectric materials like the widely used ferroelectric ceramics and monocrystals.

4.3.1 Constitutive Relation

For piezoelectric materials with at least orthotropic behavior and polarization along the $\boldsymbol{e}_3$-direction, the constitutive equation is

$$\begin{Bmatrix} \sigma_1 \\ \sigma_2 \\ \sigma_3 \\ \tau_{23} \\ \tau_{31} \\ \tau_{12} \\ D_1 \\ D_2 \\ D_3 \end{Bmatrix} = \begin{bmatrix} C_{11}^{\boldsymbol{E}} & C_{12}^{\boldsymbol{E}} & C_{13}^{\boldsymbol{E}} & 0 & 0 & 0 & 0 & 0 & -e_{31} \\ C_{12}^{\boldsymbol{E}} & C_{22}^{\boldsymbol{E}} & C_{23}^{\boldsymbol{E}} & 0 & 0 & 0 & 0 & 0 & -e_{32} \\ C_{13}^{\boldsymbol{E}} & C_{23}^{\boldsymbol{E}} & C_{33}^{\boldsymbol{E}} & 0 & 0 & 0 & 0 & 0 & -e_{33} \\ 0 & 0 & 0 & C_{44}^{\boldsymbol{E}} & 0 & 0 & 0 & -e_{24} & 0 \\ 0 & 0 & 0 & 0 & C_{55}^{\boldsymbol{E}} & 0 & -e_{15} & 0 & 0 \\ 0 & 0 & 0 & 0 & 0 & C_{66}^{\boldsymbol{E}} & 0 & 0 & 0 \\ 0 & 0 & 0 & 0 & e_{15} & 0 & \epsilon_{11}^{\boldsymbol{\varepsilon}} & 0 & 0 \\ 0 & 0 & 0 & e_{24} & 0 & 0 & 0 & \epsilon_{22}^{\boldsymbol{\varepsilon}} & 0 \\ e_{31} & e_{32} & e_{33} & 0 & 0 & 0 & 0 & 0 & \epsilon_{33}^{\boldsymbol{\varepsilon}} \end{bmatrix} \begin{Bmatrix} \varepsilon_1 \\ \varepsilon_2 \\ \varepsilon_3 \\ \gamma_{23} \\ \gamma_{31} \\ \gamma_{12} \\ E_1 \\ E_2 \\ E_3 \end{Bmatrix}. \tag{4.17}$$

Together with the mechanical and electrostatic simplifications introduced by Eqs. (4.3) and (4.8), transversely isotropic properties can be characterized for the piezoelectric coupling by

$$e_{32} = e_{31}, \qquad e_{15} = e_{24}. \tag{4.18}$$

It should be mentioned that the otherwise transversely isotropic properties of the typical piezoelectric materials, given by Table A.3 in the Appendix, show deviations of a different degree from the last relation of Eqs. (4.3) expressing the dependence of $C_{66}^{\boldsymbol{E}}$. While these deviations are relatively small in the case of the PZT ceramics, the properties of PMN-PT single crystals do not comply with this condition at all.

Partial Coupling

In the structure of the constitutive equation for the mechanically and electrostatically orthotropic piezoelectric material of Eq. (4.17), the partial coupling needs to be noted. The normal stresses and strains in all three directions are solely connected to flux density and field strength along the polarization direction:

$$\begin{Bmatrix} \sigma_1 \\ \sigma_2 \\ \sigma_3 \\ D_3 \end{Bmatrix} = \underbrace{\begin{bmatrix} C_{11}^{\boldsymbol{E}} & C_{12}^{\boldsymbol{E}} & C_{13}^{\boldsymbol{E}} & -e_{31} \\ C_{12}^{\boldsymbol{E}} & C_{22}^{\boldsymbol{E}} & C_{23}^{\boldsymbol{E}} & -e_{32} \\ C_{13}^{\boldsymbol{E}} & C_{23}^{\boldsymbol{E}} & C_{33}^{\boldsymbol{E}} & -e_{33} \\ e_{31} & e_{32} & e_{33} & \epsilon_{33}^{\boldsymbol{\varepsilon}} \end{bmatrix}}_{\mathbb{E}} \begin{Bmatrix} \varepsilon_1 \\ \varepsilon_2 \\ \varepsilon_3 \\ E_3 \end{Bmatrix}. \tag{4.19}$$

The shear stresses and strains in the planes between polarization and transverse directions are coupled to flux density and field strength along the respective transverse axis:

$$\begin{Bmatrix} \tau_{31} \\ D_1 \end{Bmatrix} = \underbrace{\begin{bmatrix} C_{55}^{\boldsymbol{E}} & -e_{15} \\ e_{15} & \epsilon_{11}^{\boldsymbol{\varepsilon}} \end{bmatrix}}_{\mathbb{G}_1} \begin{Bmatrix} \gamma_{31} \\ E_1 \end{Bmatrix} \quad \text{and} \quad \begin{Bmatrix} \tau_{23} \\ D_2 \end{Bmatrix} = \underbrace{\begin{bmatrix} C_{44}^{\boldsymbol{E}} & -e_{24} \\ e_{24} & \epsilon_{22}^{\boldsymbol{\varepsilon}} \end{bmatrix}}_{\mathbb{G}_2} \begin{Bmatrix} \gamma_{23} \\ E_2 \end{Bmatrix}. \tag{4.20}$$

Complete decoupling is found in the case of shear in the plane transverse to the polarization direction:

$$\tau_{12} = C_{66}^{\boldsymbol{E}} \gamma_{12}. \tag{4.21}$$

4.3.2 Converse Piezoelectric Effect

To illustrate the behavior of piezoelectric material, the constitutive equations of the previous subsection will be observed in further detail by means of a cube of such matter. The principal axes of the polarized macroscopically homogeneous material are aligned with the edges of the cube. For actuator applications use is made of the converse piezoelectric effect, and thus the cube has to be subjected to electrostatic fields. This is usually accomplished by supplying a pair of electrodes in the form of opposed conductive surfaces with opposed electric charges. This electric potential difference, together with the distance between the electrodes, leads to an associated electric field strength component according to Eq. (3.40). The aligned electric flux density component may be determined via the dielectric permittivities, lower third of Eq. (4.17), while the field strength and flux density components in all other directions are zero. Depending on the mechanical boundary conditions applied to the cube, either strains in the free configuration or stresses in the clamped configuration are induced. For electrostatic fields opposed or transverse to the polarization direction, the field levels are limited by the risk of repolarization.

Normal Mode Actuation

Electrostatic field components in parallel with the polarization direction induce normal mode actuation, see Eq. (4.19). Not visible in the constitutive equation, but explainable by a behavior corresponding to Poisson's effect included in the piezoelectric constants, the signs of strains or stresses parallel and transverse to the applied electrostatic fields are opposed. The deformation of a piezoelectric cube subjected to electrostatic fields in the direction of polarization is shown in Figure 4.3.

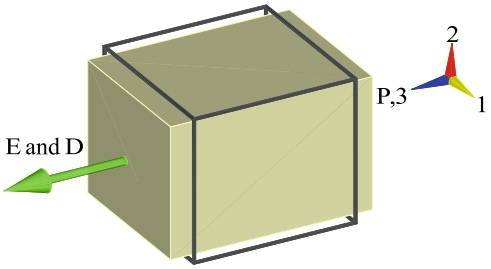

Fig. 4.3. Normal mode of the converse piezoelectric effect.

Shear Mode Actuation

Electrostatic field components transverse to the direction of polarization induce shear mode actuation, see Eq. (4.20). The particular shear strains or

shear stresses appear in the plane unfolding between the direction of the applied electrostatic field component and the polarization direction. The deformation of a piezoelectric cube subjected to electrostatic fields transverse to the direction of polarization is shown in Figure 4.4.

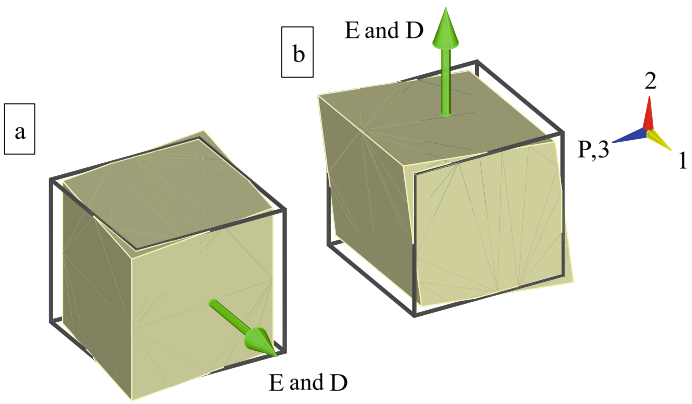

Fig. 4.4. Shear mode of the converse piezoelectric effect.

4.3.3 Direct Piezoelectric Effect

For sensor applications, use is made of the direct piezoelectric effect and thus the piezoelectric cube described above now has to be subjected to mechanical fields. Strains and stresses are applied via associated surfaces either by prescribed displacements in a clamped configuration or by applied forces in a free configuration. Besides the intended sensor application, this, of corrse, is also relevant to the case of solely passive transmission of loads. Consequently, the subsequent examinations are also important for the general application of electromechanically coupled materials in adaptive structures. For mechanical fields operating opposed or transverse to the polarization direction, the field levels are limited by the risk of repolarization similar to the actuation case.

External Electric Influences

The electrostatic fields forming in a single direction as the result of basic load cases depend on the electric boundary conditions and are thus influenced by the electrode configuration. When the electrodes on the associated surfaces are non-existent or disconnected, only the particular electric field strength component shows a constant non-zero distribution. The resulting electric potential difference with accumulating charges on the electrodes may be determined by voltage measurement and is proportional to strain or stress, respectively.

When the electrodes on the associated surfaces are connected, only the particular electric flux density component shows a constant non-zero distribution with opposed orientation. Charges cannot accumulate on the electrodes as they flow off instantaneously. For a dynamic process, this flow of charges may be determined by a current measurement, and is proportional to the strain rate, respectively stress rate. From the energetic point of view, the charge compensation must also have consequences for the mechanical fields. This becomes apparent by reorganization of the constitutive relation for these conditions and is reflected in the dissimilar stiffness and compliance matrices of Eqs. (4.10a) and (4.10b). These influences may be summarized for the basic load cases with resulting electrostatic fields in q-direction:

- Non-existent or disconnected electrodes
  $\rightarrow D_i = 0, E_{i\neq q} = 0, E_{i=q} \neq 0,$
  higher effective stiffness.
- Connected electrodes
  $\rightarrow E_i = 0, D_{i\neq q} = 0, D_{i=q} \neq 0$ (opposed orientation),
  lower effective stiffness.

These switchable properties may be used to tune the frequency response of a structure, for example, when eigenfrequencies need to be avoided during the run-up of rotating machinery. Furthermore, the connection of electrodes via resistors or inductors permits the damping or insulation of vibrations by passive means.

Normal Mode Sensing

When a cube is subjected to normal strains or stresses in any of the three spatial directions, one of the electrostatic fields, contingent upon the electric boundary conditions, is induced parallel or anti-parallel to the polarization direction. Thus, without additional information, the directions of mechanical stimulus cannot be distinguished by such a sensor. For the different cases of electric boundary conditions, the electrostatic fields developing in a piezoelectric cube subjected to normal loads are shown in Figure 4.5 together with the corresponding deformations of the transversely isotropic material.

Shear Mode Sensing

When the cube is subjected to shear strains or stresses in the plane perpendicular to the polarization direction due to the non-existent coupling, no sensor signal can be detected. In the remaining cases, a unique association of plane of shear and direction of electrostatic field is ensured as inversion of the actuator behavior. For the different cases of electric boundary conditions, the electrostatic fields developing in a piezoelectric cube subjected to shear loads are shown together with the corresponding deformations in Figure 4.6.

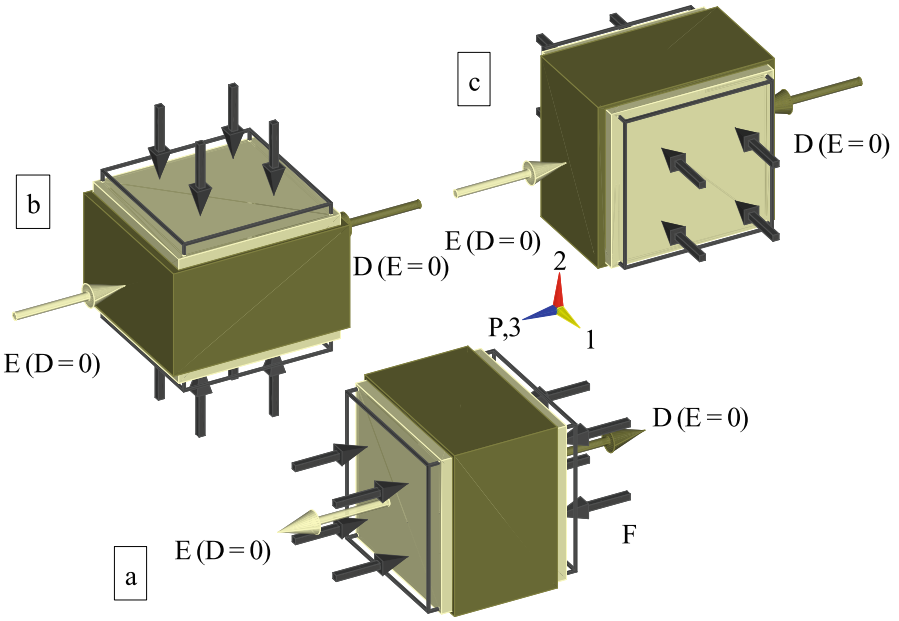

Fig. 4.5. Normal mode (surface loads F) of the direct piezoelectric effect with non-existent or disconnected ($E \neq 0$, $D = 0$; light colored state) or connected ($D \neq 0$, $E = 0$; dark colored state) electrodes normal to the e_3-direction.

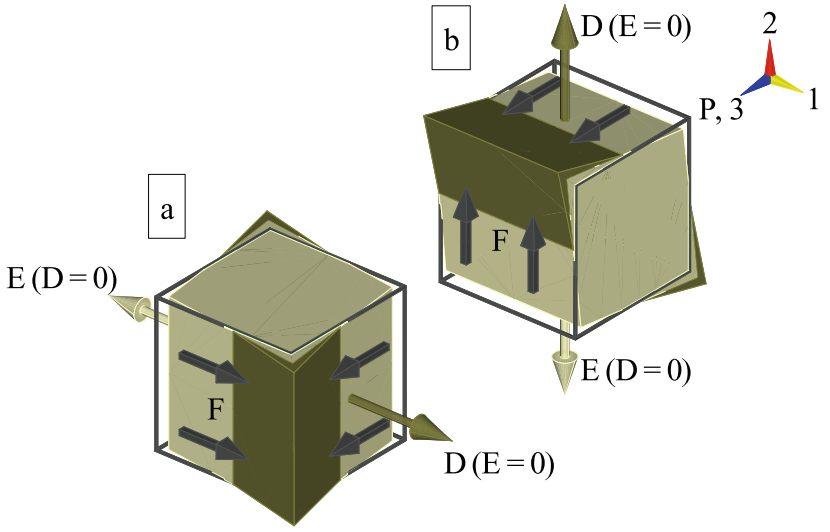

Fig. 4.6. Shear mode (surface loads F) of the direct piezoelectric effect with non-existent or disconnected ($E \neq 0$, $D = 0$; light colored state) or connected ($D \neq 0$, $E = 0$; dark colored state) electrodes (a) normal to the e_2-direction and (b) normal to the e_1-direction.

Complications

For the considered uniform mechanical fields, the induced electrostatic fields observed by means of the exemplary cube are also expected to be uniform. This holds true as long as the electrodes are appropriately mounted, thus perpendicular to the electrostatic field. Things change significantly when other surfaces are furnished with conductive elements; the previously immobile and unequal charges are now able to balance on such surfaces. This kind of disturbance has consequences for the electrostatic field and thus also for the mechanical behavior. The linear electric potential distribution, corresponding to a constant $\boldsymbol{e}_1$-direction component of the electric field strength as a result of pure shear load, is shown in Figure 4.7(a). The identical loading case, just with provision for conductivity on the surfaces transverse to the $\boldsymbol{e}_3$-direction, and the resulting non-linear inhomogeneous electric potential distribution is demonstrated in Figure 4.7(b). A noticeable decrease is observed, when the arising deformations are used to calculate the effective shear stiffness.

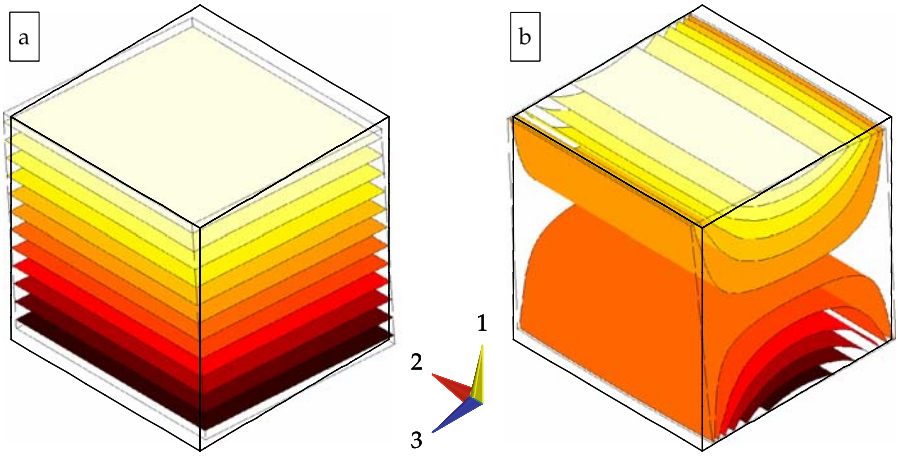

Fig. 4.7. Electric potential distribution in a piezoelectric cube subjected to shear in the 3-1-plane (a) without electrodes (b) with connected or disconnected electrodes transverse to the e_3-direction.

4.4 Constitutive Reduction

For the typical applications of piezoelectric materials, simplifying assumptions with respect to the mechanical and electrostatic fields are reasonable. These may be introduced in consequence of the spatial extent and electroding of the considered structure and, namely, are assumptions of planar mechanical and unidirectional electrostatic fields. Thereby, the variants of the latter, although

frequently discussed, have not been conclusively assessed, see for example *Benjeddou et al.* [12] or *Gopinathan et al.* [87]. The subsequent analysis in consideration of the electroding influences leads to a decisive statement.

4.4.1 Unidirectional Electrostatic Fields

For the application of electromechanically coupled materials, the electric connection in general is provided by opposing pairs of electrodes having their effective direction aligned with one of the material principal axes. When these electrodes are used for the polarization of the material, this is consequently the associated $\boldsymbol{e}_3$-direction. Neither in the actuator nor in the sensor case is such a configuration able to consider the electrostatic field components in the transverse plane responsible for the coupling with shear stresses and strains, Eqs. (4.20). This basically implies two possible assumptions in order to simplify the constitutive equations for essentially unidirectional electrostatic fields. As the simultaneous omission of electric field strength and flux density components along the transverse axes generally would have undue implications on the mechanical fields via the coupling, either the first or the latter components may be forced to zero:

- Unidirectional electric field strength $\leftrightarrow E_1 = 0, E_2 = 0$.
- Unidirectional electric flux density $\leftrightarrow D_1 = 0, D_2 = 0$.

Omission of Shear Associated Electrostatic Fields

When shear appears in the planes with corresponding piezoelectric coupling, as shown in Figure 4.6, in addition to the intended normal mode actuation or sensing, then it needs to be examined with regard to the electric boundary conditions. At first, the complications induced by electrodes on surfaces other than those associated with the individual shear case will be ignored. Therefore, the theoretically possible electric boundary conditions have the following implications, which correlate with the above assumptions:

- Non-existent or disconnected electrodes for the individual shear cases:
  $E_1 \neq 0$ respectively $E_2 \neq 0$; $D_1 = 0$ and $D_2 = 0$
  (light colored state in Figure 4.6)
  $\rightarrow$ unidirectional electric flux density.
- Connected electrodes for the individual shear cases:
  $D_1 \neq 0$ respectively $D_2 \neq 0$; $E_1 = 0$ and $E_2 = 0$
  (dark colored state in Figure 4.6)
  $\rightarrow$ unidirectional electric field strength.

For the intended normal mode actuation or sensing with electrodes responsible for the polarization direction, the latter case is practically not possible, while the prior needs to be further examined. The complications considered in

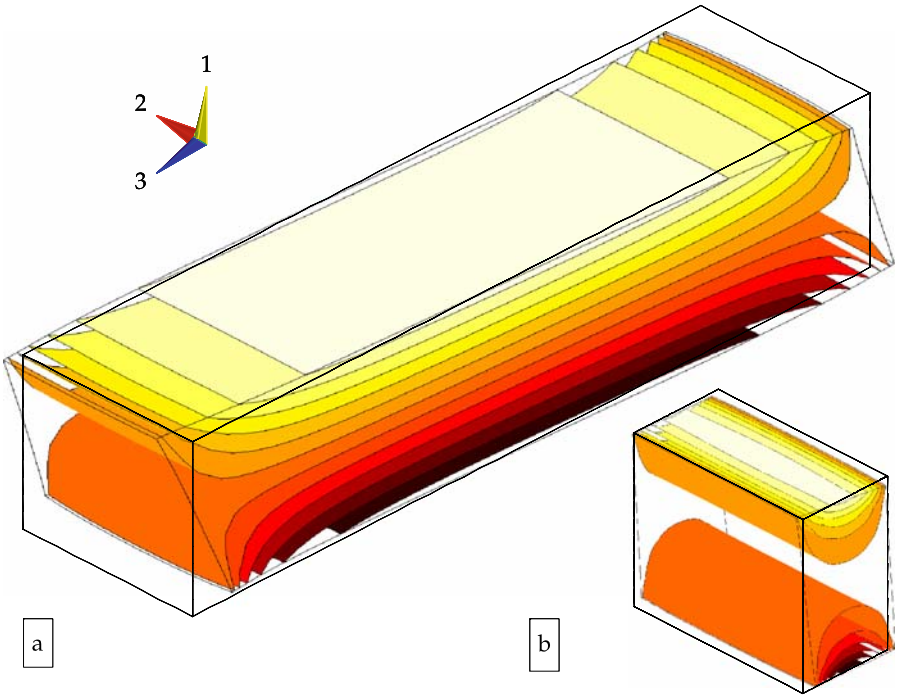

Fig. 4.8. Electric potential distribution due to shear in piezoelectric cuboids with electrodes transverse to the e_3-direction and with an aspect ratio (a) of $l_3/l_1 = 4$ and (b) of $l_3/l_1 = 1/2$.

the previous subsection have to be taken into account. As illustrated by Figure 4.7(b), the mismatched electroding disturbs the otherwise linear electric potential distribution. But away from the electrodes this influence is fading and, therefore, the relative distance of electrodes needs to be considered. The resulting overall behavior ranges between the following extremes:

- Marginal penetration by the disturbance due to mismatched electroding: $E_1 \neq 0, D_1 \approx 0, D_2 = 0$, respectively, $E_2 \neq 0, D_2 \approx 0, D_1 = 0$ (linear electric potential distribution in the center of Figure 4.8(a)) $\rightsquigarrow$ unidirectional electric flux density.
- Extensive penetration by the disturbance due to mismatched electroding: $D_1 \neq 0, E_1 \approx 0, E_2 = 0$, respectively, $D_2 \neq 0, E_2 \approx 0, E_1 = 0$ (vanishing electric potential difference in the center of Figure 4.8(b)) $\rightsquigarrow$ unidirectional electric field strength.

Unidirectional Electric Field Strength

For unidirectional electric field strength confined to the component E_3, the transverse electric flux density components D_1, D_2 as well as shear stress

components τ_{31}, τ_{23} only depend on the associated shear strains γ_{31}, γ_{23}, as illustrated by Eqs. (4.20):

$$E_1 = 0 \quad \rightarrow \quad D_1 = e_{15}\gamma_{31}, \qquad \tau_{31} = C_{55}^{\boldsymbol{E}}\gamma_{31}; \tag{4.22a}$$

$$E_2 = 0 \quad \rightarrow \quad D_2 = e_{24}\gamma_{23}, \qquad \tau_{23} = C_{44}^{\boldsymbol{E}}\gamma_{23}. \tag{4.22b}$$

The internal energy of an electrostatic system is represented by the product of the correlated field strength and flux density components, as exemplarily derived for the virtual work of internal charges, Eq. (3.53). The shear strain induced flux density components D_1 and D_2, as given in Eq. (4.22), do not contribute by virtue of the above assumption. Thus, the assumption of unidirectional electric field strength is equivalent to the neglect of shear associated electrostatic energy contributions.

Unidirectional Electric Flux Density

For the remaining case of unidirectional electric flux density confined to the component D_3, the transverse electric field strength components E_1, E_2 may be expressed in terms of the shear strains γ_{31}, γ_{23}. Therewith E_1 and E_2 can be eliminated from the constitutive equations by static condensation. Thus, this modification of Eqs. (4.20) represents a purely mechanical interaction with strengthened shear stiffnesses as the result of the piezoelectric effect:

$$D_1 = 0 \quad \rightarrow \quad E_1 = -\frac{e_{15}}{\epsilon_{11}^{\boldsymbol{\varepsilon}}}\gamma_{31} \quad \rightarrow \quad \tau_{31} = \left(C_{55}^{\boldsymbol{E}} + \frac{(e_{15})^2}{\epsilon_{11}^{\boldsymbol{\varepsilon}}}\right)\gamma_{31}; \tag{4.23a}$$

$$D_2 = 0 \quad \rightarrow \quad E_2 = -\frac{e_{24}}{\epsilon_{22}^{\boldsymbol{\varepsilon}}}\gamma_{23} \quad \rightarrow \quad \tau_{23} = \left(C_{44}^{\boldsymbol{E}} + \frac{(e_{24})^2}{\epsilon_{22}^{\boldsymbol{\varepsilon}}}\right)\gamma_{23}. \tag{4.23b}$$

Thereby, from the energetic point of view again, the shear associated electrostatic energy contributions, so to speak, are transferred to the elastic energy.

Summary of Unidirectional Electrostatic Fields

The implications of both discussed simplifications of the constitutive relations may be illustrated by summarizing all the shear cases. With the assumption of unidirectional electric field strength for the stresses of Eqs. (4.22), respectively, unidirectional electric flux density for the stresses of Eqs. (4.23), whereby the additional terms of the latter are furnished with the variables υ_{23} and υ_{31}, and Eq. (4.21), this reads as follows:

$$\begin{Bmatrix} \tau_{23} \\ \tau_{31} \\ \tau_{12} \end{Bmatrix} = \begin{bmatrix} C_{44}^{\boldsymbol{E}} + \upsilon_{23}\frac{(e_{24})^2}{\epsilon_{22}^{\boldsymbol{\varepsilon}}} & 0 & 0 \\ 0 & C_{55}^{\boldsymbol{E}} + \upsilon_{31}\frac{(e_{15})^2}{\epsilon_{11}^{\boldsymbol{\varepsilon}}} & 0 \\ 0 & 0 & C_{66}^{\boldsymbol{E}} \end{bmatrix} \begin{Bmatrix} \gamma_{23} \\ \gamma_{31} \\ \gamma_{12} \end{Bmatrix}. \tag{4.24}$$

The case of unidirectional electric field strength is expressed by $\upsilon_{23} = \upsilon_{31} = 0$, while the case of unidirectional electric flux density is indicated by $\upsilon_{23} = \upsilon_{31} = 1$. The above discussion on the influences of mismatched electroding for the shear cases identified the two unidirectional field assumptions as extremes with the actual effective properties in between. Thus, υ_{23} and υ_{31} may be determined as functions of the electrostatic field distributions affected by the geometry of structure and electrodes as well as the material properties in the ranges $0 \leqslant \upsilon_{23} \leqslant 1$ and $0 \leqslant \upsilon_{31} \leqslant 1$. This might be used to represent the macroscopic mechanical behavior of piezoelectric structures subjected to shear induced transverse electrostatic fields within the simplified framework of assumingly unidirectional electrostatic fields. Thereby the essential and beneficial consequences would be inherited as conclusively formulated:

Remark 4.4. By virtue of either unidirectional electric field strength or unidirectional electric flux density aligned with the polarization direction, the shear stresses may be completely decoupled from the electric field strengths.

Transition between Unidirectional Electrostatic Fields

In order to gain an impression of the dependencies indicated above, the essential influence of electroding geometry will be examined by means of a simple example. A cuboid of piezoelectric material PZT-5H with edge lengths $l_1 = l_2 = 1$ cm and variable l_3, also representing the distance between the two conductive surfaces transverse to the e_3-direction, is subjected to a shear load of $\tau_{31} = 10$ N/cm^2. As depicted in Figure 4.8, the resulting distributions of the electric potential and thus the shear strains are non-homogeneous. However, the average value of the shear strain γ_{31} may be requisitioned in the rearranged second line of Eq. (4.24), to determine the associated variable υ_{31} for the examined structure, as

$$\upsilon_{31} = \left(\frac{\tau_{31}}{\gamma_{31}} - C_{55}^{\boldsymbol{E}} \right) \frac{\epsilon_{11}^{\boldsymbol{\varepsilon}}}{(e_{15})^2}. \tag{4.25}$$

Based on calculations with the finite element package ANSYS, this has been done for a number of geometric configurations, as recorded in Figure 4.9. The aspect ratio l_3/l_1 of the cuboid reflects the distance between the electrodes in one direction of the shear plane (l_3) and the extent of the electrodes in the other direction of the shear plane (l_1). As expected, υ_{31} tends towards zero for relatively close electrodes while it asymptotically approaches one with increasing distance. In consideration of an additional dimensionless quantity c_f to capture further influences like material properties and boundary conditions, this behavior may be roughly approximated by the following function:

$$\upsilon_{31} = \frac{2}{\pi} \arctan \left(\frac{1}{c_f} \frac{l_3}{l_1} \right). \tag{4.26}$$

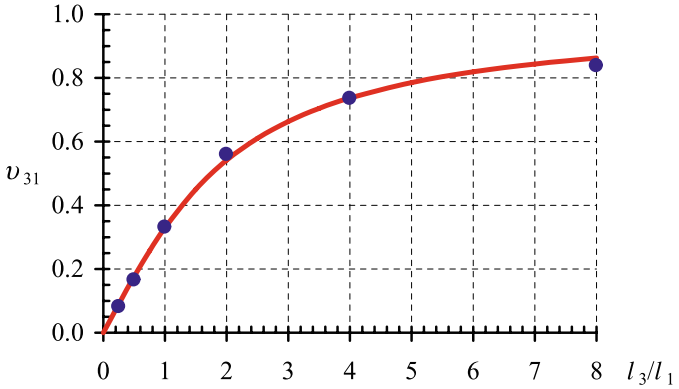

Fig. 4.9. Transition between unidirectional electric field strength ($\upsilon_{31} = 0$) and unidirectional electric flux density ($\upsilon_{31} = 1$) as a function of electroding geometry depicted by finite element calculations (•) according to Eq. (4.25) and approximated (−) as stated by Eq. (4.26) with $c_f = 1.75$.

In general, it becomes apparent that for relatively thin structures the unidirectionality of the electric field strength can be confidently assumed. A frequently occurring example is the application of through-thickness polarized piezoelectric materials as part of laminated shell-like structures with overall aspect ratios of usually less than $l_3/l_1, l_3/l_2 = 1/10$. This examination provides an unambiguous answer with respect to the ongoing debate in the literature, see for example *Benjeddou et al.* [12] or *Gopinathan et al.* [87]. The meaning for piezoelectric structures with interdigitated electrodes will be discussed together with the explanation of this concept in the following chapter. The gained insight may also be transferred to structures electroded for shear actuation or sensing but also subjected to loads in the normal directions.

4.4.2 Planar Mechanical Fields

When the spatial extent of a structure is substantially smaller in the distinguished thickness direction compared to the remaining dominating dimensions, simplifications in this respect are reasonable. Therefore, either the planar stress or the planar strain assumption may be employed for a such thin, shell-like structure. When it is unconstrained in the thickness direction, the first assumption needs to be utilized:

Remark 4.5. Normal and shear stresses in the thickness direction are assumed to be negligible small.

Considering materials with either unidirectional electric field strength or unidirectional electric flux density aligned with the polarization direction, as described in the previous subsection, different choices concerning the relative orientation of the thickness direction need to be discussed.

Planar Stress Transverse to Polarization

Assuming planar stress as of Remark 4.5 on the plane perpendicular to the polarization direction, see Figure 4.10(a), and thus aligning the latter with the thickness direction, has the following implications and consequences when substituted into Eqs. (4.19) and (4.24):

$$\begin{aligned} \sigma_3 = 0 \quad &\rightarrow \quad \varepsilon_3 = -\frac{C_{13}^{\boldsymbol{E}}}{C_{33}^{\boldsymbol{E}}}\varepsilon_1 - \frac{C_{23}^{\boldsymbol{E}}}{C_{33}^{\boldsymbol{E}}}\varepsilon_2 + \frac{e_{33}}{C_{33}^{\boldsymbol{E}}}E_3 \quad \text{and} \\ \tau_{23} = 0 \quad &\rightarrow \quad \gamma_{23} = 0, \\ \tau_{31} = 0 \quad &\rightarrow \quad \gamma_{31} = 0. \end{aligned} \tag{4.27}$$

Thereby the neglected shear stresses and consequently vanishing shear strains, given on the right-hand side of Eqs. (4.27), ensure complete constitutive equality of both variants of Remark 4.4 for this configuration. This is, on the one hand, due to the discard of those coefficients in Eq. (4.24) representing the differences and, on the other hand, due to the ultimately vanishing transverse electric flux densities to be found in the middle of Eqs. (4.22). With elimination of the normal strain in thickness direction, the constitutive relation then takes the following form:

$$\begin{Bmatrix} \sigma_1 \\ \sigma_2 \\ \tau_{12} \\ D_3 \end{Bmatrix} = \begin{bmatrix} C_{11}^{\boldsymbol{E}} - \frac{\left(C_{13}^{\boldsymbol{E}}\right)^2}{C_{33}^{\boldsymbol{E}}} & C_{12}^{\boldsymbol{E}} - \frac{C_{13}^{\boldsymbol{E}} C_{23}^{\boldsymbol{E}}}{C_{33}^{\boldsymbol{E}}} & 0 & -e_{31} + \frac{C_{13}^{\boldsymbol{E}}}{C_{33}^{\boldsymbol{E}}} e_{33} \\ C_{12}^{\boldsymbol{E}} - \frac{C_{13}^{\boldsymbol{E}} C_{23}^{\boldsymbol{E}}}{C_{33}^{\boldsymbol{E}}} & C_{22}^{\boldsymbol{E}} - \frac{\left(C_{23}^{\boldsymbol{E}}\right)^2}{C_{33}^{\boldsymbol{E}}} & 0 & -e_{32} + \frac{C_{23}^{\boldsymbol{E}}}{C_{33}^{\boldsymbol{E}}} e_{33} \\ 0 & 0 & C_{66}^{\boldsymbol{E}} & 0 \\ e_{31} - \frac{C_{13}^{\boldsymbol{E}}}{C_{33}^{\boldsymbol{E}}} e_{33} & e_{32} - \frac{C_{23}^{\boldsymbol{E}}}{C_{33}^{\boldsymbol{E}}} e_{33} & 0 & \epsilon_{33}^{\boldsymbol{\varepsilon}} + \frac{(e_{33})^2}{C_{33}^{\boldsymbol{E}}} \end{bmatrix} \begin{Bmatrix} \varepsilon_1 \\ \varepsilon_2 \\ \gamma_{12} \\ E_3 \end{Bmatrix}. \tag{4.28}$$

Planar Stress in Plane with Polarization

Assuming planar stress as of Remark 4.5 in the plane of the polarization direction, see Figure 4.10(b), and thus having the latter perpendicular to the thickness direction selected to be the $\boldsymbol{e}_2$-direction, has the following implications and consequences when substituted into Eqs. (4.19) and (4.24):

$$\begin{aligned} \sigma_2 = 0 \quad &\rightarrow \quad \varepsilon_2 = -\frac{C_{12}^{\boldsymbol{E}}}{C_{22}^{\boldsymbol{E}}}\varepsilon_1 - \frac{C_{23}^{\boldsymbol{E}}}{C_{22}^{\boldsymbol{E}}}\varepsilon_3 + \frac{e_{32}}{C_{22}^{\boldsymbol{E}}}E_{33} \quad \text{and} \\ \tau_{23} = 0 \quad &\rightarrow \quad \gamma_{23} = 0, \\ \tau_{12} = 0 \quad &\rightarrow \quad \gamma_{12} = 0. \end{aligned} \tag{4.29}$$

Since no assumptions are made here concerning the piezoelectrically coupled shear behavior in the plane spanning between the $\boldsymbol{e}_3$- and $\boldsymbol{e}_1$-direction, the

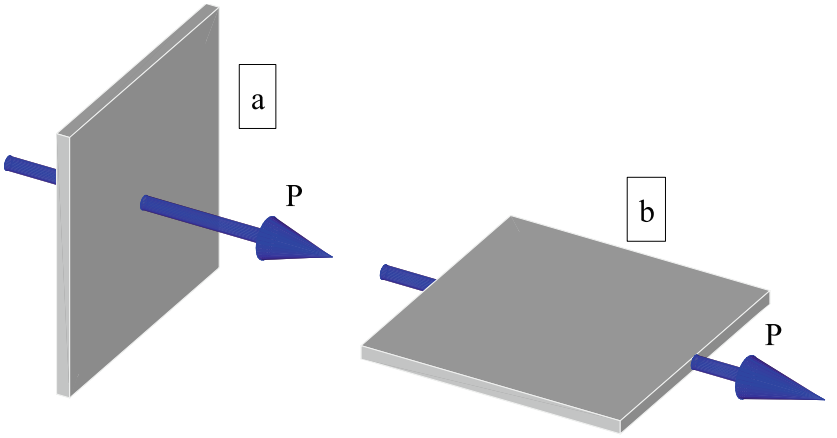

Fig. 4.10. Correlation of polarization direction (P) and plane of planar stress.

two variants of Remark 4.4 for this configuration are still to be distinguished by the additional term of the respective shear stiffness:

$$\begin{Bmatrix} \sigma_3 \\ \sigma_1 \\ \tau_{31} \\ D_3 \end{Bmatrix} = \underbrace{\begin{bmatrix} C_{33}^{\boldsymbol{E}} - \frac{\left(C_{23}^{\boldsymbol{E}}\right)^2}{C_{22}^{\boldsymbol{E}}} & C_{13}^{\boldsymbol{E}} - \frac{C_{12}^{\boldsymbol{E}} C_{23}^{\boldsymbol{E}}}{C_{22}^{\boldsymbol{E}}} & 0 & -e_{33} + \frac{C_{23}^{\boldsymbol{E}}}{C_{22}^{\boldsymbol{E}}} e_{32} \\ C_{13}^{\boldsymbol{E}} - \frac{C_{12}^{\boldsymbol{E}} C_{23}^{\boldsymbol{E}}}{C_{22}^{\boldsymbol{E}}} & C_{11}^{\boldsymbol{E}} - \frac{\left(C_{12}^{\boldsymbol{E}}\right)^2}{C_{22}^{\boldsymbol{E}}} & 0 & -e_{31} + \frac{C_{12}^{\boldsymbol{E}}}{C_{22}^{\boldsymbol{E}}} e_{32} \\ 0 & 0 & C_{55}^{\boldsymbol{E}} + \upsilon_{31} \frac{(e_{15})^2}{\epsilon_{11}^{\boldsymbol{\varepsilon}}} & 0 \\ e_{33} - \frac{C_{23}^{\boldsymbol{E}}}{C_{22}^{\boldsymbol{E}}} e_{32} & e_{31} - \frac{C_{12}^{\boldsymbol{E}}}{C_{22}^{\boldsymbol{E}}} e_{32} & 0 & \epsilon_{33}^{\boldsymbol{\varepsilon}} + \frac{(e_{32})^2}{C_{22}^{\boldsymbol{E}}} \end{bmatrix}}_{\tilde{\mathbb{Q}}} \begin{Bmatrix} \varepsilon_3 \\ \varepsilon_1 \\ \gamma_{31} \\ E_3 \end{Bmatrix}. \tag{4.30}$$

4.4.3 Planar Rotation

By virtue of the assumptions of unidirectional electrostatic fields and planar mechanical stress, the electromechanically coupled constitutive relations have been modified significantly. In example, the formulation on the left-hand side of Eq. (4.10a) reduces to Eq. (4.28) or (4.30). A transformation of coordinates on the considered plane may be performed as a rotation around the axis normal to this plane. In the case of Eq. (4.30), the base vector $\boldsymbol{e}_2$ represents the axis of rotation and thus this planar rotation may be formulated as follows:

$$\begin{Bmatrix} \sigma_x \\ \sigma_s \\ \tau_{xs} \\ D_3 \end{Bmatrix} = \underbrace{\tilde{\mathbb{T}}\tilde{\mathbb{Q}}\tilde{\mathbb{T}}^T}_{\mathbb{Q}} \begin{Bmatrix} \varepsilon_x \\ \varepsilon_s \\ \gamma_{xs} \\ E_3 \end{Bmatrix}. \tag{4.31}$$

The transformation matrix $\tilde{\mathbb{T}}$ can be adapted from the spatial case of Eq. (4.14) by removing the unnecessary rows and columns. To account for the modified arrangement of components in Eq. (4.30), the respective rows and columns also need to be exchanged in the transformation matrix; it takes the following form:

$$\tilde{\mathbb{T}} = \begin{bmatrix} \cos^2\alpha & \sin^2\alpha & 2\cos\alpha\sin\alpha & 0 \\ \sin^2\alpha & \cos^2\alpha & -2\sin\alpha\cos\alpha & 0 \\ -\sin\alpha\cos\alpha & \cos\alpha\sin\alpha & \cos^2\alpha - \sin^2\alpha & 0 \\ 0 & 0 & 0 & 1 \end{bmatrix}. \tag{4.32}$$

4.4.4 Negated Electric Field Strength

In the derived expression for the virtual work of internal contributions, Eq. (3.63), as well as in the definition of the electroelastic energy density, Eq. (3.64), the electric fields strength appears in a negated form represented by the vector $\bar{\boldsymbol{E}}$. With the adoption of such an arrangement in the associate constitutive relation, to be found on the left-hand side of Eq. (4.10a), it is possible to compensate for the unsymmetry in the matrix of constitutive properties $\mathbb{C}$ of the electromechanically coupled material. Thus a symmetric variant $\bar{\mathbb{C}} = \bar{\mathbb{C}}^T$ of this matrix may be introduced as follows:

$$\underbrace{\begin{Bmatrix} \boldsymbol{\sigma} \\ \boldsymbol{D} \end{Bmatrix}}_{\boldsymbol{Y}} = \underbrace{\begin{bmatrix} \mathbf{C}^{\boldsymbol{E}} & -\mathbf{e} \\ \mathbf{e}^T & \boldsymbol{\epsilon}^{\boldsymbol{\varepsilon}} \end{bmatrix}}_{\mathbb{C}} \underbrace{\begin{Bmatrix} \boldsymbol{\varepsilon} \\ \boldsymbol{E} \end{Bmatrix}}_{\boldsymbol{Z}} = \begin{bmatrix} \mathbf{C}^{\boldsymbol{E}} & -\mathbf{e} \\ \mathbf{e}^T & \boldsymbol{\epsilon}^{\boldsymbol{\varepsilon}} \end{bmatrix} \begin{bmatrix} \mathbf{I} & \\ & -\mathbf{I} \end{bmatrix} \begin{Bmatrix} \boldsymbol{\varepsilon} \\ -\boldsymbol{E} \end{Bmatrix} = \underbrace{\begin{bmatrix} \mathbf{C}^{\boldsymbol{E}} & \mathbf{e} \\ \mathbf{e}^T & -\boldsymbol{\epsilon}^{\boldsymbol{\varepsilon}} \end{bmatrix}}_{\bar{\mathbb{C}}} \underbrace{\begin{Bmatrix} \boldsymbol{\varepsilon} \\ \bar{\boldsymbol{E}} \end{Bmatrix}}_{\bar{\boldsymbol{Z}}}. \tag{4.33}$$

Correspondingly, the consequent modifications of the constitutive relation may be treated. For the case of planar stress and unidirectional electric in transformed coordinates, this yields:

$$\begin{Bmatrix} \sigma_x \\ \sigma_s \\ \tau_{xs} \\ D_3 \end{Bmatrix} = \underbrace{\mathbb{Q} \begin{bmatrix} 1 & 0 & 0 & 0 \\ 0 & 1 & 0 & 0 \\ 0 & 0 & 1 & 0 \\ 0 & 0 & 0 & -1 \end{bmatrix}}_{\bar{\mathbb{Q}}} \begin{Bmatrix} \varepsilon_x \\ \varepsilon_s \\ \gamma_{xs} \\ \bar{E}_3 \end{Bmatrix}. \tag{4.34}$$

Electroelastic Energy Density

In Section 3.5.1, Dirichlet's principle of minimum potential energy has been extended to electromechanically coupled problems. With the exception of referring to the required potential property, the electroelastic energy density $\mathcal{U}_0$ has not yet been further specified. With Eq. (3.64) a second relation linking the fields of the constitutive relation is available, such that it may be used

to determine the electroelastic energy density $\mathcal{U}_0$. This leads to the following formulation:

$$\mathcal{U}_0 = \frac{1}{2} \left\{ \boldsymbol{\varepsilon}^T \quad \bar{\boldsymbol{E}}^T \right\} \underbrace{\begin{bmatrix} \mathbf{C}^{\boldsymbol{E}} & \mathbf{e} \\ \mathbf{e}^T & -\boldsymbol{\epsilon}^{\boldsymbol{\varepsilon}} \end{bmatrix}}_{\bar{\mathbb{C}}} \left\{ \begin{matrix} \boldsymbol{\varepsilon} \\ \bar{\boldsymbol{E}} \end{matrix} \right\} \quad \text{with } \bar{\boldsymbol{E}} = -\boldsymbol{E},\ \bar{\mathbb{C}} = \bar{\mathbb{C}}^T. \tag{4.35}$$

It can be verified by substitution into Eq. (3.64) which should result in the constitutive relation. Thus it becomes apparent that the utilized matrix of constitutive properties has to be symmetric. While this is given for the formulation with the matrix $\bar{\mathbb{C}}$ introduced on the right-hand side of Eq. (4.33), the conventional variant $\mathbb{C}$ to the left-hand side proves to be of no avail.

4.5 Actuator and Sensor Conditions

In Section 4.3, the piezoelectric effect has been examined in an illustrative manner with respect to actuation and sensing. To quantify these findings for more complicated structures, calculation procedures can be developed, based on the principle of virtual work derived in Section 3.4. Therefore, the different variants of actuation, depending on the type of electric power supply, and of sensing, depending on the type of measurement, will be studied here with regard to the associated boundary conditions. Without practical loss of generality, the following simplification may be introduced for all instances:

Remark 4.6. For the actual application of piezoelectric materials, free charges in the volume are excluded.

$$\check{q}_\Lambda = 0. \tag{4.36}$$

Since no volume charges $\check{q}_\Lambda$ will be specified, the corresponding term in the virtual work of external charges $\delta\mathcal{V}^{ep}$ vanishes, see Eqs. (3.53) and (3.62) respectively.

4.5.1 Actuator Application with Voltage and Current Source

To induce mechanical deformation with an actuator based on piezoelectric material, electric power needs to be supplied. In electrical engineering, two ideal power sources are distinguished. A voltage source provides a constant voltage, while the wattage may then be adjusted via the current. A current source the other way round keeps the current constant, while the wattage may then be adjusted via the voltage.

Voltage Source

When a voltage source is connected to the electrodes of a piezoelectric actuator, the electric potential φ is prescribed. This includes the compensation

of possibly superimposed mechanical influences. So the electric potential φ does not represent an unknown, and thus its variation $\delta\varphi$ vanishes as well as the variation of the electric field strength $\delta\boldsymbol{E}$ in consideration of Eq. (3.39). Therewith, all contributions of the principle of virtual electric potential of Eq. (3.53) disappear:

$$\delta\varphi = 0 \quad \rightarrow \quad \delta\mathcal{V}^{ep} = 0, \qquad \delta\boldsymbol{E} = \boldsymbol{0} \quad \rightarrow \quad \delta\mathcal{U}^{ep} = 0. \tag{4.37}$$

Hence, the principle of virtual work of Eqs. (3.62) and (3.63) reduces to its mechanical part. Via the dependence of mechanical stresses $\boldsymbol{\sigma} = \boldsymbol{\sigma}(\boldsymbol{\varepsilon}, \boldsymbol{E})$ in the electromechanically coupled constitutive relation, see Eq. (4.17), the electric field strength $\boldsymbol{E}$ however enters the formulation as a parameter:

$$\int_{\Lambda} \delta\boldsymbol{\varepsilon}^T \boldsymbol{\sigma} + \delta\boldsymbol{u}^T \boldsymbol{a}\rho \,\mathrm{d}V = \int_{\partial\Lambda_\sigma} \delta\boldsymbol{u}^T \hat{\boldsymbol{f}}_{\partial\Lambda} \,\mathrm{d}A + \int_{\Lambda} \delta\boldsymbol{u}^T \check{\boldsymbol{f}}_{\Lambda} \,\mathrm{d}V. \tag{4.38}$$

Current Source

When a current source is connected to the electrodes of a piezoelectric actuator, the electric potential φ is unknown. Therefore, the contributions of the principle of virtual electric potential of Eq. (3.53) need to be retained. Since the current describes the derivative trend of charge with respect to time, it prescribes the area charge $\hat{q}_{\partial\Lambda}$ on the electrodes. An adequate formulation of the principle of virtual work from Eqs. (3.62) and (3.63), in consideration of Eq. (4.36), reads

$$\begin{aligned} &\int_{\Lambda} \begin{Bmatrix} \delta\boldsymbol{\varepsilon}^T & \delta\bar{\boldsymbol{E}}^T \end{Bmatrix} \begin{Bmatrix} \boldsymbol{\sigma} \\ \boldsymbol{D} \end{Bmatrix} + \delta\boldsymbol{u}^T \boldsymbol{a}\rho \,\mathrm{d}V \\ &\quad = \int_{\partial\Lambda} \begin{Bmatrix} \delta\boldsymbol{u}^T & -\delta\varphi \end{Bmatrix} \begin{Bmatrix} \hat{\boldsymbol{f}}_{\partial\Lambda} \\ \hat{q}_{\partial\Lambda} \end{Bmatrix} \mathrm{d}A + \int_{\Lambda} \delta\boldsymbol{u}^T \check{\boldsymbol{f}}_{\Lambda} \,\mathrm{d}V. \end{aligned} \tag{4.39}$$

4.5.2 Sensor Application with Voltage and Current Measurement

The different variants of the sensor application have become obvious from observing Figure 4.5. A mechanical load on piezoelectric material induces an electric field strength field when the electrodes are disconnected and an electric flux density field when the electrodes are connected. This corresponds to the possibilities of measurement of electric quantities. As with the actuator application, only the ideal cases shall be considered here, leaving the complications of the actual circuits, including the necessary amplification, to the competent electrical engineering literature, see for example *Tichý and Gautschi* [174].

Strain Sensor–Voltage Measurement

To determine the voltage, a measuring instrument with high inherent resistance is used such that the current and thus the flow of charges is low. In the

ideal case, this corresponds to disconnected electrodes. Then the difference of electric potential φ at the opposing electrodes and, consequently, the electric field strength $\boldsymbol{E}$ can be determined without changing the area charge $\hat{q}_{\partial\Lambda}$ on the electrodes. In practical applications, the latter is often zero, see *Carpenter* [43]. To simulate the outcome of such a measurement proportional to the strain state, it may be proceeded from Eq. (4.39) as well.

Strain Rate Sensor–Current Measurement

To determine the current, a measuring instrument with low inherent resistance is used such that the caused voltage drop is low. In the ideal case, this corresponds to connected electrodes. Then the difference of electric potential φ at the opposing electrodes levels out, and thus the electric field strength $\boldsymbol{E}$ is cancelled. This permits us to draw the conclusions as of Eq. (4.37). Consequently, the mechanical state of the system can be determined with the aid of the principle of virtual work formulation of Eq. (4.38). Via the electromechanically coupled constitutive relation, the outcome may then be utilized to deduce the electric flux density, charge, and finally the current being proportional to the strain rate.

5

Piezoelectric Composites

The integration of piezoelectric materials into composites allows for the improvement of constitutive properties as well as of failure behavior and consequently for an extension of the application spectrum. So this chapter is concerned with the conception and modeling of such piezoelectric composites for structural applications. For the prediction of the effective composite properties, different methodologies of micro-electromechanics are investigated and validated through experiments and finite element analyses.

5.1 Classification of General Composites

Composites provide the possibility to combine the advantageous characteristics of different materials and qualities are often achieved that none of the constituents possesses. Essential criteria in general are stiffness, strength, weight, damping, thermal and electric conductivity, as well as resistance against environmental influences, wear, and fatigue. Further on they make possible the optimization of anisotropic mechanical, thermomechanical, and electromechanical couplings. Introductory literature on composites is provided, for example, by *Jones* [107], *Altenbach et al.* [6], *Chawla* [50], *Matthews and Rawlings* [123]. Besides a classification by means of the constituent materials, composites may be distinguished by the spatial arrangement of the material phases. To be a composite at least two such phases need to occur whereby the matrix phase surrounds and connects one or more inclusion phases.

5.1.1 Topology of the Inclusion Phase

The diverse shapes of inclusions may be used for a classification of composites, as shown for the basic cases of particulate, fibrous, and lamellar topologies in Figure 5.1. There are also composites which represent a combination of these inclusion types. In steel concrete, for example, mineral particles and metal fibers are joined by a binder material. For aerospace applications, the

T.H. Brockmann, *Theory of Adaptive Fiber Composites*,
Solid Mechanics and Its Applications 161,

combination of glass fibers and aluminum laminae is becoming increasingly popular. The listed types of inclusions may be further categorized with respect to their geometry and relative arrangement. In the case of fibrous inclusions, there are continuous or discontinuous fibers of straight or curled shape in a regular or irregular layout. More complicated fiber structures arise when textile techniques like stitching, braiding, or knitting are involved, see for instance *Poe et al.* [142] or *Cox and Flanagan* [57].

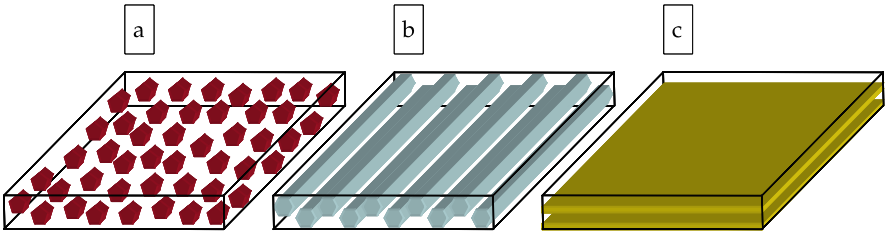

Fig. 5.1. Classification of composites by the spatial extent of inclusions: (a) particulate, (b) fibrous, (c) lamellar.

5.1.2 Laminated Composites and Laminated Fiber Composites

A prominent position is taken by the combination of lamellar inclusions of continuous as well as planar extent with only a small amount of matrix material. This description in terms of the above classification is synonymous with monolithic laminae bonded with a thin film of adhesive representing the widely used concept of laminated composites. The individual laminae do not necessarily have to be monolithic but may consist of composite materials again. With the contained inclusions being existent in fibrous shape, the outcome is a laminated fiber composite. Especially, the case of continuous, straight, and parallel fibers is of great importance with regard to lightweight structures. Corresponding to their setup, the analysis of laminated fiber composites may be organized in two steps to be subsequently demonstrated in consideration of electromechanically coupled materials. First, on the level of micro-electromechanics in this chapter, the effective properties of the laminae are determined from the characteristics of matrix and inclusions. Second, on the level of macro-electromechanics in the next chapter, the effective properties of the laminate are determined from the characteristics of the laminae.

5.2 Conception of Piezoelectric Composites

To enable actuation and sensing of structures with laminar elements like plates and shells, the application of piezoelectric materials is well established. In the

simplest case, monolithic ceramic materials are attached in the form of thin patches on one or both sides. In view of the above discussion, such an assembly constitutes a laminated composite. For any case of structural deformation, the aspired effective direction of the piezoelectric effect lies in the plane of the piezoelectric laminae. Initially areal electrodes on its top and bottom surface have been employed to provide or perceive the electrostatic field respectively, Figure 5.2(a). To avoid unintentional and possibly creeping repolarization, the directions of polarization and electric field strength should be aligned. Thus, both of these directions are oriented normal to the plane of the considered patch and only the minor piezoelectric effect in the isotropic transverse plane, as $e_{31} < e_{33}$ and $d_{31} < d_{33}$ to be found in Table A.3, can be exploited.

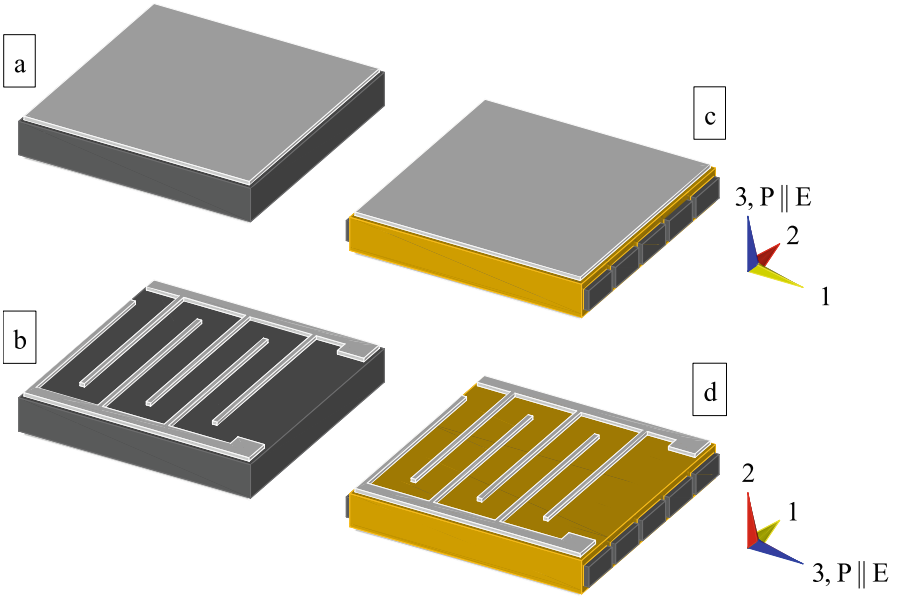

Fig. 5.2. Variants of patches for actuation or sensing: (a) monolitic material with areal electrodes, (b) monolitic material with interdigitated electrodes, (c) fiber composite with areal electrodes, (d) fiber composite with interdigitated electrodes.

5.2.1 Interdigitated Electrodes and Piezoelectric Fibers

To increase the electromechanical coupling and allow for anisotropic and thus directional actuation and sensing, the concept of interdigitated electrodes has been introduced by *Hagood et al.* [90] for monolithic piezoelectric laminae, as shown in Figure 5.2(b). Thereby in-plane placement of the parallel directions of polarization and electric field strength is permitted. These directions

jointly change sign from one interval between opposing polarity electrodes to the next and, in this manner, assure uniform behavior, see Figure 5.3. To compensate for the drawbacks caused by the brittle and inflexible nature of ceramic materials, the embedding of piezoelectric materials in the form of fibers into a polymer matrix has been implemented by *Bent et al.* [16,17] for areal electrodes, as shown in Figure 5.2(c). Thus, besides increased strength and conformability the advantageous possibility of optimizing the anisotropic properties is also gained. Further improvements are achieved when, in addition, interdigitated electrodes are applied, *Bent and Hagood* [14,15], as shown in Figure 5.2(d).

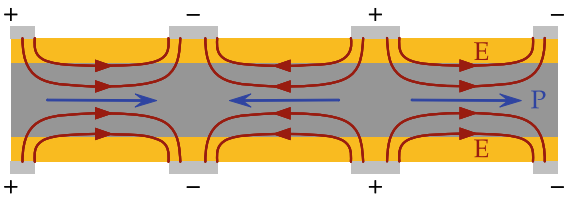

Fig. 5.3. Sectional view of the interdigitated electroding scheme with qualitative distribution of lines of electric field strength (E) and directions of polarization (P).

5.2.2 Electroding Implications

As examined in detail in Section 4.4, it is possible to simplify the constitutive relation of piezoelectric materials in consideration of loading, electroding, and associated geometry of the structure. The two variants of electroding introduced above have different implications.

Areal Electrodes

In the case of areal electrodes, as shown in Figures 5.2(a) and (c), the out-of-plane shear modes suggest, for the small characteristic ratio of thickness to the other extents of the laminae, the assumption of unidirectional electric field strength in polarization/through-thickness direction, compare with Figure 4.8(b). When only planar stress in the plane transverse to the polarization direction is regarded, then the constitutive relation anyway reduces to Eq. (4.28).

Interdigitated Electrodes

While for areal electrodes, the in-plane shear mode is free of electromechanical coupling, a structure with interdigitated electrodes, as shown in Figures 5.2(b)

and (d), exhibits such a coupling. The characteristic ratio relates the spacing between electrodes to the length of the electrode fingers. This again is very small for the existent specimens, see for example Figure 5.4. The other mode of electromechanically coupled shear occurs in the plane unfolding between the through-thickness (e_2) and the polarization (e_3) direction. Here the electric connection of the electrode pairs on the top and bottom sides, see Figure 5.3, leads to a non-homogeneous behavior in analogy to both cases of Figure 4.6(b). The conditions underneath the electrodes correspond to the case with connected electrodes, while the situation in the intervals between opposing polarity electrodes resembles the case without electrodes. When only planar stress in the plane of the laminae is regarded, this out-of-plane shear mode is discarded and the in-plane shear mode, as discussed above, implies $v_{31} = 0$ in the associated constitutive relation of Eq. (4.30).

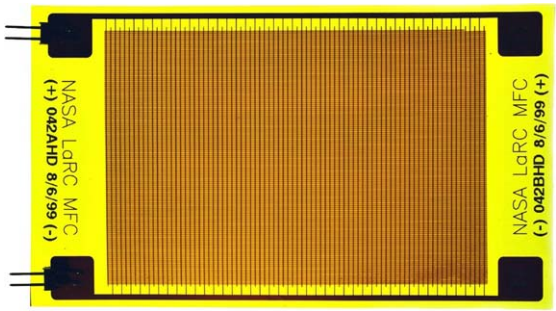

Fig. 5.4. NASA Langeley Research Center (LaRC) Macro-Fiber Composite (MFC); original photograph by the *National Aeronautics and Space Administration* [130].

5.2.3 Development Status

A number of different approaches to realizing composites with piezoelectric fibers and interdigitated electrodes have been developed or proposed. These may be distinguished by the process of fiber production and the application of electrodes. Suitable fibers can be fabricated in a sintering process from piezoelectric powders with techniques like extrusion of polymer supported powders, *Strock et al.* [171], or sol-gel spinning, *Helbig et al.* [92]. With the co-extrusion of a tube of polymer-supported piezoelectric powder filled and surrounded by material to be burned off afterwards, it is possible to produce hollow fibers, *Cannon and Brei* [42]. For these complex manufacturing processes, a greater number of parameters needs to be established and controlled in order to maintain the required quality. Less complicated and costly is the dicing of monolithic piezoelectric materials into rectangular fibers providing good accuracy and repeatability, *Wilkie et al.* [182]. Several different types of electrodes have been discussed. Interlaminar electroding structures

attached to the top and bottom sides of a piezoelectric laminae, as depicted in Figures 5.2(b) and (d), have been realized by etching copper on a supporting film, see for example *Bent and Hagood* [14] or *Wilkie et al.* [182]. Such films package the laminae and thus provide insulation to other possibly conductive laminae, for example when carbon fibers are contained. To take the electrodes closer to the fibers, the use of conductive adhesives was investigated by *Pannkoke et al.* [136]; rings of silver paint have been applied on the inside and outside of hollow fibers by *Cannon and Brei* [42]; and linked conductive rings around solid circular fibers have been proposed by *Tan and Tong* [173]. So far, only the combination of diced rectangular fibers made of PZT-5H-type material with interlaminar copper electrodes has reached batch production, *High and Wilkie* [94], see Figure 5.4. A research application of such actuators to alleviate the buffet effect at twin tail aircraft, *Sheta et al.* [162], is shown in Figure 5.5. A promising development direction of this actuator concept is the employment of fibers made of single crystal PMN-PT-type materials, as reported by *Wilkie et al.* [183], with significantly improved electromechanical coupling properties, compare Section 4.1.2 and Table A.3. Further surveys with respect to piezoelectric fiber composites are given by *Williams and Inman* [184] as well as by *Nelson* [132]. A comparison of the performance of packaged piezoelectric actuators for industrial applications representing all four variants of Figure 5.2 has been conducted by *Pretorius et al.* [145].

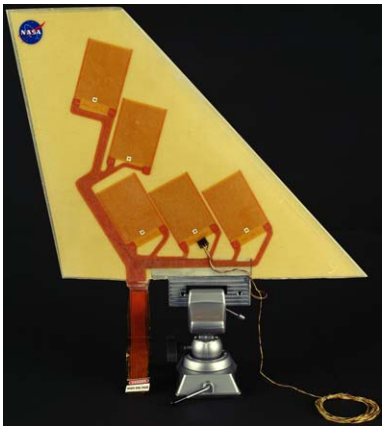

Fig. 5.5. Scaled model of a vertical tail fin with applied macro-fiber composite actuator patches; original photograph by the *National Aeronautics and Space Administration* [130].

5.2.4 Representative Volume Element and Fiber Geometry

While a composite as the whole thing is a rather complicated structure, the essential relations may be illustrated by means of a small but representative

piece of it. Such a representative volume element therefore is utilized as the basis of some analysis approaches. In order to portray the characteristics of the entire composite, it will be defined as follows:

Remark 5.1. A representative volume element is the smallest region of the composite over which mechanical as well as electrostatic fields are macroscopically uniform.

On account of the heterogeneous properties of the constituents, these fields are likely to be microscopically non-uniform. Accordingly, the appropriate geometry and boundary conditions need to be identified. Size and complexity of a representative volume element depend on the topology of the composite. Elaborate configurations are necessary, for example, to embody textile composites, whereas the consideration of a single inclusion together with the connected portion of matrix material is often sufficient. Furthermore, advantage can be taken of the symmetry of the examined region, being especially valuable for the finite element discretization. Such a simplified representative volume element is shown in Figure 5.6 for a composite patch with a single fiber layer. It contains a quarter of the cross-section of fiber and surrounding matrix and its length may be limited to half of the electrode spacing. In the conventional case without electromechanical coupling, the length in direction of the fiber is arbitrary, since stresses and strains do not vary along this direction.

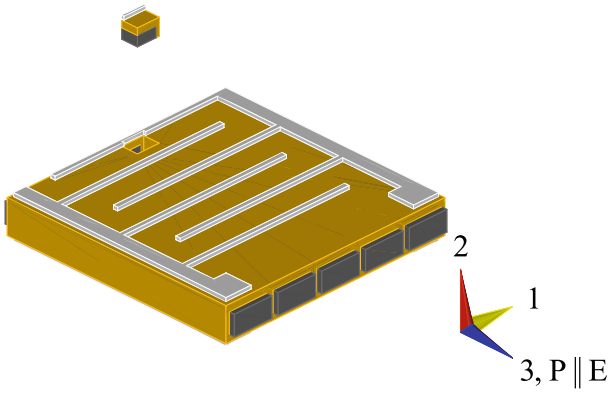

Fig. 5.6. Simplified representative volume element in consideration of fibrous inclusions and interdigitated electrodes.

Fiber Volume Fraction

The essential statement about the composition of the considered composite is provided by the fiber volume fraction ν. As the material distribution does not

change along the fiber direction, only the geometric relations in the plane of the fiber cross-section are relevant. The associated directional fiber fractions ν_1 and ν_2 may be determined from the fiber dimensions a_1^f and a_2^f and fiber spacings a_1 and a_2:

$$\nu_1 = \frac{a_1^f}{a_1}, \qquad \nu_2 = \frac{a_2^f}{a_2}, \tag{5.1a}$$

$$\nu = \nu_1 \nu_2. \tag{5.1b}$$

The characteristic cross-sectional dimensions are depicted together with electrode spacing a_3 and electrode width b_3 in Figure 5.7 by means of the simplified representative volume element.

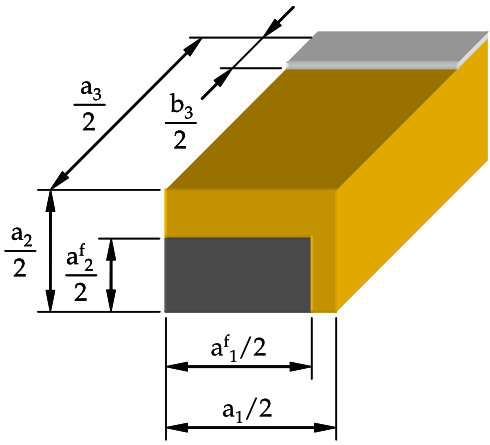

Fig. 5.7. Characteristic dimensions of the simplified representative volume element.

Fiber Cross-Sectional Shape

The cross-sectional shape of the fibers is primarily of local importance, for instance with respect to stress concentrations along the edges. Aiming at the determination of the overall behavior, only the directional fiber fractions have to be considered. This is equivalent to the mapping of an arbitrary shape onto a rectangle with the appropriate edge lengths for approaches based on representative volume elements like the one outlined above. For other approaches with an elliptic elementary fiber shape, it can be proceeded correspondingly by determining the appropriate ellipticity coefficient. Further insight may be gained using the method of cells presented by *Aboudi* [1,2]. It divides the representative volume element into subcells with interfacial conditions and thus allows for a discretization of the fiber cross-section. The examination of slices of the simplified representative volume element is considered in the work of *Tan and Tong* [173].

5.2.5 Modeling Preliminaries

To continue the analysis of laminae with piezoelectric fibers just as in the monolithic case, it is necessary to homogenize the heterogeneous properties of fibers and matrix. Thus, the objective is to determine the presupposedly homogeneous overall behavior of the composite based on the known characteristics of the individual constituents and their interaction. For this purpose, in the context of conventional composites, a greater number of theories has been developed and several have been extended to capture the implications of the piezoelectric effect. In general, the analytical homogenization methods may be roughly subdivided into two categories. On the one hand there are approaches which make use of the "Theory of Elasticity" as completely as possible, while on the other hand approaches utilize ad hoc assumptions within the framework of the "Mechanics of Materials". Representatives of both categories will be investigated in the subsequent sections. Although these approaches possess diverging abilities, which will be indicated individually, the current requirements will function as a common foundation.

Remark 5.2. The subsequent discussion of micro-electromechanical approaches to determine the macroscopic constitutive properties of a composite will be concentrated on properties within the following categories:

- Constituents
  → homogeneous, linearly elastic materials with piezoelectric properties.
- Topology
  → continuous, straight, perfectly aligned and regularly spaced fibers.
- Connection
  → perfect bonding of constituents, no direct contact between inclusions.

Typically, the fiber material is at most transversely isotropic, Eq. (4.17) with Eqs. (4.3), (4.8), and (4.18), while the matrix material is isotropic, Eq. (4.17) with Eqs. (4.4), (4.9), and vanishing piezoelectric moduli. The subsequent theories are not confined to such a behavior. However, it will be presumed that the distinguished axes are aligned. Deviating cases may be considered in conjunction with an appropriate transformation, see Section 3.2.5. In accordance with the considerations of Section 4.4.4, the notation with a negated electric field strength will be utilized throughout the entire chapter.

5.3 Micro-Electromechanics with Equivalent Inclusions

The micro-electromechanical methodology stemming from the category of the "Theory of Elasticity" to be presented in this section is capable of modeling inclusions of ellipsoidal geometry. Such a description of the inclusion geometry allows us to consider fibrous and lamellar inclusions by means of one or two semiaxes approaching infinity, respectively.

5.3.1 Mean Fields and Concentration Matrices

Subjecting a homogeneous body to homogeneous boundary conditions results in homogeneous fields. These homogeneous fields can be shown to agree with the volumetric average of the fields found in a non-homogeneous body exposed to identical boundary conditions, see *Aboudi* [1] or *Dunn and Taya* [66]. Consequently, these mean macroscopic fields may be expressed as an average of the mean fields inherent to the individual material phases weighted by their volume fraction. For electromechanically coupled composites with the volume fraction ν of a single inclusion phase, this leads to

$$\bar{\boldsymbol{Z}} = \nu \bar{\boldsymbol{Z}}^i + (1-\nu)\, \bar{\boldsymbol{Z}}^m, \tag{5.2a}$$

$$\boldsymbol{Y} = \nu \boldsymbol{Y}^i + (1-\nu)\, \boldsymbol{Y}^m. \tag{5.2b}$$

Mean stresses and electric flux densities $\boldsymbol{Y}$ as well as mean strains and electric field strengths $\bar{\boldsymbol{Z}}$ are composed of the corresponding mean fields in the inclusion and matrix phase as indicated by the superscripts i and m. Cross-connecting these fields, the constitutive relations of the homogenized composite, as well as of the individual material phases, may be given as follows:

$$\boldsymbol{Y} = \bar{\mathbb{C}} \bar{\boldsymbol{Z}}, \qquad \boldsymbol{Y}^i = \bar{\mathbb{C}}^i \bar{\boldsymbol{Z}}^i, \qquad \boldsymbol{Y}^m = \bar{\mathbb{C}}^m \bar{\boldsymbol{Z}}^m. \tag{5.3}$$

The unique dependence of strains and electric field strengths as well as stresses and electric flux densities in the individual material phases upon the overall fields of the composite may be formulated with the aid of the concentration matrices $\boldsymbol{\Xi}^i$ and $\boldsymbol{\Xi}^m$, respectively, $\boldsymbol{\Sigma}^i$ and $\boldsymbol{\Sigma}^m$:

$$\bar{\boldsymbol{Z}}^i = \boldsymbol{\Xi}^i \bar{\boldsymbol{Z}}, \quad \bar{\boldsymbol{Z}}^m = \boldsymbol{\Xi}^m \bar{\boldsymbol{Z}}, \quad \text{with } \nu \boldsymbol{\Xi}^i + (1-\nu)\, \boldsymbol{\Xi}^m = \mathbf{I}; \tag{5.4}$$

$$\boldsymbol{Y}^i = \boldsymbol{\Sigma}^i \boldsymbol{Y}, \quad \boldsymbol{Y}^m = \boldsymbol{\Sigma}^m \boldsymbol{Y}, \quad \text{with } \nu \boldsymbol{\Sigma}^i + (1-\nu)\, \boldsymbol{\Sigma}^m = \mathbf{I}. \tag{5.5}$$

Starting off with Eq. (5.2b) and subsequent substitution of stresses and electric flux densities $\boldsymbol{Y}$, $\boldsymbol{Y}^i$, and $\boldsymbol{Y}^m$ from the constitutive relations of Eq. (5.3), of strains and electric field strengths $\bar{\boldsymbol{Z}}^m$ from Eq. (5.2a) and $\bar{\boldsymbol{Z}}^i$ from Eq. (5.4), the effective properties may be written as

$$\bar{\mathbb{C}} = \nu \left(\bar{\mathbb{C}}^i - \bar{\mathbb{C}}^m \right) \boldsymbol{\Xi}^i + \bar{\mathbb{C}}^m. \tag{5.6}$$

Analogously, the inverted representation, see Eqs. (4.10), may be treated in consideration of Eq. (5.5), leading to

$$\left(\bar{\mathbb{C}}\right)^{-1} = \nu \left(\left(\bar{\mathbb{C}}^i\right)^{-1} - \left(\bar{\mathbb{C}}^m\right)^{-1} \right) \boldsymbol{\Sigma}^i + \left(\bar{\mathbb{C}}^m\right)^{-1}. \tag{5.7}$$

Thus, the effective properties $\bar{\mathbb{C}}$ of a composite are described in Eqs. (5.6) and (5.7) by the known fiber volume fraction ν and constituent properties $\bar{\mathbb{C}}^i$ and $\bar{\mathbb{C}}^m$, as well as by the concentration matrices $\boldsymbol{\Xi}^i$ and $\boldsymbol{\Sigma}^i$ of the inclusion phase to be determined by the succeeding theories.

5.3.2 Elementary Rules of Mixture

For the sake of comprehensiveness and later comparison, the most elementary options to determine the overall properties of a composite will be given here for the derived formulation. Assumptions in analogy to parallel and series connections of springs typical for the "Mechanics of Materials" are utilized, dating back to the works of *Voigt* [175] and *Reuss* [154]. The assumption of uniform strains and electric field strengths $\bar{\boldsymbol{Z}}^i = \bar{\boldsymbol{Z}}^m = \bar{\boldsymbol{Z}}$ leads with Eqs. (5.4) to the concentration matrices $\boldsymbol{\Xi}^i = \boldsymbol{\Xi}^m = \mathbf{I}$. Applied to Eq. (5.6), such a parallel connection of material phases results in the weighted addition of the electroelastic moduli:

$$\bar{\mathbb{C}} = \nu \bar{\mathbb{C}}^i + (1-\nu)\, \bar{\mathbb{C}}^m. \tag{5.8}$$

Correspondingly, the assumption of uniform stresses and electric flux densities $\boldsymbol{Y}^i = \boldsymbol{Y}^m = \boldsymbol{Y}$ leads with Eqs. (5.5) to the concentration matrices $\boldsymbol{\Sigma}^i = \boldsymbol{\Sigma}^m = \mathbf{I}$. Applied to Eq. (5.7), such a series connection of material phases results in the weighted addition involving the inverse matrices of the electroelastic moduli:

$$\begin{aligned} \left(\bar{\mathbb{C}}\right)^{-1} &= \nu \left(\bar{\mathbb{C}}^i\right)^{-1} + (1-\nu) \left(\bar{\mathbb{C}}^m\right)^{-1} \\ \rightarrow \quad \bar{\mathbb{C}} &= \left(\nu \left(\bar{\mathbb{C}}^i\right)^{-1} + (1-\nu) \left(\bar{\mathbb{C}}^m\right)^{-1}\right)^{-1}. \end{aligned} \tag{5.9}$$

The above assumptions, however, have incorrect implications. For a parallel connection of material phases, the equilibrium conditions are violated at phase boundaries, while for a series connection of material phases, the compatibility conditions may not hold at phase boundaries. Nevertheless, it can be shown that these estimates may serve as upper and lower bounds enclosing the actual electroelastic moduli of the composite. For a discussion of bounds on effective elastic properties, see *Christensen* [54].

5.3.3 Equivalence of Inclusion and Inhomogenity

Let there be a homogeneous ellipsoidal inclusion filling the domain Λ^i with the electroelastic properties $\bar{\mathbb{C}}^i$ embedded into an infinite homogeneous matrix with the electroelastic properties $\bar{\mathbb{C}}^m$. Such a composite filling the domain Λ will be subjected to uniform boundary conditions

$$\boldsymbol{Y}_{\partial\Lambda} = \boldsymbol{Y}, \quad \text{respectively} \quad \bar{\boldsymbol{Z}}_{\partial\Lambda} = \bar{\boldsymbol{Z}}. \tag{5.10}$$

The overall strains and electric field strengths $\bar{\boldsymbol{Z}}$ of the composite can be either interpreted as a response to the applied stresses and electric flux densities or are the direct implication of the boundary conditions. In absence of the inclusion, they would prevail throughout the domain Λ. The resulting strains and electric field strengths $\bar{\boldsymbol{Z}}^i$ inside the inclusion may be assembled

in consideration of perturbation fields $\bar{\boldsymbol{Z}}^{\bullet}$ caused by the deviating material properties of the inclusion:

$$\bar{\boldsymbol{Z}}^{i} = \bar{\boldsymbol{Z}} + \bar{\boldsymbol{Z}}^{\bullet}. \tag{5.11}$$

Thus, the stresses and electric flux densities inside the inclusion can be determined from the corresponding constitutive relation of Eq. (5.3) as

$$\boldsymbol{Y}^{i} = \bar{\mathbb{C}}^{i} \left(\bar{\boldsymbol{Z}} + \bar{\boldsymbol{Z}}^{\bullet} \right). \tag{5.12}$$

The considered inclusion may be replaced by matrix material subjected to additional so-called eigenfields $\bar{\boldsymbol{Z}}^{*}$ such that the stresses and electric flux densities inside the domain Λ^{i} remain unchanged and thus can be described by

$$\boldsymbol{Y}^{i} = \bar{\mathbb{C}}^{m} \left(\bar{\boldsymbol{Z}} + \bar{\boldsymbol{Z}}^{\bullet} - \bar{\boldsymbol{Z}}^{*} \right). \tag{5.13}$$

The equivalence of an inclusion with deviating material properties and an inhomogenity on account of eigenfields has been introduced for the elastic case by *Eshelby* [73] and extended to the piezoelectric case by *Deeg* [61]. It was shown that the eigenfields $\bar{\boldsymbol{Z}}^{*}$ are uniform for an ellipsoidal shape of the domain Λ^{i}. In conjunction with the presumed uniform boundary conditions on the enclosing surface $\partial\Lambda$ at infinite distance, this leads to an entirely uniform distribution of fields inside the domain Λ^{i}. Therefore, a linear transformation between perturbation fields $\bar{\boldsymbol{Z}}^{\bullet}$ and eigenfields $\bar{\boldsymbol{Z}}^{*}$ can be established:

$$\bar{\boldsymbol{Z}}^{\bullet} = \boldsymbol{\Upsilon} \bar{\boldsymbol{Z}}^{*}. \tag{5.14}$$

The constraint matrix $\boldsymbol{\Upsilon}$ depicts the effect of the constraining matrix on the inclusion and is a function of matrix material properties and ellipsoidal inclusion shape. It represents the piezoelectric analog to Eshelby's tensor in the elastic case, see *Dunn and Taya* [66]. Expressions for cylindrical inclusions to model fibrous composites are provided by *Dunn and Taya* [67] (this reference uses a different notation, $\boldsymbol{\Upsilon}$ is called $\mathbf{S}$). Equating Eqs. (5.12) and (5.13) and making use of Eq. (5.14) to replace the eigenfields $\bar{\boldsymbol{Z}}^{*}$ and Eq. (5.11) to eliminate the perturbation fields $\bar{\boldsymbol{Z}}^{\bullet}$ after some manipulations, leads to

$$\bar{\boldsymbol{Z}}^{i} = \underbrace{\left(\mathbf{I} + \boldsymbol{\Upsilon} \left(\bar{\mathbb{C}}^{m} \right)^{-1} \left(\bar{\mathbb{C}}^{i} - \bar{\mathbb{C}}^{m} \right) \right)^{-1}}_{\boldsymbol{\Xi}^{i}_{\mathrm{dil}}} \bar{\boldsymbol{Z}}. \tag{5.15}$$

The concentration matrix $\boldsymbol{\Xi}^{i}_{\mathrm{dil}}$ may be identified with the aid of Eq. (5.4). As its derivation is based on a single inclusion within an infinite matrix, it is applicable only to very low volume fractions of the inclusion or fiber phases, respectively. Such a configuration is usually denominated as a dilute concentration.

5.3.4 Non-Dilute Concentrations

To accomplish their specific task, most of composites require a portion of the inclusion phase that certainly cannot be described as dilute. Therefore, methods based on the equivalence of inclusion and inhomogenity derived above had to be developed to extend the range of applications to practicable volume fractions.

Mori–Tanaka Approach

Almost a standard procedure, due to its relative simplicity while allowing for dependable results and documented by a thorough theoretical discussion in the literature, the Mori–Tanaka approach was initiated by *Mori and Tanaka* [127]. Its major assumption may be formulated for electromechanically coupled composites as follows:

Remark 5.3. Strains and electric field strengths inside an inclusion in the non-dilute case behave with respect to the average fields of the matrix phase just like they would do in the dilute case with respect to the overall fields of the composite.

$$\bar{\boldsymbol{Z}}^i = \boldsymbol{\Xi}^i_{\mathrm{dil}} \bar{\boldsymbol{Z}}^m. \tag{5.16}$$

Since the overall fields of the composite with dilute concentration already account for the interaction between inclusion and matrix, this means that the inclusion is now considered to be embedded into a matrix containing other inclusions. Eliminating strains and electric field strengths $\bar{\boldsymbol{Z}}^m$ of the matrix phase in Eq. (5.2a) by utilization of Eq. (5.16) results after a few manipulations in

$$\bar{\boldsymbol{Z}}^i = \underbrace{\boldsymbol{\Xi}^i_{\mathrm{dil}} \left(\nu \boldsymbol{\Xi}^i_{\mathrm{dil}} + (1-\nu)\, \mathbf{I} \right)^{-1}}_{\boldsymbol{\Xi}^i_{\mathrm{MT}}} \bar{\boldsymbol{Z}}. \tag{5.17}$$

Again, the concentration matrix $\boldsymbol{\Xi}^i_{\mathrm{MT}}$ for the Mori–Tanaka approach can be identified with the aid of Eq. (5.4). It has been proposed in this form for the elastic case by *Benveniste* [18] and extended to the piezoelectric case by *Dunn and Taya* [67].

Other Approaches

There are a number of other ways to consider non-dilute concentrations within equivalent inclusion approaches. Among them are the self-consistent schemes, see *Aboudi* [1], where an inclusion is examined that is surrounded in the classical variant by an effective medium of a priori unknown properties and the generalized variant by matrix material, which again is embedded into such an effective medium. The resulting concentration matrices are comparable to the dilute case of Eq. (5.15), but with fundamental difference of a dependence

on the unknown properties. Thus, the effective properties of the composite may only be determined in a computationally expensive iterative manner. This can be avoided by replacing the effective medium with homogenization results obtained with the aid of another approach, see *Dvorak and Srinivas* [68] and *Odegard* [135] for the extension to piezoelectric materials.

5.4 Micro-Electromechanics with Sequential Stacking

The micro-electromechanical methodology stemming from the category of the "Mechanics of Materials", to be presented in this section, is base on a simplified rectangular representative volume element, as described in Section 5.2.4. Correspondingly, the fiber shape is approximated by a cuboid stretching over the full length, but aligned non-continuous inclusions may be also considered in a straightforward manner. Different from the methodology of the previous section, simplifying assumptions are imposed at the starting point of the derivation. As subsequently shown in detail, this concerns the distribution of mechanical and electrostatic fields within the individual material phases and the interaction between phases. While the rules of mixture have been applied collectively in Section 5.3.2, the latter aspect will be handled here by a field and direction specific application of the associated assumptions. For fiber composites with piezoelectric properties, such examinations have been conducted by *Bent and Hagood* [15] for the normal modes and subsequently by *Tan and Tong* [173] on the foundations laid by *Newnham et al.* [133] as well as *Smith and Auld* [165]. Further piezoelectric composite modeling approaches based on the "Mechanics of Materials" have been developed, for example, by *Banno* [8] or *Aboudi* [2].

5.4.1 Stacking of Constituents with Uniform Fields

The visual inspection of the simplified representative volume element in Figure 5.7 suggests a determination of the composite's overall behavior via the examination of the stacking of constituents in axial directions transverse to the fibers, as shown on the left and in the middle of Figure 5.8. Ahead of considering the possibilities of how to combine these elementary cases, they first of all will be studied separately. In order to gain an impression of the effective

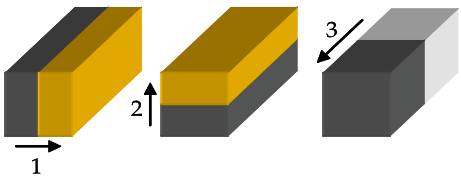

Fig. 5.8. Stacking of material phases in the axial directions.

properties of such a stack of two materials, its response to all load cases needs to be tested. Being subjected to arbitrary homogeneous boundary conditions, the mechanical and electrostatic fields within the individual material phases may not be entirely homogeneous in consequence of the dissimilar material properties. Since such effects are predominantly of local importance, they will be neglected by virtue of the uniform fields assumption:

Remark 5.4. Mechanical and electrostatic fields are assumed to be homogeneous throughout the individual material phases.

As the entire composite structure happens to be assembled from simplified representative volume elements by symmetric completion and repetition, the edges have to remain straight and parallel in any event. Transferred to the mechanical and electrostatic fields, this requirement may be fulfilled on the grounds of the following assumption:

Remark 5.5. The macroscopic mechanical and electrostatic fields either coincide with field quantities found to be identical in all material phases or result from the average of field quantities in the individual material phases weighted by their directional fraction in accordance with the scheme of Table 5.1.

Table 5.1. General assumptions for the stacking of material phases with respect to the relation of macroscopic to microscopic mechanical and electrostatic fields.

	Stress/El. Flux Density	**Strain/El. Field Strength**
Stacking Direction	coincidence	weighted average
Transverse Plane	weighted average	coincidence

These assumptions can be applied immediately in the directions e_1 and e_2 of the cross-sectional plane of the fibers. As the constitutive relation of the considered piezoelectric materials exhibits only a partial electromechanical coupling, normal modes and each of the shear modes may be treated independently, as illustrated by Eqs. (4.19) to (4.21). In accordance with the considerations of Section 4.4.4, the notation with negated electric field strength and the associated constitutive submatrices $\bar{\mathbb{E}}$, $\bar{\mathbb{G}}_1$, and $\bar{\mathbb{G}}_2$ will be utilized.

5.4.2 Normal Mode Stacking Coefficients

The implications of Remark 5.5 are summarized in Table 5.2 for the stacking of material phases transverse to the fiber direction with respect to fields associated with the normal modes. While the macroscopic mechanical and electrostatic fields carry the usual denominations, the association with the individual phases is indicated by the superscripts f and m for fields in the fiber and matrix phase respectively. The normal mode constitutive relation of Eq. (4.19)

Table 5.2. Assumptions for the stacking of material phases with respect to normal modes.

Direction	Stress/El. Flux Density	Strain/El. Field Strength
e_1	$\sigma_1 = \sigma_1^f = \sigma_1^m$ $\sigma_2 = \nu_1\sigma_2^f + (1-\nu_1)\,\sigma_2^m$ $\sigma_3 = \nu_1\sigma_3^f + (1-\nu_1)\,\sigma_3^m$ $D_3 = \nu_1 D_3^f + (1-\nu_1)\,D_3^m$	$\varepsilon_1 = \nu_1\varepsilon_1^f + (1-\nu_1)\,\varepsilon_1^m$ $\varepsilon_2 = \varepsilon_2^f = \varepsilon_2^m$ $\varepsilon_3 = \varepsilon_3^f = \varepsilon_3^m$ $\bar{E}_3 = \bar{E}_3^f = \bar{E}_3^m$
e_2	$\sigma_1 = \nu_2\sigma_1^f + (1-\nu_2)\,\sigma_1^m$ $\sigma_2 = \sigma_2^f = \sigma_2^m$ $\sigma_3 = \nu_2\sigma_3^f + (1-\nu_2)\,\sigma_3^m$ $D_3 = \nu_2 D_3^f + (1-\nu_2)\,D_3^m$	$\varepsilon_1 = \varepsilon_1^f = \varepsilon_1^m$ $\varepsilon_2 = \nu_2\varepsilon_2^f + (1-\nu_2)\,\varepsilon_2^m$ $\varepsilon_3 = \varepsilon_3^f = \varepsilon_3^m$ $\bar{E}_3 = \bar{E}_3^f = \bar{E}_3^m$

can be rewritten for every material phase in terms of those mechanical and electrostatic fields that are identical in all material phases. For the stacking in the e_1- and e_2-directions with the associated partially inverted matrices $\bar{\mathbb{F}}_1^f$, $\bar{\mathbb{F}}_1^m$ and $\bar{\mathbb{F}}_2^f$, $\bar{\mathbb{F}}_2^m$ of normal mode constitutive coefficients, this yields:

$$e_1\colon \begin{Bmatrix} \varepsilon_1^f \\ \sigma_2^f \\ \sigma_3^f \\ D_3^f \end{Bmatrix} = \bar{\mathbb{F}}_1^f \begin{Bmatrix} \sigma_1 \\ \varepsilon_2 \\ \varepsilon_3 \\ \bar{E}_3 \end{Bmatrix}, \qquad \begin{Bmatrix} \varepsilon_1^m \\ \sigma_2^m \\ \sigma_3^m \\ D_3^m \end{Bmatrix} = \bar{\mathbb{F}}_1^m \begin{Bmatrix} \sigma_1 \\ \varepsilon_2 \\ \varepsilon_3 \\ \bar{E}_3 \end{Bmatrix}, \tag{5.18a}$$

$$e_2\colon \begin{Bmatrix} \sigma_1^f \\ \varepsilon_2^f \\ \sigma_3^f \\ D_3^f \end{Bmatrix} = \bar{\mathbb{F}}_2^f \begin{Bmatrix} \varepsilon_1 \\ \sigma_2 \\ \varepsilon_3 \\ \bar{E}_3 \end{Bmatrix}, \qquad \begin{Bmatrix} \sigma_1^m \\ \varepsilon_2^m \\ \sigma_3^m \\ D_3^m \end{Bmatrix} = \bar{\mathbb{F}}_2^m \begin{Bmatrix} \varepsilon_1 \\ \sigma_2 \\ \varepsilon_3 \\ \bar{E}_3 \end{Bmatrix}. \tag{5.18b}$$

Furthermore, those mechanical and electrostatic fields that are assumed to be a weighted average, as stated in Table 5.2, may be arranged collectively. Then the vectors of the phase specific fields can be replaced by substitution of Eqs. (5.18a) and (5.18b), respectively:

$$e_1\colon \begin{Bmatrix} \varepsilon_1 \\ \sigma_2 \\ \sigma_3 \\ D_3 \end{Bmatrix} = \nu_1 \begin{Bmatrix} \varepsilon_1^f \\ \sigma_2^f \\ \sigma_3^f \\ D_3^f \end{Bmatrix} + (1-\nu_1) \begin{Bmatrix} \varepsilon_1^m \\ \sigma_2^m \\ \sigma_3^m \\ D_3^m \end{Bmatrix} = \underbrace{\left(\nu_1^f \bar{\mathbb{F}}_1^f + (1-\nu_1)\,\bar{\mathbb{F}}_1^m\right)}_{\bar{\mathbb{F}}_1} \begin{Bmatrix} \sigma_1 \\ \varepsilon_2 \\ \varepsilon_3 \\ \bar{E}_3 \end{Bmatrix}, \tag{5.19a}$$

$$e_2\colon \begin{Bmatrix} \sigma_1 \\ \varepsilon_2 \\ \sigma_3 \\ D_3 \end{Bmatrix} = \nu_2 \begin{Bmatrix} \sigma_1^f \\ \varepsilon_2^f \\ \sigma_3^f \\ D_3^f \end{Bmatrix} + (1-\nu_2) \begin{Bmatrix} \sigma_1^m \\ \varepsilon_2^m \\ \sigma_3^m \\ D_3^m \end{Bmatrix} = \underbrace{\left(\nu_2 \bar{\mathbb{F}}_2^f + (1-\nu_2)\,\bar{\mathbb{F}}_2^m\right)}_{\bar{\mathbb{F}}_2} \begin{Bmatrix} \varepsilon_1 \\ \sigma_2 \\ \varepsilon_3 \\ \bar{E}_3 \end{Bmatrix}. \tag{5.19b}$$

These still partially inverted macroscopic constitutive relations with the weighted average of material properties of both phases comprised in the matrices $\bar{\mathbb{F}}_1$ and $\bar{\mathbb{F}}_2$, may be reverted to the original form of the normal mode constitutive relations:

$$e_1\colon \begin{Bmatrix} \sigma_1 \\ \sigma_2 \\ \sigma_3 \\ D_3 \end{Bmatrix} = \bar{\mathbb{E}}^1 \begin{Bmatrix} \varepsilon_1 \\ \varepsilon_2 \\ \varepsilon_3 \\ \bar{E}_3 \end{Bmatrix}, \qquad e_2\colon \begin{Bmatrix} \sigma_1 \\ \sigma_2 \\ \sigma_3 \\ D_3 \end{Bmatrix} = \bar{\mathbb{E}}^2 \begin{Bmatrix} \varepsilon_1 \\ \varepsilon_2 \\ \varepsilon_3 \\ \bar{E}_3 \end{Bmatrix}. \tag{5.20}$$

The coefficients of the constitutive matrices $\bar{\mathbb{E}}^1$ and $\bar{\mathbb{E}}^2$, as of Eq. (4.19), thus stem from the matrices $\mathbb{F}_1$ and $\mathbb{F}_2$, respectively. They can be derived from each other by interchanging the indices 1 and 2 of directional fiber fractions as well as constitutive coefficients of fiber and matrix material again indicated by the superscripts f and m. So the presentation of these coefficients can be confined to the matrix $\bar{\mathbb{E}}^1$ as a result of the stacking of constituents in the e_1-direction. The entries of the principal diagonal contained therein are

$$C^1_{11} = \frac{C^f_{11}}{\nu_1(1 + \frac{1-\nu_1}{\nu_1}\frac{C^f_{11}}{C^m_{11}})}, \tag{5.21a}$$

$$C^1_{22} = \nu_1 C^f_{22} + (1-\nu_1)\left(C^m_{22} - \frac{(C^f_{12} - C^m_{12})^2/C^m_{11}}{1 + \frac{1-\nu_1}{\nu_1}\frac{C^f_{11}}{C^m_{11}}}\right), \tag{5.21b}$$

$$C^1_{33} = \nu_1 C^f_{33} + (1-\nu_1)\left(C^m_{33} - \frac{(C^f_{13} - C^m_{13})^2/C^m_{11}}{1 + \frac{1-\nu_1}{\nu_1}\frac{C^f_{11}}{C^m_{11}}}\right), \tag{5.21c}$$

$$-\epsilon^1_{33} = -\nu_1 \epsilon^f_{33} - (1-\nu_1)\left(\epsilon^m_{33} - \frac{(e^f_{31})^2/C^m_{11}}{1 + \frac{1-\nu_1}{\nu_1}\frac{C^f_{11}}{C^m_{11}}}\right). \tag{5.21d}$$

Those coefficient tied to the particular stacking direction, C^1_{11} in case of the e_1-direction, are represented by a series connection of phase properties, compare with Section 5.3.2. The coefficients in the transverse directions, C^1_{22}, C^1_{33}, and ϵ^1_{33} for stacking the e_1-direction, are represented by a parallel connection of phase properties complemented by a term describing the interaction with the stacking direction, which therefore again resemble a series connection. A similar behavior is found for coefficients in charge of the mechanical and piezoelectric coupling between directions transverse to the stacking direction:

$$C^1_{23} = \nu_1 C^f_{23} + (1-\nu_1)\left(C^m_{23} - \frac{(C^f_{12} - C^m_{12})(C^f_{13} - C^m_{13})/C^m_{11}}{1 + \frac{1-\nu_1}{\nu_1}\frac{C^f_{11}}{C^m_{11}}}\right), \tag{5.21e}$$

$$e_{32}^1 = \nu_1 e_{32}^f - (1-\nu_1)\, e_{31}^f \frac{(C_{12}^f - C_{12}^m)/C_{11}^m}{1 + \frac{1-\nu_1}{\nu_1}\frac{C_{11}^f}{C_{11}^m}}, \tag{5.21f}$$

$$e_{33}^1 = \nu_1 e_{33}^f - (1-\nu_1)\, e_{31}^f \frac{(C_{13}^f - C_{13}^m)/C_{11}^m}{1 + \frac{1-\nu_1}{\nu_1}\frac{C_{11}^f}{C_{11}^m}}. \tag{5.21g}$$

As the remaining mechanical and piezoelectric coupling coefficients directly affect the stacking direction, no additional terms appear but series-connection-like modifications of phase properties arise within a parallel connection:

$$C_{12}^1 = \frac{C_{12}^f + C_{12}^m \frac{1-\nu_1}{\nu_1}\frac{C_{11}^f}{C_{11}^m}}{1 + \frac{1-\nu_1}{\nu_1}\frac{C_{11}^f}{C_{11}^m}}, \quad C_{13}^1 = \frac{C_{13}^f + C_{13}^m \frac{1-\nu_1}{\nu_1}\frac{C_{11}^f}{C_{11}^m}}{1 + \frac{1-\nu_1}{\nu_1}\frac{C_{11}^f}{C_{11}^m}}, \quad e_{31}^1 = \frac{e_{31}^f}{1 + \frac{1-\nu_1}{\nu_1}\frac{C_{11}^f}{C_{11}^m}}. \tag{5.21h}$$

Due to the abandonment of piezoelectric properties for the matrix material, all of the piezoelectric coupling coefficients as well as the dielectric permittivity appear in a simplified form.

5.4.3 Shear Mode Stacking Coefficients

The implications of Remark 5.5 are summarized in Table 5.3 for the stacking of material phases transverse to the fiber direction with respect to fields associated with the shear modes. These are decoupled of one another: the electrostatic fields in the e_1- and e_2-directions interact with the shear fields in the e_2-e_3-plane and e_3-e_1-plane, respectively; the e_1-e_2-plane transverse to the fiber direction is free of piezoelectric coupling, see Eqs. (4.20) and (4.21).

Table 5.3. Assumptions for the stacking of material phases with respect to shear modes.

Direction	Stress/El. Flux Density	Strain/El. Field Strength
e_1	$\tau_{31} = \tau_{31}^f = \tau_{31}^m$ $D_1 = D_1^f = D_1^m$	$\gamma_{31} = \nu_1\gamma_{31}^f + (1-\nu_1)\,\gamma_{31}^m$ $\bar{E}_1 = \nu_1 E_1^f + (1-\nu_1)\, E_1^m$
	$\tau_{23} = \nu_1\tau_{23}^f + (1-\nu_1)\,\tau_{23}^m$ $D_2 = \nu_1 D_2^f + (1-\nu_1)\, D_2^m$	$\gamma_{23} = \gamma_{23}^f = \gamma_{23}^m$ $\bar{E}_2 = \bar{E}_2^f = \bar{E}_2^m$
	$\tau_{12} = \tau_{12}^f = \tau_{12}^m$	$\gamma_{12} = \nu_1\gamma_{12}^f + (1-\nu_1)\,\gamma_{12}^m$
e_2	$\tau_{31} = \nu_2\tau_{31}^f + (1-\nu_2)\,\tau_{31}^m$ $D_1 = \nu_2 D_1^f + (1-\nu_2)\, D_1^m$	$\gamma_{31} = \gamma_{31}^f = \gamma_{31}^m$ $\bar{E}_1 = \bar{E}_1^f = \bar{E}_1^m$
	$\tau_{23} = \tau_{23}^f = \tau_{23}^m$ $D_2 = D_2^f = D_2^m$	$\gamma_{23} = \nu_2\gamma_{23}^f + (1-\nu_2)\,\gamma_{23}^m$ $\bar{E}_2 = \nu_2 E_2^f + (1-\nu_2)\, E_2^m$
	$\tau_{12} = \tau_{12}^f = \tau_{12}^m$	$\gamma_{12} = \nu_2\gamma_{12}^f + (1-\nu_2)\,\gamma_{12}^m$

Since the coupled fields have an agreeing direction, they are subjected to the same kind of assumption of Remark 5.5. Hence, the macroscopic constitutive submatrices $\bar{\mathbb{G}}_1^1$, $\bar{\mathbb{G}}_1^2$, $\bar{\mathbb{G}}_2^1$, and $\bar{\mathbb{G}}_2^2$, where the upper index is associated with the stacking direction and the lower with the agreeing direction of the coupled mode, can be determined either directly or via complete inversion from the weighted average:

$$e_1\colon \begin{Bmatrix} \tau_{31} \\ D_1 \end{Bmatrix} = \underbrace{\left(\nu_1 \left(\bar{\mathbb{G}}_1^f \right)^{-1} + (1-\nu_1) \left(\bar{\mathbb{G}}_1^m \right)^{-1} \right)^{-1}}_{\bar{\mathbb{G}}_1^1} \begin{Bmatrix} \gamma_{31} \\ E_1 \end{Bmatrix}, \tag{5.22a}$$

$$e_2\colon \begin{Bmatrix} \tau_{31} \\ D_1 \end{Bmatrix} = \underbrace{\left(\nu_2 \bar{\mathbb{G}}_1^f + (1-\nu_2) \bar{\mathbb{G}}_1^m \right)}_{\bar{\mathbb{G}}_1^2} \begin{Bmatrix} \gamma_{31} \\ E_1 \end{Bmatrix}, \tag{5.22b}$$

$$e_1\colon \begin{Bmatrix} \tau_{23} \\ D_2 \end{Bmatrix} = \underbrace{\left(\nu_1 \bar{\mathbb{G}}_2^f + (1-\nu_1) \bar{\mathbb{G}}_2^m \right)}_{\bar{\mathbb{G}}_2^1} \begin{Bmatrix} \gamma_{23} \\ E_2 \end{Bmatrix}, \tag{5.22c}$$

$$e_2\colon \begin{Bmatrix} \tau_{23} \\ D_2 \end{Bmatrix} = \underbrace{\left(\nu_2 \left(\bar{\mathbb{G}}_2^f \right)^{-1} + (1-\nu_2) \left(\bar{\mathbb{G}}_2^m \right)^{-1} \right)^{-1}}_{\bar{\mathbb{G}}_2^2} \begin{Bmatrix} \gamma_{23} \\ E_2 \end{Bmatrix}. \tag{5.22d}$$

The plane transverse to the fiber direction is always involved with the stacking in the considered directions. Thus, for both directions, the macroscopic stress component τ_{12} of the entirely decoupled shear mode coincides with those of the individual phases and the resulting shear stiffnesses C_{66}^1 and C_{66}^2 only differ by the participating directional fiber fraction:

$$e_1\colon \tau_{12} = \left(\nu_1 \left(C_{66}^f \right)^{-1} + (1-\nu_1) \left(C_{66}^m \right)^{-1} \right)^{-1} \gamma_{12} = \underbrace{\frac{C_{66}^f}{\nu_1 (1 + (\frac{1-\nu_1}{\nu_1}) \frac{C_{66}^f}{C_{66}^m})}}_{C_{66}^1} \gamma_{12}, \tag{5.23a}$$

$$e_2\colon \tau_{12} = \left(\nu_2 \left(C_{66}^f \right)^{-1} + (1-\nu_2) \left(C_{66}^m \right)^{-1} \right)^{-1} \gamma_{12} = \underbrace{\frac{C_{66}^f}{\nu_2 (1 + (\frac{1-\nu_2}{\nu_2}) \frac{C_{66}^f}{C_{66}^m})}}_{C_{66}^2} \gamma_{12}. \tag{5.23b}$$

5.4.4 Stacking Sequences

So far, the two necessary cases of stacking of constituents have been examined for normal as well as shear modes and macroscopic constitutive relations have been obtained for each of them. In the next step, their integration with the goal to depict the simplified representative volume element needs to be considered.

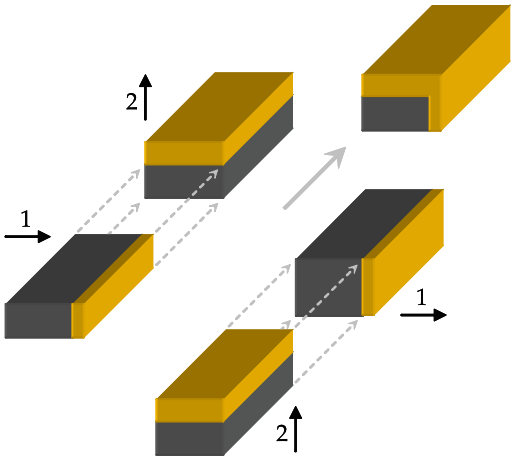

Fig. 5.9. Substitution sequences for the stacking of material phases in the fiber cross-sectional plane.

Remark 5.6. The macroscopic properties of the composite may be gained by employing the effective constitutive coefficients of one stacking direction as initial constitutive coefficients of the fiber material of the next.

Two possible sequences of these substitutions in the directions of the fiber cross-sectional plane arise, as illustrated in Figure 5.9. Thus, the parallel and series connections, as well as combinations thereof, given for instance by Eqs. (5.21a) to (5.21h), are nested in different ways with in fact diverging results. While *Bent and Hagood* [15] commit themselves to one of them without particular discussion, *Tan and Tong* [173] interpret the individually distinct coefficients in an extension of the elementary cases considered in Section 5.3.2 as upper and lower bounds on the effective composite properties. Further insight can be gained with the aid of the following considerations.

Remark 5.7. For composites in accordance with Remark 5.2 consisting of aligned transversely isotropic fiber and matrix materials, the overall material behavior is expected to be at most orthotropic and, in the case of identical directional fiber fractions ν_1 and ν_2, to be transversely isotropic.

When the two stacking sequences are applied to such a configuration with $\nu_1 = \nu_2$, in neither case is transversely isotropic material behavior predicted, but both variants show deviations which agree in magnitude but not in axial direction. Therefore however, their average is consistent with the expected transverse isotropy. Thus, the individual stacking sequences sort of introduce an artificial degree of orthotropy which may be balanced out by considering the combination of both stacking sequences. The two possible stacking sequences and their combination can be written symbolically with respect to

the stacking directions as

$$1 \Rightarrow 2, \qquad 2 \Rightarrow 1, \qquad \left\langle \begin{matrix} 1 \Rightarrow 2 \\ 2 \Rightarrow 1 \end{matrix} \right\rangle .$$

The following fact may be reflected for an illustrative explanation for such an artificial degree of orthotropy. By substituting the effective constitutive coefficients of one stacking direction as initial constitutive coefficients of the fiber material of the next, the matrix material is partitioned and subjected to diverging conditions, possibly leading to violations of equilibrium and compatibility.

5.4.5 Non-Homogeneous Electrostatic Fields

Neither the micro-electromechanical modeling approaches using equivalent inclusions nor the preceding application of the sequential stacking procedure consider non-homogeneous electrostatic fields. As long as the examined piezoelectric fiber composites are subjected to arbitrary but homogeneous mechanical as well as electrostatic fields, these approaches can be applied successfully. While these requirements may be sufficiently fulfilled with the application of areal electrodes, this is hardly the case when interdigitated electrodes are utilized, as illustrated by Figure 5.3. Between electrodes with identical polarity on the top and bottom sides, an inactive zone comes into being, while the active zone unfolds in the intervals between electrode pairs with opposing polarity. In between, a transitional region may be identified where, especially close to the electrodes, high field concentrations can be a cause for failure of the composite. For a finite element based analysis of these problems, see *Beckert and Kreher* [10].

Stacking in Fiber Direction

A suitable modeling method is sought to capture the losses of actuation and sensing authority due to the imperfect alignment of the electrostatic fields with the fiber direction. Relevant parameters are spacing a_3 and width b_3 of the electrodes as well as thickness $(a_2 - a_2^f)/2$ and dielectric properties of the matrix material between electrode and fiber in addition to the dielectric and piezoelectric properties of the fiber material. As the operative direction of the electrodes is aligned with the polarization direction, the discussion will be confined to the normal modes. The examination of the simplified representative volume element with the assistance of the stacking of constituents in the direction of the fibers is not as obvious as in the previous cases. Examining the implications of Remark 5.5 for the current case, summarized in Table 5.4, in consideration of the fact that the constituents are actually not stacked in this direction and thus the fibers with their superior properties clearly dominate the composite's behavior, suggests assuming the directional

Table 5.4. Assumptions for the stacking of material phases in fiber direction.

Direction	Stress/El. Flux Density	Strain/El. Field Strength
e_3	$\sigma_1 = \nu_3\sigma_1^f + (1-\nu_3)\,\sigma_1^m$	$\varepsilon_1 = \varepsilon_1^f = \varepsilon_1^m$
	$\sigma_2 = \nu_3\sigma_2^f + (1-\nu_3)\,\sigma_2^m$	$\varepsilon_2 = \varepsilon_2^f = \varepsilon_2^m$
	$\sigma_3 = \sigma_3^f = \sigma_3^m$	$\varepsilon_3 = \nu_3\varepsilon_3^f + (1-\nu_3)\,\varepsilon_3^m$
	$D_3 = D_3^f = D_3^m$	$\bar{E}_3 = \nu_3\bar{E}_3^f + (1-\nu_3+c_3)\,\bar{E}_3^m$

fiber fraction $\nu_3 = 1$. As the lines of electric field strength, sketched in Figure 5.3, not only pass through the fibers in the e_3-direction but, in addition, traverse the matrix material, it may be justified to introduce the additional factor c_3 in conjunction with the electric field strength $\bar{E}_3^m$ in the matrix material. In analogy to the considerations of *Bent and Hagood* [15], the factor c_3 may be roughly approximated as the share of the matrix material along the lines of the electric field strength on their way through both material phases:

$$c_3 = \frac{(a_2 - a_2^f)}{a_3 + (a_2 - a_2^f)} = \frac{(1-\nu_2)}{\frac{a_3}{a_2} + (1-\nu_2)}. \tag{5.24}$$

The appearing geometric quantities of the representative volume element are elucidated in Figure 5.7 and the associated directional fiber fractions are defined in Eq. (5.1a). In addition to assuming a rectangular path of field lines, such an approximation neglects the certainly important electrode width b_3. Thus, it primarily tackles the influences of transitional regions, while the inactive zones are left aside.

Determination of the Stacking Coefficients

To proceed just like in the other stacking cases, the constitutive relation of Eq. (4.19) may be rewritten for fiber and matrix material as follows:

$$e_3\colon \begin{Bmatrix} \sigma_1^f \\ \sigma_2^f \\ \varepsilon_3^f \\ \bar{E}_3^f \end{Bmatrix} = \mathbb{E}_3^f \begin{Bmatrix} \varepsilon_1 \\ \varepsilon_2 \\ \sigma_3 \\ D_3 \end{Bmatrix}, \qquad \begin{Bmatrix} \sigma_1^m \\ \sigma_2^m \\ \varepsilon_3^m \\ \bar{E}_3^m \end{Bmatrix} = \mathbb{E}_3^m \begin{Bmatrix} \varepsilon_1 \\ \varepsilon_2 \\ \sigma_3 \\ D_3 \end{Bmatrix}. \tag{5.25}$$

Again, those mechanical and electrostatic fields that originally have been assumed to be a weighted average, as stated in Table 5.4, may be arranged collectively and Eqs. (5.25) inserted:

$$e_3\colon \begin{Bmatrix} \sigma_1 \\ \sigma_2 \\ \varepsilon_3 \\ \bar{E}_3 \end{Bmatrix} = \begin{Bmatrix} \sigma_1^f \\ \sigma_2^f \\ \varepsilon_3^f \\ \bar{E}_3^f \end{Bmatrix} + c_3 \begin{Bmatrix} 0 \\ 0 \\ 0 \\ \bar{E}_3^m \end{Bmatrix} = \underbrace{\left(\mathbb{E}_3^f + \begin{bmatrix} 0 & 0 & 0 & 0 \\ 0 & 0 & 0 & 0 \\ 0 & 0 & 0 & 0 \\ 0 & 0 & 0 & c_3 \end{bmatrix} \mathbb{E}_3^m \right)}_{\mathbb{E}_3} \begin{Bmatrix} \varepsilon_1 \\ \varepsilon_2 \\ \sigma_3 \\ D_3 \end{Bmatrix}. \tag{5.26}$$

This still partially inverted macroscopic constitutive relation may be reverted correspondingly to the original form of the normal mode constitutive relations:

$$e_3\colon \begin{Bmatrix} \sigma_1 \\ \sigma_2 \\ \sigma_3 \\ D_3 \end{Bmatrix} = \bar{\mathbb{C}}_3^n \begin{Bmatrix} \varepsilon_1 \\ \varepsilon_2 \\ \varepsilon_3 \\ \bar{E}_3 \end{Bmatrix}, \quad \text{with} \tag{5.27a}$$

$$\bar{\mathbb{C}}_3^n = \begin{bmatrix} C_{11}^{\boldsymbol{f}} + \frac{(e_{31}^f)^2}{\epsilon_{33}^m} \frac{c_3}{1+c_3 \frac{\epsilon_{33}^f}{\epsilon_{33}^m}} & C_{12}^{\boldsymbol{f}} + \frac{e_{31}^f e_{32}^f}{\epsilon_{33}^m} \frac{c_3}{1+c_3 \frac{\epsilon_{33}^f}{\epsilon_{33}^m}} & C_{13}^{\boldsymbol{f}} + \frac{e_{31}^f e_{33}^f}{\epsilon_{33}^m} \frac{c_3}{1+c_3 \frac{\epsilon_{33}^f}{\epsilon_{33}^m}} & \frac{e_{31}^f}{1+c_3 \frac{\epsilon_{33}^f}{\epsilon_{33}^m}} \\ C_{12}^{\boldsymbol{f}} + \frac{e_{31}^f e_{32}^f}{\epsilon_{33}^m} \frac{c_3}{1+c_3 \frac{\epsilon_{33}^f}{\epsilon_{33}^m}} & C_{22}^{\boldsymbol{f}} + \frac{(e_{32}^f)^2}{\epsilon_{33}^m} \frac{c_3}{1+c_3 \frac{\epsilon_{33}^f}{\epsilon_{33}^m}} & C_{23}^{\boldsymbol{f}} + \frac{e_{32}^f e_{33}^f}{\epsilon_{33}^m} \frac{c_3}{1+c_3 \frac{\epsilon_{33}^f}{\epsilon_{33}^m}} & \frac{e_{32}^f}{1+c_3 \frac{\epsilon_{33}^f}{\epsilon_{33}^m}} \\ C_{13}^{\boldsymbol{f}} + \frac{e_{31}^f e_{33}^f}{\epsilon_{33}^m} \frac{c_3}{1+c_3 \frac{\epsilon_{33}^f}{\epsilon_{33}^m}} & C_{23}^{\boldsymbol{f}} + \frac{e_{32}^f e_{33}^f}{\epsilon_{33}^m} \frac{c_3}{1+c_3 \frac{\epsilon_{33}^f}{\epsilon_{33}^m}} & C_{33}^{\boldsymbol{f}} + \frac{(e_{33}^f)^2}{\epsilon_{33}^m} \frac{c_3}{1+c_3 \frac{\epsilon_{33}^f}{\epsilon_{33}^m}} & \frac{e_{33}^f}{1+c_3 \frac{\epsilon_{33}^f}{\epsilon_{33}^m}} \\ \frac{e_{31}^f}{1+c_3 \frac{\epsilon_{33}^f}{\epsilon_{33}^m}} & \frac{e_{32}^f}{1+c_3 \frac{\epsilon_{33}^f}{\epsilon_{33}^m}} & \frac{e_{33}^f}{1+c_3 \frac{\epsilon_{33}^f}{\epsilon_{33}^m}} & -\frac{\epsilon_{33}^f}{1+c_3 \frac{\epsilon_{33}^f}{\epsilon_{33}^m}} \end{bmatrix}. \tag{5.27b}$$

Unlike the procedure laid out above, which introduces the factor c_3, in the publications of *Bent and Hagood* [14,15] and *Bent* [13], the fraction ν_3 is set to one only for the mechanical fields, while it is retained for the electrostatic fields. The resulting constitutive matrix of Eq. (5.27b) therefore becomes non-symmetric with respect to the piezoelectric coupling coefficients. Since the undermost line of the normal mode constitutive relation is not used there any further, this has no consequences.

Discussion of the Stacking Coefficients

As intended, the geometric factor c_3 gives rise to the consideration of the dielectric properties of the matrix material. The resulting piezoelectric and dielectric properties are extended in the denominator by the product of the factor c_3 with the ratio of dielectric permittivities of fiber and matrix material $\epsilon_{33}^f/\epsilon_{33}^m$. In comparison to the pure fiber material, these properties therefore are decreased by a thick matrix layer between fibers and electrodes according to the approximation of Eq. (5.24) and by a high dielectric mismatch, which is significant for the typical materials listed in Tables A.2 and A.3. In both cases, the insulation of the fibers from the electrodes is increased and results in a reduction of effectivity of the piezoelectric coupling. The mechanical properties, as they result from the stacking in fiber direction, consist of the stiffness coefficients of the fiber material complemented by an additional term, which represents the strengthening due to the piezoelectric effect and again contains the discussed influence factors.

5.4.6 Stacking Sequences for Non-Homogeneous Electrostatic Fields

Succeeding to the above analysis, the question for the sequence of substitutions arises again in consideration of two appropriate possibilities. In accordance with Remark 5.6, either the results of the stacking in the transverse directions, Section 5.4.4, are utilized to represent the fiber phase for the stacking in the fiber direction, Section 5.4.5, or the other way round. These possibilities are illustrated in Figures 5.10(a) and (b), respectively, and may be written symbolically as

$$\left\langle \begin{matrix} 1 \Rightarrow 2 \\ 2 \Rightarrow 1 \end{matrix} \right\rangle \Rightarrow 3 \quad \text{and} \quad 3 \Rightarrow \left\langle \begin{matrix} 1 \Rightarrow 2 \\ 2 \Rightarrow 1 \end{matrix} \right\rangle .$$

The discussion with regard to the stacking in the fiber direction was bound for the loss in efficiency of the piezoelectric coupling inherent only to the fiber material. Therefore, it may be concluded to begin the substitution sequence with the e_3-direction, as the matrix material otherwise would exert additional influence by means of its share in the preceding stacking cases. Such considerations, however, depend on the definition of the factor c_3, which needs to be refined requiring detailed experimental studies and finite element simulations with non-homogeneous polarization. Figure 5.11 exemplarily illustrates the influence of the substitution sequence by means of the essential piezoelectric

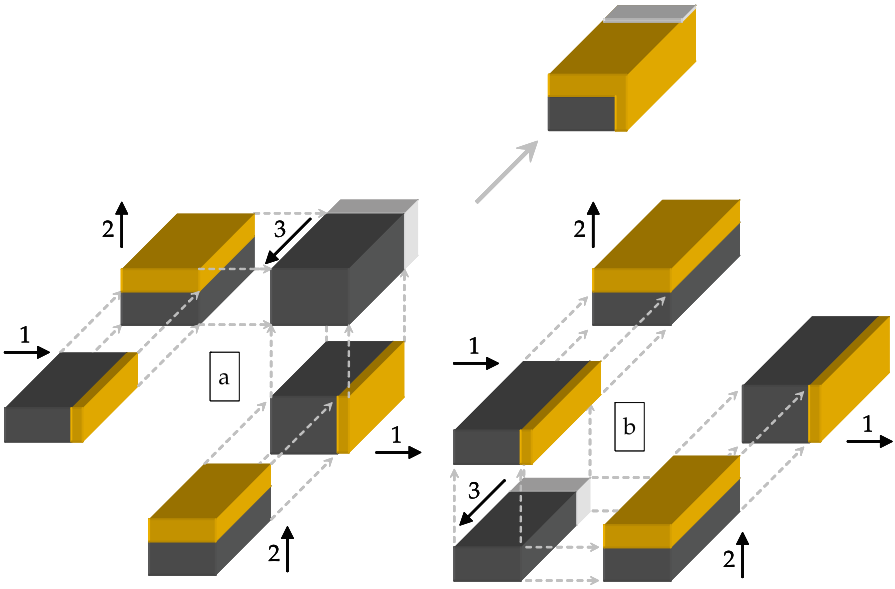

Fig. 5.10. Over-all substitution sequences for the stacking of material phases.

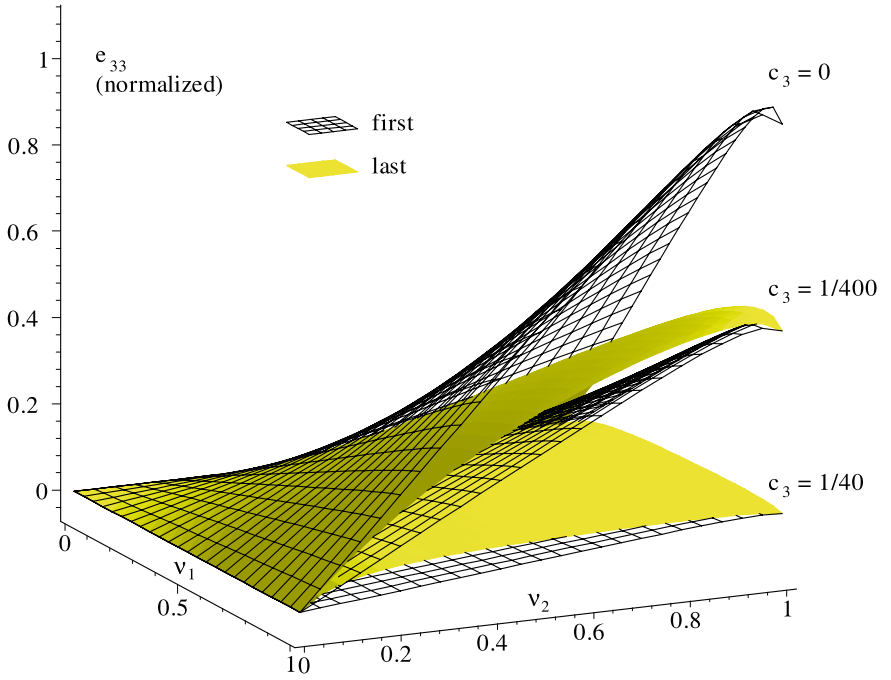

Fig. 5.11. Variation of the piezoelectric coupling coefficient e_{33} with the directional fiber fractions ν_1 and ν_2. The values are normalized with respect to the bulk piezoelectric material and homogeneous electrostatic fields. Both substitution sequences are shown for different factors c_3; the results are identical for the homogeneous conditions of $c_3 = 0$.

coupling in the fiber direction. When the coefficients of the stacking in the fiber direction are substituted first, the results have the same character as in the case of undisturbed electrostatic fields present for a factor $c_3 = 0$. When they are substituted last, distinct deviations are visible which decay with a decreasing factor c_3. Further on, the ability of piezoelectric fiber composites to improve the piezoelectric coupling over the monolithic case of $\nu_1, \nu_2 = 1$ may be observed. Finally, it shall be noted that in principle it is also possible to combine the stacking in the fiber direction to approximate the influence of non-homogeneous electrostatic fields with any other methodology lacking such a capability.

5.5 Validation of the Micro-Electromechanics

In this section, the previously derived micro-electromechanical methodologies will be validated from the results of experiments as well as finite element models. Such examinations are reported in the literature with adequate topology

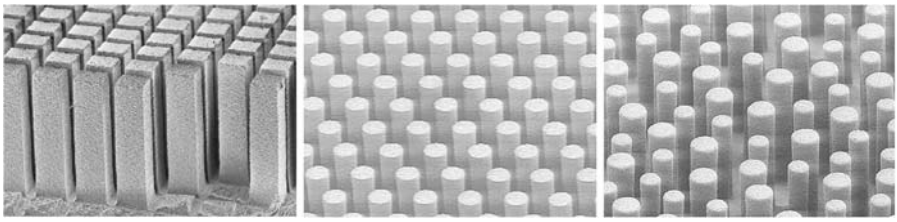

Fig. 5.12. Variants of fiber shapes and arrangements for 1–3 composites before insertation of matrix material; original photographs by the *Fraunhofer Institute for Ceramic Technologies and Systems*.

and necessary completeness only for the class of 1–3 composites, see Figure 5.12. Dating back to the connectivity terminology of *Newnham et al.* [133], this identifies composites where the piezoelectric inclusion phase is connected to itself in one direction and thus consists of continuous fibers and the matrix phase fills the remaining volume, being self-connected in all three spatial directions. Unlike piezoelectric fiber composites for structural applications, the usual 1–3 composites have fibers oriented in the thickness direction of specimens predominantly applied as ultrasonic transducers. With such a set-up, it is not necessary to employ interdigitated electrodes, but the desired electrostatic fields in the fiber direction can be accessed with areal electrodes. Further on, the arrangement of fibers in their cross-sectional plane is uniform, implying equal directional fiber fractions $\nu_1 = \nu_2$. With the subsequent comparison, it will, therefore, neither be possible to address the issues of nonhomogeneous electrostatic fields nor of arbitrary aspect ratios. Nevertheless, a fundamental validation of the Mori–Tanaka method, Section 5.3.4, relying on the constraint tensor for fibrous composites given by *Dunn and Taya* [67], as well as of the sequential stacking procedure with combined substitution sequence, Section 5.4.4, may be demonstrated.

5.5.1 Experiments and Finite Element Models

In the work of *Chan and Unsworth* [49], discs with a diameter of 14 mm and a thickness of 1.2 mm, made of Araldit D matrix and PZT 7A fibers with a square shape as well as arrangement and varying fiber volume fractions, are examined. The respective material properties are given in Tables A.2 and A.3 as provided by the manufacturer. Measurements of the bulk material properties conducted by *Chan and Unsworth* [49] have shown large variations from batch to batch and in the case of the induced strain piezoelectric coupling coefficient d_{33} led to an adjustment to $d_{33} = 167 \times 10^{-12}$ m/V. This has also been adopted by *Poizat and Sester* [143] for their finite element model of the described set-up as well as for the associated current modeling efforts. In the work of *Steinhausen* [169], 1–3 composites made of Araldit 2020 matrix and PIC 151 fibers, Tables A.2 and A.3, with varying fiber volume fraction are

examined. For this purpose, fibers with a square shape in a square arrangement, with a cylindrical shape in a hexagonal arrangement, as well as with a cylindrical shape in a statistical distribution, have been manufactured, see Figure 5.12. Unless otherwise indicated, these geometry variants do not show significant effects and will not be distinguished in the following. *Steinhausen* [169] also conducted finite element simulations, which are in good agreement with the analytical models and will be reproduced here only in uncertain cases.

5.5.2 Dielectric, Piezoelectric, and Mechanical Properties

As mentioned above, the correlation between specified and measured bulk material properties is problematic and further implications will become obvious in the subsequent detailed comparison between experiments and theory. Within the bounds of such variations and of the measurement accuracy, both representatives of the different micro-electromechanical modeling methodologies can be successfully validated.

Dielectric Properties

The dielectric permittivity ϵ_{33}^{σ} in the fiber and polarization direction exhibits a largely linear dependence on the fiber volume fraction ν. In Figures 5.13 and 5.14, the Mori–Tanaka method and the sequential stacking procedure deliver identical results, which agree well with the experimental findings. In the second of these figures, slight deviations of the slope may indicate that the material data of the constituents is not entirely precise. For the fiber material, this impression is supported by measured value for $\nu = 1$ being smaller

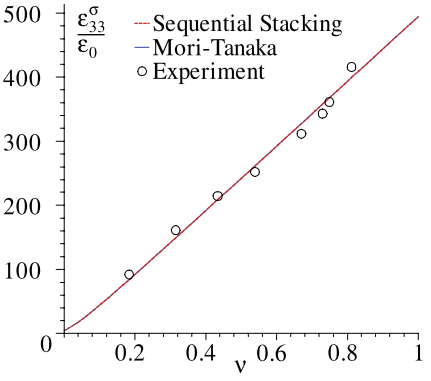

Fig. 5.13. Variation of the relative dielectric permittivity $\epsilon_{33}^{\sigma}/\epsilon_0$ with the fiber volume fraction ν; experimental results from *Chan and Unsworth* [49].

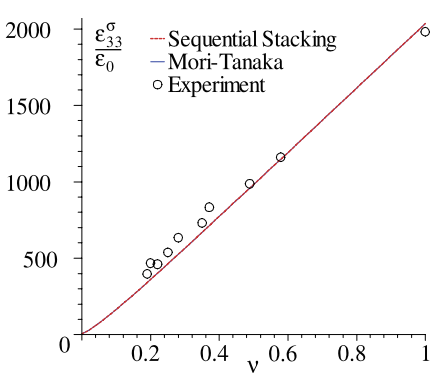

Fig. 5.14. Variation of the relative dielectric permittivity $\epsilon_{33}^{\sigma}/\epsilon_0$ with the fiber volume fraction ν; experimental results from *Steinhausen* [169].

than the presumed value at the end of the plot of the modeling results. Correspondingly, the lower fiber volume fractions point towards a higher dielectric permittivity of the matrix material.

Piezoelectric Properties

Also for the induced strain piezoelectric coupling coefficient d_{33} in the fiber and polarization direction, the modeling results cannot be distinguished and, as depicted in Figures 5.15 and 5.16, agree well with the experimental results. While there are some deviations of the experimental data points in the first of these graphs, the finite element results agree almost perfectly with the analytical modeling results. In the second of these graphs, again just a small deviation between the fiber properties according to the manufacturer and the measurement needs to be noted. Experimental investigations of the induced strain piezoelectric coupling coefficient d_{31} have been conducted by *Steinhausen* [169]. It is reported that the obvious deviations visible in Figure 5.17 are due to surface effects occurring in the experiment, which are not considered in the analytical modelling approaches. Unlike the previously examined properties, the coefficient d_{31} is sensitive to the stacking sequence in the fiber cross-sectional plane, and the conformity of the combination of substitution sequences with Mori–Tanaka as well as the finite element results supports the argumentation of Section 5.4.4.

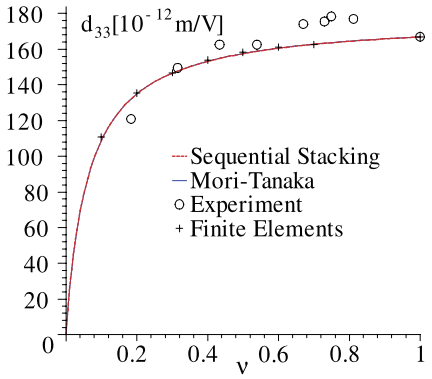

Fig. 5.15. Variation of the induced strain piezoelectric coupling coefficient d_{33} with the fiber volume fraction ν; experimental results from *Chan and Unsworth* [49] and finite element results from *Poizat and Sester* [143].

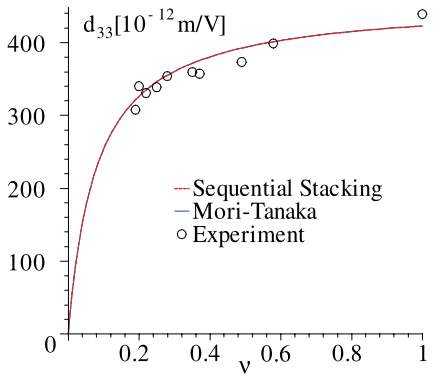

Fig. 5.16. Variation of the induced strain piezoelectric coupling coefficient d_{33} with the fiber volume fraction ν; experimental results from *Steinhausen* [169].

Mechanical Properties

The finite element analysis of *Steinhausen* [169] has identified the compliance coefficient S_{11} transverse to the fiber direction as the only one susceptible to shape and arrangement of fibers. This has been confirmed vaguely by the experiments, but in Figure 5.18 only the results for the square shape and arrangement of fibers are given. Still the slightly higher compliance values for cylindrical fibers in a hexagonal arrangement might explain the difference

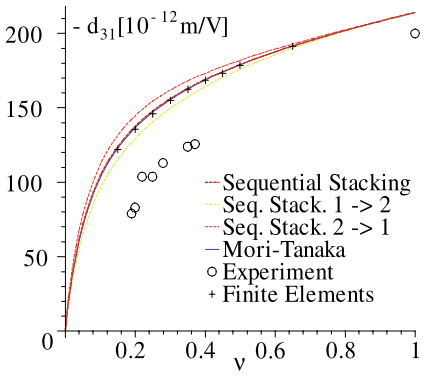

Fig. 5.17. Variation of the induced strain piezoelectric coupling coefficient d_{31} with the fiber volume fraction ν; experimental and finite element results from *Steinhausen* [169].

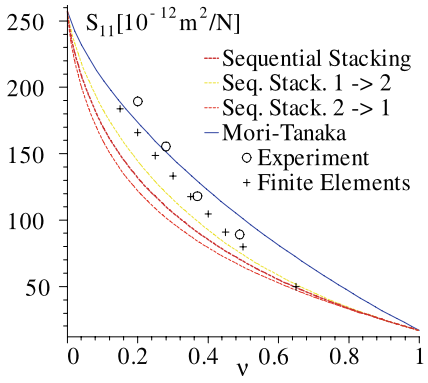

Fig. 5.18. Variation of the compliance coefficient S_{11} with the fiber volume fraction ν; experimental and finite element results from *Steinhausen* [169].

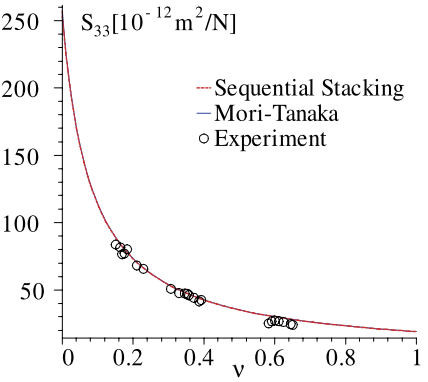

Fig. 5.19. Variation of the compliance coefficient S_{33} with the fiber volume fraction ν; experimental results from *Steinhausen* [169].

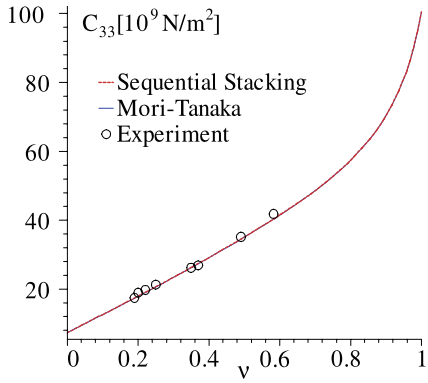

Fig. 5.20. Variation of the stiffness coefficient C_{33} with the fiber volume fraction ν; experimental results from *Steinhausen* [169].

between the Mori–Tanaka method and sequential stacking procedure as the prior emanates from round fibers and the latter from rectangular fibers. Altogether, the accord is less pleasing for this coefficient. Due to requirements of the measurement technique, *Steinhausen* [169] used different piezoelectric fibers with inaccurate material data for the determination of the compliance coefficient S_{33} in the fiber direction. Therefore, these experiments are compared in Figure 5.19 with the analytical models using the original constituent properties outlined above and yet a good correlation of results is found. Again, the Mori–Tanaka method and sequential stacking procedure lead to indistinguishable results. This also holds for the stiffness coefficient C_{33} in the fiber direction displayed in Figure 5.20.

6

Adaptive Laminated Composite Shells

In this chapter, the transition from voluminous to areal structures, as already prepared in Section 4.4, will be implemented with special regard to laminated composites and adaptive capabilities making use of the piezoelectric effect for actuation as well as sensing. Therefore, a comprehensive constitutive description is developed and appropriate kinematic relations are specified. Afterwards, possibilities of different complexity for the reduction to a less general description are considered in view of specialized application cases.

6.1 Macro-Electromechanics

The examination of the micro-electromechanics in the previous chapter aimed at the homogenized representation of fiber composites with substantial extension in all three dimensions. Within the macro-electromechanics to be considered now, the homogenized representation of laminated composites with a substantial extension only in two dimensions is sought. The graduation in terminology alludes to the course of modeling. So laminated fiber composites first pass through the analysis on the micro scale, Section 5.3 or 5.4, and after constitutive reduction, Section 4.4, they enter the analysis on the macro scale.

6.1.1 Lamination Theory

The classical lamination theory, as described by *Jones* [107] or *Whitney* [178] for conventional laminates, may be extended to model the assembly of layers or (synonymous) laminae of materials with piezoelectric properties. Here the following will be assumed:

Remark 6.1. The laminate is composed of laminae which are perfectly connected by infinitesimally thin and shear resistant bonds.

T.H. Brockmann, *Theory of Adaptive Fiber Composites*,
Solid Mechanics and Its Applications 161,

Further on, for sufficiently thin laminates, the following kinematic assumption shall be applicable, usually being denoted as the Kirchhoff–Love hypothesis in shell theory:

Remark 6.2. Normal strain and shear strains transverse to the laminate are presumed to be negligible small.

Regarding a straight line connecting two opposed points on the laminate's faces, this assumption implies that under deformation this line conserves its length and remains straight as well as perpendicular to the laminate's middle surface. Such deformations can be expressed by the remaining strains as

$$\begin{Bmatrix} \varepsilon_x \\ \varepsilon_s \\ \gamma_{xs} \\ \bar{E}_3 \end{Bmatrix} = \underbrace{\begin{Bmatrix} \varepsilon_x^0 \\ \varepsilon_s^0 \\ \gamma_{xs}^0 \\ \bar{E}_3^0 \end{Bmatrix}}_{\boldsymbol{\varepsilon}^0} + n \underbrace{\begin{Bmatrix} \kappa_x \\ \kappa_s \\ \psi_{xs} \\ \bar{F}_3 \end{Bmatrix}}_{\boldsymbol{\kappa}}. \tag{6.1}$$

Initially, the implications of the above assumption will also be adopted to describe the negated electric field strength $\bar{E}_3$. Thus, strains as well as electric field strength are confined to a linear variation through the laminate thickness with a constant portion $\boldsymbol{\varepsilon}^0$ associated with the middle surface of the laminate and a linear portion $n\boldsymbol{\kappa}$. The through thickness coordinate n has its origin at the middle surface and the gradient is represented by $\boldsymbol{\kappa}$. In the case of the strains, the latter corresponds to the curvatures of the middle surface. With such a collective description of strains and electric field strength across the layers of the laminate and the individual laminae properties $\bar{\mathbb{Q}}_k$, the stresses and electric flux density of every layer k may be determined as

$$\begin{Bmatrix} \sigma_x \\ \sigma_s \\ \tau_{xs} \\ D_3 \end{Bmatrix}_k = \bar{\mathbb{Q}}_k \begin{Bmatrix} \varepsilon_x \\ \varepsilon_s \\ \gamma_{xs} \\ \bar{E}_3 \end{Bmatrix}. \tag{6.2}$$

This equation stems from the general constitutive relation of a thin arbitrarily oriented lamina given by Eq. (4.31). Stresses and electric flux density of the individual laminae may be summarized in in-plane resultants $\boldsymbol{N}$ and out-of-plane resultants $\boldsymbol{M}$ by integration over the laminate thickness, in the latter case, in consideration of the distance to the middle surface:

$$\boldsymbol{N} = \begin{Bmatrix} N_x \\ N_s \\ N_{xs} \\ G_3 \end{Bmatrix} = \int_{-N/2}^{N/2} \begin{Bmatrix} \sigma_x \\ \sigma_s \\ \tau_{xs} \\ D_3 \end{Bmatrix}_k \mathrm{d}n = \sum_{k=1}^{K} \int_{n_{k-1}}^{n_k} \begin{Bmatrix} \sigma_x \\ \sigma_s \\ \tau_{xs} \\ D_3 \end{Bmatrix}_k \mathrm{d}n, \tag{6.3a}$$

$$\boldsymbol{M} = \begin{Bmatrix} M_x \\ M_s \\ M_{xs} \\ H_3 \end{Bmatrix} = \int_{-N/2}^{N/2} n \begin{Bmatrix} \sigma_x \\ \sigma_s \\ \tau_{xs} \\ D_3 \end{Bmatrix}_k \mathrm{d}n = \sum_{k=1}^{K} \int_{n_{k-1}}^{n_k} n \begin{Bmatrix} \sigma_x \\ \sigma_s \\ \tau_{xs} \\ D_3 \end{Bmatrix}_k \mathrm{d}n. \tag{6.3b}$$

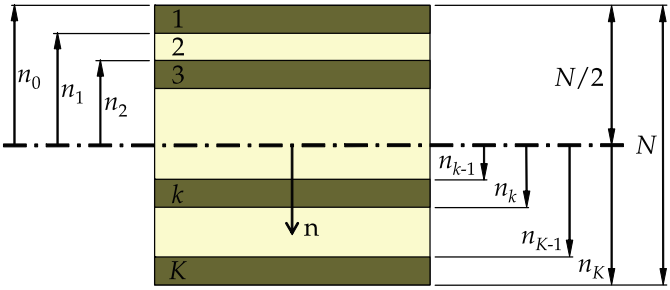

Fig. 6.1. Geometry of a laminate with K layers.

The integration over the total laminate thickness N may be replaced by the sum of integrals over the thicknesses $n_k - n_{k-1}$ of each of the altogether K laminae. The geometry of such a laminate is illustrated in Figure 6.1. The stresses and electric flux density in Eqs. (6.3) may be substituted with the aid of the laminae constitutive relation of Eq. (6.2), and the collective description of strains and electric field strength with respect to the middle surface may be introduced by Eq. (6.1). As the latter do not depend on the through thickness coordinate n, they can be removed from under the integration and summation sign for the following formulation:

$$\begin{Bmatrix} \boldsymbol{N} \\ \boldsymbol{M} \end{Bmatrix} = \begin{bmatrix} \mathbb{A} & \mathbb{B} \\ \mathbb{B} & \mathbb{D} \end{bmatrix} \begin{Bmatrix} \boldsymbol{\varepsilon}^0 \\ \boldsymbol{\kappa} \end{Bmatrix}, \tag{6.4a}$$

$$\mathbb{A} = \sum_{k=1}^{K} \bar{\mathbb{Q}}_k \left(n_k - n_{k-1}\right), \quad \mathbb{B} = \sum_{k=1}^{K} \bar{\mathbb{Q}}_k \frac{n_k^2 - n_{k-1}^2}{2}, \quad \mathbb{D} = \sum_{k=1}^{K} \bar{\mathbb{Q}}_k \frac{n_k^3 - n_{k-1}^3}{3}. \tag{6.4b}$$

6.1.2 Laminates with Groups of Electrically Paralleled Laminae

The above representation is identical to classical lamination theory just that the matrix dimensions are extended by virtue of the included electrostatic fields. But the so-far utilized analogous assumptions for the latter need to be thought over, as the effect of the electrodes on the electrostatic field distribution within the individual layer and the parallel connection of electrode pairs of several layers is not yet considered.

Remark 6.3. The electric field strength is assumed to be constant across the thickness of the individual laminae and to be identical in all laminae with paralleled electrode pairs with respect to absolute values.

While a linear through thickness variation of mechanical strains is considered, the electroding by groups of piezoelectric layers results in a piecewise

constant distribution of the in-plane electric field strength. Thus, on the one hand the electric field strength gradient F_3 introduced in Eq. (6.1) is discarded and therefore also the resultant H_3 of Eq. (6.3b) is not required anymore, while on the other hand, the electrostatic fields of electrically connected laminae have to be treated separately for every group. Corresponding to Eqs. (6.1) and (6.2), the stresses and electric flux density of layer k belonging to group g may be expressed in accordance with the above assumption. With the relative sign p_k of the electric field strength governed by the electrode connection within the group, this yields

$$\begin{Bmatrix} \sigma_x \\ \sigma_s \\ \tau_{xs} \\ D_3^g \end{Bmatrix}_k = \bar{\mathbb{Q}}_k \begin{bmatrix} 1 & 0 & 0 & 0 \\ 0 & 1 & 0 & 0 \\ 0 & 0 & 1 & 0 \\ 0 & 0 & 0 & p_k \end{bmatrix} \left\{ \begin{Bmatrix} \varepsilon_x^0 \\ \varepsilon_s^0 \\ \gamma_{xs}^0 \\ \bar{E}_3^g \end{Bmatrix} + n \begin{Bmatrix} \kappa_x \\ \kappa_s \\ \psi_{xs} \\ 0 \end{Bmatrix} \right\} \quad \text{with } p_k \in \{1, -1\}\,. \tag{6.5}$$

When the laminate resultants are formed by through thickness integration as in Eqs. (6.3), then the electrostatic fields of every group with connected electrodes have to be considered separately. Thus, individual rows and columns are introduced in the coefficient matrix of the laminate constitutive relation. Explicitly written out for two groups denoted by the letters c and d, the constitutive relation may be formulated as

$$\underbrace{\begin{Bmatrix} N_x \\ N_s \\ N_{xs} \\ \overline{M}_x \\ M_s \\ M_{xs} \\ \overline{G}_3^c \\ G_3^d \\ \vdots \end{Bmatrix}}_{\boldsymbol{L}} = \underbrace{\begin{bmatrix} \ulcorner & & \urcorner & \ulcorner & & \urcorner & \ulcorner & \urcorner & \ulcorner & \urcorner & \\ & \mathtt{A}_{1..3,1..3} & & & \mathtt{B}_{1..3,1..3} & & \mathtt{A}^c_{1..3,4} & \mathtt{A}^d_{1..3,4} & \cdots \\ \llcorner & & \lrcorner & \llcorner & & \lrcorner & \llcorner & \lrcorner & \llcorner & \lrcorner & \\ \ulcorner & & \urcorner & \ulcorner & & \urcorner & \ulcorner & \urcorner & \ulcorner & \urcorner & \\ & \mathtt{B}_{1..3,1..3} & & & \mathtt{D}_{1..3,1..3} & & \mathtt{B}^c_{1..3,4} & \mathtt{B}^d_{1..3,4} & \cdots \\ \llcorner & & \lrcorner & \llcorner & & \lrcorner & \llcorner & \lrcorner & \llcorner & \lrcorner & \\ \ulcorner & & \urcorner T & \ulcorner & & \urcorner T & \llcorner & \lrcorner & & & \\ \llcorner & \mathtt{A}^c_{1..3,4} & \lrcorner & \llcorner & \mathtt{B}^c_{1..3,4} & \lrcorner & \mathtt{A}^c_{44} & 0 & & & \\ \ulcorner & & \urcorner T & \ulcorner & & \urcorner T & & & & & \\ \llcorner & \mathtt{A}^d_{1..3,4} & \lrcorner & \llcorner & \mathtt{B}^d_{1..3,4} & \lrcorner & 0 & \mathtt{A}^d_{44} & & & \\ & \vdots & & & \vdots & & & & \ddots & & \end{bmatrix}}_{\mathbb{K}} \underbrace{\begin{Bmatrix} \varepsilon_x^0 \\ \varepsilon_s^0 \\ \gamma_{xs}^0 \\ \overline{\kappa}_x \\ \kappa_s \\ \psi_{xs} \\ \overline{\bar{E}}_3^c \\ \bar{E}_3^d \\ \vdots \end{Bmatrix}}_{\chi}. \tag{6.6}$$

The mechanical stiffness coefficients, which are unchanged in comparison to the classical lamination theory, have been arranged just as they appear in the latter. They may be determined in accordance with Eqs. (6.4b). As the remaining coefficients are involved with the negated electric field strengths $\bar{E}_3^g$ and appertaining resultants G_3^g of the electric flux density, they have to be established in consideration of the group association represented by the

functions f_k^g:

$$\begin{aligned} \mathtt{A}^g_{1..4,4} &= \sum_{k=1}^{K} f_k^g p_k \left(\bar{\mathtt{Q}}_{1..4,4}\right)_k \left(n_k - n_{k-1}\right), \\ \mathtt{B}^g_{1..3,4} &= \sum_{k=1}^{K} f_k^g p_k \left(\bar{\mathtt{Q}}_{1..3,4}\right)_k \frac{n_k^2 - n_{k-1}^2}{2}, \quad \text{with } f_k^g = \begin{cases} 1, & k \in g, \\ 0, & k \notin g. \end{cases} \end{aligned} \tag{6.7}$$

As there is no electrical connection between the considered groups, the respective coupling coefficients in the constitutive relation, given by Eq. (6.6), have to be zero. This includes the presumption that the electrodes of a piezoelectric layer in general have no influence on other piezoelectric layers, which has to be guaranteed by the stacking sequence or additional measures. The common theories provide no instruments to collate the electrostatic fields and do without resultants of the electric flux density, see *Crawley and Lazarus* [58], *Leibowitz and Vinson* [121], or *Bent et al.* [17]. Thus the resulting constitutive description is not compatible to the general form of the energy principles, compare with Eq. (3.63).

6.2 Kinematics and Equilibrium

The strain measures of the laminate have been introduced without specification of their relation to the displacements field. As the strain measures have been established with respect to the middle surface of the laminate, it will also be the reference for the displacements field.

6.2.1 General Thin Shell Kinematics

To be able to represent arbitrary shapes, the orthogonal curvilinear coordinates s_1 and s_2 on the middle surface are introduced together with the associated Lamé parameters $\mathfrak{A}_1$ and $\mathfrak{A}_2$, see for example *Dym* [69] or *Novozhilov* [134]. The undeformed middle surface is characterized by the respective principal radii R_1 and R_2 in agreement with the following condition:

Remark 6.4. Besides being thin with regard to the overall dimensions, the considered shell-like structure is presumed to have a thickness substantially smaller than its smallest radius of curvature.

A variety of theories for thin shells are available. For the anticipated applications, it is reasonable to confine the examination to linear theories:

Remark 6.5. The occurring displacements shall be small.

The well-known and generally accepted thin shell theory of *Sanders* [158] and *Koiter* [114] eliminated the deficiency of the preceding developments of

non-vanishing strains for small rigid-body motions. The kinematic relations obtained by these authors will be adapted here. The deformation of the structure are described by the displacements $\mathfrak{u}$, $\mathfrak{v}$ tangential to the middle surface along the directions of coordinates s_1, s_2 and the displacement $\mathfrak{w}$ normal to the middle surface. Therewith, the extensional strains ε_1^0, ε_2^0 and shear strain γ_{12}^0 of the middle surface are given by

$$\varepsilon_1^0 = \frac{1}{\mathfrak{A}_1}\frac{\partial \mathfrak{u}}{\partial s_1} + \frac{1}{\mathfrak{A}_1\mathfrak{A}_2}\frac{\partial \mathfrak{A}_1}{\partial s_2}\mathfrak{v} + \frac{\mathfrak{w}}{R_1}, \qquad \varepsilon_2^0 = \frac{1}{\mathfrak{A}_2}\frac{\partial \mathfrak{v}}{\partial s_2} + \frac{1}{\mathfrak{A}_1\mathfrak{A}_2}\frac{\partial \mathfrak{A}_2}{\partial s_1}\mathfrak{u} + \frac{\mathfrak{w}}{R_2}, \tag{6.8a}$$

$$\gamma_{12}^0 = \frac{1}{\mathfrak{A}_1\mathfrak{A}_2}\left(\mathfrak{A}_2\frac{\partial \mathfrak{v}}{\partial s_1} + \mathfrak{A}_1\frac{\partial \mathfrak{u}}{\partial s_2} - \frac{\partial \mathfrak{A}_1}{\partial s_2}\mathfrak{u} - \frac{\partial \mathfrak{A}_2}{\partial s_1}\mathfrak{v}\right). \tag{6.8b}$$

The bending curvatures κ_1, κ_2 and the twisting curvature ψ_{12} of the middle surface are given with respect to the rotations ϑ_1 and ϑ_2 by

$$\kappa_1 = \frac{1}{\mathfrak{A}_1}\frac{\partial \vartheta_1}{\partial s_1} + \frac{1}{\mathfrak{A}_1\mathfrak{A}_2}\frac{\partial \mathfrak{A}_1}{\partial s_2}\vartheta_2, \qquad \kappa_2 = \frac{1}{\mathfrak{A}_2}\frac{\partial \vartheta_2}{\partial s_2} + \frac{1}{\mathfrak{A}_1\mathfrak{A}_2}\frac{\partial \mathfrak{A}_2}{\partial s_1}\vartheta_1, \tag{6.9a}$$

$$\psi_{12} = \frac{1}{\mathfrak{A}_1\mathfrak{A}_2}\begin{pmatrix}\mathfrak{A}_2\frac{\partial \vartheta_2}{\partial s_1} + \mathfrak{A}_1\frac{\partial \vartheta_1}{\partial s_2} - \frac{\partial \mathfrak{A}_1}{\partial s_2}\vartheta_1 - \frac{\partial \mathfrak{A}_2}{\partial s_1}\vartheta_2 \\ + \frac{1}{2}\left(\frac{1}{R_2} - \frac{1}{R_1}\right)\left(\frac{\partial \mathfrak{A}_2\mathfrak{v}}{\partial s_1} - \frac{\partial \mathfrak{A}_1\mathfrak{u}}{\partial s_2}\right)\end{pmatrix}. \tag{6.9b}$$

As the shear strains γ_1^0 and γ_2^0, transverse to the middle surface, are negligible by virtue of the assumptions formulated in Remark 6.2, the rotations appearing above may be expressed by the displacements as follows:

$$\gamma_1^0 = \frac{1}{\mathfrak{A}_1}\frac{\partial \mathfrak{w}}{\partial s_1} - \frac{\mathfrak{u}}{R_1} + \vartheta_1, \qquad \gamma_2^0 = \frac{1}{\mathfrak{A}_2}\frac{\partial \mathfrak{w}}{\partial s_2} - \frac{\mathfrak{v}}{R_2} + \vartheta_2; \tag{6.10a}$$

$$\gamma_1^0 = 0 \quad \rightarrow \quad \vartheta_1 = \frac{\mathfrak{u}}{R_1} - \frac{1}{\mathfrak{A}_1}\frac{\partial \mathfrak{w}}{\partial s_1}, \qquad \gamma_2^0 = 0 \quad \rightarrow \quad \vartheta_2 = \frac{\mathfrak{v}}{R_2} - \frac{1}{\mathfrak{A}_2}\frac{\partial \mathfrak{w}}{\partial s_2}. \tag{6.10b}$$

6.2.2 Cylindrical Thin Shell Kinematics

Cylindrical shells in undeformed configuration are only curved along one of the coordinate directions, see Figure 6.2, and frequently appear in technical applications.

Remark 6.6. The considered shells are presumed to be cylindrical.

Due to the less complicated geometry, the representation of the kinematic relations may be simplified with the following substitutions:

$$R_1 \rightarrow \infty, \qquad R_2 = R, \tag{6.11a}$$

$$s_1 = x, \qquad s_2 = s, \qquad \mathfrak{A}_1 = \mathfrak{A}_2 = 1. \tag{6.11b}$$

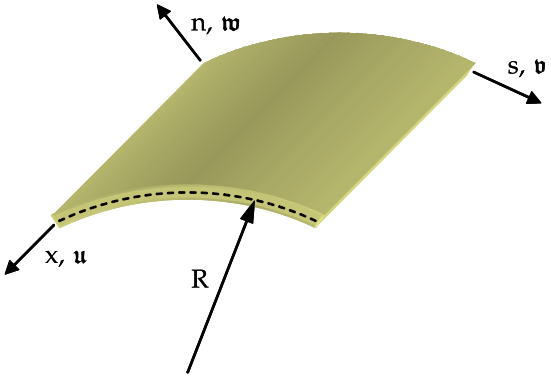

Fig. 6.2. Orientation of coordinates and displacements for a cylindrical thin shell.

Accordingly, the strain measures as well as rotations have to be renamed. Then the introduction of Eqs. (6.11) into Eqs. (6.8) and (6.9) yields:

$$\varepsilon_x^0 = \frac{\partial \mathfrak{u}}{\partial x}, \qquad \varepsilon_s^0 = \frac{\partial \mathfrak{v}}{\partial s} + \frac{\mathfrak{w}}{R}, \qquad \gamma_{xs}^0 = \frac{\partial \mathfrak{v}}{\partial x} + \frac{\partial \mathfrak{u}}{\partial s}, \tag{6.12}$$

$$\kappa_x = \frac{\partial \vartheta_x}{\partial x}, \qquad \kappa_s = \frac{\partial \vartheta_s}{\partial s}, \qquad \psi_{xs} = \frac{\partial \vartheta_s}{\partial x} + \frac{\partial \vartheta_x}{\partial s} + \underline{\frac{1}{2R}\left(\frac{\partial \mathfrak{v}}{\partial x} - \frac{\partial \mathfrak{u}}{\partial s}\right)}. \tag{6.13}$$

Similarly the rotations of Eqs. (6.10a) and, consequently, (6.10) reduce to

$$\gamma_x^0 = \frac{\partial \mathfrak{w}}{\partial x} + \vartheta_x, \qquad \gamma_s^0 = \frac{\partial \mathfrak{w}}{\partial s} - \underline{\frac{\mathfrak{v}}{R}} + \vartheta_s, \tag{6.14a}$$

$$\gamma_x^0 = 0 \quad \rightarrow \quad \vartheta_x = -\frac{\partial \mathfrak{w}}{\partial x}, \qquad \gamma_s^0 = 0 \quad \rightarrow \quad \vartheta_s = \underline{\frac{\mathfrak{v}}{R}} - \frac{\partial \mathfrak{w}}{\partial s}. \tag{6.14b}$$

and so they can be eliminated from Eqs. (6.13) resulting in

$$\kappa_x = -\frac{\partial^2 \mathfrak{w}}{\partial x^2}, \qquad \kappa_s = -\frac{\partial^2 \mathfrak{w}}{\partial s^2} + \underline{\frac{\partial}{\partial s}\left(\frac{\mathfrak{v}}{R}\right)}, \tag{6.15a}$$

$$\psi_{xs} = -2\frac{\partial^2 \mathfrak{w}}{\partial x \partial s} + \underline{\frac{\partial}{\partial x}\left(\frac{\mathfrak{v}}{R}\right) + \frac{1}{2R}\left(\frac{\partial \mathfrak{v}}{\partial x} - \frac{\partial \mathfrak{u}}{\partial s}\right)}. \tag{6.15b}$$

Thus, with Eqs. (6.12) and (6.15), the complete set of strain measures in terms of displacements is established for thin cylindrical shells. By neglecting the underlined terms of Eqs. (6.15), this formulation based on the theory of *Sanders* [158] and *Koiter* [114], may be reduced to the also well-known formulation of *Donnell* [64] or *Girkmann* [84]. Theories similar to the latter likewise have been developed by Mushtari and Vlasov, see *Novozhilov* [134]. The inspection of the constituents of terms involving the radius shows that

derivatives of displacements divided by radius as well as displacements divided by squared radius are neglected, while displacements divided by radius are retained. As the divergence in the order of magnitude of these ratios increases with the radius, such a practice appears to be reasonable, especially for greater radii of curvature with respect to the shell dimensions. The implications of the simplifications on the theory for circular cylindrical shells have been discussed extensively in the literature, see *Kempner* [111], *Hoff* [99], *Simmonds* [163], *Dym* [69].

6.2.3 Cylindrical Thin Shell Equilibrium

The principle of virtual displacements, given by Eq. (3.45), may be utilized to determine the equations of equilibrium. We will refrain from considering external loads. For the two-dimensional shell structure still with the transverse shear strains γ_x^0 and γ_s^0 and associated internal transverse forces Q_x and Q_s, the principle of virtual displacements may then be reformulated as follows:

$$\delta\mathcal{U}^{md} = \iint_{\Lambda} \begin{Bmatrix} \delta\varepsilon_x^0 \\ \delta\varepsilon_s^0 \\ \delta\gamma_{xs}^0 \\ \delta\kappa_x \\ \delta\kappa_s \\ \delta\psi_{xs} \\ \delta\gamma_x^0 \\ \delta\gamma_s^0 \end{Bmatrix}^T \begin{Bmatrix} N_x \\ N_s \\ N_{xs} \\ M_x \\ M_s \\ M_{xs} \\ Q_x \\ Q_s \end{Bmatrix} \mathrm{d}s\,\mathrm{d}x = 0. \tag{6.16}$$

The virtual strain measures are related to the virtual displacements, just as it is given for the actual case in Eqs. (6.12), (6.13), and (6.14a). When these kinematic relations are substituted into the principle, different derivatives of the virtual displacements appear. These may be eliminated with the aid of integration by parts to summarize the contributions connected to every virtual displacement. In order to satisfy the principle, each of the resulting integrands needs to vanish. Not to be pursued here, the natural boundary conditions therewith can be determined. The sought-after equilibrium conditions in directions of the coordinates x, s, and n take the following form

$$\frac{\partial}{\partial x}N_x + \frac{\partial}{\partial s}N_{xs} - \underline{\frac{1}{2}\frac{\partial}{\partial s}\left(\frac{M_{xs}}{R}\right)} = 0, \tag{6.17a}$$

$$\frac{\partial}{\partial s}N_s + \frac{\partial}{\partial x}N_{xs} + \underline{\frac{1}{2}\frac{\partial}{\partial x}\left(\frac{M_{xs}}{R}\right) + \frac{Q_s}{R}} = 0, \tag{6.17b}$$

$$\frac{\partial}{\partial x}Q_x + \frac{\partial}{\partial s}Q_s - \frac{N_s}{R} = 0, \tag{6.17c}$$

while the moment equilibrium conditions about the directions of the coordinates x and s read

$$\frac{\partial}{\partial x}M_x + \frac{\partial}{\partial s}M_{xs} - Q_x = 0, \tag{6.18a}$$

$$\frac{\partial}{\partial s}M_s + \frac{\partial}{\partial x}M_{xs} - Q_s = 0. \tag{6.18b}$$

Since the transverse shear strains γ_x^0 and γ_s^0 will be neglected by virtue of Remark 6.2, the associated internal transverse forces Q_x and Q_s may be eliminated by substitution of Eqs. (6.18) into Eqs. (6.17b) and (6.17c). Thus, the set of equilibrium conditions then consists of Eq. (6.17a) and, considering that the radius R of a cylindrical shell is not a function of the coordinate x, of the following:

$$\frac{\partial}{\partial s}N_s + \frac{\partial}{\partial x}N_{xs} + \underline{\frac{1}{R}\left(\frac{3}{2}\frac{\partial}{\partial x}M_{xs} + \frac{\partial}{\partial s}M_s\right)} = 0, \tag{6.19a}$$

$$\frac{\partial^2}{\partial x^2}M_x + 2\frac{\partial^2}{\partial x \partial s}M_{xs} + \frac{\partial^2}{\partial s^2}M_s - \frac{N_s}{R} = 0. \tag{6.19b}$$

6.3 Constitutive Reduction

From the mechanical point of view, the theory developed so far allows for the consideration of adaptive laminated shells subjected to arbitrary loads and strains within the framework of Remarks 6.1 to 6.6. For many applications, such a level of generality is not necessary as particular knowledge with respect to mission and design may be used to imposed simplifying assumptions.

6.3.1 Negligence of Strain and Stress Components

In the simplest case, certain strain measures are assumed to be negligible and thus the associated column in the matrix of constitutive properties may be eliminated. As the corresponding line in the constitutive relation with regard to the energy contribution is not required either, it can also be removed. In the other case, when an internal force or moment is to be abandoned, the corresponding line in the constitutive relation may be used to determine the associated strain measure. Substituting the result back into the remaining lines of the constitutive relation leads to an adequate condensation. Analogous procedures have already been applied in Section 4.4.

Membrane Response

Here the consequences of typical assumptions for the employment of the described shells as thin walls of a beam will be demonstrated.

Remark 6.7. Membrane response dominates the structural behavior and forces acting along the curved coordinate direction are negligible.

The reasons for these assumptions are illustrated within the context of the theory of thin-walled beams in the following chapter. The first part of Remark 6.7 demands negligence of the shell bending and twisting curvatures, while the second part sets the internal forces along the s-direction to zero:

$$\kappa_x = 0, \qquad \kappa_s = 0, \qquad \psi_{xs} = 0, \tag{6.20a}$$

$$N_s = 0. \tag{6.20b}$$

These equations are to be applied to the constitutive relation of Eq. (6.6), exemplarily for two groups of electrically paralleled laminae. By virtue of Eqs. (6.20a), the associated columns and lines are eliminated, while the condensation due to Eq. (6.20b) on top leads to an additional term in every remaining component of the constitutive matrix:

$$\begin{Bmatrix} N_x \\ N_{xs} \\ G_3^c \\ G_3^d \end{Bmatrix} = \begin{bmatrix} \mathtt{A}_{11} - \frac{(\mathtt{A}_{12})^2}{\mathtt{A}_{22}} & \mathtt{A}_{13} - \frac{\mathtt{A}_{12}\mathtt{A}_{23}}{\mathtt{A}_{22}} & \mathtt{A}_{14}^c - \frac{\mathtt{A}_{12}\mathtt{A}_{24}^c}{\mathtt{A}_{22}} & \mathtt{A}_{14}^d - \frac{\mathtt{A}_{12}\mathtt{A}_{24}^d}{\mathtt{A}_{22}} \\ \mathtt{A}_{13} - \frac{\mathtt{A}_{12}\mathtt{A}_{23}}{\mathtt{A}_{22}} & \mathtt{A}_{33} - \frac{(\mathtt{A}_{23})^2}{\mathtt{A}_{22}} & \mathtt{A}_{34}^c - \frac{\mathtt{A}_{23}\mathtt{A}_{24}^c}{\mathtt{A}_{22}} & \mathtt{A}_{34}^d - \frac{\mathtt{A}_{23}\mathtt{A}_{24}^d}{\mathtt{A}_{22}} \\ \mathtt{A}_{14}^c - \frac{\mathtt{A}_{12}\mathtt{A}_{24}^c}{\mathtt{A}_{22}} & \mathtt{A}_{34}^c - \frac{\mathtt{A}_{23}\mathtt{A}_{24}^c}{\mathtt{A}_{22}} & \mathtt{A}_{44}^c - \frac{(\mathtt{A}_{24}^c)^2}{\mathtt{A}_{22}} & -\frac{\mathtt{A}_{24}^c\mathtt{A}_{24}^d}{\mathtt{A}_{22}} \\ \mathtt{A}_{14}^d - \frac{\mathtt{A}_{12}\mathtt{A}_{24}^d}{\mathtt{A}_{22}} & \mathtt{A}_{34}^d - \frac{\mathtt{A}_{23}\mathtt{A}_{24}^d}{\mathtt{A}_{22}} & -\frac{\mathtt{A}_{24}^c\mathtt{A}_{24}^d}{\mathtt{A}_{22}} & \mathtt{A}_{44}^d - \frac{(\mathtt{A}_{24}^d)^2}{\mathtt{A}_{22}} \end{bmatrix} \begin{Bmatrix} \varepsilon_x^0 \\ \gamma_{xs}^0 \\ \bar{E}_3^c \\ \bar{E}_3^d \end{Bmatrix}. \tag{6.21}$$

It needs to be noted that those components responsible for the direct electric interaction between laminae groups are modified from 0, see Eq. (6.6), to $-\mathtt{A}_{24}^c\mathtt{A}_{24}^d/\mathtt{A}_{22}$. As the electrostatic fields of both groups have been coupled to the considered mechanical fields, the condensation of the latter has converted the indirect coupling to a virtually direct one.

Reduced Shell Response

Since the assumptions of Remark 6.7 are rather restrictive, the course of derivation in the subsequent chapters will rely on one of the following more general variants with regard to the theory of thin-walled beams:

Remark 6.8. For structures with minor influence of stress and strain states in the curved coordinate direction, either the internal loads or the strain measures may be assumed to be negligibly small for this direction.

$$N_s = 0, \qquad M_s = 0 \tag{6.22}$$

or

$$\varepsilon_s^0 = 0, \qquad \kappa_s = 0. \tag{6.23}$$

The negligence of the force N_s and the moment M_s, as of Eq. (6.22), requires two condensations to be carried out in analogy to the above discussion. The resulting properties are to be distinguished by the use of $(\grave{\cdot})$. The condensations again lead to non-zero direct electric interaction between laminae groups symbolized by $\grave{\mathtt{A}}_{44}^{cd}$. While the matrix for the reduced shell response is still symmetric, a loss of symmetry in the off-diagonal submatrices is observed and captured by $\grave{\mathtt{B}}_{31}$. Consequently, the constitutive relation reads:

$$\begin{Bmatrix} N_x \\ N_{xs} \\ M_x \\ M_{xs} \\ G_3^c \\ G_3^d \end{Bmatrix} = \begin{bmatrix} \grave{\mathtt{A}}_{11} & \grave{\mathtt{A}}_{13} & \grave{\mathtt{B}}_{11} & \grave{\mathtt{B}}_{13} & \grave{\mathtt{A}}_{14}^{c} & \grave{\mathtt{A}}_{14}^{d} \\ \grave{\mathtt{A}}_{13} & \grave{\mathtt{A}}_{33} & \grave{\mathtt{B}}_{31} & \grave{\mathtt{B}}_{33} & \grave{\mathtt{A}}_{34}^{c} & \grave{\mathtt{A}}_{34}^{d} \\ \grave{\mathtt{B}}_{11} & \grave{\mathtt{B}}_{31} & \grave{\mathtt{D}}_{11} & \grave{\mathtt{D}}_{13} & \grave{\mathtt{B}}_{14}^{c} & \grave{\mathtt{B}}_{14}^{d} \\ \grave{\mathtt{B}}_{13} & \grave{\mathtt{B}}_{33} & \grave{\mathtt{D}}_{13} & \grave{\mathtt{D}}_{33} & \grave{\mathtt{B}}_{34}^{c} & \grave{\mathtt{B}}_{34}^{d} \\ \grave{\mathtt{A}}_{14}^{c} & \grave{\mathtt{A}}_{34}^{c} & \grave{\mathtt{B}}_{14}^{c} & \grave{\mathtt{B}}_{34}^{c} & \grave{\mathtt{A}}_{44}^{c} & \grave{\mathtt{A}}_{44}^{cd} \\ \grave{\mathtt{A}}_{14}^{d} & \grave{\mathtt{A}}_{34}^{d} & \grave{\mathtt{B}}_{14}^{d} & \grave{\mathtt{B}}_{34}^{d} & \grave{\mathtt{A}}_{44}^{cd} & \grave{\mathtt{A}}_{44}^{d} \end{bmatrix} \begin{Bmatrix} \varepsilon_x^0 \\ \gamma_{xs}^0 \\ \kappa_x \\ \psi_{xs} \\ \bar{E}_3^c \\ \bar{E}_3^d \end{Bmatrix}. \tag{6.24}$$

Neglecting strain ε_s^0 and curvature κ_s, as of Eq. (6.23), allows us to delete the associated columns and rows of the matrix, respectively, vectors in the original constitutive relation of Eq. (6.6). However, Eq. (6.24) may be used to represent both cases of the reduced shell response, since the latter is included as a special case:

$$(\grave{\cdot}) = (\cdot) \quad \text{with } \grave{\mathtt{B}}_{31} = \grave{\mathtt{B}}_{13} = \mathtt{B}_{13} \text{ and } \grave{\mathtt{A}}_{44}^{cd} = 0. \tag{6.25}$$

6.3.2 Potential Energy Considerations

Another possibility to reduce the number of components in the constitutive relation of adaptive laminated shells is to employ the extended Dirichlet's principle of minimum potential energy derived in Section 3.5.1.

Remark 6.9. External mechanical loads, as well as external electric charges, will be confined to minor changes in comparison to the internal states.

Therefore, the minimization is not affected by these external influences and, consequently, Eq. (3.69) reduces to

$$\mathcal{U} \Rightarrow \min. \tag{6.26}$$

With the preceding constitutive modeling, the associated electroelastic energy density $\mathcal{U}_0$, see Eq. (3.65), may now be given for adaptive laminated shells as

$$\mathcal{U}_0 = \frac{1}{2}\boldsymbol{\chi}^T \mathbb{K} \boldsymbol{\chi} \qquad \text{with } \mathbb{K} = \mathbb{K}^T, \tag{6.27a}$$

$$= \frac{1}{2}\hat{\boldsymbol{\chi}}^T \hat{\mathbb{K}} \hat{\boldsymbol{\chi}} + \hat{\boldsymbol{\chi}}^T \mathring{\mathbb{K}} \check{\boldsymbol{\chi}} + \frac{1}{2}\check{\boldsymbol{\chi}}^T \check{\mathbb{K}} \check{\boldsymbol{\chi}}, \quad \hat{\mathbb{K}} = \hat{\mathbb{K}}^T, \check{\mathbb{K}} = \check{\mathbb{K}}^T. \tag{6.27b}$$

Here the considerations of Section 4.4.4 again warrant the symmetry of the laminate constitutive matrix $\mathbb{K}$, introduced in Eq. (6.6), together with the vector $\boldsymbol{\chi}$ consisting of shell strains and groupwise electric field strengths. Equation (6.27a) may be rewritten for an arbitrary rearrangement of the components of $\boldsymbol{\chi}$ in the vectors $\hat{\boldsymbol{\chi}}$ and $\check{\boldsymbol{\chi}}$ with the corresponding property matrices $\hat{\mathbb{K}}$, $\check{\mathbb{K}}$, and $\mathring{\mathbb{K}}$ as given by Eq. (6.27b). For such a partitioning, the constitutive relation of Eq. (6.6) with the vector $\boldsymbol{L}$ of shell internal loads and groupwise electric flux density resultants reorganized in the vectors $\hat{\boldsymbol{L}}$ and $\check{\boldsymbol{L}}$ reads as follows:

$$\begin{Bmatrix} \hat{\boldsymbol{L}} \\ \check{\boldsymbol{L}} \end{Bmatrix} = \begin{bmatrix} \hat{\mathbb{K}} & \mathring{\mathbb{K}} \\ \mathring{\mathbb{K}}^T & \check{\mathbb{K}} \end{bmatrix} \begin{Bmatrix} \hat{\boldsymbol{\chi}} \\ \check{\boldsymbol{\chi}} \end{Bmatrix}. \tag{6.28}$$

Constrained Variational Problem of Several Independent Variables

In the first instance, the general formulation of such a problem shall be considered. As the expression $\mathcal{U}_0$ is a function of functions, in the current case contained in the vector $\boldsymbol{\chi}$, it is denoted as functional. The functions and thus the functional may depend on several mutually independent variables, whereby, without loss of generality, the two-dimensional case will be examined. Correspondingly, the appearance of first derivatives of the functions is incorporated. The extremum of the integral

$$\mathcal{U} = \int_{x_0}^{x_1} \int_{s_0}^{s_1} \mathcal{U}_0(x, s, \boldsymbol{\chi}(x,s), \boldsymbol{\chi}_{,x}(x,s), \boldsymbol{\chi}_{,s}(x,s))\, \mathrm{d}s\, \mathrm{d}x \tag{6.29}$$

is sought after. The functions contained in the vector $\boldsymbol{\chi}$ will be subjected to an arbitrary number of side conditions. These constraints are of the following form:

$$\int_{x_0}^{x_1} \int_{s_0}^{s_1} \boldsymbol{\varsigma}(x, s, \boldsymbol{\chi}(x,s))\, \mathrm{d}s\, \mathrm{d}x = \boldsymbol{c}, \tag{6.30a}$$

$$\int_{x_0}^{x_1} \boldsymbol{\varsigma}(x, s, \boldsymbol{\chi}(x,s))\, \mathrm{d}x = \boldsymbol{c}\,(s)\,, \qquad \int_{s_0}^{s_1} \boldsymbol{\varsigma}(x, s, \boldsymbol{\chi}(x,s))\, \mathrm{d}s = \boldsymbol{c}\,(x)\,, \tag{6.30b}$$

$$\boldsymbol{\varsigma}\left(x, s, \boldsymbol{\chi}(x,s), \boldsymbol{\chi}_{,x}(x,s), \boldsymbol{\chi}_{,s}(x,s)\right) = \boldsymbol{0}. \tag{6.30c}$$

Euler's differential equations in conjunction with the introduction of Lagrangian multipliers constitute the necessary conditions for a minimum, see *Courant and Hilbert* [56] or *Denn* [62]. Thereby the integrand $\mathcal{U}_0$ of Eq. (6.29) is extended by the product of appropriate parameters known as Lagrangian multipliers and integrands of the side conditions. In the vectorial representation to be given here, this results in $\mathcal{U}_0 + \boldsymbol{\lambda}^T \boldsymbol{\varsigma}$ with the vector of Lagrangian multipliers $\boldsymbol{\lambda}$ and respective vector of integrands $\boldsymbol{\varsigma}$ from Eqs. (6.30). To obtain Euler's differential equations, the variation of this expression is equated to zero:

$$\frac{\partial}{\partial s}\frac{\partial}{\partial \boldsymbol{\chi}_{,s}}\left(\mathcal{U}_0 + \boldsymbol{\lambda}^T\boldsymbol{\varsigma}\right) + \frac{\partial}{\partial x}\frac{\partial}{\partial \boldsymbol{\chi}_{,x}}\left(\mathcal{U}_0 + \boldsymbol{\lambda}^T\boldsymbol{\varsigma}\right) - \frac{\partial}{\partial \boldsymbol{\chi}}\left(\mathcal{U}_0 + \boldsymbol{\lambda}^T\boldsymbol{\varsigma}\right) = \boldsymbol{0}. \tag{6.31}$$

To determine the Lagrangian multipliers, the side conditions have to be consulted. The different types of side conditions given in Eqs. (6.30), identify the dependencies of the Lagrangian multipliers. In the case of Eq. (6.30a), it is dealt with a constant, while for Eqs. (6.30b) the Lagrangian multipliers depend on the variables s, respectively x. Consequently in the general case of Eq. (6.30c), the Lagrangian multipliers are functions of all independent variables. For a sophisticated discussion of the sufficient conditions for a minimum in the calculus of variations, see the pertinent literature, for example *Funk* [77].

Actual Problem

Inspecting Eqs. (6.27), it is found that the actual problem at hand is significantly simpler and can be deduced from the above implementations. As the goal was to reduce the number of components in the constitutive relation, the vector $\boldsymbol{\chi}$ may be subdivided, see Eq. (6.27b), into a portion $\hat{\boldsymbol{\chi}}$ to be retained and a portion $\check{\boldsymbol{\chi}}$ to be expressed in terms of the prior. This can be accomplished by minimizing the electroelastic energy $\mathcal{U}$ with respect to the functions contained in the vector $\check{\boldsymbol{\chi}}$:

$$\mathcal{U} = \int_{x_0}^{x_1} \int_{s_0}^{s_1} \mathcal{U}_0(x, s, \check{\boldsymbol{\chi}}(x, s)) \, \mathrm{d}s \, \mathrm{d}x. \tag{6.32}$$

The minimization with respect to a subset of functions is permissible insofar as the examination of a subset of Euler's differential equations has no limiting implications on an eventually succeeding complete solution of the problem. The imposed side conditions will be given in the form of the right-hand side of Eqs. (6.30b) and are supposed to be linear with respect to the vector $\check{\boldsymbol{\chi}}$ involving a proportionality matrix $\boldsymbol{\Gamma}$:

$$\int_{s_0}^{s_1} \boldsymbol{\Gamma}(x, s) \; \check{\boldsymbol{\chi}}(\boldsymbol{x}, \boldsymbol{s}) \, \mathrm{d}s = \boldsymbol{c}\,(x)\,. \tag{6.33}$$

Thus, for the problem at hand, Euler's differential equations, given in general form by Eq. (6.31), reduce to

$$\frac{\partial}{\partial \check{\boldsymbol{\chi}}} \left(\mathcal{U}_0 + \boldsymbol{\lambda}^T \boldsymbol{\Gamma} \check{\boldsymbol{\chi}} \right) = \boldsymbol{0}. \tag{6.34}$$

Solving Eq. (6.34) in consideration of the electroelastic energy density $\mathcal{U}_0$ as given by Eq. (6.27b) for the vector $\check{\boldsymbol{\chi}}$, it can be established in terms of the vectors $\hat{\boldsymbol{\chi}}$ and $\boldsymbol{\lambda}$:

$$\check{\boldsymbol{\chi}} = -\check{\mathbb{K}}^{-1} \mathring{\mathbb{K}}^T \hat{\boldsymbol{\chi}} - \check{\mathbb{K}}^{-1} \boldsymbol{\Gamma}^T \boldsymbol{\lambda}. \tag{6.35}$$

Finally, the Lagrangian multipliers have to be determined by substitution of Eq. (6.35) into Eq. (6.33). The associated vector $\boldsymbol{\lambda}$ can be easily isolated as

it does not depend on the integration variable s:

$$\boldsymbol{\lambda} = -\int_{s_0}^{s_1} \left(\boldsymbol{\Gamma}\check{\mathbb{K}}^{-1}\boldsymbol{\Gamma}^T\right)^{-1} \mathrm{d}s \left(\boldsymbol{c} + \int_{s_0}^{s_1} \boldsymbol{\Gamma}\check{\mathbb{K}}^{-1}\mathring{\mathbb{K}}^T\hat{\boldsymbol{\chi}}\,\mathrm{d}s\right). \tag{6.36}$$

Congeneric findings are reported by *Volovoi and Hodges* [176] for the solely mechanical case. As noted there, similarities to a procedure applied by *Reissner and Tsai* [152] exist involving the partial inversion of the constitutive relation. Such an approach is also found in further works by *Reissner* [151], *Murakami et al.* [129], and *Jung et al.* [108].

Implications of the Potential Energy Minimization

The operating characteristics of the elaborated procedure may be recalled in the following statement:

Remark 6.10. The eliminated set of components adjusts such that the potential energy is minimal for the remaining set of components being assumed as given.

Simplifications tied to already eliminated components cannot be applied anymore. Therefore, such constraints have to be considered during the minimization with aid of the Lagrangian multipliers. To assess further consequences of the partial minimization, the result of Eq. (6.35) is substituted into the associated constitutive relation of Eq. (6.28). After a couple of rearrangements, this yields

$$\begin{Bmatrix}\hat{\boldsymbol{L}}\\ \check{\boldsymbol{L}}\end{Bmatrix} = \begin{bmatrix}\hat{\mathbb{K}} - \mathring{\mathbb{K}}\check{\mathbb{K}}^{-1}\mathring{\mathbb{K}}^T\\ \mathbf{0}\end{bmatrix}\hat{\boldsymbol{\chi}} - \begin{bmatrix}\mathring{\mathbb{K}}\check{\mathbb{K}}^{-1}\\ \mathbf{I}\end{bmatrix}\boldsymbol{\Gamma}^T\boldsymbol{\lambda}. \tag{6.37}$$

Examining the lower part of Eq. (6.37), it is observed that the shell internal loads and groupwise electric flux density resultants in the vector $\check{\boldsymbol{L}}$ only depend on the constraint contributions $\boldsymbol{\Gamma}^T\boldsymbol{\lambda}$ and thus directly reveal the implications of the minimization. Due to the integral form of the regarded side conditions, given by Eq. (6.33), the Lagrangian multipliers in the vector $\boldsymbol{\lambda}$ represent elements of internal loads or flux density resultants that are constant along the s-direction. In the case of components to be eliminated without the existence of associated side conditions, the constraint contributions vanish as a matter of course and the following can be concluded:

Remark 6.11. Minimization with respect to unconstrained components is equivalent to neglecting the corresponding internal loads or groupwise electric flux density resultants respectively.

Examining the upper part of Eq. (6.37), the shell internal loads and groupwise electric flux density resultants in the vector $\hat{\boldsymbol{L}}$ are found to be composed

of two parts. The second of them again represents the constraint contributions just that the adjustment $\mathring{\mathbb{K}}\check{\mathbb{K}}^{-1}$ is incorporated here. The first part is a function of the retained shell strains and groupwise electric field strengths in the vector $\hat{\boldsymbol{\chi}}$ depending on both the coordinates x and s. The submatrix $\hat{\mathbb{K}}$ is complemented by an additional term. It contains the transposed submatrix $\mathring{\mathbb{K}}$, originally responsible for the coupling with the eliminated vector $\check{\boldsymbol{\chi}}$, in conjunction with the above-mentioned adjustment $\mathring{\mathbb{K}}\check{\mathbb{K}}^{-1}$. As suggested by Remark 6.11, the additional term agrees with the corresponding findings of Section 6.3.1.

Example

To illustrate the above procedure, at least the set up of a typical problem will be given. Therein it is dealt with a single-cell closed cross-section beam and the associated kinematic constraints. Again for the theoretical background and information on the appearing quantities, we will refer to the subsequent chapter. The vectors and matrices to be inserted into Eqs. (6.36) and (6.37) are

$$\hat{\boldsymbol{\chi}} = \begin{Bmatrix} \varepsilon_x^0 \\ \kappa_x \\ \psi_{xs} \\ \bar{E}_3^c \\ \bar{E}_3^d \end{Bmatrix}, \qquad \check{\boldsymbol{\chi}} = \begin{Bmatrix} \varepsilon_s^0 \\ \gamma_{xs}^0 \\ \kappa_s \end{Bmatrix}, \qquad \boldsymbol{\Gamma} = \begin{bmatrix} 0 & 1 & 0 \\ 0 & 0 & 1 \\ 0 & 0 & y \\ 0 & 0 & z \end{bmatrix},$$

$$\boldsymbol{c} = \begin{Bmatrix} \frac{\partial \phi}{\partial x} \oint\limits_S r_n \, \mathrm{d}s \\ 0 \\ 0 \\ 0 \end{Bmatrix}, \qquad \boldsymbol{\lambda} = \begin{Bmatrix} \lambda_1 \\ \lambda_2 \\ \lambda_3 \\ \lambda_4 \end{Bmatrix}, \tag{6.38a}$$

$$\hat{\mathbb{K}} = \begin{bmatrix} \mathtt{A}_{11} & \mathtt{B}_{11} & \mathtt{B}_{13} & \mathtt{A}_{14}^c & \mathtt{A}_{14}^d \\ \mathtt{B}_{11} & \mathtt{D}_{11} & \mathtt{D}_{13} & \mathtt{B}_{14}^c & \mathtt{B}_{14}^d \\ \mathtt{B}_{13} & \mathtt{D}_{13} & \mathtt{D}_{33} & \mathtt{B}_{34}^c & \mathtt{B}_{34}^d \\ \mathtt{A}_{14}^c & \mathtt{B}_{14}^c & \mathtt{B}_{34}^c & \mathtt{A}_{44}^c & 0 \\ \mathtt{A}_{14}^d & \mathtt{B}_{14}^d & \mathtt{B}_{34}^d & 0 & \mathtt{A}_{44}^d \end{bmatrix}, \qquad \mathring{\mathbb{K}} = \begin{bmatrix} \mathtt{A}_{12} & \mathtt{A}_{13} & \mathtt{B}_{12} \\ \mathtt{B}_{12} & \mathtt{B}_{13} & \mathtt{D}_{12} \\ \mathtt{B}_{23} & \mathtt{B}_{33} & \mathtt{D}_{23} \\ \mathtt{A}_{24}^c & \mathtt{A}_{34}^c & \mathtt{B}_{24}^c \\ \mathtt{A}_{24}^d & \mathtt{A}_{34}^d & \mathtt{B}_{24}^d \end{bmatrix},$$

$$\check{\mathbb{K}} = \begin{bmatrix} \mathtt{A}_{22} & \mathtt{A}_{23} & \mathtt{B}_{22} \\ \mathtt{A}_{23} & \mathtt{A}_{33} & \mathtt{B}_{23} \\ \mathtt{B}_{22} & \mathtt{B}_{23} & \mathtt{D}_{22} \end{bmatrix}. \tag{6.38b}$$

By substitution of $\boldsymbol{\Gamma}$, $\check{\boldsymbol{\chi}}$, and $\boldsymbol{c}$ from Eq. (6.38a) into the side condition of Eq. (6.33) it becomes clear that the strain ε_s^0 is unconstrained and thus the internal force N_s is neglected. Further on, the integral of the shear strain γ_{xs}^0 is equated to a function of x, while in the case of the bending curvature κ_s, it is the constant zero.

7

Adaptive Thin-Walled Beams

Based upon the adaptive shell description given in the previous chapter, a thin-walled beam formulation for general anisotropic cross-sections with arbitrary open branches and/or closed cells will be derived in this chapter. After the deduction of non-linear kinematic relations for the general beam and the linear kinematic relations for the thin-walled beam, the torsional warping effects of the latter are examined. Subsequently, the constitutive relation and the equations of equilibrium are established.

7.1 General Beam Kinematics

With regard to the dynamics of rotating structures on the one hand, non-linear influences in the beam kinematics have to be taken into account, while analytical formulation of the constitutive relation of beams with complicated cross-sections on the other hand, is only possible for thin walls and linear kinematics. This gives rise to a combined procedure with a linear analysis to determine the beam properties and a succeeding non-linear analysis to investigate the global beam behavior. For the latter, a general beam with adequate kinematics will be examined first and subsequently transcribed into the intended thin-walled beams.

7.1.1 Positions and Displacements

Like in the case of the shell in Section 6.2, the displacement field needs to be specified for the beam as well. Since the course of analysis will lead to rotating beams, which rather do without curvature, we will agree on the following:

Remark 7.1. The beam will be prismatic with unvarying cross-sectional properties along a reference line which is straight in the initial state.

The coordinate x accounts for the essential dimension of the beam and initially coincides with its reference line, while the orthogonal coordinates y

T.H. Brockmann, *Theory of Adaptive Fiber Composites*,
Solid Mechanics and Its Applications 161,

and z characterize the transverse plane. In this reference system, the position $\boldsymbol{P}_o(x,y,z)$ of an arbitrary point within the undeformed beam may be described by

$$\boldsymbol{P}_o\left(x,y,z\right) = \boldsymbol{x}_o\left(x\right) + \boldsymbol{s}_o\left(y,z\right) \quad \text{with } \boldsymbol{x}_o\left(x\right) = \begin{Bmatrix} x \\ 0 \\ 0 \end{Bmatrix},\ \boldsymbol{s}_o\left(y,z\right) = \begin{Bmatrix} 0 \\ y \\ z \end{Bmatrix}. \tag{7.1}$$

The intersection point of the cross-sectional plane with the beam reference line will be called the reference point. In the initial state, the vector $\boldsymbol{x}_o(x)$ marks this reference point, while the vector $\boldsymbol{s}_o(y,z)$ specifies the position of the considered point on the cross-sectional plane. Consequently, its position $\boldsymbol{p}_o(x,y,z)$ in the deformed state can be given with the aid of the total displacement $\boldsymbol{u}_o(x,y,z)$ as

$$\boldsymbol{p}_o\left(x,y,z\right) = \boldsymbol{P}_o\left(x,y,z\right) + \boldsymbol{u}_o\left(x,y,z\right). \tag{7.2}$$

We will start with a geometrically exact specification of the total displacement. Here a separation of displacements with respect to the reference line and cross-section is utilized. Thus, the displacement of the reference point is expressed by the vector $\boldsymbol{u}(x)$, while the remaining terms account for the displacement associated with the cross-section:

$$\begin{aligned} \boldsymbol{u}_o\left(x,y,z\right) &= \boldsymbol{u}\left(x\right) + \mathbf{R}\left(x\right)\left(\boldsymbol{s}_o\left(y,z\right) + \boldsymbol{u}_\Theta\left(x,y,z\right)\right) - \boldsymbol{s}_o\left(y,z\right) \\ \text{with } \boldsymbol{u}\left(x\right) &= \begin{Bmatrix} u\left(x\right) \\ v\left(x\right) \\ w\left(x\right) \end{Bmatrix},\ \boldsymbol{u}_\Theta\left(x,y,z\right) = \begin{Bmatrix} u_\Theta\left(x,y,z\right) \\ v_\Theta\left(x,y,z\right) \\ w_\Theta\left(x,y,z\right) \end{Bmatrix}. \end{aligned} \tag{7.3}$$

The vector $\boldsymbol{u}_\Theta(x,y,z)$ contains the displacements due to the deformation of the cross-section usually entitled "warping". Together with the vector $\boldsymbol{s}_o(y,z)$, it describes the position relative to the reference point sitting on the now-deformed reference line requiring the rotational transformation $\mathbf{R}(x)$ to comply with the reference system. To gain the displacement portion, the cross-sectional position in the initial state $\boldsymbol{s}_o(y,z)$ needs to be subtracted.

7.1.2 Rotations

There are a number of possibilities including Euler angles and quaternions to express finite rotations in three dimensions, see *Gérardin and Rixen* [80]. To avoid a dependency on the sequence of three separate transformations, as encountered for example by *Hodges and Dowell* [98] or *Kaza and Kvaternik* [110], the angular coordinates of Rodriguez can be utilized, see *Gasch and Knothe* [78] or *Sauer* [159]. Therewith the transformation matrix $\mathbf{R}(x)$ can be formulated as

$$\mathbf{R}\left(x\right) = \mathbf{I} + \frac{\sin\beta}{\beta}\left\langle\boldsymbol{\beta}\left(x\right)\right\rangle + \frac{1-\cos\beta}{\beta^2}\left\langle\boldsymbol{\beta}\left(x\right)\right\rangle^2 \quad \text{with } \beta = \beta\left(x\right) = \left\|\boldsymbol{\beta}\left(x\right)\right\|. \tag{7.4}$$

This contains the rotational angle $\beta(x)$ and the skew-symmetric matrix $\langle \boldsymbol{\beta}(x) \rangle$, defined in Eq. (3.9), whereby both are associated with the vector $\boldsymbol{\beta}(x)$ of rotational parameters. In the cases of moderate or small rotations, the latter turn into the rotational angles around the axes of the reference system:

$$\boldsymbol{\beta}(x) = \begin{Bmatrix} \phi(x) \\ \beta_y(x) \\ \beta_z(x) \end{Bmatrix}. \tag{7.5}$$

For moderate rotations, Eq. (7.6a), and small rotations, Eq. (7.6b), the Rodriguez formula of Eq. (7.4) reduces as follows:

$$\sin\beta = \beta, \quad \cos\beta = 1 - \frac{\beta^2}{2} \quad \rightarrow \quad \mathbf{R}(x) = \mathbf{I} + \langle \boldsymbol{\beta}(x) \rangle + \frac{1}{2} \langle \boldsymbol{\beta}(x) \rangle^2, \tag{7.6a}$$

$$\sin\beta = \beta, \quad \cos\beta = 1 \quad \rightarrow \quad \mathbf{R}(x) = \mathbf{I} + \langle \boldsymbol{\beta}(x) \rangle. \tag{7.6b}$$

Thus, for small rotations only the sum of the identity matrix and skew-symmetric matrix remains. In any case, such rotational transformations shall be reversible and therefore orthogonality is required:

$$\mathbf{R}(x)^T \mathbf{R}(x) = \mathbf{I}. \tag{7.7}$$

The substitution of the simplified transformation matrices of Eqs. (7.6) into this condition reveals those terms which have been neglected by the associated assumptions. In the case of moderate rotations, Eq. (7.6a), and small rotations, Eq. (7.6b), these are the products of four, respectively of two, rotational angles given in Eq. (7.5). Since the rotational angles in the latter case are thereby decoupled, the outcome is identical to the results of other rotational transformations, for example involving Euler angles.

7.1.3 Simplifications

The geometrically exact specification of displacements not unexpectedly leads to fairly complicated expressions, and also for moderate rotations, it is usually sought after reduction with the aid of ordering schemes. For the sake of transparency and analytic insight, it will be continued as follows:

Remark 7.2. The beam may be subjected only to small rotations.

Applying the rotational transformation for such small rotations, as outlined in Eq. (7.6b), to the total displacement vector $\boldsymbol{u}_o(x, y, z)$ of Eq. (7.3) leads to

$$\boldsymbol{u}_o(x, y, z) = \boldsymbol{u}(x) + (\mathbf{I} + \langle \boldsymbol{\beta}(x) \rangle) (\boldsymbol{s}_o(y, z) + \boldsymbol{u}_\Theta(x, y, z)) - \boldsymbol{s}_o(y, z). \tag{7.8}$$

So far, the warping displacements $\boldsymbol{u}_\Theta(x, y, z)$ have not been considered beyond their pure existence. Yet, they somehow must be related to the displacements $\boldsymbol{u}(x)$ or rotations $\boldsymbol{\beta}(x)$ of the beam. A detailed analysis of the warping effects will be given later in this chapter, illustrating the subsequent warping-related statements.

Remark 7.3. The warping displacements are presumed to be functions of the rotational angles.

Therefore, the multiplication of the skew-symmetric matrix $\langle \boldsymbol{\beta}(x) \rangle$ with the warping displacements $\boldsymbol{u}_\Theta(x, y, z)$ in Eq. (7.8) results in products of two angles or derivatives thereof respectively. In consequence of the above discussion on the orthogonality condition, these terms have to be neglected and the expression of the total displacements simplifies significantly:

$$\boldsymbol{u}_o\,(x, y, z) = \boldsymbol{u}\,(x) + \boldsymbol{\beta}\,(x) \times \boldsymbol{s}_o\,(y, z) + \boldsymbol{u}_\Theta\,(x, y, z)\,. \tag{7.9}$$

The deformation of the cross-section is considered to be subdivided into the out-of-plane warping $u_\Theta(x, y, z)$ and the in-plane warping $v_\Theta(x, y, z)$, $w_\Theta(x, y, z)$. The latter is neglected with the introduction of a classical assumption of beam theory:

Remark 7.4. The cross-section remains undeformed in its plane.

$$v_\Theta\,(x, y, z) = 0, \qquad w_\Theta\,(x, y, z) = 0. \tag{7.10}$$

For the thin-walled beams to be subsequently discussed, this is a fairly rough assumption since the bending stiffness of their walls might be comparably low. Some approaches are reported in the literature to incorporate the in-plane deformation of the cross-section, see *Heo et al.* [93], *Rand* [148], or *Rand* [149], but in return have to accept other limitations or drawbacks. Concentrating on the out-of-plane warping here and in anticipation of the detailed discussion in Section 7.3, the associated displacement component may be described by

$$u_\Theta\,(x, y, z) = \Theta\,(y, z)\,\phi_{,x}\,(x)\,. \tag{7.11}$$

Therein the warping function $\Theta(y, z)$ accounts for the cross-sectional properties, while the lengthwise dependency is provided by the rate of twist $\phi_{,x}(x)$. Supplying Eq. (7.9) with Eq. (7.11), the components of the total displacement of the classic beam theory of Euler and Bernoulli with extension to shear flexibility and torsional warping usually associated with the names of Timoshenko, respectively Vlassov, are obtained:

$$\begin{aligned} \boldsymbol{u}_o\,(x, y, z) &= \begin{Bmatrix} u_0\,(x, y, z) \\ v_0\,(x, y, z) \\ w_0\,(x, y, z) \end{Bmatrix} \\ &= \begin{Bmatrix} u\,(x) + z\beta_y\,(x) - y\beta_z\,(x) + \Theta\,(y, z)\,\phi_{,x}\,(x) \\ v\,(x) - z\phi\,(x) \\ w\,(x) + y\phi\,(x) \end{Bmatrix}. \end{aligned} \tag{7.12}$$

Due to the elongated nature of beams in general, their resistance against extension is drastically higher than against bending. Correspondingly, the displacement $u(x)$ in the axial direction in almost any case is significantly smaller than the displacements $v(x)$, $w(x)$ in the transverse directions. Hence, the following may be concluded:

Remark 7.5. The beam may be subjected to finite displacements, whereof the displacement in the axial direction may be considered as moderate without loss of generality.

7.1.4 Strains

In order to determine the strain measures of the general beam, the Green Lagrange strain tensor for finite deformations may be utilized as outlined in Section 3.2.4. It is symmetric and contains, in general, six independent components, to be obtained from Eq. (3.17) for the total displacements $\boldsymbol{u}_0(x, y, z)$. However, due to the assumption of Remark 7.4, both normal strains and the shear strain in the cross-sectional plane have to vanish. So the remaining components are the normal strain as well as the two shear strains associated with lengthwise direction. Resorting them into a vector in consideration of the factor for the engineering shear strains, yields

$$\boldsymbol{\varepsilon}_{\mathrm{GL}}(x,y,z) = \begin{Bmatrix} \frac{\partial}{\partial x}u_0 + \frac{1}{2}(\frac{\partial}{\partial x}u_0)^2 + \frac{1}{2}(\frac{\partial}{\partial x}v_0)^2 + \frac{1}{2}(\frac{\partial}{\partial x}w_0)^2 \\ \frac{\partial}{\partial x}v_0 + \frac{\partial}{\partial y}u_0 + \frac{\partial}{\partial x}u_0\frac{\partial}{\partial y}u_0 + \frac{\partial}{\partial x}v_0\frac{\partial}{\partial y}v_0 + \frac{\partial}{\partial x}w_0\frac{\partial}{\partial y}w_0 \\ \frac{\partial}{\partial x}w_0 + \frac{\partial}{\partial z}u_0 + \frac{\partial}{\partial x}u_0\frac{\partial}{\partial z}u_0 + \frac{\partial}{\partial x}v_0\frac{\partial}{\partial z}v_0 + \frac{\partial}{\partial x}w_0\frac{\partial}{\partial z}w_0 \end{Bmatrix}. \tag{7.13}$$

Next, the components of the total displacement as given by Eq. (7.12) may be substituted into Eq. (7.13). In consideration of Remark 7.5, the derivative of the axial displacement may be neglected in comparison to unity:

$$1 + u_{,x}(x) \approx 1. \tag{7.14}$$

Thus, as well as with the abandonment of any product of two rotational angles by virtue of Remark 7.2, the remaining Green Lagrange strain components may be significantly simplified. Arranging the non-linear strain measures for finite displacements but small rotations of the beam in the vector $\breve{\boldsymbol{\varepsilon}}_{\mathrm{GL}}(x)$, leads to

$$\begin{aligned} &\boldsymbol{\varepsilon}_{\mathrm{GL}}(x,y,z) \\ &= \begin{bmatrix} 1 & 0 & 0 & 0 & z & -y & \Theta(y,z) \\ 0 & 1 & 0 & \Theta_{,y}(y,z) - z & 0 & 0 & 0 \\ 0 & 0 & 1 & \Theta_{,z}(y,z) + y & 0 & 0 & 0 \end{bmatrix} \underbrace{\begin{Bmatrix} u_{,x}(x) + \frac{1}{2}(v_{,x}(x)^2 + w_{,x}(x)^2) \\ -\beta_z(x) + v_{,x}(x) + w_{,x}(x)\,\phi(x) \\ \beta_y(x) + w_{,x}(x) - v_{,x}(x)\,\phi(x) \\ \phi_{,x}(x) \\ \beta_{y,x}(x) - v_{,x}(x)\,\phi_{,x}(x) \\ \beta_{z,x}(x) - w_{,x}(x)\,\phi_{,x}(x) \\ \phi_{,xx}(x) \end{Bmatrix}}_{\breve{\boldsymbol{\varepsilon}}_{\mathrm{GL}}(x)}. \end{aligned} \tag{7.15}$$

Analogous treatment of those Green Lagrange strain components, which are expected to vanish as discussed above, reveals only terms with products of two rotational angles. These again have to be neglected by virtue of Remark 7.2, and so the implications of Remark 7.4 are confirmed.

7.2 Thin-Walled Beam Kinematics

So far, the shape of the cross-section of the considered beams has not been discussed, while the Green Lagrange strain tensor has been brought up for a continuum only confined with respect to the deformations in the cross-sectional plane by Remark 7.4. Subsequently, a special class of cross-sectional topologies will be examined:

Remark 7.6. The beam is constructed from walls which are thin in comparison to the cross-sectional dimensions.

Under these conditions, it is possible to analytically handle beams with complex cross-sections, since the formation of the one-dimensional structure from two-dimensional walls instead of a three-dimensional continuum allows us to introduce the associated simplifications. Therefore, the relation between the strain measures of the beam and of the thin wall is sought. To describe the shape of such a cross-section, the curvilinear coordinate s may be utilized as a parameter for the cross-sectional position

$$\boldsymbol{s}_o\left(y,z\right)=\begin{Bmatrix}0\\y\\z\end{Bmatrix}=\begin{Bmatrix}0\\y\left(s\right)\\z\left(s\right)\end{Bmatrix}=\boldsymbol{s}_o\left(s\right). \tag{7.16}$$

Correspondingly, the above derivations may be adjusted to account for the coordinate s in the cross-sectional plane.

7.2.1 Differential Geometry

The curvilinear coordinate s will be given such that it represents the arc length and therefore, just as in the case of the Lamé parameters for the cylindrical shell in Section 6.2.2, the following is required:

$$\left|\frac{\partial}{\partial s}\boldsymbol{s}_o(s)\right|=\sqrt{\left(y_{,s}(s)\right)^2+\left(z_{,s}(s)\right)^2}=1. \tag{7.17}$$

The unit tangent vector $\boldsymbol{e}_s(s)$ is given by the corresponding derivative of the cross-sectional position $\boldsymbol{s}_o(s)$. Further on, the unit normal vector $\boldsymbol{e}_n(s)$ is defined orthogonal to the unit axis vector $\boldsymbol{e}_x$ in parallel to the undeformed reference line and to the unit tangent vector $\boldsymbol{e}_s(s)$. Thus, the moving trihedral is given as

$$\boldsymbol{e}_x=\begin{Bmatrix}1\\0\\0\end{Bmatrix},\qquad \boldsymbol{e}_s(s)=\frac{\frac{\partial}{\partial s}\boldsymbol{s}_o(s)}{|\frac{\partial}{\partial s}\boldsymbol{s}_o(s)|}=\begin{Bmatrix}0\\y_{,s}(s)\\z_{,s}(s)\end{Bmatrix}, \tag{7.18a}$$

$$\boldsymbol{e}_n\left(s\right)=\boldsymbol{e}_x\times\boldsymbol{e}_s\left(s\right)=\begin{Bmatrix}0\\-z_{,s}(s)\\y_{,s}(s)\end{Bmatrix}. \tag{7.18b}$$

In the description of spatial curves or surfaces, the radius of curvature is usually an absolute value and the direction of curvature is given by the unit principal normal vector, pointing towards the center of curvature. Then the unit binormal vector results from the vector product of unit tangential and unit principal normal vector, see *Råde and Westgren* [147] or *Wygodski* [185]. Instead, here the unit axis vector $\boldsymbol{e}_x$ needs to be prearranged just as the unit tangent vector $\boldsymbol{e}_s(s)$ and thus, for the sake of orthogonality, the unit normal vector $\boldsymbol{e}_n(s)$ is not necessarily oriented towards the center of the curvature, while the radius $R(s)$ may then also become negative. The sequence of spatial directions in the wall description (x, s, n) has been chosen in Eq. (7.18b) to begin with the coincidental coordinate x, as appears in the beam description (x, y, z). For this reason, a positive radius $R(s)$ is now associated with an outward oriented unit normal vector $\boldsymbol{e}_n(s)$, as visible in Figure 7.1, and a negative sign needs to be introduced into the corresponding relation:

$$-\boldsymbol{e}_n\,(s) = \frac{\partial^2}{\partial s^2}\boldsymbol{s}_o(s)R\,(s)\,. \tag{7.19}$$

With Eqs. (7.16) and (7.18), this relations allows us to express the radius $R(s)$ in terms of the cross-sectional position:

$$R\,(s) = -\frac{y_{,s}(s)}{z_{,ss}(s)} = \frac{z_{,s}(s)}{y_{,ss}(s)}. \tag{7.20}$$

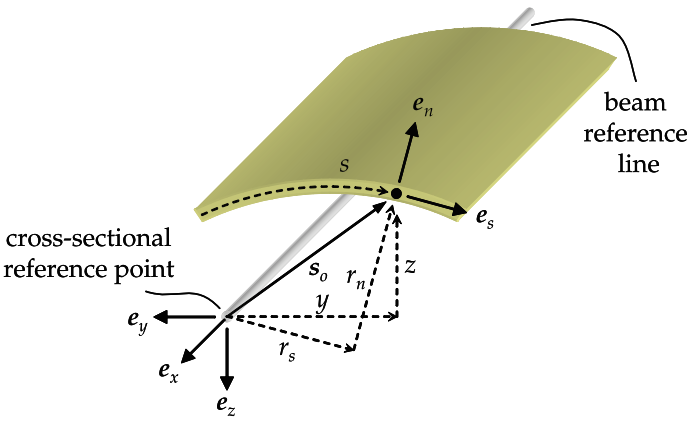

Fig. 7.1. Position of a point on the cross-section and associated unit vectors.

7.2.2 Cartesian and Curvilinear Positions and Displacements

To transform vector-valued functions from the Cartesian coordinate system of the beam to the curvilinear coordinate system of the wall, the unit vec-

tors of the latter, as given by Eq. (7.18), may be encapsulated in the matrix

$$\mathbf{E}(s) = \begin{bmatrix} \boldsymbol{e}_x & \boldsymbol{e}_s(s) & \boldsymbol{e}_n(s) \end{bmatrix}^T = \begin{bmatrix} 1 & 0 & 0 \\ 0 & y_{,s}(s) & z_{,s}(s) \\ 0 & -z_{,s}(s) & y_{,s}(s) \end{bmatrix}. \tag{7.21}$$

It is helpful to introduce the distances in wall normal direction $r_n(s)$ and in wall tangential direction $r_s(s)$ from the cross-sectional reference point to the considered point on the beam wall. They are shown in Figure 7.1 and may be gained with the above transformation:

$$\boldsymbol{r}(s) = \mathbf{E}(s)\,\boldsymbol{s}_o(s) \quad \rightarrow \quad \boldsymbol{r}(s) = \begin{Bmatrix} 0 \\ r_s(s) \\ r_n(s) \end{Bmatrix} = \begin{Bmatrix} 0 \\ y_{,s}(s)y(s) + z_{,s}(s)z(s) \\ y_{,s}(s)z(s) - z_{,s}(s)y(s) \end{Bmatrix}. \tag{7.22}$$

Then with the aid of Eq. (7.20), respectively in addition with Eq. (7.17), the following relationships are found:

$$\frac{r_s(s)}{R(s)} = r_{n,s}(s), \qquad \frac{r_n(s)}{R(s)} = 1 - r_{s,s}(s). \tag{7.23}$$

With the introduction of the parameter s, the total displacement of a point on the beam wall, according to Eq. (7.12), is given in the Cartesian coordinate system of the beam as

$$\begin{aligned} \boldsymbol{u}_o(x,s) &= \begin{Bmatrix} u_0(x,s) \\ v_0(x,s) \\ w_0(x,s) \end{Bmatrix} \\ &= \begin{Bmatrix} u(x) + z(s)\,\beta_y(x) - y(s)\,\beta_z(x) + \Theta(s)\,\phi_{,x}(x) \\ v(x) - z(s)\,\phi(x) \\ w(x) + y(s)\,\phi(x) \end{Bmatrix}. \end{aligned} \tag{7.24}$$

With separation of cross-sectional properties in the matrix $\mathbf{K}(s)$ and beam deformation descriptions in the vector $\breve{\boldsymbol{u}}(x)$, the total displacement of a point on the beam wall may also be written as

$$\boldsymbol{u}_o(x,s) = \underbrace{\begin{bmatrix} 1 & 0 & 0 & 0 & z(s) & -y(s) & \Theta(s) \\ 0 & 1 & 0 & -z(s) & 0 & 0 & 0 \\ 0 & 0 & 1 & y(s) & 0 & 0 & 0 \end{bmatrix}}_{\mathbf{K}(s)} \underbrace{\begin{Bmatrix} u(x) \\ v(x) \\ w(x) \\ \phi(x) \\ \beta_y(x) \\ \beta_z(x) \\ \phi_{,x}(x) \end{Bmatrix}}_{\breve{\boldsymbol{u}}(x)}. \tag{7.25}$$

To determine the strains in the beam wall, the total displacement must be expressed in the associated curvilinear coordinate system. With the aid of the transformation of Eq. (7.21), this may be expressed in the following form:

$$\begin{Bmatrix} \mathfrak{u}(x,s) \\ \mathfrak{v}(x,s) \\ \mathfrak{w}(x,s) \end{Bmatrix} = \mathbf{E}(s)\, \boldsymbol{u}_o(x,s). \tag{7.26}$$

7.2.3 Strains of Wall and Beam

Since the thin walls of the prismatic beams under discussion resemble the cylindrical thin shells of Section 6.2.2, the associated formulation of strains may be adopted. Thereby, also the respective assumptions are inherited. A comparison of Remarks 6.4 and 7.6 reveals that the ratio of thickness and radius of curvature is additionally confined and Remark 6.5 indicates a linear strain displacement relation. These shell strains are given by Eqs. (6.12) and (6.15). The insertion of Eqs. (7.26) and (7.24) leads to rather complicated expressions. Through tedious manipulations with the aid of Eqs. (7.17), (7.22), and (7.23), a remarkably compact formulation may be found. For the sake of correlation to the beam displacements and rotations again in anticipation of the upcoming considerations of torsional warping, the warping function $\Theta(s)$ is employed and also appears in the abbreviation

$$\Phi(s) = \Theta_{,s}(s) - r_n(s). \tag{7.27}$$

The underlining of terms in accordance with the discussion in the end of Section 6.2.2 will be retained to analyze their meaning in the context of thin-walled beams, where they are frequently neglected. So the relation between the strains in the beam wall and the displacements of the beam may be written as follows:

$$\begin{Bmatrix} \varepsilon_x^0 \\ \varepsilon_s^0 \\ \gamma_{xs}^0 \\ \kappa_x \\ \kappa_s \\ \psi_{xs} \end{Bmatrix} = \begin{bmatrix} 0 & 0 & 0 & 0 & (1-\underline{1})z_{,sss} & 0 \\ 0 & 0 & 0 & 0 & -(1-\underline{1})y_{,sss} & 0 \\ 0 & 0 & 0 & 0 & -(1-\underline{1})r_{s,ss} & 0 \\ 0 & 0 & z_{,s} & 0 & 0 & -\underline{\tfrac{1}{2}}y_{,ss} \\ 0 & 0 & -y_{,s} & 0 & 0 & -\underline{\tfrac{1}{2}}z_{,ss} \\ 1 & 0 & 0 & 0 & 0 & 0 \\ 0 & 0 & y_{,s} & 0 & 0 & (2-\underline{\tfrac{3}{2}})z_{,ss} \\ 0 & 0 & z_{,s} & 0 & 0 & -(2-\underline{\tfrac{3}{2}})y_{,ss} \\ 0 & 0 & \Phi & 0 & 0 & -2r_{s,s} + \underline{(2r_{s,s} - 2 - \tfrac{1}{2}\tfrac{\Phi}{R})} \\ z & 0 & 0 & 0 & 0 & 0 \\ -y & 0 & 0 & 0 & 0 & 0 \\ 0 & 0 & 0 & z_{,s} & 0 & 0 \\ 0 & 0 & 0 & -y_{,s} & 0 & 0 \\ \Theta & 0 & 0 & -r_s & 0 & 0 \end{bmatrix}^T \begin{Bmatrix} v \\ w \\ \phi \\ \beta_y \\ \beta_z \\ u_{,x} \\ v_{,x} \\ w_{,x} \\ \phi_{,x} \\ \beta_{y,x} \\ \beta_{z,x} \\ v_{,xx} \\ w_{,xx} \\ \phi_{,xx} \end{Bmatrix}. \tag{7.28}$$

Shell Strain Comprehension

A couple of interesting issues need to be noted here. It is shown that the cross-sectional strain component $\varepsilon_s^0(x,s)$ vanishes in accordance with Remark 7.4. The same is expected from the cross-sectional bending curvature $\kappa_s(x,s)$, but this is only the case when the underlined terms are included or the cross-sectional shape is simplified so that the appearing higher derivatives of the cross-sectional position vanish. It is even more important to retain the underlined terms for the twisting curvature $\psi_{xs}(x,s)$, since it would otherwise not be possible to introduce the beam shear strains

$$\gamma_{xy}(x) = -\beta_z(x) + v_{,x}(x), \qquad \gamma_{xz}(x) = \beta_y(x) + w_{,x}(x). \tag{7.29}$$

The key observation for a general treatment of thin-walled beams is the inevitability of an adequate strain formulation for cylindrical thin shells as presented here on the basis of the theory of *Sanders* [158] and *Koiter* [114]. Therefore, all terms have to be retained and distinction through underlinement is not necessary any more. With these considerations and the resulting initiation of the beam shear strains, Eq. (7.28) reduces significantly.

Beam Strain Comprehension

In comparison to the strain measures of the general beam in Eq. (7.15), there still exist two additional components, namely $v_{,xx}(x)$ and $w_{,xx}(x)$, which would require corresponding internal loads in the constitutive relation of the beam. Generally, this may be avoided by more or less advanced reductions, see Section 6.3, with respect to the associated bending curvature $\kappa_x(x,s)$. The derived formulation, however, allows for a more elegant proceeding. In the classical beam theory aiming at slender beams, the shear strains of Eq. (7.29) are considered to be negligible. With regard to a stouter beam geometry, at least the rate of these shear strains may be discarded:

Remark 7.7. The derivatives of the beam shear strains are assumed to be negligible.

Differentiating Eqs. (7.29), this may be utilized to express the second derivatives of reference line displacements $v(x)$ and $w(x)$ by the first derivatives of the rotations of the cross-sectional plane $\beta_y(x)$ and $\beta_z(x)$:

$$\gamma_{xy,x}(x) \approx 0 \quad \rightarrow \quad v_{,xx}(x) = \beta_{z,x}(x), \tag{7.30a}$$

$$\gamma_{xz,x}(x) \approx 0 \quad \rightarrow \quad w_{,xx}(x) = -\beta_{y,x}(x). \tag{7.30b}$$

Hence from Eq. (7.28) with the support of Eqs. (7.29) and (7.30), the desired relation between the strain measures of wall and beam can be obtained:

$$\underbrace{\begin{Bmatrix} \varepsilon_x^0(x,s) \\ \gamma_{xs}^0(x,s) \\ \kappa_x(x,s) \\ \psi_{xs}(x,s) \end{Bmatrix}}_{\boldsymbol{\varepsilon}(x,s)} = \underbrace{\begin{bmatrix} 1 & 0 & 0 & 0 \\ 0 & y_{,s}(s) & 0 & \frac{1}{2}z_{,ss}(s) \\ 0 & z_{,s}(s) & 0 & -\frac{1}{2}y_{,ss}(s) \\ 0 & \Phi(s) & 0 & -2-\frac{1}{2}\frac{\Phi(s)}{R(s)} \\ z(s) & 0 & y_{,s}(s) & 0 \\ -y(s) & 0 & z_{,s}(s) & 0 \\ \Theta(s) & 0 & -r_s(s) & 0 \end{bmatrix}^T}_{\mathbf{J}(s)} \underbrace{\begin{Bmatrix} u_{,x}(x) \\ -\beta_z(x)+v_{,x}(x) \\ \beta_y(x)+w_{,x}(x) \\ \phi_{,x}(x) \\ \beta_{y,x}(x) \\ \beta_{z,x}(x) \\ \phi_{,xx}(x) \end{Bmatrix}}_{\breve{\boldsymbol{\varepsilon}}(x)}. \tag{7.31}$$

As mentioned above, the underlying shell theory is confined to small displacements such that the description of wall strains $\boldsymbol{\varepsilon}(x,s)$, and consequently of beam strains $\breve{\boldsymbol{\varepsilon}}(x)$ of the thin-walled beam, is linear. A comparison of Eqs. (7.15) and (7.31) reveals that $\breve{\boldsymbol{\varepsilon}}(x)$ is the linearized version of $\breve{\boldsymbol{\varepsilon}}_{\mathrm{GL}}(x)$. The achievement of analogous formulations gives rise to the possibility of a combined approach, where the constitutive properties of the thin-walled beam are determined in a linear analysis while the global behavior is subsequently obtained in a non-linear analysis. In some respects, the latter is essential for the employment in a rotating environment.

7.2.4 Electric Field Strength

The above derivations are concerned with the relation between the strain measures in the beam and in the wall description. Correspondingly, such a relation is also required for the electric field strength. The latter is accessed with the aid of electrodes that necessarily connect certain areas and thus induce an equalization therein. To achieve unified behavior for the beam description, a complete connection in parallel needs to be introduced along the cross-sectional coordinate s:

Remark 7.8. The electric field strength of a group of electrically paralleled laminae in the wall is assumed to be identical in all sectors of the cross-section with respect to the absolute value.

To be able to model different actuation and sensing schemes, the relative sign of polarization and electric field strength may alternate around the cross-section. It will be summarized in the vector $\boldsymbol{p}(s)$ with an entry for every group of electrically paralleled laminae, as exemplarily introduced by Eq. (6.6):

$$\boldsymbol{p}(s) = \begin{Bmatrix} p^c(s) \\ p^d(s) \\ \vdots \end{Bmatrix} \quad \text{with } p^c(s), p^d(s), \ldots \in [1,-1]. \tag{7.32}$$

So the mechanical relation of Eq. (7.31) can be extended to incorporate the electric case. Thus, the strain and electric field strength measures of the wall,

contained in the vector $\boldsymbol{\chi}(x,s)$ as shown in Eq. (6.6), can be obtained as follows:

$$\boldsymbol{\chi}\left(x,s\right)=\left\{\begin{array}{c}\boldsymbol{\varepsilon}\left(x,s\right)\\ \bar{\boldsymbol{E}}\left(x,s\right)\end{array}\right\}=\underbrace{\begin{bmatrix}\mathbf{J}\left(s\right) & \mathbf{0}\\ \mathbf{0} & \mathbf{I}\,\boldsymbol{p}\left(s\right)\end{bmatrix}}_{\mathbb{J}(s)}\underbrace{\left\{\begin{array}{c}\breve{\boldsymbol{\varepsilon}}\left(x\right)\\ \breve{\boldsymbol{E}}\left(x\right)\end{array}\right\}}_{\breve{\boldsymbol{\chi}}(x)}. \tag{7.33}$$

The vector $\breve{\boldsymbol{\chi}}(x)$ therein again contains the strain measures $\breve{\boldsymbol{\varepsilon}}(x)$ and electric field strength measures $\breve{\boldsymbol{E}}(x)$ of the beam. The former are specified by Eq. (7.31) and the latter will be itemized as

$$\breve{\boldsymbol{E}}\left(x\right)=\left\{\breve{E}^{c}\left(x\right)\quad\breve{E}^{d}\left(x\right)\quad\ldots\right\}^{T}. \tag{7.34}$$

7.3 Torsional Out-of-Plane Warping for Thin Walls

As stated in Remark 7.4, the developed beam theory is confined to the out-of-plane warping of the cross-section. By means of Remark 7.3, the cause for such a warping displacement has been narrowed down to the three rotations of the cross-section. With respect to the undeformed beam, the bending related inclination of the cross-sectional plane represents deformations in a direction, which deviates, according to Remark 7.2, only slightly from the direction of the out-of-plane warping. So since both are almost equidirectional and the higher-order phenomenon of warping is generally presumed to be significantly smaller, the bending related out-of-plane warping may be neglected. In contrast, there is no torsion-related deformation in the out-of-plane direction besides the associated warping.

Remark 7.9. The relevant out-of-plane warping of the cross-section is governed by the influence of torsion.

7.3.1 General Formulation

In order to determine the warping displacement $u_{\Theta}(x,s)$ in accordance with Remark 7.9, the case of pure torsion of the beam needs to be considered. Therefore, all components not related to the twist angle $\phi(x)$ or warping displacement $u_{\Theta}(x,s)$, have to be omitted in the description of wall strains. Without the preemptive introduction of the warping function $\Theta(s)$ by virtue of Eqs. (7.11) and (7.27) in Eq. (7.31), this yields

$$\tilde{\varepsilon}_{x}^{0}\left(x,s\right)=u_{\Theta,x}\left(x,s\right),\quad\tilde{\gamma}_{xs}^{0}\left(x,s\right)=-r_{n}\left(s\right)\phi_{,x}\left(x\right)+u_{\Theta,s}\left(x,s\right), \tag{7.35a}$$

$$\tilde{\kappa}_{x}\left(x,s\right)=-r_{s}\left(s\right)\phi_{,xx}\left(x\right),\quad\tilde{\psi}_{xs}\left(x,s\right)=\left(\frac{r_{n}\left(s\right)}{2R\left(s\right)}-2\right)\phi_{,x}\left(x\right)-\frac{u_{\Theta,s}\left(x,s\right)}{2R\left(s\right)}. \tag{7.35b}$$

The special load case at hand is elucidated by $(\dot{\cdot})$. In the preceding examination of displacements not related to the warping effect, the constitutive relation of the shell-like wall has not been involved. Since a kinematic assumption like the vanishing shear strain $\tilde{\gamma}^0_{xs}(x,s) = 0$ for isotropic open cross-sections is not possible in the general case, the material properties need to be considered now. For isotropic closed cross-sections, this has been accomplished by means of shear flow named after *Bredt* [24], see *Roik et al.* [156], *Wiedemann* [179], or *Gjelsvik* [85]. Its constancy could be assumed in conjunction with the consideration of the internal shear force $N_{xs}(x,s)$ in the axial shell equilibrium. To assure consistency with the formulation shown to be adequate in Section 7.2, it is necessary to comply with the associated equilibrium condition of Eq. (6.17a). Therein the derivative of the internal axial force $N_x(x,s)$ may be neglected in conjunction with Remark 7.9, while the underlined term with the internal twisting moment $M_{xs}(x,s)$ appears additionally. Integration of the remaining expression yields a constant result with respect to the cross-sectional direction and shall be called warping resultant $W_{xs}(x)$:

$$\frac{\partial}{\partial s}\left(\tilde{N}_{xs}\left(x,s\right) - \frac{\tilde{M}_{xs}\left(x,s\right)}{2R\left(s\right)}\right) = 0 \quad \rightarrow \quad \tilde{N}_{xs}\left(x,s\right) - \frac{\tilde{M}_{xs}\left(x,s\right)}{2R\left(s\right)} = W_{xs}\left(x\right). \tag{7.36}$$

Remark 7.10. For pure torsion, the resultant of internal forces and moments in the warping relevant axial equilibrium is constant along the cross-sectional coordinate.

For anisotropic arbitrary cross-sections, the lines of the internal shear force and twisting moment in the constitutive relation, given by Eq. (6.24), read regarding the special case at hand:

$$\begin{aligned}\tilde{N}_{xs}(x,s) = {} & \grave{\mathtt{A}}_{13}\left(s\right)\tilde{\varepsilon}^0_x\left(x,s\right) + \grave{\mathtt{A}}_{33}\left(s\right)\tilde{\gamma}^0_{xs}\left(x,s\right) \\ & + \grave{\mathtt{B}}_{31}\left(s\right)\tilde{\kappa}_x\left(x,s\right) + \grave{\mathtt{B}}_{33}\left(s\right)\tilde{\psi}_{xs}\left(x,s\right), \end{aligned} \tag{7.37a}$$

$$\begin{aligned}\tilde{M}_{xs}(x,s) = {} & \grave{\mathtt{B}}_{13}\left(s\right)\tilde{\varepsilon}^0_x\left(x,s\right) + \grave{\mathtt{B}}_{33}\left(s\right)\tilde{\gamma}^0_{xs}\left(x,s\right) \\ & + \grave{\mathtt{D}}_{13}\left(s\right)\tilde{\kappa}_x\left(x,s\right) + \grave{\mathtt{D}}_{33}\left(s\right)\tilde{\psi}_{xs}\left(x,s\right). \end{aligned} \tag{7.37b}$$

Herein the terms vanishing due to the rigid cross-section of Remark 7.4 have been deleted and the electric influences are omitted to warrant pure torsion. When Eqs. (7.35) are substituted into Eqs. (7.37), derivatives of the warping displacement $u_\Theta(x,s)$ with respect to both coordinate directions are contained. Their influences may be estimated in accordance with *Armanios and Badir* [7] as follows:

Remark 7.11. The torsional shear force component proportional to the derivative of the warping displacement in the cross-sectional direction is assumed to dominate over the one with the derivative in the axial direction.

This assumption, which will become more obvious in view of the final warping formulation, leads from Eqs. (7.37) to reduced expressions for the internal shear force and twisting moment

$$\tilde{N}_{xs}(x,s) = \left(\grave{\mathtt{B}}_{33}(s)\left(\frac{r_n(s)}{2R(s)} - 2\right) - \grave{\mathtt{A}}_{33}(s)\, r_n(s)\right)\phi_{,x}(x) - \grave{\mathtt{B}}_{31}(s)\, r_s(s)\,\phi_{,xx}(x) + u_{\Theta,s}(x,s)\left(\grave{\mathtt{A}}_{33}(s) - \frac{\grave{\mathtt{B}}_{33}(s)}{2R(s)}\right), \tag{7.38a}$$

$$\tilde{M}_{xs}(x,s) = \left(\grave{\mathtt{D}}_{33}(s)\left(\frac{r_n(s)}{2R(s)} - 2\right) - \grave{\mathtt{B}}_{33}(s)\, r_n(s)\right)\phi_{,x}(x) - \grave{\mathtt{D}}_{13}(s)\, r_s(s)\,\phi_{,xx}(x) + u_{\Theta,s}(x,s)\left(\grave{\mathtt{B}}_{33}(s) - \frac{\grave{\mathtt{D}}_{33}(s)}{2R(s)}\right). \tag{7.38b}$$

These relations may then be substituted into Eq. (7.36) to be solved in consideration of an integration constant $C(x)$ for the warping displacement

$$u_\Theta(x,s) = \phi_{,x}(x)\int \theta_1(s)\,\mathrm{d}s + \phi_{,xx}(x)\int \theta_2(s)\,\mathrm{d}s + W_{xs}(x)\int \frac{1}{\grave{\mathtt{C}}_{33}(s)}\,\mathrm{d}s + C(x). \tag{7.39}$$

The contained integrands which depend on the cross-sectional coordinate s are described by the following functions:

$$\theta_1(s) = r_n(s) + 2\frac{\grave{\mathtt{B}}_{33}(s) - \frac{\grave{\mathtt{D}}_{33}(s)}{R(s)}}{\grave{\mathtt{C}}_{33}(s)}, \quad \theta_2(s) = \frac{\grave{\mathtt{B}}_{31}(s) - \frac{\grave{\mathtt{D}}_{13}(s)}{R(s)}}{\grave{\mathtt{C}}_{33}(s)}\, r_s(s), \tag{7.40a}$$

$$\text{with } \grave{\mathtt{C}}_{33}(s) = \grave{\mathtt{A}}_{33}(s) - \frac{3}{2}\frac{\grave{\mathtt{B}}_{33}(s)}{R(s)} + \frac{1}{2}\frac{\grave{\mathtt{D}}_{33}(s)}{R^2(s)}. \tag{7.40b}$$

7.3.2 Non-Branched Open and Closed Cross-Sections

Cross-sections without branchings can be described with the aid of the coordinate s in a continuous manner. Allowing for an uncomplicated representation, they will be treated first to illustrate the elementary connections. Since the warping displacement $u_\Theta(x,s)$ of Eq. (7.39) still contains the unknown warping resultant $W_{xs}(x)$ and integration constant $C(x)$, additional conditions are required. The appearance of $C(x)$ may be avoided when a zero passage of the warping displacement is enforced at the origin of the coordinate s, which may be chosen arbitrarily:

$$u_\Theta(x, s=0) = 0 \quad \rightarrow \quad C(x) = 0. \tag{7.41}$$

With respect to the internal forces and moments represented by $W_{xs}(x)$, it is necessary to differentiate between the different cross-sectional topologies.

Open Cross-Sections

In beam theory, the external forces act only upon the beam as a whole symbolized by the reference line. Consequently, no shell loads can be induced at the free end of an open cross-section, and then by virtue of Remark 7.10, the warping resultant will be zero all over the non-branched open cross-section:

Remark 7.12. For pure torsion, the resultant of internal forces and moments in the warping-relevant axial equilibrium vanishes due to a free end of the cross-section.

$$W_{xs}(x) = 0. \tag{7.42}$$

Thus, with Eqs. (7.41) and (7.42), the warping displacement of Eq. (7.39) reduces for non-branched open cross-sections, signified by $(\cdot)^{\cup}$, to

$$u_{\Theta}^{\cup}(x,s) = \phi_{,x}(x) \int \theta_1(s)\,\mathrm{d}s + \phi_{,xx}(x) \int \theta_2(s)\,\mathrm{d}s. \tag{7.43}$$

Closed Cross-Sections

As a matter of course, a non-branched closed cross-section has no free ends and therefore the constant warping resultant of Remark 7.10 needs to be determined. For this purpose, advantage may be taken of the fact that the warping displacement cannot possess discontinuities, since the cross-sections of the considered beams are presumed to be made of one piece:

Remark 7.13. The warping displacements are continuous throughout the cross-section.

This continuity condition of the warping displacement may be formulated for the single cell of a non-branched closed cross-section with the circumferential length S as follows:

$$\oint_S u_{\Theta,s}(x,s)\,\mathrm{d}s = 0. \tag{7.44}$$

Substituting the warping displacement of Eq. (7.39) into Eq. (7.44) allows us to determine the wanted warping resultant

$$W_{xs}(x) = -\phi_{,x}(x)\,\frac{\oint_S \theta_1(s)\,\mathrm{d}s}{\oint_S \frac{1}{\mathrm{c}_{33}(s)}\,\mathrm{d}s} - \phi_{,xx}(x)\,\frac{\oint_S \theta_2(s)\,\mathrm{d}s}{\oint_S \frac{1}{\mathrm{c}_{33}(s)}\,\mathrm{d}s}. \tag{7.45}$$

Therefore the warping displacement of the non-branched closed cross-section, signified by $(\cdot)^{\diamondsuit}$, may be gained by insertion into Eq. (7.39) as

$$\begin{aligned} u_{\Theta}^{\diamondsuit}(x,s) = {} & \phi_{,x}(x) \left(\int \theta_1(s)\,\mathrm{d}s - \oint_S \theta_1(s)\,\mathrm{d}s \frac{\int \frac{1}{\mathrm{c}_{33}(s)}\,\mathrm{d}s}{\oint_S \frac{1}{\mathrm{c}_{33}(s)}\,\mathrm{d}s} \right) \\ & + \phi_{,xx}(x) \left(\int \theta_2(s)\,\mathrm{d}s - \oint_S \theta_2(s)\,\mathrm{d}s \frac{\int \frac{1}{\mathrm{c}_{33}(s)}\,\mathrm{d}s}{\oint_S \frac{1}{\mathrm{c}_{33}(s)}\,\mathrm{d}s} \right). \end{aligned} \tag{7.46}$$

7.3.3 General Cross-Sections with Open Branches and Closed Cells

A general cross-section consists of the branches i, joined at the junctions j, and possibly forming the closed cells k. For every branch i, the warping function $u_{\Theta\_i}(x,s)$ may be derived from Eq. (7.39) with the warping resultant $W_{xs\_i}(x)$ and the integration constant $C_i(x)$, since continuity of the curvilinear coordinate s is ensured only within the branches:

$$\forall i : u_{\Theta\_i}(x,s) = \phi_{,x}(x) \int \theta_1(s)\,\mathrm{d}s + \phi_{,xx}(x) \int \theta_2(s)\,\mathrm{d}s + W_{xs\_i}(x) \int \frac{1}{\bar{c}_{33}(s)}\,\mathrm{d}s + C_i(x)\,. \tag{7.47}$$

As the curvilinear coordinate s may be defined separately for every branch, the associated directions are possibly dissimilar at junctions and around cells, see the example of Figure 7.2. To account for these dissimilar directions in the subsequent examinations, the following association functions is introduced:

$$f_j^i = \begin{cases} 1 & \text{if } i \to j, \\ -1 & \text{if } i \leftarrow j, \end{cases} \qquad f_k^i = \begin{cases} 1 & \text{if } i \rightrightarrows k, \\ -1 & \text{if } i \leftrightarrows k. \end{cases} \tag{7.48}$$

The function f_j^i introduces a negative sign when the curvilinear coordinate s in the branch i is not pointing towards the junction j. Correspondingly, the function f_k^i introduces a negative sign when the curvilinear coordinate s in the branch i does not coincide with the common sense of direction in the cell k.

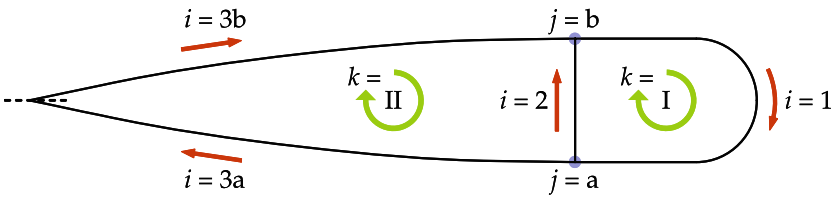

Fig. 7.2. Description of an exemplary cross-section with two adjoined cells k, formed by two junctions j and three branches i. With the optional slit at the dashed line, it may be converted into a combined cross-section consisting of a single closed cell and two branches with free ends.

Open Branches

Here those branches will be considered that do not participate in the formation of a closed cell. They possess one free end, and the same reasoning as in the

case of the non-branched open cross-section may be applied. Hence, for every open branch i not belonging to any of the closed cells k, the warping resultant $W_{xs\_i}(x)$ vanishes by virtue of Remark 7.12:

$$\forall i \notin k : W_{xs\_i}(x) = 0. \tag{7.49}$$

Closed Cells

Also, just as in the case of the non-branched closed cross-section, the warping resultant $W_{xs\_i}(x)$ does not vanish in a closed cell. In accordance with Remark 7.13, the continuity of warping displacements around such a cell may be required. The integration around closed cells must be performed in the same direction over the participating branches, see also *Gjelsvik* [85]. With the aid of the association function f_k^i, the continuity requirement may be formulated for every closed cell k with the circumferential length S_k assembled from the lengths S_i of the participating branches i as follows:

$$\forall k : \oint_{S_k} u_{\Theta,s}(x,s)\,\mathrm{d}s = \sum_{i \in k} f_k^i \int_{S_i} u_{\Theta\_i,s}(x,s)\,\mathrm{d}s = 0. \tag{7.50}$$

The connection of closed cells through the sharing of a common branch represents a statically indeterminate system. Due to the excess of branches with regard to cells and junctions respectively, the unknown warping resultants may only be determined by both continuity requirements of the cells and axial equilibrium conditions at the junctions.

Junctions

Such equilibrium conditions are only relevant for the case of multiple adjoined cells, since the warping resultants of open branches and separate cells are effectively determined by Eq. (7.49), respectively by Eq. (7.50). The axial equilibrium at the junctions j requires the consideration of the coordinate direction in the cross-sectional plane of every involved branch i captured by the association function f_j^i. Thus, the following may be formulated:

$$\forall j : \sum_{i \in j} f_j^i W_{xs\_i}(x) = 0. \tag{7.51}$$

Further on, the continuity requirement, as imposed by Remark 7.13, also applies to the warping displacements of all branches meeting at a junction, which thus have to be identical there. Since an arrangement like Eq. (7.41) can be made only for one branch, the integration constants $C_i(x)$ of the remaining branches may be determined.

7.3.4 Exemplary Configurations

To illustrate the rather abstract formulation of the general cross-section outlined above, the essential relations for two examples will be given. The first is a closed cross-section with two cells and thus represents the elementary case of a statically indeterminate system. The second examines the differences induced by a slit in one of these cells and therefore is concerned with the combination of a closed cell and two open branches.

Double Cell Cross-Section

A cross-section with two adjoining cells ($k = \mathrm{I}, \mathrm{II}$) possesses two junctions ($j = \mathrm{a}, \mathrm{b}$) connecting three branches ($i = 1, 2, 3$). For such a cross-sectional topology with a set-up as depicted in Figure 7.2, the association functions of Eqs. (7.48) are given by Tables 7.1.

Table 7.1. Association functions for a cross-section with two adjoining cells.

f_j^i	1	2	3
a	1	−1	−1
b	−1	1	1

f_k^i	1	2	3
I	1	1	0
II	0	−1	1

The continuity requirement within each cell formulated for the general case in Eq. (7.50) takes the following form for the two cells:

$$\mathrm{I}: \oint_{S_\mathrm{I}} u_{\Theta,s}(x,s)\,\mathrm{d}s = \int_{S_1} u_{\Theta\_1,s}(x,s)\,\mathrm{d}s + \int_{S_2} u_{\Theta\_2,s}(x,s)\,\mathrm{d}s = 0, \tag{7.52a}$$

$$\mathrm{II}: \oint_{S_\mathrm{II}} u_{\Theta,s}(x,s)\,\mathrm{d}s = \int_{S_3} u_{\Theta\_3,s}(x,s)\,\mathrm{d}s - \int_{S_2} u_{\Theta\_2,s}(x,s)\,\mathrm{d}s = 0. \tag{7.52b}$$

Since all three branches meet at both of the junctions, identical relations for the warping resultant as of Eq. (7.51) are gained:

$$\mathrm{a}, \mathrm{b}: W_{xs\_1}(x) - W_{xs\_2}(x) - W_{xs\_3}(x) = 0. \tag{7.53}$$

The warping displacements $u_{\Theta\_1}(x,s)$, $u_{\Theta\_2}(x,s)$, $u_{\Theta\_3}(x,s)$ in the three branches are sought after as given by Eq. (7.47). Thus, the three warping resultants $W_{xs\_1}(x)$, $W_{xs\_2}(x)$, $W_{xs\_3}(x)$ and integration constants C_1, C_2, C_3 need to be determined. Since the latter vanish with the substitution of the cross-sectional derivative of the warping displacement into Eqs. (7.52), the resulting two relations, together with Eq. (7.53), may serve to solve for the three warping resultants. As the continuity of warping displacements within each of the two cells is already ensured, compatibility between cells, also with reference to Remark 7.13, may be required at either junction:

$$\mathrm{a}: u_{\Theta\_1}(x, S_1) = u_{\Theta\_2}(x, 0) = u_{\Theta\_3}(x, 0), \tag{7.54a}$$

$$\mathrm{b}: u_{\Theta\_1}(x, 0) = u_{\Theta\_2}(x, S_2) = u_{\Theta\_3}(x, S_3). \tag{7.54b}$$

Besides the utilization of two independent relations out of these four relations, additional information is necessary to determine the three integration constants. Here the zero passage of the warping displacement in the manner of Eq. (7.41) may be introduced for one of the branches. For the example at hand, this could be given for the center of the web as follows:

$$u_{\Theta\_2}\left(x, \frac{S_2}{2}\right) = 0.$$

So, the integration constants can be found and the warping displacement completed. However, since the formulation is rather lengthy, it will be omitted here and, instead, only the result is shown in Figure 7.3.

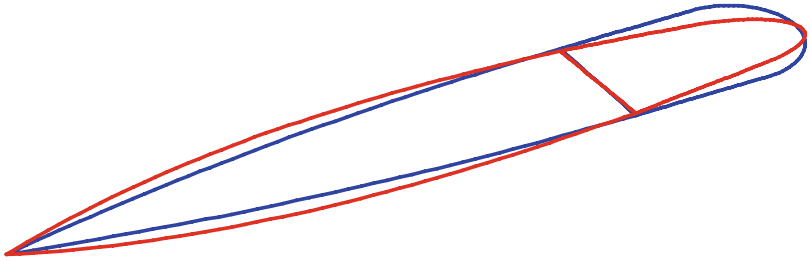

Fig. 7.3. Warping displacement of a cross-section with two closed cells and all through identical constitutive properties.

Combined Cross-Section

When one of the cells of the previous configuration is slit, for example, at the dashed line in Figure 7.2, then four branches ($i = 1, 2, 3\mathrm{a}, 3\mathrm{b}$) and still two junctions ($j = \mathrm{a}, \mathrm{b}$) need to be considered. The remaining closed cell ($k = \mathrm{I}$) is formed by the two branches ($i = 1, 2$), while the other two ($i = 3\mathrm{a}, 3\mathrm{b}$) have free ends. As required by Eq. (7.49), the warping resultants of the latter therefore have to vanish:

$$W_{xs\_3\mathrm{a}}(x) = 0, \qquad W_{xs\_3\mathrm{b}}(x) = 0. \tag{7.55}$$

Consequently, they do not influence the axial equilibrium at the junctions and, hence, Eq. (7.53) reduces to

$$\mathrm{a}, \mathrm{b}: W_{xs\_1}(x) - W_{xs\_2}(x) = 0. \tag{7.56}$$

As a matter of course, the continuity requirement for the warping displacement of the retained cell in Eq. (7.52a) remains valid, while Eq. (7.52b) has to be dropped. Instead, the continuity requirement at the junctions, given by Eqs. (7.54), is modified such that three of the four relations are independent:

$$\text{a} : u_{\Theta\_1}(x, S_1) = u_{\Theta\_2}(x, 0) = u_{\Theta\_3\text{a}}(x, 0), \tag{7.57}$$

$$\text{b} : u_{\Theta\_1}(x, 0) = u_{\Theta\_2}(x, S_2) = u_{\Theta\_3\text{b}}(x, S_{3\text{b}}). \tag{7.58}$$

The resulting warping displacement is shown in Figure 7.4. Since identical geometric and constitutive properties have been employed, it becomes obvious, in comparison to Figure 7.3, that open branches are much more susceptible to warping than closed cells.

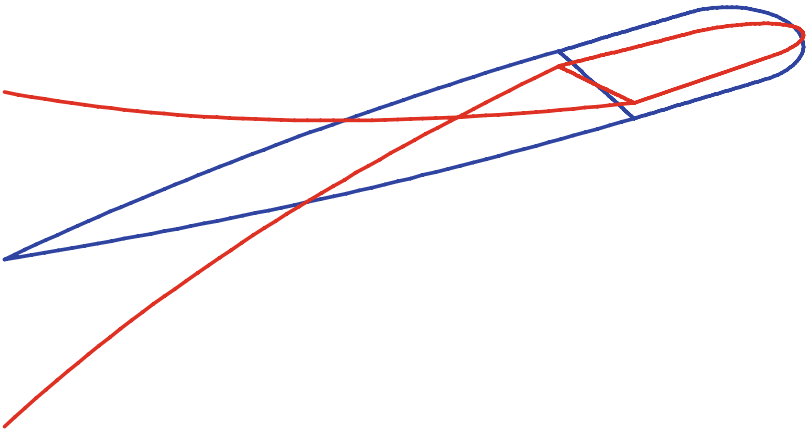

Fig. 7.4. Warping displacement of a cross-section with a closed cell as well as two open branches and all through identical constitutive properties.

7.3.5 Consistency Contemplations

As stated by Remark 6.4, the wall thickness of the considered beams is small in comparison to the cross-sectional dimensions, being reflected in $r_n(s)$ and $r_s(s)$, and to the radius of curvature $R(s)$. These geometric orders of magnitude also enter the constitutive description of the laminated beam wall in Eq. (6.4b). The plate stiffness coefficients $\grave{\mathtt{D}}_{13}(s)$ and $\grave{\mathtt{D}}_{33}(s)$ and coupling stiffnesses $\grave{\mathtt{B}}_{31}(s)$ and $\grave{\mathtt{B}}_{33}(s)$ essentially depend upon the difference of cubed, respectively squared, laminae positions in the thickness direction, while the membrane stiffness $\grave{\mathtt{A}}_{33}(s)$ is a function of the laminae thicknesses. To comply with Remark 6.4, it is necessary to revise the formulation of the warping

displacement with its integrands given by Eqs. (7.40a) and (7.40b). Allowing for different degrees of approximation, a thorough treatment shows the domination of the membrane response:

$$\theta_1(s) \approx r_n(s), \qquad \theta_2(s) \approx 0, \quad \text{and} \quad \check{\mathtt{C}}_{33}(s) \approx \check{\mathtt{A}}_{33}(s). \tag{7.59}$$

Also in consideration of the rather small influence of the warping effect in general, it seems reasonable to refrain from higher order warping influences associated with the second derivative of twist $\phi_{,xx}(x)$.

Remark 7.14. For the approximation of the torsional out-of-plane warping displacement, only the dependence upon the rate of twist will be considered.

Thus, the description of the warping displacement breaks up into a component with axial dependence, the rate of twist $\phi_{,x}(x)$, and one with cross-sectional dependence, the warping function $\Theta(s)$, like that being used in Section 7.2:

$$u_\Theta(x,s) = \Theta(s)\,\phi_{,x}(x). \tag{7.60}$$

Resulting Simplifications

The implications of the approximation introduced by Eqs. (7.59) will be demonstrated by means of the warping functions for the non-branched cross-sections. In the case of an open topology, as described by Eq. (7.43), even though the wall properties are anisotropic and may vary along the cross-sectional coordinate, the result is a purely geometric warping function

$$\Theta^{\cup}(s) = \int r_n(s)\,\mathrm{d}s. \tag{7.61}$$

In consideration of Eq. (7.27), this simplification leads in Eq. (7.31) to the decoupling of the shear strain $\gamma^0_{xs}(x,s)$ from the twist rate $\phi_{,x}(x)$. This is not given in the case of closed cross-sections, since an additional term is contained in the warping function

$$\Theta^{\diamondsuit}(s) = \int r_n(s)\,\mathrm{d}s - 2A_0 \frac{\int \frac{1}{\check{\mathtt{A}}_{33}(s)}\,\mathrm{d}s}{\oint_S \frac{1}{\check{\mathtt{A}}_{33}(s)}\,\mathrm{d}s}. \tag{7.62}$$

When the constitutive properties of the wall are constant all around the cell, their influence vanishes and a purely geometric warping function remains, identical to the one determined via the shear flow of *Bredt* [24] for the isotropic case:

$$\Theta^{\diamondsuit}(s) = \int r_n(s)\,\mathrm{d}s - 2A_0 \frac{s}{S}. \tag{7.63}$$

In Eqs. (7.62) and (7.63), the area enclosed by the wall of the single cell can be identified and abbreviated by A_0. Analogously, such an abridgment may

be introduced for cross-sections with multiple cells with the area A_k enclosed by cell k:

$$\oint_S r_n(s)\,\mathrm{d}s = 2A_0, \tag{7.64a}$$

$$\forall k : \oint_{S_k} r_n(s)\,\mathrm{d}s = \sum_{i\in k} f_k^i \int_{S_i} r_n(s)\,\mathrm{d}s = 2A_k. \tag{7.64b}$$

7.4 Rotating Beams

So far, the beam itself has been described in detail. Now, it will be considered as part of a rotating system. To herald the examination of inertia effects, it is necessary to link the above kinematic relations to the description of a guided motion.

7.4.1 Rotor Kinematics

With regard to a guided motion around a fixed axis of rotation, it is essential to refer to three different frames of reference. First, the inertial reference frame defines the global origin. Second, the rotating reference frame implements the rotation around the origin. And third, the moving reference frame is associated with the mounting point of the beam. There the beam will be attached with the following implications:

Remark 7.15. Clamped boundary conditions apply at the origin of the beam's coordinate.

Thus, the considered moving reference frame agrees with the coordinate system introduced to describe the beam. Therein the position of an arbitrary point is represented by the vector $\boldsymbol{p}_o(x,s,t)$ according to Eq. (7.2) with the modified cross-sectional description for thin-walled beams of Eq. (7.16) in view of Eq. (7.1) and depending on time to accommodate dynamic beam deformations. This position may be expressed in the inertial reference frame by the vector

$$\boldsymbol{p}(x,s,t) = \mathbf{T}_\Omega(t)\left(\boldsymbol{r} + \mathbf{T}_{321}(t)\,\boldsymbol{p}_o(x,s,t)\right). \tag{7.65}$$

The position of the moving reference frame with respect to the rotating reference frame is given by the vector $\boldsymbol{r}$, while its orientation is specified by the rotational transformation $\mathbf{T}_{321}(t)$. This may be assembled from the rotations around individual axes:

$$\mathbf{T}_{321}(t) = \mathbf{T}_3(t)\,\mathbf{T}_2(t)\,\mathbf{T}_1(t)$$

$$\text{with } \mathbf{T}_3(t) = \begin{bmatrix} \cos(\alpha_3(t)) & -\sin(\alpha_3(t)) & 0 \\ \sin(\alpha_3(t)) & \cos(\alpha_3(t)) & 0 \\ 0 & 0 & 1 \end{bmatrix},$$

$$\mathbf{T}_2(t) = \begin{bmatrix} \cos(\alpha_2(t)) & 0 & \sin(\alpha_2(t)) \\ 0 & 1 & 0 \\ -\sin(\alpha_2(t)) & 0 & \cos(\alpha_2(t)) \end{bmatrix}, \tag{7.66}$$

$$\mathbf{T}_1(t) = \begin{bmatrix} 1 & 0 & 0 \\ 0 & \cos(\alpha_1(t)) & -\sin(\alpha_1(t)) \\ 0 & \sin(\alpha_1(t)) & \cos(\alpha_1(t)) \end{bmatrix}.$$

Since the Cardan angles $\alpha_3(t)$, $\alpha_2(t)$, and $\alpha_1(t)$ are prescribed parameters, a discussion on the uniqueness of representation in analogy to Section 7.1.2 is not necessary and we may simply agree upon their sequence. The orientation of the rotating reference frame relative to the inertial reference frame is described by the rotational transformation

$$\mathbf{T}_\Omega(t) = \begin{bmatrix} \cos(\alpha_\Omega(t)) & -\sin(\alpha_\Omega(t)) & 0 \\ \sin(\alpha_\Omega(t)) & \cos(\alpha_\Omega(t)) & 0 \\ 0 & 0 & 1 \end{bmatrix}. \tag{7.67}$$

For the sake of simplicity, the orientation of the inertial reference frame may be chosen such that one of its axes represents the axis of rotation. In the case of Eq. (7.67), the rotation occurs around the third axis of the inertial reference frame.

7.4.2 Transformation Properties

The angle $\alpha_\Omega(t)$ may be expressed in terms of the angular velocity $\Omega(t)$ as follows:

$$\alpha_\Omega(t) = \int \Omega(t)\,\mathrm{d}t. \tag{7.68}$$

Then the derivatives in time of the rotational transformation $\mathbf{T}_\Omega(t)$, as given by Eq. (7.67), are of the following form:

$$\mathbf{T}_{\Omega,t}(t) = \Omega(t)\,\mathbf{T}'_\Omega(t), \qquad \mathbf{T}_{\Omega,tt}(t) = \Omega_{,t}(t)\,\mathbf{T}'_\Omega(t) + \Omega^2(t)\,\mathbf{T}''_\Omega(t). \tag{7.69}$$

The matrices $\mathbf{T}'_\Omega(t)$ and $\mathbf{T}''_\Omega(t)$ contained therein represent the external derivatives and consequently read

$$\mathbf{T}'_\Omega(t) = \begin{bmatrix} -\sin(\alpha_\Omega(t)) & -\cos(\alpha_\Omega(t)) & 0 \\ \cos(\alpha_\Omega(t)) & -\sin(\alpha_\Omega(t)) & 0 \\ 0 & 0 & 0 \end{bmatrix}, \tag{7.70a}$$

$$\mathbf{T}''_\Omega(t) = \begin{bmatrix} \cos(\alpha_\Omega(t)) & -\sin(\alpha_\Omega(t)) & 0 \\ \sin(\alpha_\Omega(t)) & \cos(\alpha_\Omega(t)) & 0 \\ 0 & 0 & 0 \end{bmatrix}. \tag{7.70b}$$

In the subsequent derivation, products of the matrix transpose of the transformation $\mathbf{T}_\Omega(t)$ with itself or its derivatives will appear. The decisive property of these products is a separation of the time-dependent components from the matrix structure, such that the angular velocity $\Omega(t)$ and its derivative turn up only as scalar factors:

$$\mathbf{T}_\Omega^T(t)\,\mathbf{T}_\Omega(t) = \mathbf{I}, \tag{7.71a}$$

$$\mathbf{T}_\Omega^T(t)\,\mathbf{T}_{\Omega,t}(t) = \Omega(t)\,\mathbf{I}', \tag{7.71b}$$

$$\mathbf{T}_\Omega^T(t)\,\mathbf{T}_{\Omega,tt}(t) = \Omega_{,t}(t)\,\mathbf{I}' + \Omega^2(t)\,\mathbf{I}''. \tag{7.71c}$$

The matrices $\mathbf{I}$, $\mathbf{I}'$, and $\mathbf{I}''$ are the identity matrix, and are filled with an antimetric submatrix and a negated identity submatrix, respectively:

$$\mathbf{I} = \begin{bmatrix} 1 & 0 & 0 \\ 0 & 1 & 0 \\ 0 & 0 & 1 \end{bmatrix}, \qquad \mathbf{I}' = \begin{bmatrix} 0 & -1 & 0 \\ 1 & 0 & 0 \\ 0 & 0 & 0 \end{bmatrix}, \qquad \mathbf{I}'' = \begin{bmatrix} -1 & 0 & 0 \\ 0 & -1 & 0 \\ 0 & 0 & 0 \end{bmatrix}. \tag{7.72}$$

Analogous considerations also hold for the other above-mentioned transformations of Eq. (7.66). However, when products of such matrices with incorporated time dependence are nested, complications arise as soon as the central product contains a derivative. Thus, time-dependent matrices do not occur, for example, in the product $\mathbf{T}_1^T(t)\mathbf{T}_\Omega^T(t)\mathbf{T}_\Omega(t)\mathbf{T}_1(t)$, which still yields the identity matrix, but cannot be avoided for the likes of $\mathbf{T}_1^T(t)\mathbf{T}_\Omega^T(t)\mathbf{T}_{\Omega,t}(t)\mathbf{T}_1(t)$.

8

Virtual Work Statements

To determine the equations of equilibrium as well as the constitutive relations of the beam, the principle of virtual work may be applied and its individual contributions be examined, respectively. Thus, the foundations for an analytic solution with regard to the statics of the non-rotating structure can be provided. Furthermore, the principle of virtual work will serve to set up the equations of motion in consideration of the dynamics of the rotating structure. This, in addition, requires the study of inertia effects and the inclusion of stiffening effects due to kinematic non-linearity with reference to relatively slender and flexible beams. The derivation of the principle of virtual work for the general case is presented in Section 3.4, and it will now be adapted and extended to depict adaptive thin-walled beams. Therefore, the various virtual work contributions will be discussed individually.

8.1 Internal Virtual Work

The virtual work of internal contributions is assembled in Section 3.4.6 from the virtual strain energy and virtual work of internal charges, as supplied by the principle of virtual displacements and of virtual electric potential, respectively. In Eq. (3.63), the virtual work of internal contributions is given for a volumetric object. The preceding analysis accomplished a reduction to two dimensions for the shell-like wall and to one dimension for the beam. Consequently, the expression for the virtual work of internal contributions may be reformulated for the wall $\delta\mathcal{U}(t)$ and for the beam $\delta\breve{\mathcal{U}}(t)$ as follows:

$$\delta\breve{\mathcal{U}}(t) = \int_X \delta\breve{\boldsymbol{\chi}}^T(x)\,\breve{\boldsymbol{L}}(x,t)\,\mathrm{d}x, \tag{8.1a}$$

$$\updownarrow$$

$$\begin{aligned}\delta\mathcal{U}(t) &= \int_X \int_S \delta\boldsymbol{\chi}^T(x,s)\,\boldsymbol{L}(x,s,t)\,\mathrm{d}s\,\mathrm{d}x \\ &= \int_X \delta\breve{\boldsymbol{\chi}}^T(x) \int_S \mathbb{J}^T(s)\,\boldsymbol{L}(x,s,t)\,\mathrm{d}s\,\mathrm{d}x.\end{aligned} \tag{8.1b}$$

T.H. Brockmann, *Theory of Adaptive Fiber Composites*,
Solid Mechanics and Its Applications 161,

In the lower line, use has been made of the relation between strain and electric field strength measures of wall and beam, provided by Eq. (7.33) and adapted to the virtual expressions.

8.1.1 Internal Loads of Beam and Wall

As a matter of course, the virtual work needs to be independent of the description. Thus, equating Eqs. (8.1) allows us to associate the internal mechanical as well as electric loads of beam $\breve{\boldsymbol{L}}(x,t)$ and wall $\boldsymbol{L}(x,s,t)$:

$$\delta\mathcal{U}\left(t\right)=\delta\breve{\mathcal{U}}\left(t\right)\quad\rightarrow\quad\breve{\boldsymbol{L}}\left(x,t\right)=\int_{S}\mathbb{J}^{T}\left(s\right)\boldsymbol{L}\left(x,s,t\right)\,\mathrm{d}s. \tag{8.2}$$

Obtaining the entries of the matrix $\mathbb{J}(s)$ of Eq. (7.33) from Eqs. (7.31) and (7.32) leads, with the internal loads $\boldsymbol{L}(x,s,t)$ of the wall as listed in Eq. (6.6), to

$$\breve{\boldsymbol{L}}\left(x,t\right)=\begin{Bmatrix}\breve{N}(x,t)\\ \breve{Q}_{y}(x,t)\\ \breve{Q}_{z}(x,t)\\ \breve{M}_{x}(x,t)\\ \breve{M}_{y}(x,t)\\ \breve{M}_{z}(x,t)\\ \breve{Q}_{w}(x,t)\\ -\\ \breve{G}^{c}\left(x,t\right)\\ \breve{G}^{d}\left(x,t\right)\\ \vdots\end{Bmatrix}=\begin{Bmatrix}\int_{S}N_{x}\left(x,s,t\right)\,\mathrm{d}s\\ \int_{S}y_{,s}\left(s\right)N_{xs}\left(x,s,t\right)+\frac{1}{2}z_{,ss}\left(s\right)M_{xs}\left(x,s,t\right)\,\mathrm{d}s\\ \int_{S}z_{,s}\left(s\right)N_{xs}\left(x,s,t\right)-\frac{1}{2}y_{,ss}\left(s\right)M_{xs}\left(x,s,t\right)\,\mathrm{d}s\\ \int_{S}\Phi\left(s\right)N_{xs}\left(x,s,t\right)-(2+\frac{1}{2}\frac{\Phi(s)}{R(s)})M_{xs}\left(x,s,t\right)\,\mathrm{d}s\\ \int_{S}z\left(s\right)N_{x}\left(x,s,t\right)+y_{,s}\left(s\right)M_{xx}\left(x,s,t\right)\,\mathrm{d}s\\ \int_{S}-y\left(s\right)N_{x}\left(x,s,t\right)+z_{,s}\left(s\right)M_{xx}\left(x,s,t\right)\,\mathrm{d}s\\ \int_{S}\Theta\left(s\right)N_{x}\left(x,s,t\right)-r_{s}\left(s\right)M_{xx}\left(x,s,t\right)\,\mathrm{d}s\\ -\\ \int_{S}p^{c}\left(s\right)G_{3}^{c}\left(x,s,t\right)\,\mathrm{d}s\\ \int_{S}p^{d}\left(s\right)G_{3}^{d}\left(x,s,t\right)\,\mathrm{d}s\\ \vdots\end{Bmatrix}. \tag{8.3}$$

8.1.2 Constitutive Relation

The constitutive relation of an adaptive laminated composite shell is given in Eq. (6.6). Being considered for the thin wall of the beam, the lines, respectively columns, associated with the cross-sectional strain component $\varepsilon_{s}^{0}(x,s)$ and bending curvature $\kappa_{s}(x,s)$ can be dropped in accordance with Remark 7.4. To comply with the specification of a prismatic beam in Remark 7.1, also with regard to the material properties, the latter need to be constant along the lengthwise direction and thus the constitutive matrix $\mathbb{K}(s)$ only depends on the cross-sectional coordinate. The constitutive relation of the wall and the corresponding formulation for the beam with the constitutive matrix $\mathbb{P}$ then

read:

$$\boldsymbol{L}(x,s,t) = \mathbb{K}(s)\,\boldsymbol{\chi}(x,s,t)\,, \qquad \breve{\boldsymbol{L}}(x,t) = \mathbb{P}\breve{\boldsymbol{\chi}}(x,t)\,. \tag{8.4}$$

Insertion of these constitutive relations into the virtual work of internal loads of the wall $\delta\mathcal{U}(t)$ and of the beam $\delta\breve{\mathcal{U}}(t)$ as expressed by Eqs. (8.1) results in

$$\delta\breve{\mathcal{U}}(t) = \int_X \delta\breve{\boldsymbol{\chi}}^T(x)\,\mathbb{P}\breve{\boldsymbol{\chi}}(x,t)\,\mathrm{d}x, \tag{8.5a}$$

$$\updownarrow$$

$$\begin{aligned}\delta\mathcal{U}(t) &= \int_X \int_S \delta\boldsymbol{\chi}^T(x,s)\,\mathbb{K}(s)\,\boldsymbol{\chi}(x,s,t)\,\mathrm{d}s\,\mathrm{d}x \\ &= \int_X \delta\breve{\boldsymbol{\chi}}^T(x) \int_S \mathbb{J}^T(s)\,\mathbb{K}(s)\,\mathbb{J}(s)\,\mathrm{d}s\breve{\boldsymbol{\chi}}(x,t)\,\mathrm{d}x.\end{aligned} \tag{8.5b}$$

For the lower line, use has been made again of the relation between strain and electric field strength measures of wall and beam provided by Eq. (7.33). Similarly, the constitutive matrix of the beam may be identified:

$$\delta\mathcal{U}(t) = \delta\breve{\mathcal{U}}(t) \quad \rightarrow \quad \mathbb{P} = \int_S \mathbb{J}^T(s)\,\mathbb{K}(s)\,\mathbb{J}(s)\,\mathrm{d}s. \tag{8.6}$$

8.1.3 Constitutive Coefficients

For the considered beams of arbitrary cross-sections with anisotropic walls and adaptive capabilities, a multitude of mechanical and electromechanical coupling mechanisms arise. They are reflected in the off-diagonal entries of the beam constitutive matrix $\mathbb{P}$. As defined in Eq. (8.6), the latter contains the geometry and warping functions responsible for couplings that may be attributed to the cross-sectional level, as well as the constitutive coefficients of the shell. These entries of the matrix $\mathbb{K}(s)$ may be again assigned to two different coupling levels. Coupling on the laminae level is founded on the existence of associated off-diagonal entries in the property matrix $\mathbb{Q}$ of the individual laminae, see Eq. (4.31). It may also appear in the case of symmetric laminates. Coupling on the laminate level, in contrast stems from a non-symmetric set-up of the laminate. For the case at hand, the shell stiffness coefficients $\grave{\mathtt{A}}_{13}(s)$, $\grave{\mathtt{B}}_{13}(s)$, $\grave{\mathtt{B}}_{31}(s)$, and $\grave{\mathtt{D}}_{13}(s)$ represent the mechanical coupling on the laminae level, while the coefficients $\grave{\mathtt{B}}_{11}(s)$, $\grave{\mathtt{B}}_{13}(s)$, $\grave{\mathtt{B}}_{31}(s)$, $\grave{\mathtt{B}}_{33}(s)$ characterize the mechanical coupling on the laminate level. Since the coefficients $\grave{\mathtt{B}}_{13}(s)$ and $\grave{\mathtt{B}}_{31}(s)$ are associated with both levels, they only exist when both requirements are fulfilled. Analogously, also the electromechanical coefficients can be associated with the constitutive coupling levels. Such a classification may be used to examine the consequences of simplifying assumptions on the different levels.

Mechanical Coefficients on the Principal Diagonal

The beam stiffness coefficients on the principal diagonal of the matrix $\mathbb{P}$ associated with extension, $\mathtt{P}_{11}$, bending, $\mathtt{P}_{55}$, $\mathtt{P}_{66}$, and warping, $\mathtt{P}_{77}$, depend on the shell stiffnesses associated with the lengthwise extension, $\grave{\mathtt{A}}_{11}(s)$, bending, $\check{\mathtt{D}}_{11}(s)$, and the coupling $\check{\mathtt{B}}_{11}(s)$:

$$\mathtt{P}_{11} = \int_S \grave{\mathtt{A}}_{11}(s)\, \mathrm{d}s, \tag{8.7a}$$

$$\mathtt{P}_{55} = \int_S \grave{\mathtt{A}}_{11}(s)\, z^2(s) + 2\check{\mathtt{B}}_{11}(s)\, z(s)\, y_{,s}(s) + \check{\mathtt{D}}_{11}(s)\, y_{,s}^2(s)\, \mathrm{d}s, \tag{8.7b}$$

$$\mathtt{P}_{66} = \int_S \grave{\mathtt{A}}_{11}(s)\, y^2(s) - 2\check{\mathtt{B}}_{11}(s)\, y(s)\, z_{,s}(s) + \check{\mathtt{D}}_{11}(s)\, z_{,s}^2(s)\, \mathrm{d}s, \tag{8.7c}$$

$$\mathtt{P}_{77} = \int_S \grave{\mathtt{A}}_{11}(s)\, \Theta^2(s) - 2\check{\mathtt{B}}_{11}(s)\, \Theta(s)\, r_s(s) + \check{\mathtt{D}}_{11}(s)\, r_s^2(s)\, \mathrm{d}s. \tag{8.7d}$$

The other beam stiffness coefficients on the principal diagonal associated with shear, $\mathtt{P}_{22}$, $\mathtt{P}_{33}$, and torsion, $\mathtt{P}_{44}$, are functions of the shell stiffnesses associated with shear, $\grave{\mathtt{A}}_{33}(s)$, twist, $\check{\mathtt{D}}_{33}(s)$, and the coupling $\check{\mathtt{B}}_{33}(s)$:

$$\mathtt{P}_{22} = \int_S \grave{\mathtt{A}}_{33}(s)\, y_{,s}^2(s) + \check{\mathtt{B}}_{33}(s)\, y_{,s}(s)\, z_{,ss}(s) + \check{\mathtt{D}}_{33}(s)\, \frac{z_{,ss}^2(s)}{4}\, \mathrm{d}s, \tag{8.8a}$$

$$\mathtt{P}_{33} = \int_S \grave{\mathtt{A}}_{33}(s)\, z_{,s}^2(s) - \check{\mathtt{B}}_{33}(s)\, z_{,s}(s)\, y_{,ss}(s) + \check{\mathtt{D}}_{33}(s)\, \frac{y_{,ss}^2(s)}{4}\, \mathrm{d}s, \tag{8.8b}$$

$$\begin{aligned}\mathtt{P}_{44} = \int_S \grave{\mathtt{A}}_{33}(s)\, \Phi^2(s) - 2\check{\mathtt{B}}_{33}(s)\, \Phi(s) \left(2 + \frac{\Phi(s)}{2R(s)}\right) \\ + \check{\mathtt{D}}_{33}(s) \left(2 + \frac{\Phi(s)}{2R(s)}\right)^2 \mathrm{d}s.\end{aligned} \tag{8.8c}$$

Off-Diagonal Mechanical Coefficients without Laminae Level Coupling

Likewise, the beam stiffness coefficients which couple extension, bending in both directions, and warping depend on the shell stiffnesses associated with the lengthwise extension, bending, and coupling between them:

$$\mathtt{P}_{15} = \int_S \grave{\mathtt{A}}_{11}(s)\, z(s) + \check{\mathtt{B}}_{11}(s)\, y_{,s}(s)\, \mathrm{d}s, \tag{8.9a}$$

$$\mathtt{P}_{16} = \int_S -\grave{\mathtt{A}}_{11}(s)\, y(s) + \check{\mathtt{B}}_{11}(s)\, z_{,s}(s)\, \mathrm{d}s, \tag{8.9b}$$

$$\mathtt{P}_{17} = \int_S \grave{\mathtt{A}}_{11}(s)\, \Theta(s) - \check{\mathtt{B}}_{11}(s)\, r_s(s)\, \mathrm{d}s, \tag{8.9c}$$

$$\mathtt{P}_{56} = \int_S -\grave{\mathtt{A}}_{11}(s)\, y(s)\, z(s) - \grave{\mathtt{B}}_{11}(s)\,(y(s)\, y_{,s}(s) - z(s)\, z_{,s}(s)) + \grave{\mathtt{D}}_{11}(s)\, y_{,s}(s)\, z_{,s}(s)\, \mathrm{d}s, \tag{8.9d}$$

$$\mathtt{P}_{57} = \int_S \grave{\mathtt{A}}_{11}(s)\, \Theta(s)\, z(s) + \grave{\mathtt{B}}_{11}(s)\,(\Theta(s)\, y_{,s}(s) - r_s(s)\, z(s)) - \mathtt{D}_{11}(s)\, r_s(s)\, y_{,s}(s)\, \mathrm{d}s, \tag{8.9e}$$

$$\mathtt{P}_{67} = \int_S -\grave{\mathtt{A}}_{11}(s)\, \Theta(s)\, y(s) + \grave{\mathtt{B}}_{11}(s)\,(\Theta(s)\, z_{,s}(s) + r_s(s)\, y(s)) - \grave{\mathtt{D}}_{11}(s)\, r_s(s)\, z_{,s}(s)\, \mathrm{d}s. \tag{8.9f}$$

The beam stiffness coefficients, which couple shear in both directions and torsion, are functions of the shell stiffnesses associated with shear, twist, and the coupling between them:

$$\mathtt{P}_{23} = \int_S \grave{\mathtt{A}}_{33}(s)\, y_{,s}(s)\, z_{,s}(s) + \frac{\grave{\mathtt{B}}_{33}(s)}{2}\,(z_{,s}(s)\, z_{,ss}(s) - y_{,s}(s)\, y_{,ss}(s)) - \grave{\mathtt{D}}_{33}(s)\, \frac{y_{,ss}(s)\, z_{,ss}(s)}{4}\, \mathrm{d}s, \tag{8.10a}$$

$$\mathtt{P}_{24} = \int_S \grave{\mathtt{A}}_{33}(s)\, \Phi(s)\, y_{,s}(s) + \grave{\mathtt{B}}_{33}(s) \left(\Phi(s)\, \frac{z_{,ss}(s)}{2} - \left(2 + \frac{\Phi(s)}{2R(s)}\right) y_{,s}(s)\right) - \grave{\mathtt{D}}_{33}(s) \left(2 + \frac{\Phi(s)}{2R(s)}\right) \frac{z_{,ss}(s)}{2}\, \mathrm{d}s, \tag{8.10b}$$

$$\mathtt{P}_{34} = \int_S \grave{\mathtt{A}}_{33}(s)\, \Phi(s)\, z_{,s}(s) - \grave{\mathtt{B}}_{33}(s) \left(\Phi(s)\, \frac{y_{,ss}(s)}{2} + \left(2 + \frac{\Phi(s)}{2R(s)}\right) z_{,s}(s)\right) + \grave{\mathtt{D}}_{33}(s) \left(2 + \frac{\Phi(s)}{2R(s)}\right) \frac{y_{,ss}(s)}{2}\, \mathrm{d}s. \tag{8.10c}$$

Off-Diagonal Mechanical Coefficients with Laminae Level Coupling

The remaining beam stiffness coefficients depend on the shell stiffnesses that result from coupling on the laminae level. This concerns the coupling between shear and extension, $\grave{\mathtt{A}}_{13}(s)$, between extension and lengthwise curvature, $\grave{\mathtt{B}}_{13}(s)$ and $\grave{\mathtt{B}}_{31}(s)$, as well as between lengthwise curvature and twist, $\grave{\mathtt{D}}_{13}(s)$. So, the beam stiffness coefficients responsible for the coupling of extension with shear and torsion read:

$$\mathtt{P}_{12} = \int_S \grave{\mathtt{A}}_{13}(s)\, y_{,s}(s) + \frac{\grave{\mathtt{B}}_{13}(s)}{2} z_{,ss}(s)\, \mathrm{d}s, \tag{8.11a}$$

$$\mathtt{P}_{13} = \int_S \grave{\mathtt{A}}_{13}(s)\, z_{,s}(s) - \frac{\grave{\mathtt{B}}_{13}(s)}{2} y_{,ss}(s)\, \mathrm{d}s, \tag{8.11b}$$

$$\mathtt{P}_{14} = \int_S \grave{\mathtt{A}}_{13}(s)\, \Phi(s) - \grave{\mathtt{B}}_{13}(s) \left(2 + \frac{\Phi(s)}{2R(s)}\right) \mathrm{d}s. \tag{8.11c}$$

The beam stiffness coefficients in charge of the coupling between shear and bending have the subsequent form:

$$\begin{aligned}\mathtt{P}_{25} = \int_S & \grave{\mathtt{A}}_{13}(s)\, z(s)\, y_{,s}(s) + \grave{\mathtt{B}}_{13}(s)\, z(s)\, \frac{z_{,ss}(s)}{2} + \grave{\mathtt{B}}_{31}(s)\, y_{,s}^2(s) \\ & + \grave{\mathtt{D}}_{13}(s)\, y_{,s}(s)\, \frac{z_{,ss}(s)}{2}\, \mathrm{d}s,\end{aligned} \tag{8.12a}$$

$$\begin{aligned}\mathtt{P}_{36} = \int_S & -\grave{\mathtt{A}}_{13}(s)\, y(s)\, z_{,s}(s) + \grave{\mathtt{B}}_{13}(s)\, y(s)\, \frac{y_{,ss}(s)}{2} + \grave{\mathtt{B}}_{31}(s)\, z_{,s}^2(s) \\ & - \grave{\mathtt{D}}_{13}(s)\, z_{,s}(s)\, \frac{y_{,ss}(s)}{2}\, \mathrm{d}s,\end{aligned} \tag{8.12b}$$

$$\begin{aligned}\mathtt{P}_{26} = \int_S & -\grave{\mathtt{A}}_{13}(s)\, y(s)\, y_{,s}(s) - \grave{\mathtt{B}}_{13}(s)\, y(s)\, \frac{z_{,ss}(s)}{2} + \grave{\mathtt{B}}_{31}(s)\, y_{,s}(s)\, z_{,s}(s) \\ & + \grave{\mathtt{D}}_{13}(s)\, z_{,s}(s)\, \frac{z_{,ss}(s)}{2}\, \mathrm{d}s,\end{aligned} \tag{8.12c}$$

$$\begin{aligned}\mathtt{P}_{35} = \int_S & \grave{\mathtt{A}}_{13}(s)\, z(s)\, z_{,s}(s) - \grave{\mathtt{B}}_{13}(s)\, z(s)\, \frac{y_{,ss}(s)}{2} + \grave{\mathtt{B}}_{31}(s)\, y_{,s}(s)\, z_{,s}(s) \\ & - \grave{\mathtt{D}}_{13}(s)\, y_{,s}(s)\, \frac{y_{,ss}(s)}{2}\, \mathrm{d}s.\end{aligned} \tag{8.12d}$$

The beam stiffness coefficients accounting for the coupling of bending and twist are given as follows:

$$\begin{aligned}\mathtt{P}_{45} = \int_S & \mathtt{A}_{13}(s)\, \Phi(s)\, z(s) - \mathtt{B}_{13}(s) \left(\left(2 + \frac{\Phi(s)}{2R(s)}\right) z(s) - \Phi(s)\, y_{,s}(s)\right) \\ & - \mathtt{D}_{13}(s) \left(2 + \frac{\Phi(s)}{2R(s)}\right) y_{,s}(s)\, \mathrm{d}s,\end{aligned} \tag{8.13a}$$

$$\begin{aligned}\mathtt{P}_{46} = \int_S & -\mathtt{A}_{13}(s)\, \Phi(s)\, y(s) + \mathtt{B}_{13}(s) \left(\left(2 + \frac{\Phi(s)}{2R(s)}\right) y(s) + \Phi(s)\, z_{,s}(s)\right) \\ & - \mathtt{D}_{13}(s) \left(2 + \frac{\Phi(s)}{2R(s)}\right) z_{,s}(s)\, \mathrm{d}s.\end{aligned} \tag{8.13b}$$

Finally, the beam stiffness coefficients associated with the coupling of shear and torsion with warping read:

$$\mathtt{P}_{27} = \int_S \grave{\mathtt{A}}_{13}(s)\,\Theta(s)\,y_{,s}(s) + \grave{\mathtt{B}}_{13}(s)\,\Theta(s)\,\frac{z_{,ss}(s)}{2} - \grave{\mathtt{B}}_{31}(s)\,r_s(s)\,y_{,s}(s) - \grave{\mathtt{D}}_{13}(s)\,r_s(s)\,\frac{z_{,ss}(s)}{2}\,\mathrm{d}s, \tag{8.14a}$$

$$\mathtt{P}_{37} = \int_S \grave{\mathtt{A}}_{13}(s)\,\Theta(s)\,z_{,s}(s) - \grave{\mathtt{B}}_{13}(s)\,\Theta(s)\,\frac{y_{,ss}(s)}{2} - \grave{\mathtt{B}}_{31}(s)\,r_s(s)\,z_{,s}(s) + \grave{\mathtt{D}}_{13}(s)\,r_s(s)\,\frac{y_{,ss}(s)}{2}\,\mathrm{d}s, \tag{8.14b}$$

$$\mathtt{P}_{47} = \int_S \grave{\mathtt{A}}_{13}(s)\,\Phi(s)\,\Theta(s) - \grave{\mathtt{B}}_{13}(s)\left(2+\frac{\Phi(s)}{2R(s)}\right)\Theta(s) - \grave{\mathtt{B}}_{31}(s)\,\Phi(s)\,r_s(s) + \grave{\mathtt{D}}_{13}(s)\left(2+\frac{\Phi(s)}{2R(s)}\right)r_s(s)\,\mathrm{d}s. \tag{8.14c}$$

Electromechanical Coefficients

Corresponding to the mechanical coefficients, those representing the electromechanical coupling due to the piezoelectric effect also may be arranged. The induction and detection of extension, bending, and warping of the beam depends on the electromechanical shell coefficients associated with extension, $\grave{\mathtt{A}}^c_{14}(s)$, and lengthwise curvature, $\grave{\mathtt{B}}^c_{14}(s)$:

$$\mathtt{P}_{18} = \int_S \grave{\mathtt{A}}^c_{14}(s)\,p^c(s)\,\mathrm{d}s, \tag{8.15a}$$

$$\mathtt{P}_{58} = \int_S \left(\grave{\mathtt{A}}^c_{14}(s)\,z(s) + \grave{\mathtt{B}}^c_{14}(s)\,y_{,s}(s)\right)p^c(s)\,\mathrm{d}s, \tag{8.15b}$$

$$\mathtt{P}_{68} = \int_S \left(-\grave{\mathtt{A}}^c_{14}(s)\,y(s) + \grave{\mathtt{B}}^c_{14}(s)\,z_{,s}(s)\right)p^c(s)\,\mathrm{d}s, \tag{8.15c}$$

$$\mathtt{P}_{78} = \int_S \left(\grave{\mathtt{A}}^c_{14}(s)\,\Theta(s) - \grave{\mathtt{B}}^c_{14}(s)\,r_s(s)\right)p^c(s)\,\mathrm{d}s. \tag{8.15d}$$

The induction and detection of shear and torsion of the beam is governed by those electromechanical shell coefficients associated with shear, $\grave{\mathtt{A}}^c_{34}(s)$, and twist, $\grave{\mathtt{B}}^c_{34}(s)$:

$$\mathtt{P}_{28} = \int_S \left(\grave{\mathtt{A}}^c_{34}(s)\,y_{,s}(s) + \grave{\mathtt{B}}^c_{34}(s)\,\frac{z_{,ss}(s)}{2}\right)p^c(s)\,\mathrm{d}s, \tag{8.16a}$$

$$\mathtt{P}_{38} = \int_S \left(\grave{\mathtt{A}}^c_{34}(s)\,z_{,s}(s) - \grave{\mathtt{B}}^c_{34}(s)\,\frac{y_{,ss}(s)}{2}\right)p^c(s)\,\mathrm{d}s, \tag{8.16b}$$

$$\mathtt{P}_{48} = \int_S \left(\grave{\mathtt{A}}^c_{34}(s)\,\Phi(s) - \grave{\mathtt{B}}^c_{34}(s)\left(2+\frac{\Phi(s)}{2R(s)}\right)\right)p^c(s)\,\mathrm{d}s. \tag{8.16c}$$

The dielectric permittivity properties, summarized for the shell in the coefficient $\grave{\mathtt{A}}^c_{44}(s)$, are considered for the beam by integration over the cross-section:

$$\mathtt{P}_{88} = \int_S \tilde{\mathtt{A}}^c_{44}(s)\,(p^c(s))^2\,\mathrm{d}s = \int_S \tilde{\mathtt{A}}^c_{44}(s)\,\mathrm{d}s. \tag{8.17}$$

For further groups of electrically paralleled laminae, the formulation is analogous.

Open Cross-Section Peculiarity

A prominent property of a non-branched and branched open cross-section as well as of open branches within a combined cross-section will be marked here. By virtue of Eqs. (7.42) and (7.59), a purely geometric warping function is found in these cases, as exemplarily shown for the non-branched open cross-section in Eq. (7.61). Accordingly, the abbreviation $\Phi(s)$ introduced in Eq. (7.27) vanishes:

$$\Phi^{\cup}(s) = 0. \tag{8.18}$$

This has thorough consequences for all torsion-related entries of the beam constitutive matrix $\mathbb{P}$, since it eliminates the dependence on the membrane properties stemming from the shell constitutive sub-matrix $\mathbb{A}(s)$. The torsional stiffness $\mathtt{P}_{44}$ of Eq. (8.8c) is only governed by the twisting stiffness of the wall:

$$\mathtt{P}^{\cup}_{44} = \int_S 4\tilde{\mathtt{D}}_{33}(s)\,\mathrm{d}s. \tag{8.19}$$

Since a diagonal entry of the constitutive matrix must not be zero, it is explained why those thin-walled beam theories, which only account for the membrane response, are limited to closed cross-sections. The above argument correspondingly applies to contributions of open branches within a combined cross-section.

8.1.4 Partially Prescribed Electric Potential

In Section 4.5, the different variants of actuation and sensing with regard to the type of electric power supply and electric measurement, respectively, are discussed. For actuation in conjunction with a voltage source and sensing via current measurement, the electric potential is identified to be a prescribed quantity. Consequently, the variation of the corresponding electric field strength vanishes and the principle of virtual work therefore needs to be modified. To provide a general description, the vector of electric field strength $\breve{\boldsymbol{E}}(x,t)$, containing the values for all groups of electrically paralleled laminae, may be split into two parts, $\breve{\boldsymbol{E}}_{\dagger}(x,t)$ and $\breve{\boldsymbol{E}}_{\ddagger}(x,t)$. Herein, the unknown fields are elucidated by $()_{\dagger}$ and the prescribed fields by $()_{\ddagger}$. The virtual work of internal contributions, given by Eq. (8.5a), therefore can be rewritten as

$$\delta\breve{\mathcal{U}}(t) = \int_X \underbrace{\left\{\delta\breve{\boldsymbol{\varepsilon}}^T(x) \quad \delta\breve{\boldsymbol{E}}_\dagger^T(x) \quad \delta\breve{\boldsymbol{E}}_\ddagger^T(x)\right\}}_{\delta\boldsymbol{\chi}^T(x)} \underbrace{\begin{bmatrix} \mathbf{p} & \mathbf{p}_\dagger & \mathbf{p}_\ddagger \\ \mathbf{p}_\dagger^T & \mathbf{I}\boldsymbol{p}_\dagger & \mathbf{0} \\ \mathbf{p}_\ddagger^T & \mathbf{0} & \mathbf{I}\boldsymbol{p}_\ddagger \end{bmatrix}}_{\mathbb{P}} \underbrace{\begin{Bmatrix} \breve{\boldsymbol{\varepsilon}}(x,t) \\ \breve{\boldsymbol{E}}_\dagger(x,t) \\ \breve{\boldsymbol{E}}_\ddagger(x,t) \end{Bmatrix}}_{\breve{\boldsymbol{\chi}}(x,t)} \mathrm{d}x. \tag{8.20}$$

The decomposition of the constitutive matrix $\mathbb{P}$ of the beam reveals its purely mechanical part $\mathbf{p}$, its electromechanically coupled parts $\mathbf{p}_\dagger$ and $\mathbf{p}_\ddagger$, and its dielectric diagonal entries $\boldsymbol{p}_\dagger$ and $\boldsymbol{p}_\ddagger$. As addressed above, the virtual electric field strength of the prescribed fields vanishes and thus $\delta\breve{\boldsymbol{E}}_\ddagger(x) = \mathbf{0}$. The summary of vectors and matrices with regard to the remaining degrees of freedom of the beam, comes to

$$\delta\boldsymbol{\mu}(x) = \begin{Bmatrix} \delta\breve{\boldsymbol{\varepsilon}}(x) \\ \delta\breve{\boldsymbol{E}}_\dagger(x) \end{Bmatrix}, \qquad \mathbf{P} = \begin{bmatrix} \mathbf{p} & \mathbf{p}_\dagger \\ \mathbf{p}_\dagger^T & \mathbf{I}\boldsymbol{p}_\dagger \end{bmatrix}, \qquad \boldsymbol{\mu}(x,t) = \begin{Bmatrix} \breve{\boldsymbol{\varepsilon}}(x,t) \\ \breve{\boldsymbol{E}}_\dagger(x,t) \end{Bmatrix}. \tag{8.21}$$

Thus, the virtual work of internal contributions may be written in terms of functions of the mechanical and electric degrees of freedom in $\delta\breve{\mathcal{U}}^{me}(t)$ and electric parameters in $\delta\breve{\mathcal{U}}^{pe}(t)$ such that

$$\delta\breve{\mathcal{U}}(t) = \underbrace{\int_X \delta\breve{\boldsymbol{\mu}}^T(x)\,\mathbf{P}\breve{\boldsymbol{\mu}}(x,t)\,\mathrm{d}x}_{\delta\breve{\mathcal{U}}^{me}(t)} + \underbrace{\int_X \delta\breve{\boldsymbol{\varepsilon}}^T(x)\,\mathbf{p}_\ddagger\breve{\boldsymbol{E}}_\ddagger(x,t)\,\mathrm{d}x}_{\delta\breve{\mathcal{U}}^{pe}(t)}. \tag{8.22}$$

For obvious reasons, such a partition cannot be carried out before the constitutive relation is introduced. Nevertheless, the formulation with internal loads given by Eq. (8.1a) reduces for the vector $\breve{\boldsymbol{L}}_\dagger(x,t)$ of the mechanical loads and those electric loads not associated with an electric parameter, to

$$\delta\breve{\mathcal{U}}(t) = \int_X \delta\breve{\boldsymbol{\mu}}^T(x)\,\breve{\boldsymbol{L}}_\dagger(x,t)\,\mathrm{d}x. \tag{8.23}$$

8.2 External Virtual Work

Since beam theory is concerned with the representation of structures with essentially one dimension of extent, the mechanical and electric loads applied to volumes and areas in Eq. (3.62) need to be assigned to the beam reference line. The virtual work $\delta\breve{\mathcal{V}}^{me}(t)$ of such loads will be defined subsequently and, furthermore, the virtual work $\delta\breve{\mathcal{V}}^{dl}(t)$ of inertia loads will be derived for rotating systems. So, the virtual work of external loads altogether for the beam reads:

$$\delta\breve{\mathcal{V}}(t) = \delta\breve{\mathcal{V}}^{me}(t) + \delta\breve{\mathcal{V}}^{dl}(t). \tag{8.24}$$

8.2.1 Applied Load Contributions

The virtual work $\delta\breve{\mathcal{V}}^{me}(t)$ of applied mechanical and electric loads involves the virtual variant $\delta\breve{\boldsymbol{\nu}}(x)$ of the degrees of freedom $\breve{\boldsymbol{\nu}}(x,t)$ of the beam and the actual applied loads $\breve{\boldsymbol{l}}(x,t)$, resulting in

$$\delta\breve{\mathcal{V}}^{me}(t) = \int_X \delta\breve{\boldsymbol{\nu}}^T(x)\,\breve{\boldsymbol{l}}(x,t)\,\mathrm{d}x. \tag{8.25}$$

Therefore, only applied loads associated with a degree of freedom are considered, while consequently those associated with a parameter are discarded, corresponding to the nature of the employed electric circuits. The vector $\breve{\boldsymbol{\nu}}(x,t)$ is assembled from the mechanical degrees of freedom $\breve{\boldsymbol{u}}(x,t)$, which appear in Eq. (7.25), and from the electric degrees of freedom $\breve{\boldsymbol{\varphi}}(x,t)$, such that

$$\breve{\boldsymbol{\nu}}(x,t) = \begin{Bmatrix} \breve{\boldsymbol{u}}(x,t) \\ \breve{\boldsymbol{\varphi}}(x,t) \end{Bmatrix} \quad \text{with } \breve{\boldsymbol{\varphi}}(x,t) = \begin{Bmatrix} \varphi^c(x,t) & \varphi^d(x,t) & \dots \end{Bmatrix}^T, \tag{8.26}$$

$$\breve{\boldsymbol{u}}(x,t) = \begin{Bmatrix} u(x,t) & v(x,t) & w(x,t) & \phi(x,t) & \beta_y(x,t) & \beta_z(x,t) & \phi_{,x}(x,t) \end{Bmatrix}^T.$$

Applied mechanical loads $\breve{\boldsymbol{n}}(x,t)$ and applied electric loads $\breve{\boldsymbol{g}}(x,t)$ form the vector of actual applied loads $\breve{\boldsymbol{l}}(x,t)$. With the designation of its components in analogy to the internal loads of Eq. (8.3), it reads

$$\breve{\boldsymbol{l}}(x,t) = \begin{Bmatrix} \breve{\boldsymbol{n}}(x,t) \\ \breve{\boldsymbol{g}}(x,t) \end{Bmatrix} \quad \text{with } \breve{\boldsymbol{g}}(x,t) = \begin{Bmatrix} \breve{g}^c(x,t) & \breve{g}^d(x,t) & \dots \end{Bmatrix}^T, \tag{8.27}$$

$$\breve{\boldsymbol{n}}(x,t) = \begin{Bmatrix} \breve{n}(x,t) & \breve{q}_y(x,t) & \breve{q}_z(x,t) & \breve{m}_x(x,t) & \breve{m}_y(x,t) & \breve{m}_z(x,t) & \breve{q}_w(x,t) \end{Bmatrix}^T.$$

8.2.2 Inertia Load Contributions

D'Alembert's principle in the Lagrangian version has been obtained in Section 3.4.5 in terms of virtual displacements and actual accelerations. Since it needs to be accounted for a superimposed guided motion, the position $\boldsymbol{p}(x,s,t)$ in the inertial frame of reference, as described by Eq. (7.65), has to be taken into consideration. With the density $\rho(s,n)$ in accordance with Remark 7.1, the virtual work of inertia forces originating from Eq. (3.59) then reads

$$\delta\breve{\mathcal{V}}^{dl}(t) = -\int_\Lambda \delta\boldsymbol{p}^T(x,s,t)\,\boldsymbol{p}_{,tt}(x,s,t)\rho(s,n)\,\mathrm{d}V. \tag{8.28}$$

Taking the variation of Eq. (7.65), the global virtual position vector $\delta\boldsymbol{p}(x,s,t)$ in the inertial reference frame may be obtained in terms of the local virtual position vector $\delta\boldsymbol{p}_o(x,s)$ in the moving reference frame:

$$\delta\boldsymbol{p}(x,s,t) = \mathbf{T}_\Omega(t)\,\mathbf{T}_{321}(t)\,\delta\boldsymbol{p}_o(x,s). \tag{8.29}$$

Correspondingly, the acceleration $\boldsymbol{p}_{,tt}(x,s,t)$ as the second derivative of the global position can be gained from Eq. (7.65). When this is done in consideration of Eqs. (7.69) and (7.70) and the rotational properties of Eqs. (7.71) and (7.72) are introduced to the vector product in the integrand of Eq. (8.28), we obtain

$$\begin{aligned}
&\delta\boldsymbol{p}^T(x,s,t)\,\boldsymbol{p}_{,tt}(x,s,t)\\
&\quad=\delta\boldsymbol{p}_o^T(x,s)\mathbf{T}_{321}^T(t)\left(\Omega_{,t}(t)\,\mathbf{I}'+\Omega^2(t)\,\mathbf{I}''\right)\left(\boldsymbol{r}+\mathbf{T}_{321}(t)\,\boldsymbol{p}_o(x,s,t)\right)\\
&\qquad+2\delta\boldsymbol{p}_o^T(x,s)\mathbf{T}_{321}^T(t)\left(\Omega(t)\,\mathbf{I}'\right)\left(\mathbf{T}_{321}(t)\,\boldsymbol{p}_{o,t}(x,s,t)+\mathbf{T}_{321,t}(t)\,\boldsymbol{p}_o(x,s,t)\right)\\
&\qquad+\delta\boldsymbol{p}_o^T(x,s)\mathbf{T}_{321}^T(t)\\
&\qquad\quad\left(\mathbf{T}_{321}(t)\,\boldsymbol{p}_{o,tt}(x,s,t)+2\mathbf{T}_{321,t}(t)\,\boldsymbol{p}_{o,t}(x,s,t)+\mathbf{T}_{321,tt}(t)\,\boldsymbol{p}_o(x,s,t)\right).
\end{aligned}\tag{8.30}$$

In view of the above discussion on the transformation properties, it needs to be noted that Eq. (8.30) and thus the resulting equations of motion contain time-dependent matrices. The mathematical theory for such non-autonomous systems has primarily been developed with regard to a periodic dependence on time. The most prominent approaches to solve these systems are the methods of *Floquet* [75] and of *Hill* [95]. For further details, see *Prothmann* [146], *Gasch and Knothe* [78], or *Meirovitch* [125]. To pave the way for an eventually autonomous system with a less expensive theoretical framework, not to exceed the scope of the study at hand, we will abstain from a time-dependent orientation of the clamping of the beam.

Remark 8.1. The rotation around an axis of the inertial reference frame will be the only guided motion of the considered system.

Thus, the rotational transformation at the clamped end of the beam is restricted to a constant description of the orientation:

$$\mathbf{T}_{321}(t)=\mathbf{T}_{321}=\mathbf{T}_3\mathbf{T}_2\mathbf{T}_1\quad\text{with }\alpha_3(t)=\alpha_3,\ \alpha_2(t)=\alpha_2,\ \alpha_1(t)=\alpha_1.\tag{8.31}$$

To determine the virtual work of inertia forces in terms of the beam displacements, the latter are used to express the beam positions and the derivatives and variation thereof respectively, as governed by Eqs. (7.2) and (7.25):

$$\boldsymbol{p}_o(x,s,t)=\boldsymbol{P}_o(x,s)+\mathbf{K}(s)\,\breve{\boldsymbol{u}}(x,t)\quad\rightarrow\quad\begin{aligned}\boldsymbol{p}_{o,t}(x,s,t)&=\mathbf{K}(s)\,\breve{\boldsymbol{u}}_{,t}(x,t),\\ \boldsymbol{p}_{o,tt}(x,s,t)&=\mathbf{K}(s)\,\breve{\boldsymbol{u}}_{,tt}(x,t),\\ \delta\boldsymbol{p}_o(x,s)&=\mathbf{K}(s)\,\delta\breve{\boldsymbol{u}}(x).\end{aligned}\tag{8.32}$$

Then substitution of Eq. (8.30) into (8.28) leads, with simplifications due to Eq. (8.31), to an expression with the following classification of inertia terms:

$$
\begin{aligned}
\delta\breve{\mathcal{V}}^{dl}(t) = -\int_X \delta\breve{\boldsymbol{u}}^T(x)\,(& \\
& \mathbf{M}''\breve{\boldsymbol{u}}_{,tt}(x,t) && \text{relative acc.—effects without rotation}\\
& +\mathbf{M}'2\Omega(t)\,\breve{\boldsymbol{u}}_{,t}(x,t) && \text{Coriolis acc.—gyroscopic effects}\\
& +\mathbf{M}\Omega^2(t)\,\breve{\boldsymbol{u}}(x,t) && \text{centrifugal acc.—effects due to deformation}\\
& +\boldsymbol{m}(x)\,\Omega^2(t) && \text{centrifugal acc.—effects in initial state}\\
& +\mathbf{M}'\Omega_{,t}(t)\,\breve{\boldsymbol{u}}(x,t) && \text{angular acc.—effects due to deformation}\\
& +\boldsymbol{m}'(x)\,\Omega_{,t}(t) && \text{angular acc.—effects in initial state}\\
&)\,\mathrm{d}x. && (8.33)
\end{aligned}
$$

The appearing matrices and vectors contain the integration over the cross-section and, as anticipated, do not vary with time:

$$\mathbf{M}'' = \int_S \mathbf{K}^T(s)\,\mathbf{K}(s)\int_N \rho(s,n)\;\mathrm{d}n\,\mathrm{d}s, \tag{8.34a}$$

$$\mathbf{M}' = \int_S \mathbf{K}^T(s)\,\mathbf{T}_{321}^T\mathbf{I}'\mathbf{T}_{321}\mathbf{K}(s)\int_N \rho(s,n)\;\mathrm{d}n\,\mathrm{d}s, \tag{8.34b}$$

$$\mathbf{M} = \int_S \mathbf{K}^T(s)\,\mathbf{T}_{321}^T\mathbf{I}''\mathbf{T}_{321}\mathbf{K}(s)\int_N \rho(s,n)\;\mathrm{d}n\,\mathrm{d}s, \tag{8.34c}$$

$$\boldsymbol{m}'(x) = \int_S \mathbf{K}^T(s)\,\mathbf{T}_{321}^T\mathbf{I}'(\boldsymbol{r}+\mathbf{T}_{321}\boldsymbol{P}_o(x,s))\int_N \rho(s,n)\;\mathrm{d}n\,\mathrm{d}s, \tag{8.34d}$$

$$\boldsymbol{m}(x) = \int_S \mathbf{K}^T(s)\,\mathbf{T}_{321}^T\mathbf{I}''(\boldsymbol{r}+\mathbf{T}_{321}\boldsymbol{P}_o(x,s))\int_N \rho(s,n)\;\mathrm{d}n\,\mathrm{d}s. \tag{8.34e}$$

As already obvious from the classification of terms in Eq. (8.33), the inertia properties contained in the matrix $\mathbf{M}''$ are those of the non-rotating beam. Therefore, they are necessarily independent of its orientation, which is assured by the transformation property of the sequence of time-independent matrices such that $\mathbf{T}_{321}^T\mathbf{T}_{321} = \mathbf{I}$.

8.2.3 Equilibrium and Boundary Conditions

With the aid of the principle of virtual work, the equilibrium and boundary conditions can be obtained for the quasi-static case, where, in principle, loads may change over time but inertia effects are not considered. The contributions required for this purpose have been already obtained and will be joined together in the following. The internal virtual work $\delta\breve{\mathcal{U}}(t)$ is given by Eq. (8.23), while the external virtual work $\delta\breve{\mathcal{V}}(t)$ of Eq. (8.24) reduces for the quasi-static case to those contributions $\delta\breve{\mathcal{V}}^{me}(t)$ due to the applied loads specified in Eq. (8.25). For the considered situation, the simplified principle of virtual work then reads:

$$\delta\breve{\mathcal{U}}(t) = \delta\breve{\mathcal{V}}(t) \quad\rightarrow\quad \int_X \delta\breve{\boldsymbol{\mu}}^T(x)\,\breve{\boldsymbol{L}}_{\dagger}(x,t)\;\mathrm{d}x = \int_X \delta\breve{\boldsymbol{\nu}}^T(x)\,\breve{\boldsymbol{l}}(x,t)\,. \tag{8.35}$$

As was done in Section 6.2.3 to obtain the equilibrium equations of the shell, integration by parts is applied to the principle of virtual work with the objective of eliminating the appearing derivatives of the beam's degrees of freedom. The geometric boundary conditions (first column) for a cantilever configuration are employed to warrant admissible displacement states. To satisfy the principle, the integrands collected for all virtual displacements have to vanish, giving the equilibrium equations (second column). The remaining terms yield the natural boundary conditions (third column) at the free end:

$$u\,(x=0)=0, \qquad \breve{n}\,(x,t)+\breve{N}_{,x}\,(x,t)=0, \qquad \breve{N}\,(x=X)=0, \tag{8.36a}$$

$$v\,(x=0)=0, \qquad \breve{q}_y\,(x,t)+\breve{Q}_{y,x}\,(x,t)=0, \qquad \breve{Q}_y\,(x=X)=0, \tag{8.36b}$$

$$w\,(x=0)=0, \qquad \breve{q}_z\,(x,t)+\breve{Q}_{z,x}\,(x,t)=0, \qquad \breve{Q}_z\,(x=X)=0, \tag{8.36c}$$

$$\beta_y\,(x=0)=0, \qquad \breve{m}_y\,(x,t)-\breve{Q}_z\,(x,t)+\breve{M}_{y,x}\,(x,t)=0, \qquad \breve{M}_y\,(x=X)=0, \tag{8.36d}$$

$$\beta_z\,(x=0)=0, \qquad \breve{m}_z\,(x,t)+\breve{Q}_y\,(x,t)+\breve{M}_{z,x}\,(x,t)=0, \qquad \breve{M}_z\,(x=X)=0. \tag{8.36e}$$

The coupling of warping and torsion is manifested in the equilibrium equations, as they do not appear separately:

$$\breve{m}_x\,(x,t)+\breve{M}_{x,x}\,(x,t)-\breve{q}_{w,x}\,(x,t)-\breve{Q}_{w,xx}\,(x,t)=0, \tag{8.37a}$$

$$\phi\,(x=0)=0, \qquad \breve{M}_x\,(x=X)-\breve{q}_w\,(x=X)-\breve{Q}_{w,x}\,(x=X)=0, \tag{8.37b}$$

$$\phi_{,x}\,(x=0)=0, \qquad \breve{Q}_w\,(x=X)=0. \tag{8.37c}$$

The above procedure also provides corresponding sets of equations for the electric loads of every group of electrically paralleled laminae:

$$\varphi^c\,(x=0)=0, \qquad \breve{g}^c\,(x,t)+\breve{G}^c_{,x}\,(x,t)=0, \qquad \breve{G}^c\,(x=X)=0, \tag{8.38a}$$

$$\varphi^d\,(x=0)=0, \qquad \breve{g}^d\,(x,t)+\breve{G}^d_{,x}\,(x,t)=0, \qquad \breve{G}^d\,(x=X)=0. \tag{8.38b}$$

$$\vdots \qquad\qquad \vdots \qquad\qquad \vdots$$

8.3 Second-Order Theory

First-order theories are bound to the equilibrium of the undeformed system and therefore are basically suitable for small deformations. Second-order theories consider the equilibrium of the slightly deformed system and are necessary to investigate tensioned flexible structures as well as buckling phenomena. Since the behavior in this context is frequently dominated by the normal force, it is commonly not accounted for the other initial internal loads, while

they will be included in the subsequent derivation. Non-linear theories do not suffer from the implications of the different linearization procedures and are able to depict larger deformations as they occur, for example, in the post-buckling state. The capabilities of such elaborate theories have to be acquired at the cost of analytic insight and computational efficiency. With reference to Section 7.1, it would be possible to employ a geometrically exact description without reducing to small rotations, as of Remark 7.2. Such theories have been developed and advanced, for instance, by *Simo and Vu-Quoc* [164], *Hodges* [97], and *Gruttmann et al.* [89] for beams without adaptive capabilities.

8.3.1 Additional Internal Load Contributions

The non-linear strain measures for the most general comprehensible case, involving finite displacements but small rotations of the beam, are derived in Section 7.1 and given by Eq. (7.15). In accordance with the calculus of variations, see *Funk* [77], the virtual variant of these strain measures reads

$$\delta\breve{\boldsymbol{\varepsilon}}_{GL}(x) = \underbrace{\begin{Bmatrix} \delta u_{,x}(x) \\ -\delta\beta_z(x) + \delta v_{,x}(x) \\ \delta\beta_y(x) + \delta w_{,x}(x) \\ \delta\phi_{,x}(x) \\ \delta\beta_{y,x}(x) \\ \delta\beta_{z,x}(x) \\ \delta\phi_{,xx}(x) \end{Bmatrix}}_{\delta\breve{\boldsymbol{\varepsilon}}(x)} + \underbrace{\begin{Bmatrix} v_{,x}(x)\,\delta v_{,x}(x) + w_{,x}(x)\,\delta w_{,x}(x) \\ \phi(x)\,\delta w_{,x}(x) + w_{,x}(x)\,\delta\phi(x) \\ -\phi(x)\,\delta v_{,x}(x) - v_{,x}(x)\,\delta\phi(x) \\ 0 \\ -\phi_{,x}(x)\,\delta v_{,x}(x) - v_{,x}(x)\,\delta\phi_{,x}(x) \\ -\phi_{,x}(x)\,\delta w_{,x}(x) - w_{,x}(x)\,\delta\phi_{,x}(x) \\ 0 \end{Bmatrix}}_{\delta\acute{\boldsymbol{\varepsilon}}(x)}. \tag{8.39}$$

As shown here, the strains may be split into the linear part $\delta\breve{\boldsymbol{\varepsilon}}(x)$ and the non-linear part $\delta\acute{\boldsymbol{\varepsilon}}(x)$. The prior corresponds to the variation of the linear strain measures as they are obtained for the thin-walled beam in Section 7.2 and given by Eq. (7.31). Further on, the internal loads vector $\breve{\boldsymbol{N}}(x,t)$ of the beam can be subdivided into the portion $\acute{\boldsymbol{N}}(x,t)$, associated with the initial configuration, and the portion $\grave{\boldsymbol{N}}(x,t)$ related to the superposed deformation. Then the virtual strain energy $\delta\mathcal{U}^{md}(t)$, based on the general formulation of Eq. (3.45), may be written for the beam as follows:

$$\begin{aligned}
&\delta\mathcal{U}^{md}(t) \\
&\quad= \int_X \delta\breve{\boldsymbol{\varepsilon}}_{GL}^T(x)\,\breve{\boldsymbol{N}}(x,t)\,\mathrm{d}x \quad \text{with } \breve{\boldsymbol{N}}(x,t) = \grave{\boldsymbol{N}}(x,t) + \acute{\boldsymbol{N}}(x,t) \\
&\quad= \underbrace{\int_X \delta\breve{\boldsymbol{\varepsilon}}^T(x)\,\breve{\boldsymbol{N}}(x,t)\,\mathrm{d}x}_{\delta\breve{\mathcal{U}}^{md}(t)} + \underbrace{\int_X \delta\acute{\boldsymbol{\varepsilon}}^T(x)\,\acute{\boldsymbol{N}}(x,t)\,\mathrm{d}x}_{\delta\breve{\mathcal{U}}^{ms}(t)} \\
&\qquad+ \underbrace{\int_X \delta\acute{\boldsymbol{\varepsilon}}^T(x)\,\grave{\boldsymbol{N}}(x,t)\,\mathrm{d}x}_{\to 0}.
\end{aligned} \tag{8.40}$$

In the last line of Eq. (8.40), Eq. (8.39) is introduced and expressions are multiplied out. The first term represents the linearized virtual strain energy $\delta\breve{\mathcal{U}}^{md}(t)$. The initial internal loads vector $\acute{\boldsymbol{N}}(x,t)$ can be determined in advance, while the vector $\grave{\boldsymbol{N}}(x,t)$ of the other internal loads needs to be substituted with the aid of a constitutive relation. Therefore, the second term is free of non-linear products, while the third term contains such products and, consequently, will be neglected. Such a second-order theory corresponds to the equilibrium of the slightly deformed system and contributes the virtual work of initial stresses $\delta\breve{\mathcal{U}}^{ms}(t)$. Thus, the virtual work of internal mechanical and electric loads with regard to Eq. (8.22) amounts to

$$\delta\breve{\mathcal{U}}(t) = \delta\breve{\mathcal{U}}^{me}(t) + \delta\breve{\mathcal{U}}^{pe}(t) + \delta\breve{\mathcal{U}}^{ms}(t). \tag{8.41}$$

Known Initial Internal Loads

The internal loads vector $\breve{\boldsymbol{N}}(x,t)$ constitutes the mechanical part of the combined internal loads $\breve{\boldsymbol{L}}(x,t)$ of the beam as given by Eq. (8.3). Correspondingly, the initial internal loads vector $\acute{\boldsymbol{N}}(x,t)$ and the associated initial external loads vector $\acute{\boldsymbol{n}}(x,t)$ have the following components:

$$\acute{\boldsymbol{N}}(x,t) = \left\{\acute{N}(x,t) \quad \acute{Q}_y(x,t) \quad \acute{Q}_z(x,t) \quad \acute{M}_x(x,t) \quad \acute{M}_y(x,t) \quad \acute{M}_z(x,t) \quad \acute{Q}_w(x,t)\right\}^T, \tag{8.42a}$$

$$\acute{\boldsymbol{n}}(x,t) = \left\{\acute{n}(x,t) \quad \acute{q}_y(x,t) \quad \acute{q}_z(x,t) \quad \acute{m}_x(x,t) \quad \acute{m}_y(x,t) \quad \acute{m}_z(x,t) \quad \acute{q}_w(x,t)\right\}^T. \tag{8.42b}$$

As outlined above, the initial internal loads need to be known and, for this purpose, may be determined with the aid of the first-order theory developed so far. Due to the absence of non-linear strains related to both rotation and warping, only normal and transverse forces, as well as bending moments, have to be obtained. In accordance with the equilibrium equations and natural boundary conditions of Eq. (8.36), these can be expressed as

$$\acute{N}(x,t) = \int_x^X \acute{n}(x,t)\,\mathrm{d}x, \tag{8.43a}$$

$$\acute{Q}_y(x,t) = \int_x^X \acute{q}_y(x,t)\,\mathrm{d}x, \quad \acute{Q}_z(x,t) = \int_x^X \acute{q}_z(x,t)\,\mathrm{d}x, \tag{8.43b}$$

$$\acute{M}_y(x,t) = \int_x^X \acute{m}_y(x,t) - \acute{Q}_z(x,t)\,\mathrm{d}x, \quad \acute{M}_z(x,t) = \int_x^X \acute{m}_z(x,t) + \acute{Q}_y(x,t)\,\mathrm{d}x. \tag{8.43c}$$

8.3.2 Reformulation

Next, the non-linear part $\delta\acute{\boldsymbol{\varepsilon}}(x)$ of the virtual strain measures, given by Eq. (8.39), and initial internal loads $\acute{\boldsymbol{N}}(x,t)$, given by Eq. (8.42a), will be sub-

stituted into the virtual work of initial stresses $\delta\breve{\mathcal{U}}^{ms}(t)$ of Eq. (8.40). Thereby virtual and actual displacement, respectively rotation, derivatives can be resorted into the appropriate vectors $\delta\breve{\boldsymbol{u}}_{,x}(x)$ and $\breve{\boldsymbol{u}}_{,x}(x,t)$, while the known initial internal load components may be arranged in the matrices $\hat{\mathbf{G}}(x,t)$ and $\check{\mathbf{G}}(x,t)$:

$$\delta\breve{\mathcal{U}}^{ms}(t) = \int_X \begin{pmatrix} \delta\breve{\boldsymbol{u}}_{,x}^T(x)\ \hat{\mathbf{G}}(x,t)\ \breve{\boldsymbol{u}}_{,x}(x,t) \\ +\delta\breve{\boldsymbol{u}}^T(x)\ \check{\mathbf{G}}^T(x,t)\ \breve{\boldsymbol{u}}_{,x}(x,t) \\ +\delta\breve{\boldsymbol{u}}_{,x}^T(x)\ \check{\mathbf{G}}(x,t)\ \breve{\boldsymbol{u}}(x,t) \end{pmatrix} \mathrm{d}x. \tag{8.44}$$

Unlike the matrix $\hat{\mathbf{G}}(x,t)$, but compensated by the dual appearance in Eq. (8.44), the matrix $\check{\mathbf{G}}(x,t)$ is not symmetric:

$$\hat{\mathbf{G}}(x,t) = \begin{bmatrix} 0 & 0 & 0 & 0 & 0 & 0 & 0 \\ 0 & \acute{N}(x,t) & 0 & -\acute{M}_y(x,t) & 0 & 0 & 0 \\ 0 & 0 & \acute{N}(x,t) & -\acute{M}_z(x,t) & 0 & 0 & 0 \\ 0 & -\acute{M}_y(x,t) & -\acute{M}_z(x,t) & 0 & 0 & 0 & 0 \\ 0 & 0 & 0 & 0 & 0 & 0 & 0 \\ 0 & 0 & 0 & 0 & 0 & 0 & 0 \\ 0 & 0 & 0 & 0 & 0 & 0 & 0 \end{bmatrix}, \tag{8.45a}$$

$$\check{\mathbf{G}}(x,t) = \begin{bmatrix} 0 & 0 & 0 & 0 & 0 & 0 & 0 \\ 0 & 0 & 0 & -\acute{Q}_z(x,t) & 0 & 0 & 0 \\ 0 & 0 & 0 & \acute{Q}_y(x,t) & 0 & 0 & 0 \\ 0 & 0 & 0 & 0 & 0 & 0 & 0 \\ 0 & 0 & 0 & 0 & 0 & 0 & 0 \\ 0 & 0 & 0 & 0 & 0 & 0 & 0 \\ 0 & 0 & 0 & 0 & 0 & 0 & 0 \end{bmatrix}. \tag{8.45b}$$

The underlying mechanical degrees of freedom $\breve{\boldsymbol{u}}(x,t)$ are given by Eq. (8.26). The matrices $\hat{\mathbf{G}}(x,t)$ and $\check{\mathbf{G}}(x,t)$ contain the initial internal loads to be determined with the aid of Eqs. (8.43). They depend on the initial external loads $\acute{\boldsymbol{n}}(x,t)$, which in turn are composed of the applied external loads $\breve{\boldsymbol{n}}(x,t)$ and those rotational effects that concern the initial state. The latter have been obtained implicitly within the derivation of the virtual work of inertia loads. They are marked in Eq. (8.33), and consequently the initial external loads are given by

$$\acute{\boldsymbol{n}}(x,t) = \breve{\boldsymbol{n}}(x,t) - \boldsymbol{m}(x)\,\Omega^2(t) - \boldsymbol{m}'(x)\,\Omega_{,t}(t). \tag{8.46}$$

9

Solution Variants

In Section 2.5, the application of adaptive fiber composites to influence the behavior of helicopter rotor blades is outlined. To simulate such a system, an adaptive beam, as considered in the two previous chapters, needs to be examined in the rotating environment. Besides the already complicated interactions due to arbitrary mechanical and electromechanical couplings, this requires consideration of additional couplings due to gyroscopic and second-order theory effects. Consequently, the general problem may only be solved with the aid of discretization, to be accomplished here by means of the finite element method. Analytic solutions of manageable complexity, however, may be found for simplified problems and can be utilized for fundamental studies and to support the validation of the finite element solution.

9.1 Statics of the Non-Rotating Structure

To assess and compare the performance of different configurations, it is sufficient to regard the static behavior of the non-rotating structure in conjunction with the voltage source driven actuator application, as discussed in Section 4.5. With the subsequently described restrictions, it is possible to derive an analytic solution.

9.1.1 Configuration Restrictions

An outline of various actuation schemes has been given in Figure 2.10. On account of the efficiency with regard to the helicopter application, we will here focus the derivation of an analytic solution on the variants of twist actuation. This requires the coupled consideration of extension and torsion as well as warping and torsion of the beam. The prior is represented by the stiffness coefficient P_{14} in the constitutive relation and the latter by the equilibrium of Eq. (8.37a). To ease the solution, shear and bending of the beam will only be coupled with each other. This comprises the stiffness coefficients P_{25} and P_{36}

T.H. Brockmann, *Theory of Adaptive Fiber Composites*,
Solid Mechanics and Its Applications 161,

in the constitutive relation as well as a crosswise connection in the equilibrium of Eqs. (8.36d) and (8.36e). For such a configuration, the constitutive matrix $\mathbf{P}$ of Eq. (8.6) with the coefficients of Eqs. (8.7) to (8.17) reduces to

$$\mathbb{P} = \begin{bmatrix} P_{11} & 0 & 0 & P_{14} & 0 & 0 & 0 & P_{18} & 0 \\ 0 & P_{22} & 0 & 0 & P_{25} & 0 & 0 & 0 & 0 \\ 0 & 0 & P_{33} & 0 & 0 & P_{36} & 0 & 0 & 0 \\ P_{14} & 0 & 0 & P_{44} & 0 & 0 & 0 & P_{48} & 0 \\ 0 & P_{25} & 0 & 0 & P_{55} & 0 & 0 & 0 & 0 \\ 0 & 0 & P_{36} & 0 & 0 & P_{66} & 0 & 0 & 0 \\ 0 & 0 & 0 & 0 & 0 & 0 & P_{77} & 0 & P_{79} \\ P_{18} & 0 & 0 & P_{48} & 0 & 0 & 0 & P_{88} & 0 \\ 0 & 0 & 0 & 0 & 0 & 0 & P_{79} & 0 & P_{99} \end{bmatrix}. \tag{9.1}$$

For the sake of clarity, separate groups of electrically paralleled laminae are provided. On the one hand, the electromechanical coupling with respect to extension and torsion is captured by the coefficients P_{18} and P_{48}, while on the other hand, the warping aspects are depicted by the coefficient P_{79}. In addition to the issue of actuation, the application of constant and linear external loads to the beam will be permitted. Exemplarily, the lengthwise line force $\breve{n}(x)$, the transverse line forces $\breve{q}_y(x)$ and $\breve{q}_z(x)$, as well as the torsional line moment $\breve{m}_x(x)$, are taken into account:

$$\breve{n}(x) = \breve{\mathfrak{n}}_x x + \breve{n}_x, \quad \breve{q}_y(x) = \breve{\mathfrak{q}}_y x + \breve{q}_y, \quad \breve{q}_z(x) = \breve{\mathfrak{q}}_z x + \breve{q}_z, \quad \breve{m}_x(x) = \breve{\mathfrak{m}}_x x + \breve{m}_x. \tag{9.2}$$

The static behavior of the non-rotating structure will be examined by means of the properties outlined above. These can be summarized as follows:

Remark 9.1. The sought analytic solution will consider the constitutive coupling of extension and torsion as well as of shear and bending in combination with actuation of extension, torsion, and warping as well as constant and linear external loads in view of the line forces and torsional line moment.

9.1.2 Extension, Torsion, and Warping Solution

The described configuration allows us to deal with two separate problems, whereof the solution involving extension, torsion, and warping will be presented first. To attain more accessible solutions, a normalized lengthwise coordinate ξ is introduced with the total length X of the considered beam:

$$\xi = \frac{x}{X}. \tag{9.3}$$

The two equilibrium equations, provided by Eqs. (8.36a) and (8.37a), can be solved separately with their boundary conditions and external line loads of Eqs. (9.2) for the internal normal force $\breve{N}(x)$ and for the internal twisting

moment $\breve{M}_x(x)$. The latter contains the first derivative of the internal warping bimoment $\breve{Q}_w(x)$. These three internal loads can be substituted with the aid of the corresponding lines of the constitutive relation, given on the right-hand side of Eqs. (8.4) with the constitutive matrix of Eq. (9.1).

Twisting Angle

Both of the two resulting equations contain the first derivative of the lengthwise displacement $u(x)$. Therefore, the latter can be eliminated in order to solve a single third-order differential equation for the twisting angle $\phi(x)$. With the normalized coordinate of Eq. (9.3) and compiled coefficients, the solution to the beam torsion can be finally described by

$$\begin{aligned}\phi(\xi) = &-\left(\frac{\xi^3}{6} + \left(\frac{1}{\lambda^2} - \frac{1}{2}\right)(\xi - \eta_1(\xi)) + \eta_0(\xi)\right)\varrho_{\text{linear}} - (\xi - \eta_1(\xi))\,\varrho_{\text{twist}} \\ &-\left(\frac{\xi^2}{2} - \xi + \eta_1(\xi) + \eta_0(\xi)\right)\varrho_{\text{const}} + \eta_0(\xi)\,\varrho_{\text{warp}}. \end{aligned} \tag{9.4}$$

The impact of linear and constant applied line loads is contained in the constants ϱ_{linear} and ϱ_{const}, while the induction of direct and extension coupled twist and of warping coupled twist is expressed by the constants ϱ_{twist} respectively ϱ_{warp}:

$$\varrho_{\text{linear}} = \frac{\breve{\mathfrak{m}}_x P_{11} - \breve{\mathfrak{n}}_x P_{14}}{P_{11}P_{44} - P_{14}^2} X^3, \qquad \varrho_{\text{const}} = \frac{\breve{m}_x P_{11} - \breve{n}_x P_{14}}{P_{11}P_{44} - P_{14}^2} X^2, \tag{9.5a}$$

$$\varrho_{\text{twist}} = \frac{P_{11}P_{48} - P_{14}P_{18}}{P_{11}P_{44} - P_{14}^2} X \breve{E}^c, \qquad \varrho_{\text{warp}} = \frac{P_{79}}{P_{77}} X^2 \breve{E}^d. \tag{9.5b}$$

The particular solution, which represents the influence of the warping effect on the lengthwise shape of the twist, is comprised in the functions $\eta_1(\xi)$ and $\eta_0(\xi)$:

$$\eta_1(\xi) = \frac{\sinh(\lambda) - \sinh(\lambda(1-\xi))}{\lambda\cosh(\lambda)}, \qquad \eta_0(\xi) = \frac{1 - \cosh(\lambda\xi)}{\lambda^2\cosh(\lambda)}. \tag{9.6}$$

Similar to the formulations of *Mehn* [124] or *Rehfield et al.* [150], the constant λ can be identified as a decay length parameter:

$$\lambda = \sqrt{\frac{P_{11}P_{44} - P_{14}^2}{P_{11}P_{77}}} X. \tag{9.7}$$

A warping restraint, resulting, for example, from the clamping at one end of a beam, locally enhances the beams resistance against torsion. Its influence however fades with the distance from its point of application depending on the geometry and stiffness properties of the beam, which are comprised in the

decay length parameter λ. Small values indicate that the warping restraint significantly affects the global torsional behavior of the beam. This is given, for instance, in the case of beams with a relatively stout geometry. A more detailed analysis will be conducted in Section 10.2.1. The effect on the twist actuation becomes clear with the study of Figure 9.1. With increasing constant λ in the function $\eta_1(\xi)$, the fading of the warping restraint influence on the otherwise linear direct and extension coupled torsion, $-(\xi - \eta_1(\xi))\varrho_{\text{twist}}$ in Eq. (9.4), accelerates, and so the actuation efficiency improves. On the contrary for warping coupled torsion, $\eta_0(\xi)\varrho_{\text{warp}}$ in Eq. (9.4), smaller values of the constant λ in the function $\eta_0(\xi)$ are favorable.

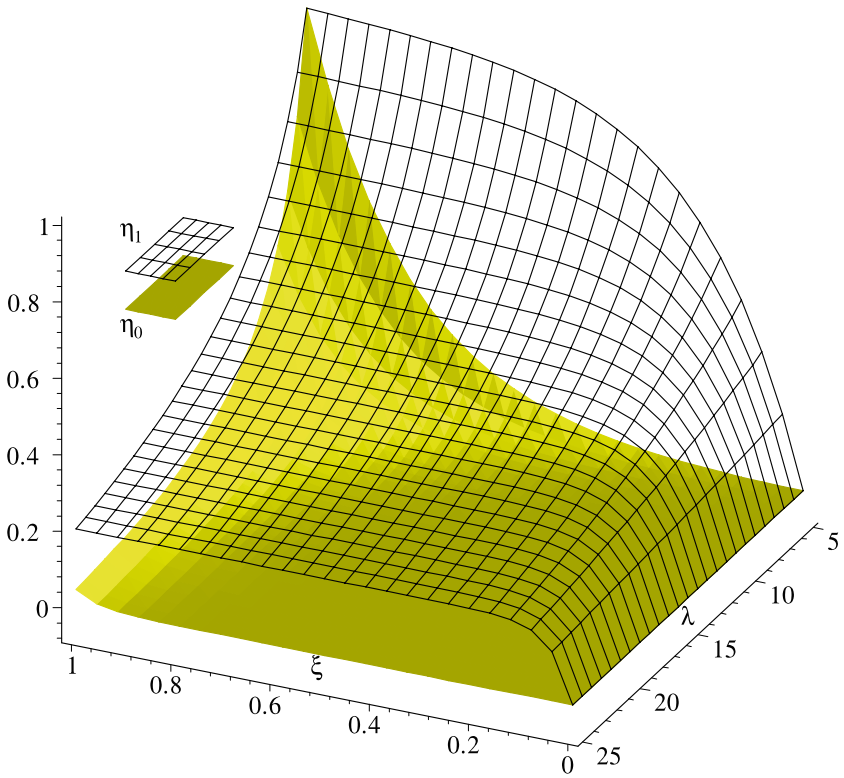

Fig. 9.1. Normalized influence of the decay length parameter λ on the shape of the non-linear twist components $\eta_1(\xi)$ and $\eta_0(\xi)$.

Lengthwise Displacement

Again with the normalized coordinate of Eq. (9.3), the lengthwise displacement $u(\xi)$ can be obtained by integration of the associated differential equa-

tion in consideration of the geometric boundary conditions. While the contained twisting angle $\phi(\xi)$ is given by Eq. (9.4), the solution reads

$$u(\xi) = \frac{1}{P_{11}} \left(\breve{\mathfrak{n}}_x X^3 \left(-\frac{\xi^3}{6} + \frac{\xi}{2} \right) + \breve{n}_x X^2 \left(-\frac{\xi^2}{2} + \xi \right) - P_{18} \breve{E}^c X \xi - P_{14} \phi(\xi) \right). \tag{9.8}$$

9.1.3 Shear and Bending Solution

To complete the analytical solution for the simplified case outlined in Remark 9.1, the remaining four equilibrium equations for shear and bending need to be considered. The external line loads contained therein are again provided by Eqs. (9.2), and the internal loads are supplied by the right one of Eqs. (8.4) in conjunction with Eq. (9.1). Further on, the beam shear angles are eliminated by virtue of Eq. (7.29).

Inclination Angles

With the above substitutions, the equilibrium relations of Eqs. (8.36b) and (8.36d) as well as Eqs. (8.36c) and (8.36e) may be combined such that each resulting equation contains the axial derivative of one of the sought inclination angles of the cross-section. Integration in consideration of the clamped boundary conditions at one end, then yields

$$\begin{aligned} \beta_y(\xi) = &\left(\breve{\mathfrak{q}}_y X \left(\frac{\xi^3}{6} - \frac{\xi}{2} \right) + \breve{q}_y \left(\frac{\xi^2}{2} - \xi \right) \right) \frac{P_{25} X^2}{P_{22} P_{55} - P_{25}^2} \\ &- \left(\breve{\mathfrak{q}}_z X \left(\frac{\xi^4}{24} - \frac{\xi^2}{4} + \frac{\xi}{3} \right) + \breve{q}_z \left(\frac{\xi^3}{6} - \frac{\xi^2}{2} + \frac{\xi}{2} \right) \right) \frac{P_{22} X^3}{P_{22} P_{55} - P_{25}^2}, \end{aligned} \tag{9.9a}$$

$$\begin{aligned} \beta_z(\xi) = &\left(\breve{\mathfrak{q}}_z X \left(\frac{\xi^3}{6} - \frac{\xi}{2} \right) + \breve{q}_z \left(\frac{\xi^2}{2} - \xi \right) \right) \frac{P_{36} X^2}{P_{33} P_{66} - P_{36}^2} \\ &+ \left(\breve{\mathfrak{q}}_y X \left(\frac{\xi^4}{24} - \frac{\xi^2}{4} + \frac{\xi}{3} \right) + \breve{q}_y \left(\frac{\xi^3}{6} - \frac{\xi^2}{2} + \frac{\xi}{2} \right) \right) \frac{P_{33} X^3}{P_{33} P_{66} - P_{36}^2}. \end{aligned} \tag{9.9b}$$

Transverse Displacements

Analogously, the equilibrium relations of Eqs. (8.36b) and (8.36d) as well as Eqs. (8.36c) and (8.36e) may be combined so that the axial derivatives of the inclination angles are eliminated. Then each resulting equation contains one of the inclination angles besides the axial derivative of one of the transverse displacements. It may be solved for the latter by integration, again in consideration of the clamped boundary conditions at one end, to find

$$v(\xi) = X \int \beta_z(\xi)\,\mathrm{d}\xi - \left(\breve{\mathfrak{q}}_y X\left(\frac{\xi^3}{6} - \frac{\xi}{2}\right) + \breve{q}_y\left(\frac{\xi^2}{2} - \xi\right)\right)\frac{P_{55}X^2}{P_{22}P_{55} - P_{25}^2} + \left(\breve{\mathfrak{q}}_z X\left(\frac{\xi^4}{24} - \frac{\xi^2}{4} + \frac{\xi}{3}\right) + \breve{q}_z\left(\frac{\xi^3}{6} - \frac{\xi^2}{2} + \frac{\xi}{2}\right)\right)\frac{P_{25}X^3}{P_{22}P_{55} - P_{25}^2}, \tag{9.10a}$$

$$w(\xi) = -X \int \beta_y(\xi)\,\mathrm{d}\xi - \left(\breve{\mathfrak{q}}_z X\left(\frac{\xi^3}{6} - \frac{\xi}{2}\right) + \breve{q}_z\left(\frac{\xi^2}{2} - \xi\right)\right)\frac{P_{66}X^2}{P_{33}P_{66} - P_{36}^2} - \left(\breve{\mathfrak{q}}_y X\left(\frac{\xi^4}{24} - \frac{\xi^2}{4} + \frac{\xi}{3}\right) + \breve{q}_y\left(\frac{\xi^3}{6} - \frac{\xi^2}{2} + \frac{\xi}{2}\right)\right)\frac{P_{36}X^3}{P_{33}P_{66} - P_{36}^2}. \tag{9.10b}$$

9.2 Dynamics of the Rotating Structure

To obtain a solution without the substantial restrictions dictated by insisting on an analytical approach, the finite element method will be utilized in this section. The diverse approaches to model various aspects of helicopter rotor blades without adaptive capabilities have been reviewed by *Hodges* [96] and *Kunz* [117].

9.2.1 Virtual Work Roundup

Following from the general principle of virtual work of Eq. (3.41), the equality of internal and external virtual work is also demanded for the beam and shall serve as the basis for the derivation of the equations of motion:

$$\delta\breve{\mathcal{U}}(t) = \delta\breve{\mathcal{V}}(t). \tag{9.11}$$

The internal virtual work $\delta\breve{\mathcal{U}}(t)$ is given by Eq. (8.41), and its individual contributions are specified in Eqs. (8.22) and (8.44). The reformulation in terms of the combined vectors of mechanical and electric variables, see Eqs. (8.21) and (8.26), results in

$$\begin{aligned}
\delta\breve{\mathcal{U}}(t) = {} & \int_X \delta\breve{\boldsymbol{\mu}}^T(x) \begin{bmatrix} \mathbf{p} & \mathbf{p}_\dagger \\ \mathbf{p}_\dagger^T & \mathbf{I}p_\dagger \end{bmatrix} \breve{\boldsymbol{\mu}}(x,t)\,\mathrm{d}x \Big\} \delta\breve{\mathcal{U}}^{me}(t) \\
& + \int_X \delta\breve{\boldsymbol{\mu}}^T(x) \begin{bmatrix} \mathbf{p}_\ddagger \\ \mathbf{0} \end{bmatrix} \breve{\boldsymbol{E}}_\ddagger(x,t)\,\mathrm{d}x \Big\} \delta\breve{\mathcal{U}}^{pe}(t) \\
& + \int_X \left(\begin{array}{l} \delta\breve{\boldsymbol{\nu}}_{,x}^T(x) \begin{bmatrix} \hat{\mathbf{G}}(x,t) & \mathbf{0} \\ \mathbf{0} & \mathbf{0} \end{bmatrix} \breve{\boldsymbol{\nu}}_{,x}(x,t) \\ \quad + \delta\breve{\boldsymbol{\nu}}^T(x) \begin{bmatrix} \check{\mathbf{G}}(x,t) & \mathbf{0} \\ \mathbf{0} & \mathbf{0} \end{bmatrix}^T \breve{\boldsymbol{\nu}}_{,x}(x,t) \\ \quad + \delta\breve{\boldsymbol{\nu}}_{,x}^T(x) \begin{bmatrix} \check{\mathbf{G}}(x,t) & \mathbf{0} \\ \mathbf{0} & \mathbf{0} \end{bmatrix} \breve{\boldsymbol{\nu}}(x,t) \end{array} \right) \mathrm{d}x. \Big\} \delta\breve{\mathcal{U}}^{ms}(t)
\end{aligned} \tag{9.12}$$

The external virtual work $\delta\breve{\mathcal{V}}(t)$ is given by Eq. (8.24), and its individual contributions are specified in Eqs. (8.25) and (8.33). Again in terms of the combined vectors of mechanical and electric variables, this leads to

$$\begin{aligned}
&\delta\breve{\mathcal{V}}\,(t) \\
&\quad = \int_X \delta\breve{\boldsymbol{\nu}}^T\,(x)\,\breve{\boldsymbol{l}}(x,t)\,\mathrm{d}x \qquad\qquad \Bigg\}\,\delta\breve{\mathcal{V}}^{me}\,(t) \\
&\quad - \int_X \delta\breve{\boldsymbol{\nu}}^T\,(x) \left(\begin{array}{l} \begin{bmatrix} \mathbf{M}'' & \mathbf{0} \\ \mathbf{0} & \mathbf{0} \end{bmatrix} \breve{\boldsymbol{\nu}}_{,tt}(x,t) + 2\Omega(t) \begin{bmatrix} \mathbf{M}' & \mathbf{0} \\ \mathbf{0} & \mathbf{0} \end{bmatrix} \breve{\boldsymbol{\nu}}_{,t}\,(x,t) \\ \quad + \Omega^2\,(t) \begin{bmatrix} \mathbf{M} & \mathbf{0} \\ \mathbf{0} & \mathbf{0} \end{bmatrix} \breve{\boldsymbol{\nu}}\,(x,t) + \Omega^2\,(t) \begin{Bmatrix} \boldsymbol{m}\,(x) \\ \mathbf{0} \end{Bmatrix} \\ \quad + \Omega_{,t}\,(t) \begin{bmatrix} \mathbf{M}' & \mathbf{0} \\ \mathbf{0} & \mathbf{0} \end{bmatrix} \breve{\boldsymbol{\nu}}\,(x,t) + \Omega_{,t}\,(t) \begin{Bmatrix} \boldsymbol{m}'\,(x) \\ \mathbf{0} \end{Bmatrix} \end{array} \right) \mathrm{d}x. \Bigg\}\,\delta\breve{\mathcal{V}}^{dl}\,(t)
\end{aligned} \tag{9.13}$$

9.2.2 Finite Element Formulation

Above, the various terms of the principle of virtual work have been compiled, containing different temporal and spatial derivatives of the mechanical displacements and rotations as well as of the electric potential of the adaptive beam. In the finite element approach, these continuous functions have to be approximated by discrete values at certain nodal points with adequate local interpolations in between. The degrees of freedom at such nodal points associated with a beam finite element may be summarized in the element vector $\breve{\boldsymbol{\nu}}_i(t)$. When elements with two nodes are chosen, the degrees of freedom at both element ends are contained:

$$\breve{\boldsymbol{\nu}}_i\,(t) = \begin{Bmatrix} \breve{\boldsymbol{u}}_{j=i-1}\,(t) \\ \breve{\boldsymbol{\varphi}}_{j=i-1}\,(t) \\ \breve{\boldsymbol{u}}_{j=i}\,(t) \\ \breve{\boldsymbol{\varphi}}_{j=i}\,(t) \end{Bmatrix} \quad \text{with } \breve{\boldsymbol{u}}_j\,(t) = \begin{Bmatrix} u_j(t) \\ v_j(t) \\ w_j(t) \\ \phi_j(t) \\ \beta_{y;j}(t) \\ \beta_{z;j}(t) \\ \phi_{,x;j}(t) \end{Bmatrix},\ \breve{\boldsymbol{\varphi}}_j\,(t) = \begin{Bmatrix} \varphi_j^c\,(t) \\ \varphi_j^d\,(t) \\ \vdots \end{Bmatrix}. \tag{9.14}$$

Discretization

For a problem of structural mechanics, the geometric boundary conditions are essential and thus have to be fulfilled to obtain an admissible displacement state. In the process of discretization, this has to be taken into account for the continuity requirements to be warranted by the interpolation functions at the element boundaries. Thus, the beam displacements $u(x,t)$, $v(x,t)$, $w(x,t)$

and cross-sectional rotations $\beta_y(x,t)$, $\beta_z(x,t)$ may be approximated with C^0 continuous linear Lagrange polynomials:

$$f_0(x_i) = \frac{1}{2} - \frac{x_i}{l_i}, \qquad f_1(x_i) = \frac{1}{2} + \frac{x_i}{l_i}. \tag{9.15}$$

Analogously, such linear Lagrange polynomials will be utilized for the approximation of the electric potential distributions. In the case of the beam twist, consideration of the warping torsion is associated with the twist rate, so C^1 continuity is required and can be achieved by the use of cubic Hermite polynomials:

$$g_0(x_i) = \frac{1}{2} - \frac{3}{2}\frac{x_i}{l_i} + 2\left(\frac{x_i}{l_i}\right)^3, \quad h_0(x_i) = \left[\frac{1}{8} - \frac{1}{4}\frac{x_i}{l_i} - \frac{1}{2}\left(\frac{x_i}{l_i}\right)^2 + \left(\frac{x_i}{l_i}\right)^3\right] l_i, \tag{9.16a}$$

$$g_1(x_i) = \frac{1}{2} + \frac{3}{2}\frac{x_i}{l_i} - 2\left(\frac{x_i}{l_i}\right)^3, \quad h_1(x_i) = \left[-\frac{1}{8} - \frac{1}{4}\frac{x_i}{l_i} + \frac{1}{2}\left(\frac{x_i}{l_i}\right)^2 + \left(\frac{x_i}{l_i}\right)^3\right] l_i. \tag{9.16b}$$

By abandoning the warping effect, the beam torsion problem may also be treated with linear Lagrange polynomials. For the interpolation functions of Eqs. (9.15) and (9.16), the element coordinate x_i is introduced with its origin at the center of the element and the element length l_i. Thus, the continuous blade coordinate x can be expressed with the aid of the distance L_i to the element coordinate origin:

$$x = L_i + x_i \quad \text{with } L_i = \sum_{k=1}^{i-1} l_k + \frac{l_i}{2}. \tag{9.17}$$

The discretization of the mechanical and electric degrees of freedom $\breve{\boldsymbol{\nu}}(x,t)$, as well as of mechanical strains and electric field strengths $\breve{\boldsymbol{\mu}}(x,t)$, may be formulated with the aid of the interpolation functions encapsulated in the matrices $\mathbf{A}(x_i)$ and $\mathbf{B}(x_i)$ as follows:

$$\breve{\boldsymbol{\nu}}(x,t) = \mathbf{A}(x_i)\breve{\boldsymbol{\nu}}_i(t), \tag{9.18a}$$

$$\breve{\boldsymbol{\mu}}(x,t) = \mathbf{B}(x_i)\breve{\boldsymbol{\nu}}_i(t). \tag{9.18b}$$

The interpolation functions have been arranged in the matrix $\mathbf{A}(x_i)$ for both nodes, whereas those for the mechanical degrees of freedom are contained in the matrix $\mathbf{A}_j(x_i)$ and for the electric degrees of freedom in the matrix $\mathbf{A}_j^{\dagger}(x_i)$. As the rate of twist $\phi_{,x}(x,t)$ is the longitudinal derivative of the twist $\phi(x,t)$, the derivatives of the dedicated polynomials appear:

$$\mathbf{A}(x_i) = \begin{bmatrix} \mathbf{A}_{j=0}(x_i) & \mathbf{0} & \mathbf{A}_{j=1}(x_i) & \mathbf{0} \\ \mathbf{0} & \mathbf{A}^{\dagger}_{j=0}(x_i) & \mathbf{0} & \mathbf{A}^{\dagger}_{j=1}(x_i) \end{bmatrix} \quad \text{with } \mathbf{A}^{\dagger}_{j}(x_i) = \mathbf{I} f_j(x_i), \tag{9.19a}$$

$$\mathbf{A}_j(x_i) = \begin{bmatrix} f_j(x_i) & 0 & 0 & 0 & 0 & 0 & 0 \\ 0 & f_j(x_i) & 0 & 0 & 0 & 0 & 0 \\ 0 & 0 & f_j(x_i) & 0 & 0 & 0 & 0 \\ 0 & 0 & 0 & g_j(x_i) & 0 & 0 & h_j(x_i) \\ 0 & 0 & 0 & 0 & f_j(x_i) & 0 & 0 \\ 0 & 0 & 0 & 0 & 0 & f_j(x_i) & 0 \\ 0 & 0 & 0 & g_{j,x_i}(x_i) & 0 & 0 & h_{j,x_i}(x_i) \end{bmatrix}. \tag{9.19b}$$

The analogous matrix $\mathbf{B}(x_i)$ of interpolation functions for the mechanical strains and electric field strengths arises, when the discretization of the degrees of freedom, as given by Eq. (9.18a), is substituted into the vector $\breve{\boldsymbol{\mu}}(x,t)$ of mechanical strains and electric field strengths and thus leads to Eq. (9.18b).

Element Matrices

Replacing the integral over the beam length by the sum of the integrals over the element lengths and introducing the interpolations, as developed above, leads from Eq. (9.11) with Eqs. (9.12) and (9.13) to the discretized principle of virtual work:

$$\sum_{i=1}^{I} \delta\breve{\boldsymbol{\nu}}_i^T \begin{pmatrix} \mathbf{M}_i'' \breve{\boldsymbol{\nu}}_{i,tt}(t) + 2\Omega(t)\,\mathbf{M}_i' \breve{\boldsymbol{\nu}}_{i,t}(t) \\ \quad + \left(\mathbf{P}_i + \mathbf{G}_i(t) + \Omega^2(t)\,\mathbf{M}_i + \Omega_{,t}(t)\,\mathbf{M}_i'\right) \breve{\boldsymbol{\nu}}_i(t) \\ \quad + \boldsymbol{p}_i(t) + \Omega^2(t)\,\boldsymbol{m}_i + \Omega_{,t}(t)\,\boldsymbol{m}_i' - \boldsymbol{l}_i(t) \end{pmatrix} = 0. \tag{9.20}$$

Since the virtual variants of the degrees of freedom are not time-dependent, the element vector $\delta\breve{\boldsymbol{\nu}}_i^T$ appearing with every term can be factored out. Those of the individual matrices of the principle stemming from the virtual work of internal loads are constructed as follows:

$$\mathbf{P}_i = \int_{-l_i/2}^{l_i/2} \mathbf{B}^T(x_i) \begin{bmatrix} \mathbf{p} & \mathbf{p}_{\dagger} \\ \mathbf{p}_{\dagger}^T & \mathbf{I}p_{\dagger} \end{bmatrix} \mathbf{B}(x_i)\,\mathrm{d}x_i, \tag{9.21a}$$

$$\boldsymbol{p}_i(t) = \int_{-l_i/2}^{l_i/2} \mathbf{B}^T(x_i) \begin{bmatrix} \mathbf{p}_{\ddagger} \\ \mathbf{0} \end{bmatrix} \breve{\boldsymbol{E}}_{\ddagger}(x_i,t)\,\mathrm{d}x_i, \tag{9.21b}$$

$$\mathbf{G}_i(t) = \int_{-l_i/2}^{l_i/2} \begin{pmatrix} \mathbf{A}_{,x}^T(x_i) \begin{bmatrix} \hat{\mathbf{G}}(x_i,t) & \mathbf{0} \\ \mathbf{0} & \mathbf{0} \end{bmatrix} \mathbf{A}_{,x}(x_i) \\ \quad + \mathbf{A}^T(x_i) \begin{bmatrix} \breve{\mathbf{G}}(x_i,t) & \mathbf{0} \\ \mathbf{0} & \mathbf{0} \end{bmatrix}^T \mathbf{A}_{,x}(x_i) \\ \quad + \mathbf{A}_{,x}^T(x_i) \begin{bmatrix} \breve{\mathbf{G}}(x_i,t) & \mathbf{0} \\ \mathbf{0} & \mathbf{0} \end{bmatrix} \mathbf{A}(x_i) \end{pmatrix} \mathrm{d}x_i. \tag{9.21c}$$

The vector $\breve{\boldsymbol{E}}_{\ddagger}(x_i,t)$ of electric field strength parameters and the geometric stiffness matrices $\hat{\mathbf{G}}(x_i,t)$ and $\breve{\mathbf{G}}(x_i,t)$ take the element coordinate x_i into account and result from their equivalents with continuous coordinate x in conjunction with the considerations manifested in Eq. (9.17). The same holds for the vectors $\boldsymbol{m}(x_i)$ and $\boldsymbol{m}'(x_i)$, capturing the initial state inertia effects as they appear in the remaining matrices originating from the virtual work of external loads:

$$\mathbf{M}_i'' = \int_{-l_i/2}^{l_i/2} \mathbf{A}^T(x_i) \begin{bmatrix} \mathbf{M}'' & \mathbf{0} \\ \mathbf{0} & \mathbf{0} \end{bmatrix} \mathbf{A}(x_i)\,\mathrm{d}x_i, \quad \boldsymbol{l}_i(t) = \int_{-l_i/2}^{l_i/2} \mathbf{A}^T(x_i)\breve{\boldsymbol{l}}(x,t)\,\mathrm{d}x_i, \tag{9.22a}$$

$$\mathbf{M}_i' = \int_{-l_i/2}^{l_i/2} \mathbf{A}^T(x_i) \begin{bmatrix} \mathbf{M}' & \mathbf{0} \\ \mathbf{0} & \mathbf{0} \end{bmatrix} \mathbf{A}(x_i)\,\mathrm{d}x_i, \quad \boldsymbol{m}_i' = \int_{-l_i/2}^{l_i/2} \mathbf{A}^T(x_i) \begin{bmatrix} \boldsymbol{m}'(x_i) \\ \mathbf{0} \end{bmatrix} \mathrm{d}x_i, \tag{9.22b}$$

$$\mathbf{M}_i = \int_{-l_i/2}^{l_i/2} \mathbf{A}^T(x_i) \begin{bmatrix} \mathbf{M} & \mathbf{0} \\ \mathbf{0} & \mathbf{0} \end{bmatrix} \mathbf{A}(x_i)\,\mathrm{d}x_i, \quad \boldsymbol{m}_i = \int_{-l_i/2}^{l_i/2} \mathbf{A}^T(x_i) \begin{bmatrix} \boldsymbol{m}(x_i) \\ \mathbf{0} \end{bmatrix} \mathrm{d}x_i. \tag{9.22c}$$

All integrations may be performed symbolically. To avoid the implications of the effect, which might appear in the context of the description of the Timoshenko beam, a reduced integration scheme is applied, see for example *Hughes* [101]. Alternatively, one may start off from four nodes per element for the transverse displacements and rotations using cubic Lagrange polynomials for the interpolation and then reduce the degrees of freedom by means of a static condensation, see *Knothe and Wessels* [113].

System Assembly

To set up the equations of the complete system, the boundary conditions have to be introduced. As the beam will be clamped at the innermost node with number 0, the assembly of the system matrices may simply begin with node number 1. Sorting the element matrices and vectors, given in Eqs. (9.21) and (9.22), into their equivalents on the system level, denoted by $(\mathring{})$, allows us to formulate the equation of motion for the system, discretized with the aid of the finite elements, as

$$\mathring{\mathbf{M}}''\mathring{\boldsymbol{\nu}}_{,tt}(t) + 2\Omega(t)\,\mathring{\mathbf{M}}'\mathring{\boldsymbol{\nu}}_{,t}(t) + \mathring{\mathbf{P}}_{\Sigma}(t)\,\mathring{\boldsymbol{\nu}}(t) = \mathring{\boldsymbol{p}}_{\Sigma}(t)\,. \tag{9.23}$$

The constitutive properties, geometric stiffness influences, and deformation-associated inertia effects are summarized in the matrix $\mathring{\mathbf{P}}_{\Sigma}(t)$, while the applied loads, piezoelectric coupling implications of the electric parameters, as well as initial state inertia effects, are joined in the vector $\mathring{\boldsymbol{p}}_{\Sigma}(t)$:

$$\mathring{\mathbf{P}}_{\Sigma}(t) = \mathring{\mathbf{P}} + \mathring{\mathbf{G}}(t) + \Omega^2(t)\,\mathring{\mathbf{M}} + \Omega_{,t}(t)\,\mathring{\mathbf{M}}', \tag{9.24a}$$

$$\mathring{\boldsymbol{p}}_{\Sigma}(t) = \mathring{\boldsymbol{l}}(t) - \mathring{\boldsymbol{p}}(t) - \Omega^2(t)\,\mathring{\boldsymbol{m}} - \Omega_{,t}(t)\,\mathring{\boldsymbol{m}}'. \tag{9.24b}$$

Simplifications

Time-dependent system matrices are relevant only to special technical applications and would require comparatively complicated solution procedures, as already pointed out in Section 8.2.2. For this reason, the general system described by Eqs. (9.23) and (9.24) will be simplified accordingly.

Remark 9.2. To assure time-independent system matrices, the angular velocity of the considered rotation is presumed to be constant and other time variant influences will be excluded.

Thus, the appearing angular acceleration and consequently the associated inertia effects are eliminated:

$$\Omega(t) = \Omega = \text{const.} \quad \rightarrow \quad \Omega_{,t}(t) = 0. \tag{9.25}$$

Furthermore, the angular velocity will be incorporated into each of the connected matrices to facilitate a more concise formulation:

$$\mathring{\mathbf{M}}'_{\Omega}(\Omega) = 2\Omega\mathring{\mathbf{M}}', \qquad \mathring{\mathbf{M}}_{\Omega}(\Omega) = \Omega^2\mathring{\mathbf{M}}, \qquad \mathring{\boldsymbol{m}}_{\Omega}(\Omega) = \Omega^2\mathring{\boldsymbol{m}}. \tag{9.26}$$

Then the equation of motion and its compound matrix, respectively vector, given by Eqs. (9.23) and (9.24), may be rewritten for the simplified case of time-invariant matrices, as demanded by Remark 9.2, in the following form:

$$\mathring{\mathbf{M}}''\mathring{\boldsymbol{\nu}}_{,tt}(t) + \mathring{\mathbf{M}}'_{\Omega}(\Omega)\,\mathring{\boldsymbol{\nu}}_{,t}(t) + \mathring{\mathbf{P}}_{\Sigma}(\Omega)\,\mathring{\boldsymbol{\nu}}(t) = \mathring{\boldsymbol{p}}_{\Sigma}(t,\Omega) \tag{9.27a}$$

$$\text{with } \mathring{\mathbf{P}}_{\Sigma}(\Omega) = \mathring{\mathbf{P}} + \mathring{\mathbf{G}}(\Omega) + \mathring{\mathbf{M}}_{\Omega}(\Omega), \tag{9.27b}$$

$$\mathring{\boldsymbol{p}}_{\Sigma}(t,\Omega) = \mathring{\boldsymbol{l}}(t) - \mathring{\boldsymbol{p}}(t) - \mathring{\boldsymbol{m}}_{\Omega}(\Omega). \tag{9.27c}$$

9.2.3 Solution

The system of differential equations, provided by Eqs. (9.27), is of the gyroscopic undamped type with time-invariant matrices, see *Gasch and Knothe* [78]. The mass matrix $\mathring{\mathbf{M}}''$ is symmetric, the gyroscopic matrix $\mathring{\mathbf{M}}'_{\Omega}(\Omega)$ is antimetric and the stiffness matrix $\mathring{\mathbf{P}}_{\Sigma}(\Omega)$ is symmetric as well as positive definite. The symmetry properties are inherited from the continuous beam description and become obvious, for instance, in Eqs. (8.34) by means of the matrices $\mathbf{I}$, $\mathbf{I}'$, $\mathbf{I}''$ from Eqs. (7.72). The solution to the problem at hand consists of three parts that are to be determined separately in the following.

Steady-State Solution

The steady-state solution is concerned with the oscillation-free system, thus $\mathring{\boldsymbol{\nu}}_{,tt}(t)$ and $\mathring{\boldsymbol{\nu}}_{,t}(t)$ are excluded, and the effects of the time-invariant portion of loads are retained, which are the constant applied loads, the piezoelectric coupling implications, and the rotation induced loads:

$$\mathring{\mathbf{P}}_{\Sigma}(\Omega)\,\mathring{\boldsymbol{\nu}}_s = \mathring{\boldsymbol{l}} - \mathring{\boldsymbol{p}} - \mathring{\boldsymbol{m}}_{\Omega}(\Omega)\,. \tag{9.28}$$

Inversion of the overall stiffness matrix $\mathring{\mathbf{P}}_{\Sigma}(\Omega)$ is necessary to find the wanted steady-state displacements, rotations, and electric potentials encapsulated in the vector $\mathring{\boldsymbol{\nu}}_s$. Prerequisite is the determination of the initial internal loads contained in the geometric stiffness matrix $\mathring{\mathbf{G}}(\Omega)$ in accordance with Remark 9.2 and the considerations of Section 8.3.

Homogeneous Solution

After the separation of the steady-state solution, the natural oscillations are to be found as the solution to the homogeneous system of differential equations. However, since the electric degrees of freedom are not associated with anything like the mechanical mass, all matrices except of the constitutive matrix $\mathring{\mathbf{P}}$ are singular. Therefore, the electric degrees of freedom need to be eliminated by means of a static condensation. Those submatrices with components connected either to the mechanical or to the electrical degrees of freedom are elucidated by the additional index m, respectively e, while the index me represents the coupling portions. Then the homogeneous system of differential equations may be rewritten as

$$\mathring{\mathbf{M}}''_m \mathring{\boldsymbol{\nu}}^*_{h,tt}(t) + \mathring{\mathbf{M}}'_{\Omega;m}(\Omega)\,\mathring{\boldsymbol{\nu}}^*_{h,t}(t) + \underbrace{\left(\mathring{\mathbf{P}}_{\Sigma;m}(\Omega) - \mathring{\mathbf{P}}_{me}\mathring{\mathbf{P}}_e^{-1}\mathring{\mathbf{P}}_{me}^T\right)}_{\mathring{\mathbf{P}}_{\Sigma;c}(\Omega)} \mathring{\boldsymbol{\nu}}^*_h(t) = \mathbf{0}. \tag{9.29}$$

For the given type, solely imaginary or solely real eigenvalues are expected, portending to either critically stable or monotonously instable behavior. The usual exponential set-up is applied, leading to the eigenvalue problem to be solved:

$$\mathring{\boldsymbol{\nu}}^*_h(t) = \mathring{\boldsymbol{\nu}}^*_H e^{\lambda t} \quad \rightarrow \quad \left(\mathring{\mathbf{M}}''_m\lambda^2 + \mathring{\mathbf{M}}'_{\Omega;m}(\Omega)\,\lambda + \mathring{\mathbf{P}}_{\Sigma;c}(\Omega)\right)\mathring{\boldsymbol{\nu}}^*_H = \mathbf{0}. \tag{9.30}$$

For the numerical handling, the eigenvalue problem is converted into the general form, where the upper part resembles the original problem and the lower one delivers an identity:

$$\left(\begin{bmatrix}\mathring{\mathbf{M}}'_{\Omega;m}(\Omega) & \mathring{\mathbf{P}}_{\Sigma;c}(\Omega)\\ \mathring{\mathbf{P}}_{\Sigma;c}(\Omega) & \mathbf{0}\end{bmatrix} - \lambda\begin{bmatrix}-\mathring{\mathbf{M}}''_m & \mathbf{0}\\ \mathbf{0} & \mathring{\mathbf{P}}_{\Sigma;c}(\Omega)\end{bmatrix}\right)\begin{Bmatrix}\lambda\mathring{\boldsymbol{\nu}}^*_H\\ \mathring{\boldsymbol{\nu}}^*_H\end{Bmatrix} = \begin{Bmatrix}\mathbf{0}\\ \mathbf{0}\end{Bmatrix}. \tag{9.31}$$

As the outcome, a list of eigenvalues λ_k and the modal matrix $\mathbf{H}^*$ with the pairwise conjugate complex eigenvectors of the general problem is obtained. Due to the normalization of the eigenvectors, the solution has to be matched to the initial conditions. This is done when the overall solution is assembled and for this purpose the vector $\boldsymbol{h}^*$ is provided. The homogeneous solution thus takes the following form:

$$\begin{Bmatrix} \mathring{\boldsymbol{\nu}}^*_{h,t}(t) \\ \mathring{\boldsymbol{\nu}}^*_{h}(t) \end{Bmatrix} = \mathbf{H}^* \underbrace{\begin{bmatrix} \ddots & & \\ & e^{\lambda_k t} & \\ & & \ddots \end{bmatrix}}_{\mathring{\mathbf{E}}^*(t)} \boldsymbol{h}^*. \tag{9.32}$$

Since the homogeneous solution only takes the mechanical degrees of freedom into account, its vector and matrix dimensions do not match the other parts of the solution. This may be adjusted by the introduction of empty rows and columns at the appropriate positions. To symbolize this modification, the marker $(\cdot)^*$ may be dropped and Eq. (9.32) rewritten as

$$\begin{Bmatrix} \mathring{\boldsymbol{\nu}}_{h,t}(t) \\ \mathring{\boldsymbol{\nu}}_{h}(t) \end{Bmatrix} = \mathbf{H}\mathring{\mathbf{E}}(t)\boldsymbol{h}. \tag{9.33}$$

Particular Solution

At this point, the time-dependent applied loads and piezoelectric coupling implications of the electric parameters on the right-hand side of the equations of motion have to be taken into account:

$$\mathring{\mathbf{M}}''\mathring{\boldsymbol{\nu}}_{p,tt}(t) + \mathring{\mathbf{M}}'_{\Omega}(\Omega)\,\mathring{\boldsymbol{\nu}}_{p,t}(t) + \mathring{\mathbf{P}}_{\Sigma}(\Omega)\,\mathring{\boldsymbol{\nu}}_{p}(t) = \mathring{\boldsymbol{l}}(t) - \mathring{\boldsymbol{p}}(t). \tag{9.34}$$

An investigation will be conducted for a mechanical or electric harmonic excitation with a multiple n of the rotor angular frequency Ω, where $\mathring{\boldsymbol{l}}_p$ and $\mathring{\boldsymbol{p}}_p$ are the respective peak amplitudes:

$$\mathring{\boldsymbol{l}}(t) - \mathring{\boldsymbol{p}}(t) = \left(\mathring{\boldsymbol{l}}_p - \mathring{\boldsymbol{p}}_p\right)\cos n\Omega t = \frac{1}{2}\left(\mathring{\boldsymbol{l}}_p - \mathring{\boldsymbol{p}}_p\right)\left(\mathrm{e}^{i\cdot n\Omega t} + \mathrm{e}^{-i\cdot n\Omega t}\right). \tag{9.35}$$

The solution approach can be handled in real or complex notation. The latter is chosen, as the system of equations to be solved is smaller and the banded structure of the involved matrices is sustained. Therefore, the following set-up is used:

$$\mathring{\boldsymbol{\nu}}_p(t) = \mathring{\boldsymbol{\nu}}_{+}\mathrm{e}^{i\cdot n\Omega t} + \mathring{\boldsymbol{\nu}}_{-}\mathrm{e}^{-i\cdot n\Omega t}. \tag{9.36}$$

Introducing this set-up, two separate sets of equations are obtained:

$$\left(-\mathring{\mathbf{M}}''n^2\Omega^2 + i\mathring{\mathbf{M}}'(\Omega)\,n\Omega + \mathring{\mathbf{P}}_{\Sigma}(\Omega)\right)\mathring{\boldsymbol{\nu}}_{+} = \frac{1}{2}\left(\mathring{\boldsymbol{l}}_p - \mathring{\boldsymbol{p}}_p\right), \tag{9.37a}$$

$$\left(-\mathring{\mathbf{M}}''n^2\Omega^2 - i\mathring{\mathbf{M}}'(\Omega)\,n\Omega + \mathring{\mathbf{P}}_{\Sigma}(\Omega)\right)\mathring{\boldsymbol{\nu}}_{-} = \frac{1}{2}\left(\mathring{\boldsymbol{l}}_p - \mathring{\boldsymbol{p}}_p\right). \tag{9.37b}$$

The complex amplitude vectors $\mathring{\boldsymbol{\nu}}_+$ and $\mathring{\boldsymbol{\nu}}_-$ are conjugates and so the solution can be simplified in the following way:

$$\mathring{\boldsymbol{\nu}}_p(t) = 2\Re\left(\mathring{\boldsymbol{\nu}}_+ \mathrm{e}^{i\cdot n\Omega t}\right). \tag{9.38}$$

Solution Assembly

So far, the individual parts of the solution have been obtained and may be pieced together at this point:

$$\begin{Bmatrix} \mathring{\boldsymbol{\nu}}_{,t}(t) \\ \mathring{\boldsymbol{\nu}}(t) \end{Bmatrix} = \begin{Bmatrix} \mathbf{0} \\ \mathring{\boldsymbol{\nu}}_s \end{Bmatrix} + \begin{Bmatrix} \mathring{\boldsymbol{\nu}}_{h,t}(t) \\ \mathring{\boldsymbol{\nu}}_h(t) \end{Bmatrix} + \begin{Bmatrix} \mathring{\boldsymbol{\nu}}_{p,t}(t) \\ \mathring{\boldsymbol{\nu}}_p(t) \end{Bmatrix}. \tag{9.39}$$

Still the homogeneous solution of Equation (9.33) has to be matched with the initial conditions. Therefore, the solution at the initial point in time $t_0 = 0$ takes the following form:

$$\begin{Bmatrix} \mathring{\boldsymbol{\nu}}_{,t}(t_0) \\ \mathring{\boldsymbol{\nu}}(t_0) \end{Bmatrix} = \begin{Bmatrix} \mathbf{0} \\ \mathring{\boldsymbol{\nu}}_s \end{Bmatrix} + \mathbf{H}\boldsymbol{h} + \begin{Bmatrix} \mathbf{0} \\ \mathring{\boldsymbol{\nu}}_p(t_0) \end{Bmatrix}. \tag{9.40}$$

Isolating the hitherto undetermined vector $\boldsymbol{h}$ and substituting it back into the homogeneous solution completes the last required step:

$$\begin{Bmatrix} \mathring{\boldsymbol{\nu}}_{h,t}(t) \\ \mathring{\boldsymbol{\nu}}_h(t) \end{Bmatrix} = \mathbf{H}\mathring{\mathbf{E}}(t)\mathbf{H}^{-1}\left(\begin{Bmatrix} \mathring{\boldsymbol{\nu}}_{,t}(t_0) \\ \mathring{\boldsymbol{\nu}}(t_0) \end{Bmatrix} - \begin{Bmatrix} \mathbf{0} \\ \mathring{\boldsymbol{\nu}}_s \end{Bmatrix} - \begin{Bmatrix} \mathbf{0} \\ \mathring{\boldsymbol{\nu}}_p(t_0) \end{Bmatrix}\right). \tag{9.41}$$

10

Demonstration and Validation

The sequence of theories developed throughout the foregoing chapters, leading the way from piezoelectric composites via adaptive laminated composite shells to adaptive thin-walled beams, allows for examinations of almost arbitrary complexity. The attempt to provide examples for the full spectrum of capabilities will be dropped in favor of an application-oriented approach. Hence, the subsequent investigations will be carried out in view of the integral actuation of structures with certain similarity to helicopter rotor blades.

10.1 Beam Configurations

To comply with the objective of demonstration and validation, it is necessary to engage in example configurations which, on the one hand, are as simple as possible to warrant intelligibility and, on the other hand, retain enough features to illustrate the essential capabilities. This effort will be made in this section, starting with the electric configuration to implement potentially rewarding actuation and sensing schemes.

10.1.1 Actuation and Sensing Schemes

In Section 2.5.1, the various beam actuation concepts are presented using the classification illustrated in Figure 2.10. Analogously applying to sensing, we distinguish between normal (lengthwise) and shear mode actuation in the plane of the wall as well as between its consistent and sectorial application across the plane of the cross-section.

Wall Strain Modes

Beyond in-plane actuation and sensing associated with the normal strain $\varepsilon_x^0(x,s)$ and the shear strain $\gamma_{xs}^0(x,s)$ of the shell, the derived beam formulation is capable of analyzing the out-of-plane effects associated with the

T.H. Brockmann, *Theory of Adaptive Fiber Composites*,
Solid Mechanics and Its Applications 161,

bending curvature $\kappa_x(x,s)$ and the twisting curvature $\psi_{xs}(x,s)$ of the shell. However, with the exception of the plate strip, the actuation, respectively sensing, effectiveness with regard to the curvatures $\kappa_x(x,s)$ and $\psi_{xs}(x,s)$ will be small by virtue of the beam geometry. For this reason, no further light will be thrown on the out-of-plane effects during subsequent examinations.

Wall Electroding Sectors

The change of the relative sign of electric field strength and polarization is associated with the reversal of the deformation direction. To actuate or sense the different beam deformations, the cross-section can be divided into sectors with alternating polarization but with common electric field strength by appropriate interconnection of electrodes. For a clear correlation, these sectors need to be delimited by the relevant principal axes of the cross-section, as shown in Figure 10.1.

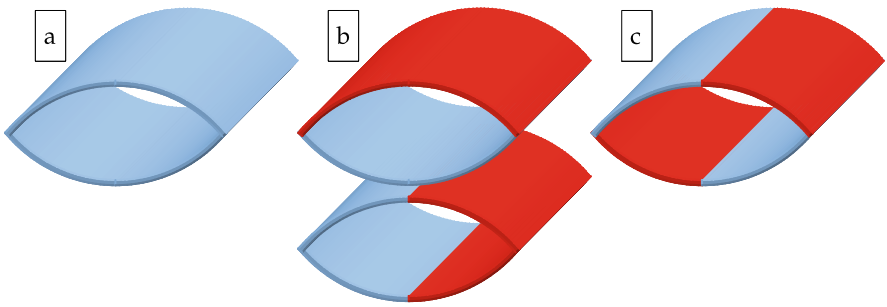

Fig. 10.1. Relative sign of electric field strength and polarization in the cross-sectional sectors.

Beam Schemes

The beam behavior is governed by the interplay of lay-up related wall modes and electroding specific wall sectors. For simple cross-sections, as in Figure 10.1, and exposure of the walls to pure normal strain or pure shear strain, the beam behavior may be classified as described in Table 10.1. Consistent shear of the walls throughout the entire cross-section is directly related to beam torsion. Extension of the walls in the lengthwise direction of cause corresponds to beam extension. Normal as well as shear strains with alternating signs in the cross-sectional quadrants are connected to out-of-plane warping of the cross-section. Extension and warping of both latter examples may also be combined with torsion by means of couplings due to the anisotropy of the walls and the geometry of the cross-section, respectively. Similarly, couplings

with bending could be utilized, but are less applicable due to the unwanted implications of the susceptibility to vibrations and external forces. The preceding considerations give rise to various schemes for actuation and sensing of beam deformations.

Table 10.1. Actuation or sensing of beam deformations by virtue of strain modes and electroding sectors of the wall.

	Consistent (a)	**2 Sectors** (b)	**4 Sectors** (c)
Normal Mode	extension	bending	warping
Shear Mode	torsion	shear	warping

Example Configuration Considerations

The simultaneous consideration of actuation and sensing, as instituted by the developed theory, becomes interesting as soon as a control unit is incorporated into the simulation. Since this would exceed the scope of the work at hand, we will refrain from such additional complexity within the exemplary calculations. Thus, the consequences for the electrical interconnection of layers read:

Remark 10.1. A single group of electrically paralleled laminae is taken into account for the example configuration.

Due to the reversibility of the piezoelectric effect and the accomplished homogeneous representation of mechanical and electric measures, it is sufficient to prove the reliability of the method for either actuation or sensing in order to validate both.

Example Configuration Schemes

With regard to the above discussions and with the integral blade actuation for the helicopter application in mind, as illustrated in Section 2.5, the example configuration schemes will be focused as follows:

Remark 10.2. Applicable beam schemes aiming at twist actuation will be examined.

The necessary arrangements with reference to the lay-up of Figure 10.2 and the formulations of the relative sign of electric field strength and polarization of Eqs. (6.5) and (7.32), see also Figure 10.1, are given in Table 10.2. These three actuation schemes, plus its variants, combining the different applicable coupling and actuation types, subsequently will be implemented and their efficiency compared.

Scheme *I* consists of two layer pairs with opposing fiber orientations and relative polarizations, whereas the relative polarization around the cross-section is constant over all quadrants. Thus, it represents two pairs of helical windings one of which contracts while the other expands, resulting in beam twist of similar direction but compensation of beam elongation.

Scheme *II* consists of a central lengthwise oriented layer surrounded by a layer pair with uniform fiber orientation. With an expansion of this unidirectional helical winding, twist and elongation of the beam are induced in the case of variant *a*. With an expansion of the lengthwise oriented fibers, elongation of the beam is achieved and complemented with twist via the passive coupling due to the helical winding in the case of variant *c*. Both mechanisms are employed simultaneously in the case of variant *b*. The relative polarization around the cross-section remains constant for any of the variants.

Scheme *III* consists of two layer pairs with opposing fiber orientations and relative polarizations. To induce warping deformation and consequently beam twist, the relative polarization around the cross-section alternates from quadrant to quadrant. Similar results could be achieved just by using lengthwise oriented fibers with such an alternating relative polarization. But without adjustable fiber orientations, it would not be possible to adapt to given stiffness properties, especially with regard to torsion.

Table 10.2. Actuation schemes with layup and polarization configuration for the torsional deformation of a beam.

			Wall Lay-Up		**Relative Polarization**						
					Layers			**Quadrants**			
Coupling	**Actuation**	**Scheme**	$\frac{H_0}{H_1}$	$\frac{\alpha_1}{\alpha_2}$	p_0	p_1	p_2	$p(q_1)$	$p(q_2)$	$p(q_3)$	$p(q_4)$
none	torsion	*I*	0	−1		1	−1	1	1	1	1
torsion & extension	torsion	*II a*	*h*	1	0	1	1	1	1	1	1
	torsion & extension	*II b*	*h*	1	1	1	1	1	1	1	1
	extension	*II c*	*h*	1	1	0	0	1	1	1	1
torsion & warping	warping	*III*	0	−1		1	−1	1	−1	1	−1

10.1.2 Set-Up of Walls

Multiple layers of piezoelectric composites consisting of polymer matrix material and piezoceramic fibers form the walls of the considered beams. The properties of typical materials are given in Tables A.2 and A.3, respectively. For the calculations which are presented later in this chapter, the data of *Epon*

9405 resin and *PZT-5H* fibers is utilized. The resulting adaptive fiber composites are subjected to the following peak value of the electric field strength:

$$\breve{E}^c, \breve{E}^d = \pm 10^6 \ \frac{\mathrm{V}}{\mathrm{m}}. \tag{10.1}$$

Such a fixing of the electric field strength implies the utilization of a voltage source for the actuator application, as described in Section 4.5.

Arrangement of Fibers

The geometry on the micro-electromechanics level will be included into the upcoming elementary examinations. To confine the range of variables of the considered problem to the essential ones, we will abstain from analyzing details beyond the fiber volume fraction ν. For a transversely isotropic layout of continuous fibers, the directional fiber fractions, defined in Eqs. (5.1), then become

$$\nu_1 = \nu_2 = \sqrt{\nu}, \qquad \nu_3 = 1. \tag{10.2}$$

Since the sequential stacking procedure could be shown to produce results of equivalent quality, see Section 5.5, with a little more flexibility and less numerical expenditure in comparison to the Mori–Tanaka method, it will be applied for the example calculations. Following the discussion of Section 5.4.6, the factor c_3 intended to map the disturbance of electrostatic fields close to the electrodes will be omitted:

$$c_3 = 0. \tag{10.3}$$

To avoid the arbitrary increase of complexity without a gain of insight, the following simplifications shall apply:

Remark 10.3. The composite material used for the subsequent beam configurations will be made of the same constituents and have identical fiber volume fractions.

Arrangement of Layers

Since the properties of the lay-up will be included in this study, a wall configuration has to be considered that allows for the representation of all anticipated effects and for the adjustment to any stiffness demand. This can be conveniently realized by a lamina in the center with fixed fiber orientation along the beam's lengthwise direction accompanied by two laminae on every side. Although the developed model is capable of capturing the full range of anisotropic couplings, the out-of-plane effects should be excluded here to avoid blurring the results:

Remark 10.4. The beam walls to be examined will be symmetric with respect to thickness and orientation of associated layers.

Such a symmetric laminate, as shown in Figure 10.2, is characterized with the aid of the layer orientation angles α_0, α_1 and α_2 as well as the thicknesses H_0, H_1, and H_2. For subsequent studies, fewer parameters are required and the following simplifications are reasonable:

Remark 10.5. The fiber orientation of the center layer will be aligned with the lengthwise axis of the beam and the off-center layers will be of equal thickness.

$$\alpha_0 = 0, \qquad H_2 = H_1. \tag{10.4}$$

To ease the representation, the thickness ratio h of the aligned center layer and arbitrary oriented off-center layers will be introduced as follows:

$$h = \frac{H_0}{H_1}. \tag{10.5}$$

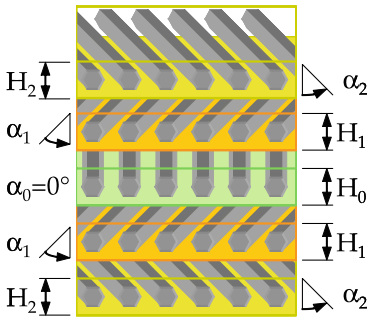

Fig. 10.2. Set-up of the beam wall.

10.1.3 Set-Up of Cross-Sections

The presented theory is able to cope with thin-walled beams of arbitrary cross-section. This includes highly complex configurations with any combination of closed cells and open branches. In the absence of correspondingly defined requirements and since such a complexity is not necessary for the purpose of elementary examination and validation, the focus will be placed upon two rather unpretentious set-ups, see Figures 10.3 and 10.4. With regard to the continuity of the wall set-up, the following will be agreed:

Remark 10.6. The wall properties will be constant all around the circumferential contour of the exemplary cross-sections.

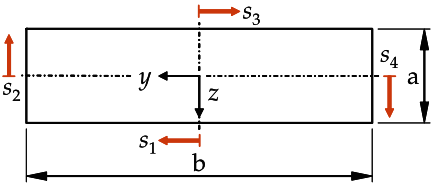

Fig. 10.3. Characterization of a rectangular single-cell cross-section.

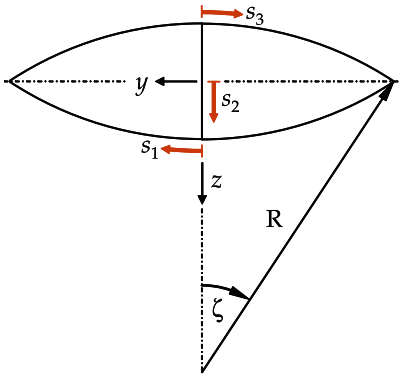

Fig. 10.4. Characterization of a convex double-cell cross-section.

Rectangular Single-Cell Cross-Section

The most simple case with sufficient adjustment options is the rectangular single-cell cross-section as depicted by Figure 10.3. To describe such a geometry, a separate coordinate s_i may be introduced with its origin in the middle of each of the four segments i of $2S_i$ length:

$$s_i = -S_i \ldots S_i \quad \text{for } i = 1,2,3,4 \text{ with } S_1 = S_3 = \frac{b}{2},\ S_2 = S_4 = \frac{a}{2}. \tag{10.6}$$

The cross-sectional dimensions of such a box beam are given by the height a and width b. Thus, the piecewise parameter representation of the wall curve assumes the following form:

$$y(s_1) = s_1, \qquad y(s_2) = \frac{b}{2}, \qquad y(s_3) = -s_3, \qquad y(s_4) = -\frac{b}{2}, \tag{10.7a}$$

$$z(s_1) = \frac{a}{2}, \qquad z(s_2) = -s_2, \qquad z(s_3) = -\frac{a}{2}, \qquad z(s_4) = s_4. \tag{10.7b}$$

To achieve actuation or sensing according to schemes I or II of Table 10.2, the relative sign of electric field strength and polarization needs to be constant all over the cross-section:

$$p^c(s_1) = p^c(s_2) = p^c(s_3) = p^c(s_4) = 1. \tag{10.8}$$

To utilize the warping effect, as illustrated by scheme III of Table 10.2, the relative sign has to alternate from quadrant to quadrant of the box beam:

$$p^d(s_1 > 0) = p^d(s_2 < 0) = 1, \qquad p^d(s_2 > 0) = p^d(s_3 < 0) = -1, \tag{10.9a}$$

$$p^d(s_3 > 0) = p^d(s_4 < 0) = 1, \qquad p^d(s_4 > 0) = p^d(s_1 < 0) = -1. \tag{10.9b}$$

Convex Double-Cell Cross-Section

Further on, to consider an example with curved walls as well as multiple cells, a convex cross-section with a central web will be established, as illustrated by Figure 10.4. In this case, three segments with associated curvilinear coordinates are sufficient:

$$s_i = -S_i \dots S_i \quad \text{for } i = 1,2,3 \text{ with } S_1 = S_3 = \zeta R,\ S_2 = R\,(1 - \cos\zeta)\,. \tag{10.10}$$

The dimensions of such a cross-section may be defined via the constant radius of curvature R and generating half-angle ζ. So, the piecewise parameter representation of the wall curve assumes the following form:

$$y\,(s_1) = R \sin\left(\frac{s_1}{R}\right), \quad y\,(s_2) = 0, \quad y\,(s_3) = -R \sin\left(\frac{s_3}{R}\right), \tag{10.11a}$$

$$z\,(s_1) = R\left(\cos\left(\frac{s_1}{R}\right) - \cos\zeta\right), \ z\,(s_2) = s_2, \ z\,(s_3) = -R\left(\cos\left(\frac{s_3}{R}\right) - \cos\zeta\right). \tag{10.11b}$$

To achieve actuation or sensing according to schemes *I* or *II* of Table 10.2, the relative sign of electric field strength and polarization needs to be constant around the circumference of the cross-section:

$$p^c\,(s_1) = p^c\,(s_3) = 1. \tag{10.12}$$

To utilize the warping effect, as illustrated by scheme *III* of Table 10.2, the relative sign has to alternate from quadrant to quadrant of the convex cross-section:

$$p^d\,(s_1 > 0) = 1, \qquad p^d\,(s_3 < 0) = -1, \tag{10.13a}$$

$$p^d\,(s_3 > 0) = 1, \qquad p^d\,(s_1 < 0) = -1. \tag{10.13b}$$

Due to its alignment with a principal axis, the web of the considered cross-section is free of warping influences:

$$p^c\,(s_2) = 0. \tag{10.14}$$

10.1.4 Constitutive Coefficients

The properties of the beam cross-section are manifested in the constitutive coefficients as given in their general formulation in Section 8.1.3. Subsequently, we will briefly illustrate, how they are obtained.

General Procedure

Due to the symmetry of the wall set-up, as demanded in Remark 10.4, those shell stiffness coefficients in charge of the coupling between in-plane and out-of-plane behavior vanish. By virtue of Remark 10.6, the properties of the

beam wall may be drawn out of the cross-sectional integrals. Further on, the latter may be split and consequently solved with the aid of the piecewise representations of the wall curves and the sectorial description of the relative electroding sign of Table 10.2.

Specific Illustration

For clarity, the printout of the results will be confined to the simple box beam of Eqs. (10.7). For the immediate, respectively later, use in order to ease the representation, the following ratios characterizing the box-beam geometry will be introduced:

$$\mathtt{n}_{a/b} = \frac{a}{b}, \qquad \mathtt{n}_{X/b} = \frac{X}{b}. \tag{10.15}$$

Then the beam stiffness coefficients, depending on the shell stiffnesses associated with lengthwise extension and bending from Eqs. (8.7), become

$$P_{11} = 2\grave{\mathtt{A}}_{11}\left(1+\mathtt{n}_{a/b}\right)b, \tag{10.16a}$$

$$P_{55} = \frac{\grave{\mathtt{A}}_{11}}{6}\left(3+\mathtt{n}_{a/b}\right)\mathtt{n}_{a/b}^2 b^3 + 2\grave{\mathtt{D}}_{11}b, \tag{10.16b}$$

$$P_{66} = \frac{\grave{\mathtt{A}}_{11}}{6}\left(1+3\mathtt{n}_{a/b}\right)b^3 + 2\grave{\mathtt{D}}_{11}\mathtt{n}_{a/b}b, \tag{10.16c}$$

$$P_{77} = \frac{\grave{\mathtt{A}}_{11}}{24}\frac{\left(1-\mathtt{n}_{a/b}\right)^2}{1+\mathtt{n}_{a/b}}\mathtt{n}_{a/b}^2 b^5 + \frac{\grave{\mathtt{D}}_{11}}{6}\left(1+\mathtt{n}_{a/b}\right)\left(\mathtt{n}_{a/b}^2 - \mathtt{n}_{a/b}+1\right)b^3. \tag{10.16d}$$

Correspondingly, the beam stiffness coefficients, depending on the shell stiffnesses associated with shear and twist from Eqs. (8.8), take the following form:

$$P_{22} = 2\grave{\mathtt{A}}_{33}b, \qquad P_{33} = 2\grave{\mathtt{A}}_{33}\mathtt{n}_{a/b}b, \tag{10.16e}$$

$$P_{44} = 2\grave{\mathtt{A}}_{33}\frac{\mathtt{n}_{a/b}^2}{1+\mathtt{n}_{a/b}}b^3 + 8\grave{\mathtt{D}}_{33}\left(1+\mathtt{n}_{a/b}\right)b. \tag{10.16f}$$

Those non-zero beam stiffness coefficients, depending on the shell stiffnesses associated with the coupling between lengthwise extension and shear, read

$$P_{14} = -2\grave{\mathtt{A}}_{13}\mathtt{n}_{a/b}b^2, \qquad P_{25} = \grave{\mathtt{A}}_{13}\mathtt{n}_{a/b}b^2, \qquad P_{36} = \grave{\mathtt{A}}_{13}\mathtt{n}_{a/b}b^2. \tag{10.16g}$$

With regard to the electromechanical coefficients of the beam, two different cases need to be distinguished. For schemes *I* and *II* of Table 10.2 with consistent electric conditions around the cross-section, given by Eqs. (10.8), the following coefficients are applicable:

$$P_{18} = 2\grave{\mathtt{A}}_{14}^{c}\left(1+\mathtt{n}_{a/b}\right)b, \qquad P_{48} = -2\grave{\mathtt{A}}_{34}^{c}\mathtt{n}_{a/b}b^2, \qquad P_{88} = 2\grave{\mathtt{A}}_{44}^{c}\left(1+\mathtt{n}_{a/b}\right)b. \tag{10.16h}$$

For scheme *III* with changes in the electric sign between adjacent quadrants, as described by Eqs. (10.9), the electromechanical coefficients of the beam become

$$P_{79} = -\frac{\grave{\mathtt{A}}^{d}_{14}}{4}\frac{(1-\mathtt{n}_{a/b})^2}{1+\mathtt{n}_{a/b}}\mathtt{n}_{a/b}b^3, \qquad P_{99} = 2\grave{\mathtt{A}}^{d}_{44}\left(1+\mathtt{n}_{a/b}\right)b. \tag{10.16i}$$

Since there is no need for simultaneous actuation with different schemes and thus the number of groups of electrically paralleled laminae has been limited to one in Remark 10.1, either Eqs. (10.16h) or (10.16i) are defined for the example at hand.

10.2 Elementary Examinations

The goal of these examinations is, on the one hand, to gain some insight into the behavior of beams with adaptive fiber composites and, on the other, to derive an optimal configuration for the numerical studies following in Section 10.3. The starting point is the analytic solution regarding the statics of the non-rotating structure as developed in Section 9.1. With the helicopter application in view, special attention is given to the torsion problem. Unreasonable complication should to be avoided at this stage of analysis by virtue of the following restriction:

Remark 10.7. These examinations are carried out by means of the box beam as described by Eqs. (10.16) and will be limited to the membrane response of Eq. (6.20).

10.2.1 Beam Geometry Influences on the Actuation Schemes

With regard to the actuation capabilities, the solution to the beam torsion problem, as given by Eq. (9.4), contains two different parts indicated by the constants ϱ_{twist} and ϱ_{warp}. The prior is in charge of direct and extension-coupled twist, schemes *I* and *II* of Table 10.2, and the latter of warping-coupled twist, scheme *III* of Table 10.2. The influence of the overall beam geometry on the efficiency of the actuation schemes will be analyzed on this basis.

Solution in Terms of Characteristic Ratios

Besides the geometric ratios of Eq. (10.15), the passive and active constitutive coefficients of the beam wall may be represented with reference to the lengthwise shell stiffness as follows:

$$\mathtt{a}_{13} = \frac{\grave{\mathtt{A}}_{13}}{\grave{\mathtt{A}}_{11}}, \qquad \mathtt{a}_{33} = \frac{\grave{\mathtt{A}}_{33}}{\grave{\mathtt{A}}_{11}}, \qquad \mathtt{a}^{c}_{14} = \frac{\grave{\mathtt{A}}^{c}_{14}}{\grave{\mathtt{A}}_{11}}, \qquad \mathtt{a}^{c}_{34} = \frac{\grave{\mathtt{A}}^{c}_{34}}{\grave{\mathtt{A}}_{11}}, \qquad \mathtt{a}^{d}_{14} = \frac{\grave{\mathtt{A}}^{d}_{14}}{\grave{\mathtt{A}}_{11}}. \tag{10.17}$$

With these stiffness ratios and the limitation to membrane response, as stated in Remark 10.7, the dimensionless constants ϱ_{twist} and ϱ_{warp} from Eqs. (9.5b) as well as the decay-length parameter λ from Eq. (9.7) can be rewritten as

$$\varrho_{\text{twist}} = -\mathtt{n}_{X/b}\frac{1+\mathtt{n}_{a/b}}{\mathtt{n}_{a/b}}\frac{\mathtt{a}^c_{34}-\mathtt{a}_{13}\mathtt{a}^c_{14}}{\mathtt{a}_{33}-\mathtt{a}^2_{13}}\breve{E}^c, \qquad \varrho_{\text{warp}} = -6\frac{\mathtt{n}^2_{X/b}}{\mathtt{n}_{a/b}}\mathtt{a}^d_{14}\breve{E}^d, \tag{10.18a}$$

$$\lambda = 4\frac{\mathtt{n}_{X/b}}{1-\mathtt{n}_{a/b}}\sqrt{3\,(\mathtt{a}_{33}-\mathtt{a}^2_{13})}. \tag{10.18b}$$

While the otherwise unchanged functions $\eta_1(\xi)$ and $\eta_0(\xi)$ of Eqs. (9.6) make use of the above decay-length parameter λ, the complete solution for the beam twist due to actuation without the implications of external loads reduces from Eq. (9.4) to

$$\phi\,(\xi) = -\,(\xi-\eta_1\,(\xi))\,\varrho_{\text{twist}} + \eta_0\,(\xi)\,\varrho_{\text{warp}}. \tag{10.19}$$

The first term represents the direct and extension-coupled torsion with a principally linear distribution along the beam length, disturbed by the non-linear influences of the warping effect comprised in the function $\eta_1(\xi)$. The second term captures the warping-coupled torsion with its non-linear behavior described by the function $\eta_0(\xi)$.

Geometry Influence Discussion

Keeping all the constitutive ratios of Eqs. (10.17) as well as the appearing electric field strength values constant, while varying the geometric ratios of Eqs. (10.15), allows for the anticipated examination of the efficiency of the different actuation schemes. For the graphical representations to be displayed subsequently, the rotation induced at the beam tip is normalized via division by the maximum result within the considered ranges of the two beam aspect ratios. For direct and extension-coupled twist, schemes *I* and *II* of Table 10.2, the first term of the solution in Eq. (10.19) applies and is shown in Figure 10.5. As it was to be expected, the influence of the ratio $\mathtt{n}_{X/b}$ is predominantly linear. Hence, the longer the beam is dimensioned, the greater the tip rotation becomes. Further on, the deviation of cross-sectional aspect ratio $\mathtt{n}_{a/b}$ from unity results for fixed wall properties in a reduction of the torsional stiffness and thus serves as an explanation for the increase of the tip twist. For warping-coupled twist, scheme *III* of Table 10.2, the second term of the solution in Eq. (10.19) is relevant and plotted in Figure 10.6. Regarding the cross-sectional aspect ratio $\mathtt{n}_{a/b}$, the argumentation with the torsional stiffness in this case should similarly hold. Since the quadratic occurrences of the ratio $\mathtt{n}_{X/b}$, within the constant ϱ_{warp} and in the denominator of the function $\eta_0(\xi)$, cancel each other out, there is hardly any influence of the relative beam length visible in the examined range of values. The only warping restraint of the configuration at hand is located at the clamped end of the beam. It is the source for a non-vanishing rate of twist and consequently

the warping coupling. Its influence may be slightly enlarged by an increase in the beam length. Alternatively, this could give rise to segmented designs with several warping restraints.

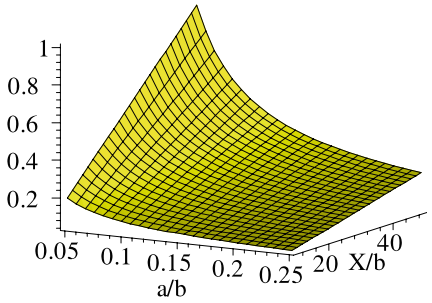

Fig. 10.5. Geometry influence on the direct and extension-coupled twist actuation (normalized).

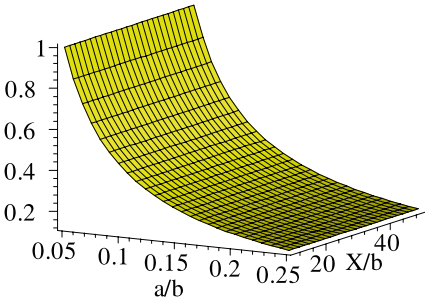

Fig. 10.6. Geometry influence on the warping-coupled twist actuation (normalized).

10.2.2 Beam Property Adaptation

To obtain results within the same order of magnitude as expected from the initially given application example of helicopter rotor blades, the data of an existing main rotor system will be utilized. The corresponding diagonal entries P_{11} to P_{66} of the beam stiffness matrix are given in Table B.1 for the BO105 of Bölkow/MBB/Eurocopter. The characteristic ratios regarding geometry and stiffness of the box beam will now be fitted as far as possible to the real-life example. Although such an agreement of properties is rather insignificant for the numerical validation, some premises might be formulated to define the configuration. First of all, the torsional stiffness should match, since it is closely related to the major objective of these examinations. Then, however, the stiffness request in the lengthwise direction of the beam cannot be fulfilled. Furthermore, one additional deviation has to be accepted:

Remark 10.8. The tensional stiffness P_{11} and the chordwise shear stiffness P_{22} are accepted to exhibit deviations from the application example data.

Cross-Sectional Aspect Ratio

Division of the shear stiffness coefficients of the beam, see Eq. (10.16e), by each other directly yields the cross-sectional aspect ratio

$$\mathtt{n}_{a/b} = \frac{P_{33}}{P_{22}}. \tag{10.20}$$

Similarly, the bending stiffness coefficients, see Eqs. (10.16b) and (10.16c), may be divided by each other. The resulting polynomial equation has three solutions, whereof only one is real:

$$\mathtt{n}_{a/b}^3 + 3\mathtt{n}_{a/b}^2 - 3\mathtt{n}_{a/b}\frac{P_{55}}{P_{66}} - \frac{P_{55}}{P_{66}} = 0. \tag{10.21}$$

The results of Eqs. (10.20) and (10.21) do not agree exactly. These, as well as further discrepancies, are caused by the fact that the single-cell thin-walled box beam, naturally, is not able to represent the properties of a solid configuration with multiple materials and complicated geometry. Consequently, one or the other beam stiffness coefficient cannot be accurately matched. The prioritization of Remark 10.8 gives preference to the result of Eq. (10.21). With the values of Table B.1, the cross-sectional aspect ratio is gained:

$$\mathtt{n}_{a/b} = 0.133. \tag{10.22}$$

Beam Aspect Ratio

The division of the torsional stiffness by a shear stiffness can be solved for the width b of the box beam. This can be done for each of the shear stiffness coefficients:

$$b = \sqrt{\frac{1+\mathtt{n}_{a/b}}{\mathtt{n}_{a/b}^2}\frac{P_{44}}{P_{22}}} \quad \text{or} \quad b = \sqrt{\frac{1+\mathtt{n}_{a/b}}{\mathtt{n}_{a/b}}\frac{P_{44}}{P_{33}}}. \tag{10.23}$$

In accordance with Remark 10.8, the variant involving the flapwise shear stiffness on the right-hand side of Eq. (10.23) is selected. Then with the values of Eq. (10.22) and Table B.1, the beam aspect ratio may be determined:

$$b = 0.216 \text{ m}, \qquad X = 4.54 \text{ m} \quad \longrightarrow \quad \mathtt{n}_{X/b} = 21.0. \tag{10.24}$$

Alternatively, the box beam width b could also be gained from dividing the one or the other bending stiffness by the tensional stiffness. Then, however, the torsional stiffness would be exceeded significantly and therefore such a procedure should be avoided, see Remark 10.8.

Relative Shear Stiffness

Analogously, the division of the torsional stiffness by a bending stiffness may be solved with Eq. (10.17) for the relative shear stiffness $\mathtt{a}_{33}$ of the box-beam wall. This again can be done for each of the bending stiffness coefficients:

$$\mathtt{a}_{33} = \frac{P_{44}}{P_{55}}\frac{(1+\mathtt{n}_{a/b})(3+\mathtt{n}_{a/b})}{12} \quad \text{or} \quad \mathtt{a}_{33} = \frac{P_{44}}{P_{66}}\frac{(1+\mathtt{n}_{a/b})(1+3\mathtt{n}_{a/b})}{12\mathtt{n}_{a/b}^2}. \tag{10.25}$$

Since the relationship between the stiffness coefficients P_{55} and P_{66} has been utilized to establish the cross-sectional aspect ratio $\mathtt{n}_{a/b}$ in Eq. (10.22), both variants of Eq. (10.25) with the values of Table B.1 provide identical results:

$$\mathtt{a}_{33} = 0.210. \tag{10.26}$$

Deviation Contemplations

With the characteristic ratios obtained above, it may now be possible to check how large the deviations tolerated by Remark 10.8 are. The shell stiffness coefficients $\grave{\mathtt{A}}_{11}$ and $\grave{\mathtt{A}}_{33}$ can be determined by substitution of Eqs. (10.23) and subsequently Eq. (10.22) into those beam stiffness coefficients of Eqs. (10.16), which are exactly kept and contain the respective shell stiffness coefficients to be solved for. Thus, all diagonal entries of the beam stiffness matrix can be calculated as given in Table 10.3 together with the deviations from the example application data, see Table B.1. The great discrepancy in the tensional stiffness P_{11} is due to the fact that the thin-walled box beam is not able to employ fibers close to its neutral axis, where they would primarily contribute to the tensional stiffness.

Table 10.3. Diagonal entries of the beam stiffness matrix resulting from the property adaptation with deviations from the application example data, see Table B.1.

Coefficient	Units	Value	Deviation
P_{11}	10^6 N	36.1	−50.5 %
P_{22}	10^6 N	6.71	+8.58 %
P_{33}	10^6 N	0.89	0
P_{44}	10^3 Nm^2	4.85	0
P_{55}	10^3 Nm^2	6.82	0
P_{66}	10^3 Nm^2	173	0
P_{77}	Nm^4	16.8	

10.2.3 Wall Geometry Optimization

On the one hand, the relative coupling stiffness $\mathtt{a}_{13}$ of the box-beam wall requiring knowledge about one of the coupling coefficients of the beam stiffness matrix and, on the other hand, those ratios of Eq. (10.17) representing the adaptive properties, are not prescribed. These remnants of the box-beam configuration will be specified through the study of the following optimization problem:

Remark 10.9. Optimize the box-beam configuration with the objective of attaining maximum tip twist in consideration of the different actuation schemes while satisfying the stiffness and geometry constraints of Section 10.2.2.

The basis of these examinations are the set-up of walls and the associated actuation schemes as described in Sections 10.1.2 and 10.1.1, respectively. The variables of the optimization problem at hand are the layer orientation angles α_1 and α_2, the relative thickness h of the central, lengthwise oriented fiber layer, and the fiber volume fraction ν. The effects of the relative sign of electric field strength and polarization, being allowed to change between layers as well as between sectors, are represented in a discrete manner by the actuation schemes of Table 10.2.

Satisfaction of the Stiffness and Geometry Constraints

To integrate the constraint on the relative shear stiffness $\mathtt{a}_{33}$, the corresponding relation from Eqs. (10.17) needs to be filled with the appearing stiffness coefficients, see Eq. (6.24). It may be rearranged so that the layer thickness ratio h, necessary to fulfill the constraint value of Eq. (10.26), is found for any combination of the variables α_1, α_2, and ν:

$$h = h\left(\alpha_1, \alpha_2, \nu\right). \tag{10.27}$$

The behavior represented by Eq. (10.27) is visualized for a fixed fiber volume fraction in Figure 10.7. It may be recognized that not all angular combinations are permissible, as the layer thickness ratio h must not become negative. Since no adaptive properties have been involved so far, these findings are valid for all actuation schemes. The use of Eq. (10.27) for substitution into

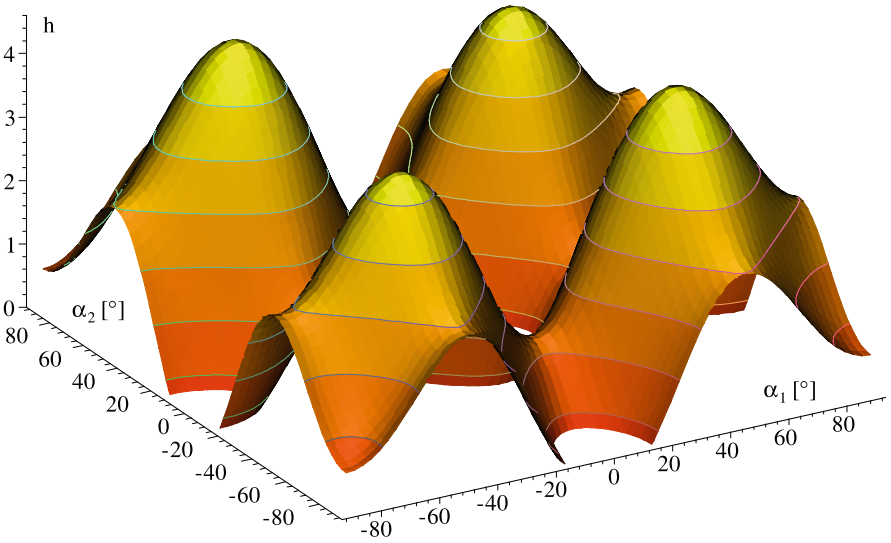

Fig. 10.7. Relative thickness of the lengthwise oriented fiber layer for a fiber volume fraction $\nu = 0.475$.

the objective function guarantees the satisfaction of the stiffness constraint and eliminates the variable h. The geometry constraints of Eqs. (10.22) and (10.24) are directly inserted.

Compilation of the Objective Function

The objective function of this optimization problem is the evaluation of the twist solution, being given by Eq. (10.19) in conjunction with Eqs. (10.17) and (10.18), at the free end of the beam. For the constitutive coefficients appearing in the respective ratios, the relative layer thickness h of Eq. (10.27) is required besides the material properties and the particular actuation scheme configuration from Table 10.2. After introduction of the geometry constraints, specified in Eqs. (10.22) and (10.24), the tip twist may be found for any combination of the variables α_1, α_2, and ν:

$$\phi = \phi\left(\alpha_1, \alpha_2, \nu, \xi = 1\right). \tag{10.28}$$

The behavior represented by Eq. (10.28) is exemplarily visualized for the cases of direct twist actuation (scheme *I* of Table 10.2) in Figure 10.8 and combined actuation of coupled extension and twist (scheme *IIb* of Table 10.2) in Figure 10.9 for a fixed fiber volume fraction.

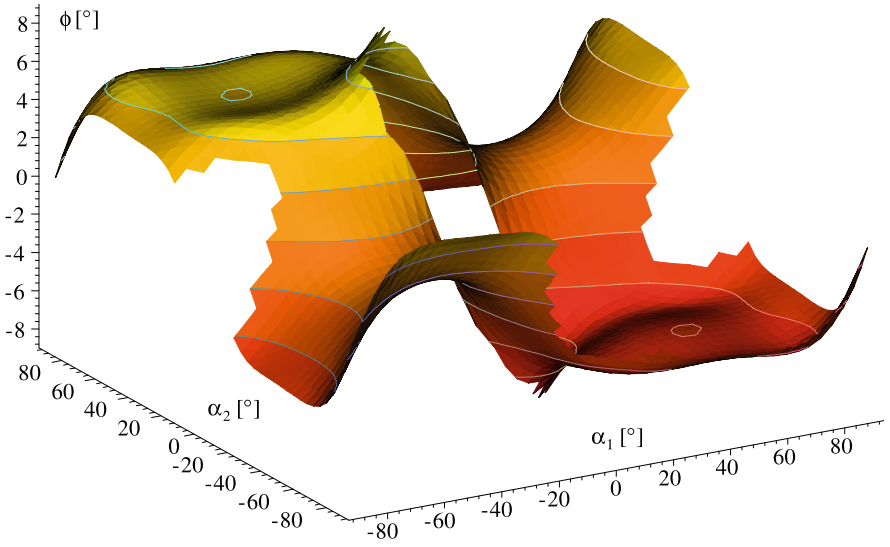

Fig. 10.8. Beam tip rotation due to direct twist actuation for a fiber volume fraction $\nu = 0.475$.

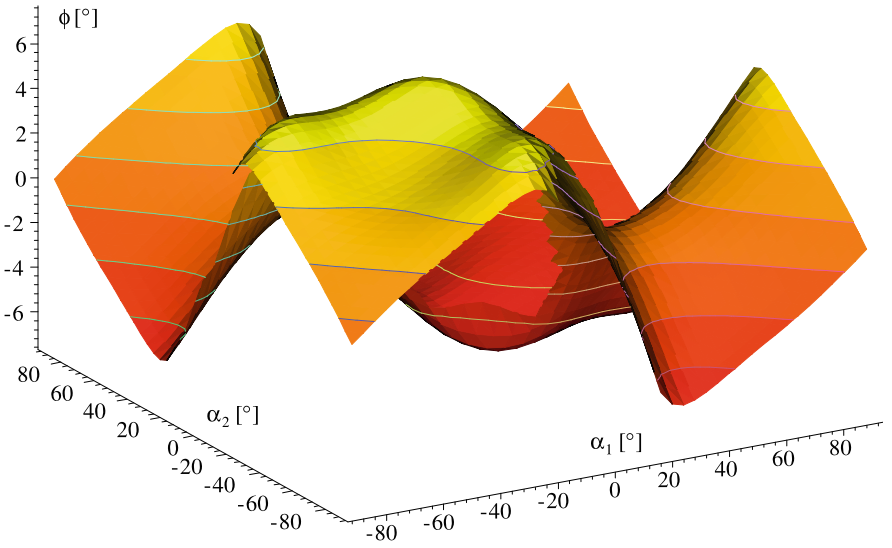

Fig. 10.9. Beam tip rotation due to combined actuation of coupled extension and twist for a fiber volume fraction $\nu = 0.475$.

Comparison of the Different Schemes

The joint observation of Figures 10.8 and 10.7 shows that the wanted extreme values are associated with the disappearance of the lengthwise-oriented fiber layer. This is not the case for any of the schemes involving the coupled extension and twist (schemes *IIa*, *IIb*, *IIc* of Table 10.2) as revealed, for example, by Figure 10.9. The maximum tip twist results for all schemes are given in Table 10.4.

Table 10.4. Maximum tip twist for the different actuation schemes and a fiber volume fraction $\nu = 0.475$.

Coupling	Actuation	Scheme	Tip Twist
none	torsion	*I*	9.45°
torsion & extension	torsion	*II a*	5.73°
	torsion & extension	*II b*	7.70°
	extension	*II c*	1.99°
torsion & warping	warping	*III*	0.139°

By far the best result is achieved by the direct twist actuation (scheme *I*) without utilization of anisotropic couplings. Regarding those schemes using such couplings between torsion and extension, the one with the combined actu-

ation of the helical wound as well as the lengthwise oriented fibers (scheme *IIb*) is superior to the pure variants. It does not involve passive fibers and, consequently, there is no need for surmounting the associated stiffness. Active warping torsion is not able to provide any similar results for this example configuration with a decay-length parameter $\lambda \approx 70$. Further on, the implementation would be more expensive due to the necessary segmented electroding. Nevertheless, the efficiency improves for comparatively short beams, as it is visible by comparing Figures 10.5 and 10.6 as well as by examining the function $\eta_0(\xi)$ in Figure 9.1.

Influence of the Fiber Volume Fraction

All the results shown above have been calculated for a fiber volume fraction $\nu = 0.475$. This value represents the optimum for the direct twist actuation and is very close to the optima of the other schemes. In Figure 10.10, the dependence of tip twist as well as layer orientation and thickness is exemplarily depicted for the direct twist scheme. The layer thickness H_1 therein is obtained by taking the formulation for one of the exactly preserved stiffness coefficients of the example rotor blade, see Remark 10.8 and Table 10.3, supplying it with all the known constitutive and configurative data, and solving it for the required value. As obvious here but applicable also for the other cases, it is found that the influence of the fiber volume fraction is rather good-natured, confirming the calculations with a collective value of the fiber volume fraction.

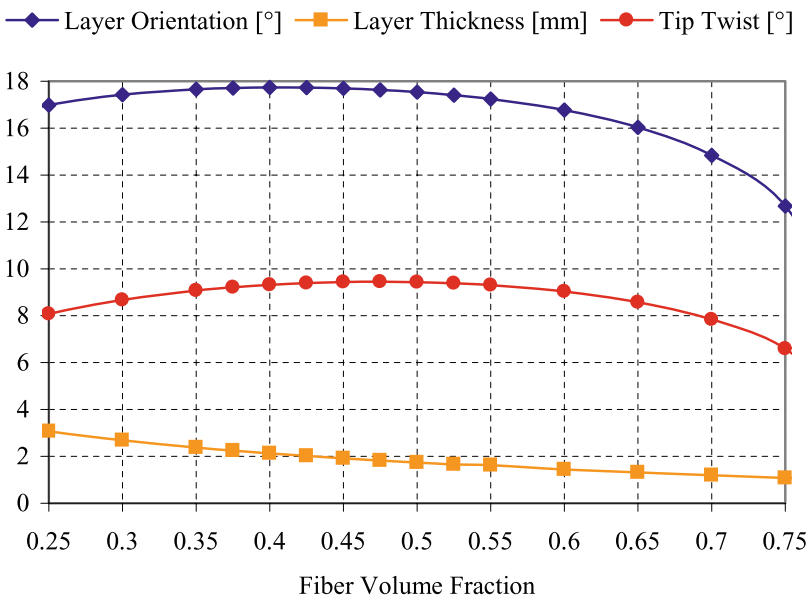

Fig. 10.10. Influence of the fiber volume fraction on the necessary layer orientation and thickness as well as on the resulting tip twist for the direct twist actuation.

10.3 Validation and Evaluation

While the analytical solution limited to the static problem has been applied at least in a simplified fashion for the elementary examinations of Section 10.2, the finite element solution capable of capturing the general problem has not yet been employed. Both solution variants will now be checked against each other and against an entirely independent approach with a commercial finite element software.

10.3.1 Reference Configurations

Again, the exemplary application data of the BO105 rotor system of Table B.1 will be employed. Thus, a beam of length X, clamped perpendicularly to the axis of rotation at the radius $\bar{X}$, is rotating with the angular velocity Ω. For the sake of simplicity, the precone angle as well as the angle of attack, included in the presented theory, are not put into operation. Since we have abstained from modeling the complexity associated with the blade attachment, the dynamic response results cannot be expected to be comparable to those of a real helicopter. Dissimilar to the considerations of Section 10.2, with the membrane response assumption of Remark 10.7, the shell representation may now be taken into account. Besides the already used geometry of the rectangular single-cell cross-section, the analysis will be extended to the convex double-cell cross-section, both being described in Section 10.1.3.

Rectangular Single-Cell Cross-Section

The most efficient configuration resulting from the optimization will be adopted for the subsequent calculations. This, namely, has been the direct twist actuation (scheme I of Tables 10.2 and 10.4). The relevant specifications concerning the geometry of the cross-section are given by Eqs. (10.22) and (10.24) or may be gathered for the wall set-up from Figure 10.10:

$$\alpha_1 = -\alpha_2 = -17.6^\circ, \qquad H_1 = 1.82 \text{ mm}. \tag{10.29}$$

On this basis, the complete set of constitutive coefficients of the beam can be calculated according to Eqs. (10.16). Due to the symmetric lay-up with balanced layer orientation of the selected scheme, the walls do not exhibit any coupling between the lengthwise extension and shear ($\mathtt{\tilde{A}}_{13} = 0$). Consequently, the beam neither possesses couplings between extension and torsion ($P_{14} = 0$) nor between bending and shear ($P_{25}, P_{36} = 0$). The remaining, non-vanishing coefficients are given for the two reduced shell response variants in Table 10.5 together with the relative deviations from membrane response as considered in Table 10.3. The enhanced calculation using the shell description without cross-sectional loads, Eqs. (6.22), leads to a stiffening of the affected coefficients by less than one percent. On the contrary, the shell description without cross-sectional strains, Eqs. (6.23), shows greater deviations since it is valid only for

the rather special case where any contraction or expansion of the cross-section is counteracted, for example, by an internal pressurization of the beam.

Table 10.5. Constitutive properties of the exemplary beam configuration with rectangular single-cell cross-section.

		Shell without Cross-Sectional Loads, see Eq. (6.22)		**Strains**, see Eq. (6.23)	
Coefficient	**Units**	Value	Deviation [%]	Value	Deviation [%]
P_{11}	10^6 N	36.1	0	41.2	+12.2
P_{22}	10^6 N	6.71	0	6.71	0
P_{33}	10^6 N	0.890	0	0.890	0
P_{44}	10^3 Nm^2	4.88	+0.70	4.88	0
P_{55}	10^3 Nm^2	6.85	+0.52	7.81	+12.7
P_{66}	10^3 Nm^2	173	+0.00	197	+12.2
P_{77}	Nm^4	17.0	+0.82	19.3	+12.9
P_{48}	$10^{-3}\ \frac{\text{Nm}}{\text{V}}$	0.178	0	0.178	0
P_{88}	$10^{-12}\ \frac{\text{Nm}^2}{\text{V}^2}$	11.4	0	11.4	0

Convex Double-Cell Cross-Section

The curved cross-section is divided by a central web into two cells. The associated geometric description is given by Eqs. (10.10) and (10.11). On this basis, the radius of curvature R and generating half-angle ζ may be expressed in terms of the beam width b and the ratio $\mathtt{n}_{a/b}$ between the extents along the cross-sectional axes:

$$\begin{aligned} &y\,(s_1 = S_1) = R\sin\zeta = \tfrac{b}{2}, \\ &z\,(s_1 = 0) = R\,(1-\cos\zeta) = \mathtt{n}_{a/b}\tfrac{b}{2} \end{aligned} \quad \longrightarrow \quad \tan\zeta = \frac{2\mathtt{n}_{a/b}}{1+\mathtt{n}_{a/b}^2},\ R = \frac{1+\mathtt{n}_{a/b}^2}{4\mathtt{n}_{a/b}}b. \tag{10.30}$$

Although such a shape still is symmetric with regard to both principal axes, adaptation of beam properties and optimization of wall geometry cannot be accomplished with such simple measures as available for the box beam. Not to exceed the scope of the work at hand, here we will desist from the thrills of sophisticated optimization procedures; elementary literature is provided by *Collatz and Wetterling* [55] or *Pierre* [141]. Since convex cross-section and airfoil profile are similar to a certain extent, the blade chord b will be utilized directly, as given by Table B.1. Together with arbitrary fixing of the cross-sectional aspect ratio $\mathtt{n}_{a/b}$, the generating half-angle ζ and radius of curvature R, according to Eq. (10.30), read as follows:

$$b = 0.27\text{ m}, \qquad \mathtt{n}_{a/b} = 0.155 \quad \longrightarrow \quad \zeta = 17.6°, \qquad R = 0.446\text{ m}. \tag{10.31}$$

In Remarks 10.3 to 10.6, the wall properties around the circumferential contour have been specified. For the central web, however, an altered configuration may be selected. In the beam property adaptation of Section 10.2.2 for

the rectangular single-cell cross-section, it has not been possible to get close to the tensional stiffness of the example application data due to the lack of fibers close to the neutral axis. This can be improved by furnishing the web with purely lengthwise oriented fibers with the greatest possible stiffness. To comply with the assumption of thin walls, included in Remark 6.4, the thickness of the web will be limited to 1/10 of its height. Adding tensional stiffness to the center of the cross-section requires a reduction around the contour and thus allows for a thinner skin and/or increased fiber angle. Such a configuration of the wall geometry is given in the following.

$$\text{Web:} \quad H_0 = 4.19 \text{ mm}, \qquad H_1 = 0 \text{ mm}, \tag{10.32a}$$

$$\text{Skin:} \quad H_0 = 0 \text{ mm}, \qquad H_1 = 0.55 \text{ mm}, \qquad \alpha_1 = -\alpha_2 = 22.5^\circ. \tag{10.32b}$$

Using high modulus carbon fibers for the web, see Table A.1, the geometry specified by Eqs. (10.31) and (10.32) leads to the beam properties given in Table 10.6 being approximately within the same order of magnitude of the example application data, see Table B.1. Unlike the case of the box beam, the couplings between bending and shear (P_{25}, P_{36}) do not only depend on the coupling of lengthwise extension and shear ($\mathtt{\grave{A}}_{13} = 0$) but also on the bending and twist ($\mathtt{\check{D}}_{13} \neq 0$) of the outer wall. Such effects, however, are beyond the scope of the membrane response assumption. Due to the limited thickness of the web, the selected configuration shows only a minor increase in the tensional stiffness. Further on, the centered web aligned with one cross-sectional axis is not able to fully depict the influence pertaining to the both axes as exerted in real life by a solid spar.

10.3.2 Reference Calculations

The stiffening due to the assumption of a cross-section without strains, respectively curvatures, in its plane visible in the right-hand columns of Tables 10.5 and 10.6, has been found to be not very realistic. Hence, the subsequent calculations will be conducted by means of the assumption of a cross-section without loads in its plane. The results obtained for such a shell description of the beam walls are, furthermore, to be compared to the outcome of the significantly simpler membrane description. As briefly mentioned in the introduction to this section, three different solution approaches will be examined. The associated individual restrictions are discussed in the following.

Analytic Approach

Within the bounds of the underlying theory, the analytic solution derived in Section 9.1 can be regarded as exact. It is confined to the statics of the non-rotating structure as well as certain constitutive couplings and load configurations. Special cases, like the elongation of the rotating beam due to centrifugal forces, may be simulated with the appropriate choice of loads.

Table 10.6. Constitutive properties of the exemplary beam configuration with convex double-cell cross-section.

Coefficient	Units	Membrane, see Eq. (6.20)	Shell without Loads, see Eq. (6.22)	Cross-Sectional Strains, see Eq. (6.23)
P_{11}	10^6 N	39.2	39.2	44.2
P_{22}	10^6 N	6.17	6.17	6.17
P_{33}	10^6 N	0.929	0.929	0.929
P_{44}	10^3 Nm^2	4.84	4.86	4.86
P_{55}	10^3 Nm^2	6.81	6.81	7.98
P_{66}	10^3 Nm^2	77.3	77.3	107.8
P_{77}	Nm^4	0.798	0.822	1.14
P_{25}	Nm	0	0.827	1.11
P_{36}	Nm	0	0.0264	0.0355
P_{48}	10^{-3} $\frac{\text{Nm}}{\text{V}}$	0.172	0.172	0.172
P_{88}	10^{-12} $\frac{\text{Nm}^2}{\text{V}^2}$	6.31	6.31	6.31

Beam Finite Elements

Due to the discretization and interpolation, the finite element method is categorized as an approximation. The corresponding details are shown throughout the course of derivation of the beam finite element solution in Section 9.2. With identical underlying theory but without all the restrictions necessary to obtain an analytical solution, it is able provide answers to a wide range of problems.

Shell Finite Elements

As outlined in Section 4.2.5, the implementation of anisotropic thermal effects in commercial finite element codes may be utilized to simulate the implications of the piezoelectric effect. To capture the behavior of thin-walled beams with cross-sections as defined above, spatial shell elements may be employed. With this methodology, however, it is not possible to examine problems with dynamic actuation. The beams with rectangular and convex cross-sections have been discretized with 2200, respectively 2300, SHELL99 elements of ANSYS as exemplarily shown for the latter case in Figure 10.11.

10.3.3 Static Behavior

Since neither the analytic approach nor the application of shell finite elements is able to handle the general problem of dynamic actuation and response in the rotating environment, the developed beam finite elements need to be counterchecked by means of the individual solution components, see Section 9.2.3.

Fig. 10.11. Discretization of the convex cross-section beam with shell finite elements.

Beam Extension due to Centrifugal Forces

First, the steady-state solution with the elongation of the blade resulting from the centrifugal forces will be examined. The formulation for the analytical approach is provided by Eq. (9.8). The required linear and constant portions of the line force $\breve{n}(x)$ in the lengthwise direction depicting the centrifugal effects are

$$\breve{\mathfrak{n}}_x = \mathtt{m}\Omega^2, \qquad \breve{n}_x = \breve{\mathfrak{n}}_x \bar{X}. \tag{10.33}$$

The contained constant $\mathtt{m}$ represents mass per length of the beam. For the two different cross-sections under consideration, it takes the following form.

$$\text{Rectangular cross-section:} \quad \mathtt{m} = 8\left(1 + \mathtt{n}_{a/b}\right) bH_1\rho, \tag{10.34a}$$

$$\text{Convex cross-section:} \quad \mathtt{m} = 4\zeta R \underbrace{4H_1\rho}_{\text{skin}} + 2\left(1 - \cos\zeta\right) R \underbrace{H_0\rho}_{\text{web}}. \tag{10.34b}$$

Although the stiffness properties are largely similar, the total masses of the two beam variants differ significantly due to the diversity of construction and materials. While the single-cell rectangular cross-section possesses a mass of 33.8 kg, the double-cell convex cross-section beam gets by with only 20.0 kg. The beam elongation in response to the centrifugal force field is shown for the different calculation approaches in Table 10.7. Since both beams are free of extension torsion coupling ($P_{14} = 0$), no plate properties are involved in the solution to the lengthwise displacement, see Eqs. (9.8) and (8.7a). Therefore, the comparison of the two analytic variants cannot show any divergence to be induced by the membrane response assumption. Both finite element solutions are very close to each other and show only minor deviations to the analytical solution. Therewith, the vector of centrifugal forces $\mathring{\boldsymbol{m}}_{\Omega}(\Omega)$ as well as the longitudinal components of the beam stiffness matrix $\mathring{\mathbf{P}}_{\Sigma}(\Omega)$ of Eqs. (9.27) and (9.28), respectively, are successfully checked.

Table 10.7. Beam extension due to centrifugal forces.

Method	Shell Assumption	Rect. Single-Cell $u(\xi=1)$ [cm]	Rect. Single-Cell Error [%]	Conv. Double-Cell $u(\xi=1)$ [cm]	Conv. Double-Cell Error [%]
analytic	no cross-sec. loads, Eq. (6.22)	1.4204		0.7760	
	membrane response, Eq. (6.20)	1.4204	0	0.7760	0
beam FE	no cross-sec. loads, Eq. (6.22)	1.4252	+0.34	0.7774	+0.18
shell FE	ANSYS SHELL99	1.4245	+0.30	0.7817	+0.74

Beam Torsion due to Piezoelectric Coupling

Next, a constant electric field will be applied to the piezoelectric composites within the non-rotating structure to verify the constant factor of the piezoelectric actuation vector $\mathring{\boldsymbol{p}}(t)$ as well as the torsional components of the beam stiffness matrix $\mathring{\mathbf{P}}_{\Sigma}(\Omega)$. This is done in consideration of the warping effect with cubic Hermite shape functions and without the warping effect using linear Lagrange polynomials, see Section 9.2.2. The first shows good agreement with the exact analytical solution and the shell finite element model, while in the latter case the torsional rigidity is notably smaller due to abandonment of the warping restraint at the clamped end. Naturally, the actuation vectors in both cases are identical. The values of the resulting blade tip rotation are given in Table 10.8.

Table 10.8. Beam torsion due to piezoelectric coupling.

Method	Shell Assumption	Rect. Single-Cell $\phi(\xi=1)$ [°]	Rect. Single-Cell Error [%]	Conv. Double-Cell $\phi(\xi=1)$ [°]	Conv. Double-Cell Error [%]
analytic	no cross-sec. loads, Eq. (6.22)	9.4479		9.1983	
	membrane response, Eq. (6.20)	9.4484	+0.01	9.1987	+0.00
beam FE	no cross-sec. loads, Eq. (6.22)	9.4184	−0.31	9.2076	+0.10
	— ” —, without warping	9.5436	+1.01	9.2408	+0.46
shell FE	ANSYS SHELL99	9.4584	+0.11	9.2185	+0.22

Different from above, plate properties ($\check{\mathtt{D}}_{33}$) are involved in the solution to the twisting angle, see Eqs. (9.4), (9.5), and (8.8c). Due to the closed cross-sections and thin walls, the implications of the membrane response assumption are very small for the cases at hand. However, this changes drastically with the consideration of open cross-section topologies just as well covered by the developed theory, where the torsional stiffness (P_{44}) of the beam is solely governed by the twisting stiffness ($\check{\mathtt{D}}_{33}$) of the walls. As an example, the box beam subjected to piezoelectrically induced torsion is shown for the shell finite element approach in Figure 10.12. Close to the clamped end, the influence of the warping restraint on the beam twist becomes visible.

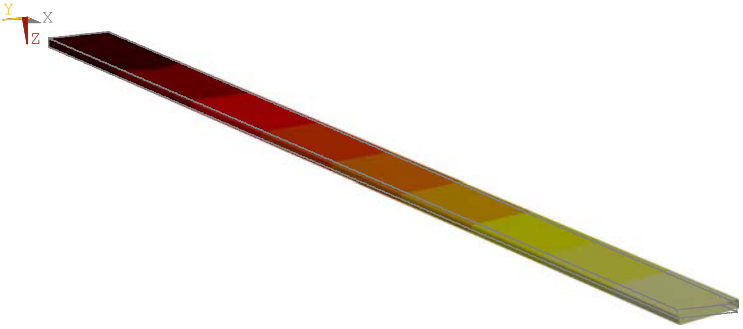

Fig. 10.12. Torsion of the rectangular cross-section beam via piezoelectric coupling.

10.3.4 Free Vibrations

Since the essential parts of the right-hand side of the differential equation system, given by Eqs. (9.27), have demonstrated their operability, the homogeneous solution will be examined in detail to complete the inspection of the left-hand side. As there is no analytic approach available to capture the dynamic behavior, the subsequent comparison comprises the formulations with the developed beam finite elements and with the commercial shell finite elements. The resulting natural frequencies ω for all modes up to the third torsional mode are given in Table 10.9 for the non-rotating system as well as in Table 10.10 for the rotating system.

Table 10.9. Natural angular frequencies of the non-rotating systems.

ω[1/s]	**Rect. Single-Cell**		**Conv. Double-Cell**	
Mode Shape	Beam FE	Shell FE	Beam FE	Shell FE
1^{st} lead-lag	25.92	25.88	22.56	22.61
2^{nd} lead-lag	159.39	158.69	139.79	139.81
3^{rd} lead-lag	433.67	430.11	384.80	383.51
1^{st} flap	5.17	5.16	6.70	6.72
2^{nd} flap	32.28	31.92	41.84	41.82
3^{rd} flap	89.80	87.37	116.42	115.08
4^{th} flap	174.33	164.96	226.13	217.91
5^{th} flap	284.84	258.11	369.70	340.62
6^{th} flap	419.67	357.34	545.08	470.48
7^{th} flap	577.01	452.55	750.04	569.63
1^{st} torsion	127.36	121.84	148.89	145.25
2^{nd} torsion	382.69	314.74	446.71	372.29
3^{rd} torsion	639.82	424.57	744.63	491.20

Table 10.10. Natural angular frequencies of the rotating systems.

ω[1/s]	**Rect. Single-Cell**		**Conv. Double-Cell**	
Mode Shape	Beam FE	Shell FE	Beam FE	Shell FE
1^{st} lead-lag	34.73	34.99	32.27	32.53
2^{nd} lead-lag	193.13	192.98	177.46	177.86
3^{rd} lead-lag	473.34	470.79	428.97	428.58
1^{st} flap	48.23	48.41	48.92	48.93
2^{nd} flap	121.18	120.61	124.58	123.32
3^{rd} flap	210.86	208.71	225.04	217.71
4^{th} flap	323.10	315.72	355.98	330.90
5^{th} flap	456.24	435.27	515.80	453.23
1^{st} torsion	127.07	138.17	148.64	154.21
2^{nd} torsion	382.59	342.50	446.63	382.56
3^{rd} torsion	639.82	471.60	744.58	508.03

Influence of the Rotation

Comparing the natural frequencies of the non-rotating and rotating system, consistently reveals a moderate increase for the lead-lag modes and a steep increase for the flapping modes. The deviating imprints of the rotational stiffening are founded on the significantly dissimilar structural stiffness properties with regard to the respective cross-sectional axis. This behavior is also being reflected in the associated mode shapes as visible in the example of Figure 10.13 for the fifth bending mode shape of the rectangular cross-section beam and Figure 10.14 for the third lead-lag mode shape of the convex cross-section beam. With the increase of beam internal loads towards the center of rotation, the oscillation amplitudes decrease, while the wavelength is stretched. For the developed beam finite elements, such effects are captured by virtue of the second-order theory of Section 8.3. Its derivation, however, does not indicate similar effects for either rotation or warping, see Eq. 8.39. Consequently, frequencies as well as shapes of the torsional modes are not sensitive to rotation in the beam finite element model. In contrast, the shell finite element model shows at least a small dependence.

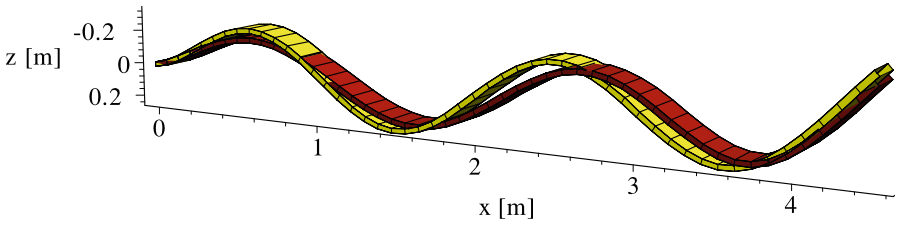

Fig. 10.13. Fifth flapping mode of the rectangular cross-section beam for the non-rotating (light) and rotating (dark) system (beam finite elements).

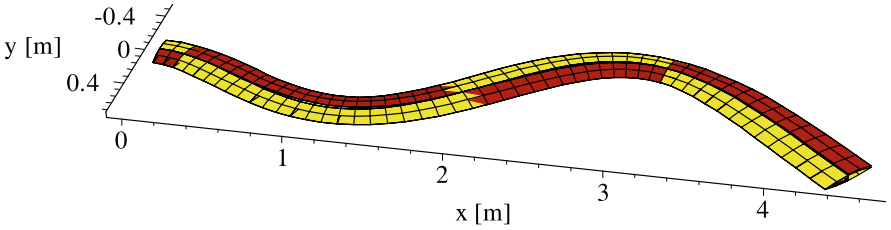

Fig. 10.14. Third lead-lag mode of the convex cross-section beam for the non-rotating (light) and rotating (dark) system (beam finite elements).

Influence of the Modeling Approach

The natural frequencies of the lower lead-lag and flapping modes agree very well across the models with beam and shell finite elements. The higher ones show an increasing divergence which cannot be counteracted by a refined discretization. The reason for the divergence can be found in those effects exhibited by the shell description that are not included in the beam description. Most prominent among these are the implications of the classical assumption of beam theory, see Remark 7.4. Stating that the preservation of the cross-sectional shape in its plane is equivalent to the infinite bending stiffness of the walls in this plane, such properties obviously do not correspond to the observations made with the shell model visible in Figures 10.15 and 10.16. It becomes clear that the neglected warping deformation in the cross-sectional plane, capable of depicting the local inertia effects of the walls, increasingly gains importance in comparison to the global inertia effects of the beam with higher frequencies and shorter wavelengths. The aspect ratio of the latter with the corresponding edge length of the cross-section may be considered in analogy to buckling phenomena. In the case of the torsional behavior, the

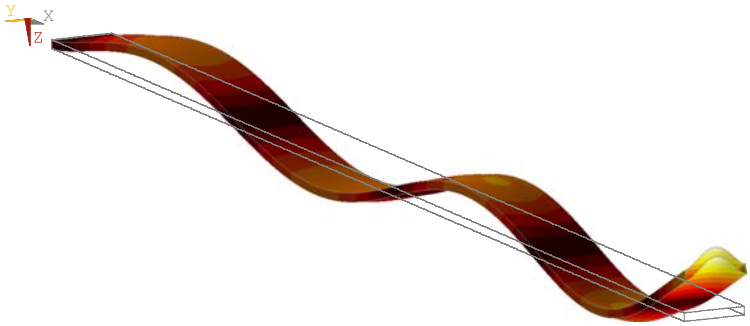

Fig. 10.15. Fifth flapping mode of the rectangular cross-section beam subjected to rotation (shell finite elements).

discrepancy of the natural frequencies with ascending mode shapes is even more articulate. The considered warping displacements are confined to proportionality with the twist rate and to the direction out of the cross-sectional plane, see Remarks 7.3 and 7.4 leading to Eq. (7.11). Just like in the case of the lead-lag and flapping modes, there are no means of accounting for local inertia effects of the walls and resulting decrease of natural frequencies. In Figures 10.17 and 10.18, the cross-sectional deformations are already noticeable for the first torsional mode but become excessive for the third torsional mode. In addition to relatively thin walls, both example configurations possess very slim cross-sections being fairly disadvantageous in this context.

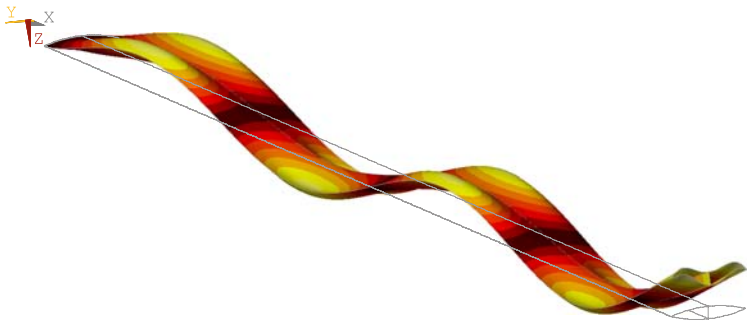

Fig. 10.16. Fifth flapping mode of the convex cross-section beam subjected to rotation (shell finite elements).

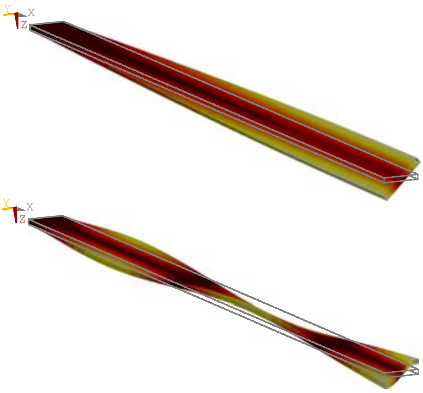

Fig. 10.17. First and third torsional modes of the rectangular cross-section beam not subjected to rotation (shell finite elements).

Fig. 10.18. First and third torsional modes of the convex cross-section beam not subjected to rotation (shell finite elements).

Influence of the Cross-Section

In all cases, the agreement of beam and shell finite element results for the convex double-cell cross-section is superior to the rectangular single-cell cross-section. On the one hand, the outer walls of the first are thinner and thus more flexible, but on the other hand, they contribute only a part of the total mass. Further on, the convex shape and particularly the stiff web, stabilize the cross-sectional shape. Consequently, the beam with a convex double-cell cross-section is less sensitive to the influence of the local inertia effects of the walls in comparison to the global inertia effects of the beam. Moreover, the not yet explicitly mentioned discrepancy of beam and shell finite element results for the first torsional mode as well as the rotation dependence of natural frequencies for torsional mode shapes in the shell model, are diminished with the convex double-cell cross-section. Therefore, it is permissible to conclude that the discovered deviations on the whole are due to the different handling of the cross-section with the use of beam and shell finite elements respectively. So which of these two modeling approaches is more appropriate? As always, there are two faces to the truth. Regarding the results in correspondence with the input data, the shell representation, presuming proper implementation, is clearly more precise. However, the input data already represents an idealization, since the actual structure, which in the given example is equipped with a foam core and thus is prevented from noticeable deformations of the cross-sectional shape, has been replaced by its thin-walled likeness. To conclude, further pieces of the beam stiffness matrix $\mathring{\mathbf{P}}_{\Sigma}(\Omega)$ as well as mass matrix $\mathring{\mathbf{M}}''$ and gyroscopic matrix $\mathring{\mathbf{M}}'_{\Omega}(\Omega)$ may be regarded as validated.

10.3.5 Forced Vibrations

As far as available, the counter-check of individual solution components, see Section 9.2.3, has been successfully completed in Sections 10.3.3 and 10.3.4. The developed beam finite elements may now be employed for their proprietary task of simulating the universal dynamic behavior of adaptive thin-walled beams. In the most general case, the developed theory is able to describe the mechanical as well as the electric response to combined mechanical and electric excitation. In the context of Remark 10.1, the example configuration has been simplified to handle either actuation or sensing and with the helicopter rotor blade application in mind, the prior has been pursued. So finally, the response of the rotating beam to a piezoelectrically induced twist actuation will be sought. To visualize the result, the twist angle of the last node is selected from the overall solution of Eq. (9.41) and displayed over time in Figure 10.19. Since the harmonic excitation with the threefold of the rotor angular frequency is close to the frequency of the first torsional mode of the employed box beam, the plot shows the characteristic beat pattern. With this last step, the three-dimensional dynamic behavior of

an adaptive thin-walled beam in a rotating environment is completely predictable.

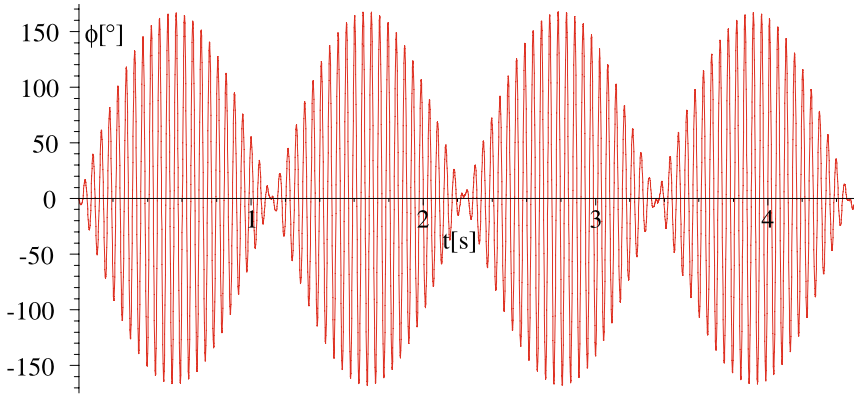

Fig. 10.19. Tip twist of the box beam in response to harmonic excitation with the threefold of the rotor angular frequency.

11

Conclusion

In this final chapter, we will attempt to review the findings attained during the various steps of theory derivation and subsequent validation as well as to present the prospect of potential future development.

11.1 Summary

Adaptive fiber composites have been examined on the basis of a thorough, systematic treatment of the theory across a wide spectrum from piezoelectric material behavior to the dynamics of rotating structures. Making a point of consistency and continuity, the derived formulations are accompanied by several innovations and improvements, the most relevant of which will be recalled below:

- Extension of Dirichlet's principle of minimum potential energy to electromechanically coupled problems.
- Deduction of simplifying assumptions for piezoelectric materials in consideration of spatial extent and electroding configuration via examination of associated implications on spatial field distributions.
- Proposition of an enhanced micro-electromechanical model to determine the constitutive properties of piezoelectric composites based on the sequential stacking of constituents with uniform fields.
- Derivation of a comprehensive description of composite shells with piezoelectric layers in arbitrary configuration for possibly combined actuation and sensing.
- Development of a novel theory for thin-walled beams with arbitrary cross-sections incorporating more than the usual membrane properties without additional degrees of freedom.
- Consideration of shear flexibility, torsional warping, and electromechanical coupling as well as of rotational effects by virtue of including an extended set of second-order terms.

T.H. Brockmann, *Theory of Adaptive Fiber Composites*,
Solid Mechanics and Its Applications 161,

- Derivation of an analytic solution to gain insight into the static behavior of structures with adaptive capabilities and to be used for adjustment and optimization of beam configurations.
- Derivation of a general solution via the formulation of spatial beam finite elements, accounting for arbitrary combinations of actuator and sensor applications with voltage and current source, respectively measurement, to capture the dynamic behavior of the rotating structure.

To ensure the soundness of the various assumptions and simplifications made throughout the course of derivation as well as to exclude errors in the implementation, the obtained results have been successfully counterchecked using completely independent approaches. Therein, the following steps are regarded, in particular:

- Validation of the micro-electromechanical model for piezoelectric composites with the aid of experimental and finite element modeling results available in the literature.
- Validation of the beam finite elements by comparison of solution components to those attainable with commercial shell finite elements for example configurations with a rectangular single-cell and a convex double-cell cross-section approximating the properties of an actual helicopter rotor blade.

Using the presented comprehensive formulation of the theoretical framework and the associated elementary examinations, the recognition and utilization of causal relationships, in view of the manipulation of structural behavior with adaptive means, is facilitated. With the resulting spatial beam finite elements, a versatile modeling tool can be provided as a basis for further investigations.

11.2 Perspective

The focus of this work is directed towards the structural aspects of adaptive systems with associated actuation and sensing capabilities. The consequential next step therefore would be to consider the linkage with various control models to make the abilities of the complete system accessible. With regard to the application case of helicopter rotor blades, coupling with an aerodynamics model would allow us to perform the aeroelastic analyses necessary to prove the effectiveness of the concept. Furthermore, noise emission and impact on the environment might be simulated by means of an acoustics model. To enhance the comparability of the developed adaptive thin-walled beam representation with the real rotor system, it could be refined with additional features, like pre-twist, non-rigid blade mounting, or cyclic pitch to cover forward flight conditions. Another direction for the extension of the developed theory is the incorporation of alternative constitutive models to take other multifunctional materials into account. This could be interesting, especially for the example of composites with electromechanical coupling through carbon nanotubes.

To ensure correctness of the partially complex derivation, the symbolic mathematics software Maple has been employed for each and every step, including implementation of the beam finite elements. The numeric computations could be carried out with the support of integrated routines from the library of the Numerical Algorithms Group (NAG). Nevertheless, the computational performance and, moreover, the user-friendliness have never surpassed the level of a development tool. Therefore, an implementation involving fast equation-solvers and an easy-to-use interface is advisable. This could be accomplished, for instance, through the extension of an existing finite element or multi-body dynamics code, which in addition would allow for combination with a variety of other elements. While the presented example calculations have so far revealed only a touch of the genuine capabilities, such a software would enable the comfortable accomplishment of comprehensive design studies. The results to be obtained therewith should be put into practice with the construction of test specimens and be compared to the ensuing experimental results.

A

Material Properties

Table A.1. Properties of the applied reinforcement material.

	Carbon Fibers, Ref. [116]			
Units	Stiffness Constants		Engineering Constants	
$10^9 \frac{\mathrm{N}}{\mathrm{m}^2}$	$C_{11} = C_{22}$	20.0	$E_1 = E_2$	15.0
	C_{12}	9.98	E_3	232
	$C_{13} = C_{23}$	6.45	$G_{13} = G_{23}$	5.01
	C_{33}	235	G_{12}	24.0
	$C_{44} = C_{55}$	24.0	$\nu_{13} = \nu_{23}$	0.0139
	C_{66}	5.01	ν_{12}	0.495
$10^3 \frac{\mathrm{kg}}{\mathrm{m}^3}$	Density ρ	1.8*		

Table A.2. Properties of polymer materials.

		Araldite D	**Araldite 2020**	**Epon 9405**
Constants	**Units**	Ref. [49]	Ref. [169]	prod. data
$C_{11} = C_{22} = C_{33}$	$10^9 \frac{\mathrm{N}}{\mathrm{m}^2}$	8.0	7.28	4.57
$C_{12} = C_{13} = C_{23}$		4.4	4.46	2.46
$C_{44} = C_{55} = C_{66}$		1.8	1.41	1.05
$E_1 = E_2 = E_3$	$10^9 \frac{\mathrm{N}}{\mathrm{m}^2}$	4.88	3.89	2.85
$\nu_{12} = \nu_{13} = \nu_{23}$		0.35	0.38	0.35*
$\frac{\epsilon_{11}}{\epsilon_0} = \frac{\epsilon_{22}}{\epsilon_0} = \frac{\epsilon_{33}}{\epsilon_0}$		4	5	4*
ρ	$10^3 \frac{\mathrm{kg}}{\mathrm{m}^3}$			1.161

* estimated

T.H. Brockmann, *Theory of Adaptive Fiber Composites*,
Solid Mechanics and Its Applications 161,

Table A.3. Properties of piezoelectric materials.

Constants	Units	PZT-5A Ref. [20]	PZT-5H Ref. [20]	PZT-7A Ref. [19]	PMN-30%PT Ref. [186]
$C_{11}^{\boldsymbol{E}} = C_{22}^{\boldsymbol{E}}$	$10^9 \frac{\mathrm{N}}{\mathrm{m}^2}$	121	126	148	117
$C_{12}^{\boldsymbol{E}}$		75.4	79.5	76.2	103
$C_{13}^{\boldsymbol{E}} = C_{23}^{\boldsymbol{E}}$		75.2	84.1	74.2	101
$C_{33}^{\boldsymbol{E}}$		111	117	131	108
$C_{44}^{\boldsymbol{E}} = C_{55}^{\boldsymbol{E}}$		21.1	23.0	25.3	71
$C_{66}^{\boldsymbol{E}}$		22.6	23.5	36.0	66
$S_{11}^{\boldsymbol{E}} = S_{22}^{\boldsymbol{E}}$	$10^{-12} \frac{\mathrm{m}^2}{\mathrm{N}}$	16.4	16.5	10.7	52.0
$S_{12}^{\boldsymbol{E}}$		−5.74	−4.78	−3.2	−18.9
$S_{13}^{\boldsymbol{E}} = S_{23}^{\boldsymbol{E}}$		−7.22	−8.45	−4.6	−31.1
$S_{33}^{\boldsymbol{E}}$		18.8	20.7	13.9	67.7
$S_{44}^{\boldsymbol{E}} = S_{55}^{\boldsymbol{E}}$		47.5	43.5	39.4	14.0
$S_{66}^{\boldsymbol{E}}$		44.3	42.6	27.8	15.2
$E_1^{\boldsymbol{E}} = E_2^{\boldsymbol{E}}$	$10^9 \frac{\mathrm{N}}{\mathrm{m}^2}$	61.5	60.0	95.0	19.3
$E_3^{\boldsymbol{E}}$		53.4	48.2	81.9	15.3
$G_{13}^{\boldsymbol{E}} = G_{23}^{\boldsymbol{E}}$		21.1	23.0	25.3	71.0
$G_{12}^{\boldsymbol{E}}$		22.6	23.5	36.0	66.0
$\nu_{13}^{\boldsymbol{E}} = \nu_{23}^{\boldsymbol{E}}$		0.441	0.510	0.384	0.581
$\nu_{12}^{\boldsymbol{E}}$		0.349	0.291	0.322	0.379
$e_{31} = e_{32}$	$\frac{\mathrm{N}}{\mathrm{Vm}}$	−5.4	−6.55	−2.11	−2.4
e_{33}		15.8	23.3	9.5	27.1
$e_{15} = e_{24}$		12.3	17.0	9.2	13.6
$d_{31} = d_{32}$	$10^{-12} \frac{\mathrm{m}}{\mathrm{V}}$	−171	−274	−60	−921
d_{33}		374	593	150	1981
$d_{15} = d_{24}$		584	741	362	190
$\frac{\epsilon_{11}^{\boldsymbol{\varepsilon}}}{\epsilon_0} = \frac{\epsilon_{22}^{\boldsymbol{\varepsilon}}}{\epsilon_0}$		916	1700	460	3307
$\frac{\epsilon_{33}^{\boldsymbol{\varepsilon}}}{\epsilon_0}$		830	1470	235	1242
$\frac{\epsilon_{11}^{\boldsymbol{\sigma}}}{\epsilon_0} = \frac{\epsilon_{22}^{\boldsymbol{\sigma}}}{\epsilon_0}$		1730	3130	840	3600
$\frac{\epsilon_{33}^{\boldsymbol{\sigma}}}{\epsilon_0}$		1700	3400	425	7800
ρ	$10^3 \frac{\mathrm{kg}}{\mathrm{m}^3}$	7.75	7.5	7.6	8.04
T_{CP}	°C	365	193	350	

B

Helicopter Rotor Properties

Table B.1. Stiffness and geometry properties of the BO 105 main rotor system, Ref. [170].

Constants	Units	Values	Description
P_{11}	10^6 N	73.0	tensional stiffness
P_{22}	10^6 N	6.18	chordwise shear stiffness
P_{33}	10^6 N	0.89	flapwise shear stiffness
P_{44}	10^3 Nm^2	4.85	torsional stiffness
P_{55}	10^3 Nm^2	6.82	chordwise bending stiffness
P_{66}	10^3 Nm^2	173	flapwise bending stiffness
$\bar{X}$	m	0.37	radius of blade bolt position
X	m	4.54	blade length from bolt to tip
b	m	0.27	blade chord
Ω	1/s	44.4	rotor angular velocity

T.H. Brockmann, *Theory of Adaptive Fiber Composites*,
Solid Mechanics and Its Applications 161,

References

[1] J. Aboudi, *Mechanics of Composite Materials—A Unified Micromechanical Approach*. Studies in Applied Mechanics (Elsevier Science Publishers, Amsterdam, 1991)

[2] J. Aboudi, Micromechanical prediction of the effective coefficients of thermo-piezoelectric multiphase composites. J. Intell. Mater. Syst. Struct. **9**, 713–722 (1998)

[3] K. Adachi, G. Park, D.J. Inman, Shunting macro-fiber composite actuator for structural damping, in *Noise and Vibration Engineering: Proceedings of ISMA 2002*, ed. by P. Sas, B. Van Hal (Katholieke Universiteit Leuven, Leuven, 2002), pp. 411–419

[4] H. Allik, T.J.R. Hughes, Finite element method for piezoelectric vibration. Int. J. Numer. Methods Eng. **2**, 151–157 (1970)

[5] M. Allongue, H.J. Marze, F. Potdevin, The quiet helicopter—from research to reality, in *Proceedings of the American Helicopter Society 55th Annual Forum* (American Helicopter Society, Montreal, 1999)

[6] H. Altenbach, J. Altenbach, R. Rikards, *Einführung in die Mechanik der Laminat- und Sandwichtragwerke* (Deutscher Verlag für Grundstoffindustrie, Stuttgart, 1996)

[7] E.A. Armanios, A.M. Badir, Free vibration analysis of anisotropic thin-walled closed-section beams. AIAA J. **33**(10), 1905–1910 (1995)

[8] H. Banno, Recent developments of piezoelectric ceramic products and composites of synthetic rubber and piezoelectric ceramic particles. Ferroelectrics **50**, 3–12 (1983)

[9] W. Becker, D. Gross, *Mechanik elastischer Körper und Strukturen* (Springer, Berlin, 2002)

[10] W. Beckert, W.S. Kreher, Modelling piezoelectric modules with interdigitated electrode structures. Comput. Mater. Sci. **26**, 36–45 (2003)

[11] W. Beitz, K.H. Küttner, *Dubbel—Taschenbuch für den Maschinenbau*, 14th edn. (Springer, Berlin, 1981)

[12] A. Benjeddou, J.F. Deü, S. Letombe, Free vibrations of simply-supported piezoelectric adaptive plates: An exact sandwich formulation. Thin-Walled Struct. **40**, 573–593 (2002)

T.H. Brockmann, *Theory of Adaptive Fiber Composites*,
Solid Mechanics and Its Applications 161,

[13] A.A. Bent, *Active fiber composites for structural actuation*. Ph.D. Thesis, Massachusetts Inst. of Tech. (1997)
[14] A.A. Bent, N.W. Hagood, Improved performance in piezoelectric fiber composites using interdigitated electrodes, in *Smart Structures and Materials 1995: Smart Materials*, ed. by A.P. Jardine. Proceedings of SPIE, vol. 2441 (SPIE, Bellingham, 1995), pp. 196–212
[15] A.A. Bent, N.W. Hagood, Piezoelectric fiber composites with interdigitated electrodes. J. Intell. Mater. Syst. Struct. **8**, 903–919 (1997)
[16] A.A. Bent, N.W. Hagood, J.P. Rodgers, Anisotropic actuation with piezoelectric fiber composites, in *Proceedings of the 4th International Conference on Adaptive Structures and Technologies, Cologne, Germany* (CRC Press, Boca Raton, 1993), pp. 418–433
[17] A.A. Bent, N.W. Hagood, J.P. Rodgers, Anisotropic actuation with piezoelectric fiber composites. J. Intell. Mater. Syst. Struct. **6**(3), 338–349 (1995)
[18] Y. Benveniste, A new approach to the application of Mori–Tanaka's theory in composite materials. Mech. Mater. **6**, 147–157 (1987)
[19] D. Berlincourt, H.H.A. Krueger, *Properties of specialized Clevite ceramics*. Technical Report TP-232, Morgan Electro Ceramics
[20] D. Berlincourt, H.H.A. Krueger, C. Near, *Properties of piezoelectricity ceramics*. Technical Report TP-226, Morgan Electro Ceramics
[21] R.L. Bielawa, *Rotary Wing Structural Dynamics and Aeroelasticity*. AIAA Education Series (American Institute of Aeronautics and Astronautics, Washington, 1992)
[22] E.R. Booth, M.L. Wilbur, Acoustic aspects of active-twist rotor control, in *Proceeding of the American Helicopter Society 58th Annual Forum* (American Helicopter Society, Montreal, 2002)
[23] A.R.S. Bramwell, G. Done, D. Balmford, *Bramwell's Helicopter Dynamics* (Butterworth Heinemann, Oxford, 2001)
[24] R. Bredt, Kritische Bemerkungen zur Drehungselastizität. Z. Ver. Dtsch. Ing. **40**, 785 (1896)
[25] K.S. Brentner, F. Farassat, Helicopter noise prediction: The current status and future direction. J. Sound Vib. **170**(1), 79–96 (1994)
[26] T.H. Brockmann, R. Lammering, An analytic approach to piezoelectric fiber composites—from micromechanics modeling to beam behavior. Z. Angew. Math. Mech. **81**(2), 281–282 (2001)
[27] T.H. Brockmann, R. Lammering, Analysis of piezoelectric fiber composite beams, in *Smart Structures and Materials 2001: Smart Structures and Integrated Systems*, ed. by L. Porter Davies. Proceedings of SPIE, vol. 4327 (SPIE, Bellingham, 2001), pp. 460–471
[28] T.H. Brockmann, R. Lammering, Analysis of piezoelectric fiber composite structures and finite element validation, in *Solids, Structures, and Coupled Problems in Engineering: Proceedings of ECCM 2001*, ed. by Z. Waszczyszyn, J. Pamin (Vesalius, Cracow, 2001)
[29] T.H. Brockmann, R. Lammering, An analytic approach to piezoelectric fiber composites—design study of active beams with closed cross-sections. Proc. Appl. Math. Mech. **1**(1), 139–140 (2002)
[30] T.H. Brockmann, R. Lammering, Dynamics of rotating piezoelectric fiber composite beams, in *Noise and Vibration Engineering: Proceedings of ISMA 2002*, ed. by P. Sas, B. Van Hal (Katholieke Universiteit Leuven, Leuven, 2002), pp. 167–176

[31] T.H. Brockmann, R. Lammering, Adaptive concepts to reduce noise and vibrations of helicopter rotors, in *Anwendungen der Akustik in der Wehrtechnik*, ed. by B. Nolte (Studiengesellschaft der DWT, Bonn, 2002), pp. 12–26
[32] T.H. Brockmann, R. Lammering, Active damping of helicopter rotor blades with piezoelectric fiber composites, in *Second International Workshop on Damping Technologies: Materials and Devices for the Next Decade* (Universiteit Stellenbosch, Stellenbosch, 2003)
[33] T.H. Brockmann, R. Lammering, Finite beam elements for rotating piezoelectric fiber composite structures, in *Computational Fluid and Solid Mechanics 2003*, ed. by K.J. Bathe (Elsevier, Amsterdam, 2003)
[34] T.H. Brockmann, R. Lammering, Helicopter rotor blade dynamics with adaptive fiber composites, in *Jahrbuch 2004 der Deutschen Gesellschaft Für Luft- und Raumfahrt Lilienthal-Oberth e.V.* (DGLR, Bonn, 2004)
[35] T.H. Brockmann, R. Lammering, Beam finite elements for rotating piezoelectric fiber composite structures. J. Intell. Mater. Syst. Struct. **17**(5), 431–448 (2006)
[36] T.H. Brockmann, R. Lammering, F. Yang, Modelling and computational analysis of structures with integrated piezoelectric material, in *Proceedings of the II ECCOMAS Thematic Conference on Smart Structures and Materials*, ed. by C.A. Mota Soares (ECCOMAS, Lisbon, 2005)
[37] T.H. Brockmann, R. Lammering, F. Yang, Modelling and computational analysis of structures with integrated piezoelectric material. Mech. Adv. Mater. Struct. **13**(5), 371–378 (2006)
[38] G. Brunk, M. Kraska, *Tensorrechnung*. Technische Universität Berlin, Institut für Mechanik (1998)
[39] A. Budó, *Theoretische Mechanik*. Hochschulbücher für Physik (VEB Deutscher Verlag der Wissenschaften, Berlin, 1974)
[40] A. Büter, *Untersuchung adaptiver Konzepte zur Reduktion von Hubschraubervibrationen, zur Minderung des Hubschrauberlärms und zur Steigerung der aerodynamischen Effizienz*. Ph.D. Thesis, RWTH, Aachen, DLR Braunschweig (1998)
[41] W.G. Cady, *Piezoelectricity—An Introduction to the Theory and Applications of Electromechanical Phenomena in Crystals* (Dover, New York, 1964)
[42] B.J. Cannon, D. Brei, Feasibility study of microfabrication by coextrusion (MFCX) hollows fibers for active composites. J. Intell. Mater. Syst. Struct. **11**, 659–670 (2000)
[43] M.J. Carpenter, Using energy methods to derive beam finite elements incorporating piezoelectric materials. J. Intell. Mater. Syst. Struct. **8**, 26–40 (1997)
[44] C.E.S. Cesnik, *Wing shape deformation for high-performance aerial vehicles*. ICASE Morphing Seminar Series. Presentation (2002)
[45] C.E.S. Cesnik, R. Palacios, Modeling piezocomposite actuators embedded in slender structures, in *44th AIAA/ASME/ASCE/AHS Structures, Structural Dynamics, and Materials Conference*. AIAA, vol. 2003-1803 (AIAA, Norfolk, 2003).
[46] C.E.S. Cesnik, S.J. Shin, On the modeling of integrally actuated helicopter blades. Int. J. Solids Struct. **38**(10–13), 1765–1789 (2001)
[47] C.E.S. Cesnik, S. Shin, W.K. Wilkie, M.L. Wilbur, P.H. Mirick, Modeling, design, and testing of the NASA/Army/MIT active twist rotor prototype blade, in *Proceedings of the American Helicopter Society 55th Annual Forum* (AHS, Montreal, 1999).

[48] C.E.S. Cesnik, S.J. Shin, M.L. Wilbur, Dynamic response of active twist rotor blades. Smart Mater. Struct. **10**(1), 62–76 (2001)
[49] H.L.W. Chan, J. Unsworth, Simple model for piezoelectric Ceramic/Polymer 1–3 composites used in ultrasonic transducer applications. IEEE Trans. Ultrason., Ferroelectr. Freq. Control **36**(4), 434–441 (1989)
[50] K.K. Chawla, *Composite Materials—Science and Engineering* (Springer, New York, 1998)
[51] P.C. Chen, I. Chopra, A feasibility study to build a smart rotor: Induced-strain actuation of airfoil twisting using piezoceramic crystals, in *Smart Structures and Intelligent Systems (Proceedings)*, vol. 1917 (SPIE, Bellingham, 1993), pp. 238–254
[52] P.C. Chen, I. Chopra, Hover testing of smart rotor with induced-strain actuation of blade twist. AIAA J. **35**(1), 6–16 (1997)
[53] I. Chopra, Review of state of art of smart structures and integrated systems. AIAA J. **40**(11), 2145–2187 (2002)
[54] R.M. Christensen, *Mechanics of Composite Materials* (Wiley, New York, 1979)
[55] L. Collatz, W. Wetterling, *Optimierungsaufgaben*. Heidelberger Taschenbücher (Springer, Berlin, 1971)
[56] R. Courant, D. Hilbert, *Methoden der Mathematischen Physik*, vols. 1 & 2 (Springer, Berlin, 1968)
[57] B.N. Cox, G. Flanagan, *Handbook of analytical methods for textile composites*. Technical Report NASA Contractor Report 4750, NASA Langley Research Center (1997)
[58] E.F. Crawley, K.B. Lazarus, Induced strain actuation of isotropic and anisotropic plates. AIAA J. **29**(6), 944–951 (1991)
[59] J. Curie, P. Curie, Développement, par pression, de l'électricité polaire dans les cristaux hémièdres à faces inclinées. C. R. Hebd. Séances Acad. Sci. **91**, 294–295 (1880)
[60] J. Curie, P. Curie, Sur l'électricité polaire dans les cristaux hémièdres à faces inclinées. C. R. Hebd. Séances Acad. Sci. **91**, 383–386 (1880)
[61] W.F. Deeg, *The analysis of dislocation, crack, and inclusion problems in piezoelectric solids*. Ph.D. Thesis, Stanford University (1980)
[62] M.M. Denn, *Optimization by Variational Methods* (McGraw-Hill Book Company, New York, 1969)
[63] B. Domke, *Aviation images*, www.b-domke.de/AviationImages.html (2002)
[64] L.H. Donnell, *Stability of thin-walled tubes under torsion*. Technical Report NACA Report No. 479, National Advisory Committee for Aeronautics (1933)
[65] A.J. Du Plessis, N. Hagood, *Modeling and experimental testing of twist actuated single cell composite beams for helicopter blade control*. Master's Thesis, Massachusetts Inst. of Tech. (1996)
[66] M.L. Dunn, M. Taya, An analysis of piezoelectric composite materials containing ellipsoidal inhomogenities. Proc. R. Soc. Lond. A **443**, 265–287 (1993)
[67] M.L. Dunn, M. Taya, Micromechanics predictions of the effective electroelastic moduli of piezoelectric composites. Int. J. Solids Struct. **30**(2), 161–175 (1993)
[68] G.J. Dvorak, M.V. Srinivas, New estimates of overall properties of heterogeneous solids. J. Mech. Phys. Solids **47**, 899–920 (1999)
[69] C.L. Dym, *Introduction to the Theory of Shells* (Pergamon, Oxford, 1974)
[70] C.L. Dym, I.H. Shames, *Solid Mechanics: A Variational Approach*. Advanced Engineering Series (McGraw-Hill Book Company, New York, 1973)

[71] B. Edwards, C. Cox, *Revolutionary concepts for helicopter noise reduction—S.I.L.E.N.T. program*. Technical Report CR-2002-211650, NASA, Langley Research Center (2002)
[72] J.E. Elspass, M. Flemming, *Aktive Funktionsbauweisen* (Springer, Berlin, 1998)
[73] J.D. Eshelby, The determination of the elastic field of an ellipsoidal inclusion, and related problems. Proc. R. Soc. Lond. A **241**, 376–396 (1957)
[74] J. Fischer, *Elektrodynamik: Ein Lehrbuch* (Springer, Berlin, 1976)
[75] G. Floquet, Sur les équations différentielles linéaires à coefficients périodiques. Ann. Ec. Norm. **12**(2), 37–89 (1883)
[76] B.D. Freed, V. Babuska, Finite element modeling of composite piezoelectric structures with MSC/NASTRAN, in *Smart Structures and Materials 1997: Smart Structures and Integrated Systems*. Proceedings of SPIE, vol. 3041 (SPIE, Bellingham, 1997), pp. 676–688
[77] P. Funk, *Variationsrechnung und ihre Anwendung in Physik und Technik*, 2nd edn. Die Grundlehren der mathematischen Wissenschaften in Einzeldarstellung, vol. 94 (Springer, Berlin, 1970)
[78] R. Gasch, K. Knothe, *Strukturdynamik*, vols. 1 & 2 (Springer, Berlin, 1987 & 1989)
[79] W. Gembler, Leise Hubschrauber Zelle, Abschlußbericht 20 H 95 07 A. EUROCOPTER Deutschland GmbH (1999)
[80] M. Gérardin, D. Rixen, Parametrization of finite rotations in computational dynamics: A review. Rev. Europ. Élém. Finis **4**, 497–553 (1995)
[81] K. Ghandi, N.W. Hagood, *Nonlinear modeling and characterisation techniques for phase transition in electro-mechanically coupled devices*. Ph.D. Thesis, Massachusetts Inst. of Tech. (1998)
[82] G.L. Ghiringhelli, P. Masarati, P. Mantegazza, *Analysis of an Actively Twisted Rotor by Multi-Body Global Modeling*. ASME Mechanics and Materials Conference (Blacksburg, Virginia, 1999)
[83] C. Giacovazzo, *Fundamentals of Crystallography* (Oxford University Press, London, 2002)
[84] K. Girkmann, *Flächentragwerke—Einführung in die Elastostatik der Scheiben, Platten, Schalen und Faltwerken*, 6th edn. (Springer, Wien, 1963)
[85] A. Gjelsvik, *The Theory of Thin-Walled Bars* (Wiley, New York, 1981)
[86] H. Goldstein, *Klassische Mechanik*, 3rd edn. (Akademische Verlagsgesellschaft, Frankfurt am Main, 1974)
[87] S.V. Gopinathan, V.V. Varadan, V.K. Varadan, A review and critique of theories for piezoelectric laminates. Smart Mater. Struct. **9**, 24–48 (2000)
[88] A.E. Green, W. Zerna, *Theoretical Elasticity* (Oxford University Press, London, 1975)
[89] F. Gruttmann, R. Sauer, W. Wagner, A geometric nonlinear eccentric 3D-beam element with arbitrary cross-section. Comput. Methods Appl. Mech. Eng. **160**, 383–400 (1998)
[90] N. Hagood, R. Kindel, K. Ghandi, P. Gaudenzi, Improving transverse actuation of piezoceramics using interdigitated surface electrodes, in *Smart Structures and Materials 1993: Smart Structures and Intelligent Systems*, ed. by M.E. Regelbrugge. Proceedings of SPIE, vol. 1917 (SPIE, Bellingham 1993), pp. 341–352

[91] W.G. Hankel, *Elektrische Untersuchungen. XV. Abhandlung: Ueber die aktino- und piezoelektrischen Eigenschaften des Bergkrystalles und ihre Beziehung zu den thermoelektrischen.* Abhandlungen der königlich sächsischen Gesellschaft der Wissenschaften, vol. 12(20) (Hirzel, Leipzig, 1881)
[92] J. Helbig, W. Glaubitt, H. Spaniol, P. Vierhaus, U. Lange, R. Hansch, W. Watzka, D. Sporn, Development and technology of doped sol-gel derived lead zirconate titanate fibers. Smart Mater. Struct. **12**, 987–992 (2003)
[93] S. Heo, J.H. Kim, Y.Y. Kim, Significance of distortion in thin-walled closed beam section design. Int. J. Solids Struct. **40**, 633–648 (2003)
[94] J.W. High, W.K. Wilkie, *Method for fabricating NASA-standard macro-fiber composite piezoelectric actuators.* Technical Report NASA/TM-2003-212427, NASA (2003)
[95] G.W. Hill, On the part of the motion of the linear perigee which is a function of the mean motions of the sun and moon. Acta Math. **8**, 1–36 (1886)
[96] D.H. Hodges, Review of composite rotor blade modeling. AIAA J. **28**(3), 561–565 (1990)
[97] D.H. Hodges, A mixed variational formulation based on exact intrinsic equations for dynamics of moving beams. Int. J. Solids Struct. **26**(11), 1253–1273 (1990)
[98] D.H. Hodges, E.H. Dowell, *Nonlinear equations of motion for the elastic bending and torsion of twisted nonuniform rotor blades.* NASA Technical Note NASA TN D-7818, National Aeronautics and Space Administration, Washington DC (1974)
[99] N.J. Hoff, The accuracy of Donnell's equation. J. Appl. Mech. **22**, 329–334 (1955)
[100] R. Holland, E.P. EerNisse, Variational evaluation of admittances of multielectroded three-dimensional piezoelectric structures. IEEE Trans. Sonics Ultrason. **15**, 119–132 (1968)
[101] T.J.R. Hughes, *The Finite Element Method* (Prentice-Hall, Englewood Cliffs, 1987)
[102] A. Huxley, *Brave New World* (Chatto and Windus, London, 1932)
[103] T. Ikeda, *Fundamentals of Piezoelectricity* (Oxford University Press, London, 1990)
[104] Institute of Electrical and Electronics Engineers. *Standard on Piezoelectricity, Std 176-1978* (IEEE, New York, 1978)
[105] M. Itskov, *Tensor Algebra and Tensor Analysis for Engineers—With Applications to Continuum Mechanics* (Springer, Berlin, 2007)
[106] H. Janocha (ed.), *Adaptronics and Smart Structures—Basics, Materials, Design, and Applications* (Springer, Berlin, 1999)
[107] R.M. Jones, *Mechanics of Composite Materials* (Scripta Book Company, Washington, 1975)
[108] S.N. Jung, V.T. Nagaraj, I. Chopra, Refined structural model for thin- and thick-walled composite rotor blades. AIAA J. **40**(1), 105–116 (2002)
[109] M. Kamlah, Ferroelectric and ferroelastic piezoceramics—modeling of electromechanical hysteresis phenomena. Contin. Mech. Thermodyn. **13**(4), 219–268 (2001)
[110] K.R.V. Kaza, R.G. Kvaternik, *Nonlinear aeroelastic equations for combined flapwise bending, chordwise bending, torsion, and extension of twisted nonuniform blades in forward flight.* Technical Memorandum TM 74059, NASA (1977)

[111] J. Kempner, Remarks on Donnell's equations. J. Appl. Mech. **22**, 117–118 (1955)
[112] V. Klöppel, B. Enenkel, et al., ADASYS I—Adaptives dynamisches System für Hubschrauber, Abschlußbericht 20 H 99 06 A. EUROCOPTER Deutschland GmbH (2001)
[113] K. Knothe, H. Wessels, *Finite Elemente—Eine Einführung für Ingenieure* (Springer, Berlin, 1999)
[114] W.T. Koiter, A consistent first approximation in the general theory of thin elastic shells, in *Proceedings of the Symposium on the Theory of Thin Elastic Shells*, ed. by W. Koiter. Internation Union of Theoretical and Applied Mechanics (North-Holland, Amsterdam, 1960), pp. 12–33
[115] P. Konstanzer, *Decentralized vibration control for active helicopter rotor blades*. Ph.D. Thesis, Universität Stuttgart, Stuttgart, Germany (2002)
[116] R.D. Kriz, W.S. Stinchcomb, Elastic moduli of transversely isotropic fibers and their composites. Exp. Mech. **19**, 41–49 (1979)
[117] D.L. Kunz, Survey and comparison of engineering beam theories for helicopter rotor blades. J. Aircr. **31**(3), 473–478 (1994)
[118] C. Lanczos, *The Variational Principles of Mechanics*. Mathematical Expositions (University of Toronto Press, Toronto, 1977)
[119] P.D. Lax, *Linear Algebra and Its Applications*, 2nd edn. Pure and Applied Mathematics (Wiley-Interscience, New York, 2007)
[120] G. Lehner, *Elektromagnetische Feldtheorie für Ingenieure und Physiker* (Springer, Berlin, 2004)
[121] M. Leibowitz, J.R. Vinson, *Intelligent composites: Design and analysis of composite material structures involving piezoelectric material layers*. Technical Report 91-54, Center for Composite Materials, University of Delaware, Newark, Delaware, USA (1991)
[122] G.A. Lesieutre, Vibration damping and control using shunted piezoelectric materials. Shock Vib. Dig. **30**(3), 187–195 (1998)
[123] F.L. Matthews, R.D. Rawlings, *Composite Materials—Engineering and Science* (CRC Press, Boca Raton, 1999)
[124] R. Mehn, *Ein Beitrag zur Theorie von anisotropen dünnwandigen Stäben* (VDI-Verlag, Düsseldorf, 1986)
[125] L. Meirovitch, *Methods of Analytical Dynamics*. Advanced Engineering Series (McGraw-Hill Book Company, New York, 1970)
[126] D. Morgenstern, I. Szabó, *Vorlesungen über Theoretische Mechanik*. Die Grundlehren der mathematischen Wissenschaften in Einzeldarstellung, vol. 112 (Springer, Berlin, 1961)
[127] T. Mori, K. Tanaka, Average stress in matrix and average elastic energy of materials with misfit inclusions. Acta Metall. **21**, 571–574 (1973)
[128] A.J. Moulson, J.M. Herbert, *Electroceramics: Materials, Properties, Applications* (Wiley, New York, 2003)
[129] H. Murakami, E. Reissner, J. Yamakawa, Anisotropic beam theories with shear deformation. J. Appl. Mech. **63**, 660–668 (1996)
[130] National Aeronautics and Space Administration. NASA Technical Reports Server, http://ntrs.nasa.gov (2008)
[131] J.G. Nelson, R.R. Neurgaonkar, J.R. Oliver, C. Larson, S.K. Dobbi, J.S. Rosenthal, Piezoelectric technology: Research and applications, in *Smart Materials and Structures 1998: Smart Materials Technologies*, ed. by M.R. Wuttig. Proceedings of SPIE, vol. 3324 (SPIE, Bellingham, 1998)

[132] L.J. Nelson, Smart piezoelectric fibre composites. Mater. Sci. Technol. **18**(11), 1245–1256 (2002)
[133] R.E. Newnham, D.P. Skinner, L.E. Cross, Connectivity and piezoelectric-pyroelectric composites. Mater. Res. Bull. **13**, 525–536 (1978)
[134] V.V. Novozhilov, *Thin Shell Theory* (Wolters-Noordhoff Publishing, Groningen, 1970)
[135] G.M. Odegard, *Constitutive modeling of piezoelectric polymer composites*. NASA Contractor Report NASA/CR-2003-212681, National Aeronautics and Space Administration, Langley Research Center, Hampton, Virginia, USA (2003)
[136] K. Pannkoke, T. Gesang, M. Clüver, D. Sporn, A. Schönecker, Strukturkonform integrierbare Funktionsmodule auf der Basis von PZT-Fasern, in *Verbundwerkstoffe und Werkstoffverbunde* (Wiley, New York, 1999), pp. 582–586
[137] C. Park, I. Chopra, Modeling piezoceramic actuation of beams in torsion. AIAA J. **34**(12), 2582–2589 (1996)
[138] C.K. Park, C. Walz, I. Chopra, Bending and torsion models of beams with induced strain actuators, in *Smart Structures and Intelligent Systems (Proceedings)*, vol. 1917 (SPIE, Bellingham, 1993), pp. 192–215
[139] M. Päsler, *Prinzipe der Mechanik* (de Gruyter, Berlin, 1968)
[140] R. Paul, *Elektrotechnik: Grundlagenlehrbuch*, vols. 1 & 2 (Springer, Berlin, 1993 & 1994)
[141] D.A. Pierre, *Optimization Theory with Applications*. Series in Decision and Control (Wiley, New York, 1969)
[142] G.G. Poe, H.B. Dexter, I.S. Raju, A review of the NASA textile composites research. J. Aircr. **36**(5), 876–884 (1999)
[143] C. Poizat, M. Sester, Effective properties of composites with embedded piezoelectric fibers. Comput. Mater. Sci. **16**, 89–97 (1999)
[144] W. Prager, *Introduction to Mechanics of Continua* (Ginn and Company, Boston, 1961)
[145] J. Pretorius, M. Hugo, R. Spangler, A comparison of packaged piezoactuators for industrial applications, in *Smart Structures and Materials 2004: Industrial and Commercial Applications of Smart Structures Technologies*, ed. by E.H. Anderson. Proceedings of SPIE (SPIE, Bellingham, 2004), pp. 131–142
[146] T. Prothmann, *Zur Identifikation periodisch parametererregter Systeme*. Ph.D. Thesis, Universität der Bundeswehr Hamburg, Hamburg (2003)
[147] L. Råde, B. Westgren, *Mathematics Handbook for Science and Engineering* (Birkhäuser, Boston, 1995)
[148] O. Rand, In-plane warping effects in thin-walled box beams. AIAA J. **38**(3), 542–544 (2000)
[149] O. Rand, Nonlinear in-plane warping deformation in elastically coupled open thin-walled beams. Comput. Struct. **79**, 281–291 (2001)
[150] L.W. Rehfield, A.R. Atilgan, D.H. Hodges, Nonclassical behavior of thin-walled composite beams with closed cross sections. J. Am. Helicopter Soc. **35**(2), 42–50 (1990)
[151] E. Reissner, On a certain mixed variational theorem and a proposed application. Int. J. Numer. Methods Eng. **20**, 1366–1368 (1984)
[152] E. Reissner, W.T. Tsai, Pure bending, stretching, and twisting of anisotropic cylindrical shells. J. Appl. Mech. **39**, 148–154 (1972)
[153] J.R. Reitz, F.J. Milford, R.W. Christy, *Foundations of Electromagnetic Theory*. Addison-Wesley Series in Physics (Addison-Wesley, Reading, 1979)

[154] A. Reuss, Berechnung der Fließgrenze von Mischkristallen auf Grund der Plastizitätsbedingung für Einkristalle. Z. Angew. Math. Mech. **9**, 49–58 (1929)
[155] J. Rodgers, N.W. Hagood, Preliminary mach-scale hover testing of an integral twist-actuated rotor blade, in *Smart Structures and Materials 1998: Smart Structures and Integrated Systems*, ed. by M.E. Regelbrugge. Proceedings of SPIE, vol. 3329 (SPIE, Bellingham, 1998), pp. 291–308
[156] K. Roik, J. Carl, J. Lindner, *Biegetorsionsprobleme gerader dünnwandiger Stäbe* (Verlag von Wilhelm Ernst & Sohn, Berlin, 1972)
[157] M.B. Rubin, *Cosserat Theories: Shells, Rods and Points*. Solid Mechanics and Its Applications (Kluwer Academic, Dordrecht, 2000)
[158] J.L. Sanders, *An improved first-approximation theory for thin shells*. Technical Report NASA TR R-24, National Aeronautics and Space Administration, Langley Research Center (1959)
[159] R. Sauer, Eine einheitliche Finite-Elemente-Formulierung für Stab- und Schalentragwerke mit endlichen Rotationen. Bericht, Universität Karlsruhe (1998)
[160] C. Schaefer, M. Päsler, *Einführung in die theoretische Physik*, vols. 1 & 3 (de Gruyter, Berlin, 1970 & 1950)
[161] F.H. Schmitz, Y.H. Yu, Helicopter impulsive noise: Theoretical and experimental status. J. Sound Vib. **109**(3), 361–422 (1986)
[162] E.F. Sheta, R.W. Moses, L.J. Huttsell, V.J. Harrand, Active control of F/A-18 vertical tail buffeting using piezoelectric actuators, in *44th AIAA/ASME/ASCE/AHS/ASC Structures, Structural Dynamics & Materials Conference*. AIAA, vol. 2003-1887 (AIAA, Norfolk, 2003)
[163] J.G. Simmonds, A set of simple, accurate equations for circular cylindrical elastic shells. Int. J. Solids Struct. **2**, 525–541 (1966)
[164] J.C. Simo, L. Vu-Quoc, On the dynamics in space of rods undergoing large motions—a geometrically exact approach. Comput. Methods Appl. Mech. Eng. **66**, 125–161 (1988)
[165] W.A. Smith, B.A. Auld, Modeling 1–3 composite piezoelectrics: Thickness-mode oscillations. IEEE Trans. Ultrason. Ferroelectr. Freq. Control **38**(1), 40–47 (1991)
[166] I.S. Sokolnikoff, *Mathematical Theory of Elasticity* (McGraw-Hill Book Company, New York, 1956)
[167] I.S. Sokolnikoff, *Tensor Analysis Theory and Applications to Geometry and Mechanics of Continua* (Wiley, New York, 1964)
[168] R. Staufenbiel, J. Schreier, G. Neuwerth, *Lärmerzeugung von Hubschraubern unter besonderer Berücksichtigung des Heckrotors*. Forschungsberichte des Landes Nordrhein-Westfalen Nr. 3144, Minister für Wissenschaft und Forschung (1982)
[169] R. Steinhausen, *Charakterisierung und Modellierung piezoelektrischer 1–3 Komposite*. Ph.D. Thesis, Martin-Luther-Universität Halle-Wittenberg (2002)
[170] H. Strehlow, B. Enenkl, *Zusammenstellung der BO105-Blattdaten*. Data sheets (1999)
[171] H.B. Strock, M.R. Pascucci, M.V. Parish, A.A. Bent, T.R. Shrout, Active PZT fibers: A commercial production process, in *Smart Structures and Materials 1999: Smart Materials Technologies*, ed. by M.R. Wuttig. Proceedings of SPIE (SPIE, Bellingham, 1999), pp. 22–31
[172] I. Szabó, *Höhere Technische Mechanik: Nach Vorlesungen* (Springer, Berlin, 1977)

[173] P. Tan, L. Tong, Micro-electromechanics models for piezoelectric-fiber-reinforced composite materials. Comput. Sci. Technol. **61**, 759–769 (2001)
[174] J. Tichý, G.H. Gautschi, *Piezoelektrische Meßtechnik: Physikalische Grundlagen, Kraft-, Druck- und Beschleunigungsaufnehmer, Verstärker* (Springer, Berlin, 1980)
[175] W. Voigt, Über die Beziehung zwischen den beiden Elastizitätskonstanten isotroper Körper. Ann. Phys. **38**, 573–587 (1889)
[176] V.V. Volovoi, D.H. Hodges, Theory of anisotropic thin-walled beams. J. Appl. Mech. **67**, 453–459 (2000)
[177] G. Wempner, *Mechanics of Solids with Applications to Thin Bodies*. Advances Engineering Series (McGraw-Hill Book Company, New York, 1973)
[178] J.M. Whitney, *Structural Analysis of Laminated Anisotropic Plates* (Technomic Publishing Company, Lancaster, 1987)
[179] J. Wiedemann, *Leichtbau—Elemente & Konstruktion*, vols. 1 & 2 (Springer, Berlin, 1986 & 1989)
[180] M.L. Wilbur, W.T. Yeager, M.K. Sekula, Further examination of the vibratory loads reduction results from the NASA/ARMY/MIT active twist rotor test, in *Proceedings of the American Helicopter Society 58th Annual Forum* (American Helicopter Society, Montreal, 2002)
[181] W.K. Wilkie, K.C. Park, *An aeroelastic analysis of helicopter blades incorporating piezoelectric fiber composite twist actuation*. Technical Memorandum TM 110252, NASA (1996)
[182] W.K. Wilkie, R.G. Bryant, J.W. High, R.L. Fox, R.F. Hellbaum, A. Jalink, B.D. Little, P.H. Mirick, Low-cost piezocomposite actuator for structural control applications, in *Smart Structures and Materials 2000: Industrial and Commercial Applications of Smart Structures Technologies*, ed. by J.H. Jacobs. Proceedings of SPIE, vol. 3991 (SPIE, Bellingham, 2000)
[183] W.K. Wilkie, D.J. Inman, J.M. Lloyd, J.W. High, Anisotropic piezocomposite actuator incorporating machined PMN-PT single crystal fibers, in *45th AIAA/ASME/ASCE/AHS/ASC Structures, Structural Dynamics & Materials Conference, Palm Springs, California, USA*. AIAA, vol. 2004-1889 (AIAA, Washington, 2004)
[184] R.B. Williams, D.J. Inman, An overview of composite actuators with piezoelectric fibers, in *Proceedings of the 20th International Modal Analysis Conference*, Los Angeles, California, USA (2002)
[185] M.J. Wygodski, *Höhere Mathematik—Griffbereit* (Friedr. Vieweg + Sohn, Braunschweig, 1973)
[186] R. Zhang, B. Jiang, W. Jiang, W. Cao, Elastic, dielectric and piezoelectric coefficients of domain engineered $0.70Pb(Mg_{1/3}Nb_{2/3})O_3$–$0.30PbTiO_3$ single crystal, in *Fundamental Physics of Ferroelectrics 2002*, vol. 626, ed. by R.E. Cohen (Amer. Inst. of Physics Publ. Srvs., Washington, 2002), pp. 188–197
[187] D. Zhou, *Experimental investigation of non-linear constitutive behavior of PZT piezoceramics*. Ph.D. Thesis, Universität Karlsruhe (TH), Karlsruhe (2003)
[188] R. Zurmühl, S. Falk, *Matrizen und ihre Anwendungen für Angewandte Mathematiker, Physiker und Ingenieure*, vols. 1 & 2 (Springer, Berlin, 1984)

Index

T.H. Brockmann, *Theory of Adaptive Fiber Composites*,
Solid Mechanics and Its Applications 161,